

BONNER METEOROLOGISCHE ABHANDLUNGEN

Heft 92 (2021) (ISSN 0006-7156)

Herausgeber: Andreas Hense

Sebastian Brune

**DER WAVELET-BASIERTE ORGANISATIONSSINDEX
ALS MASS DER KONVEKTIVEN ORGANISATION
ÜBER DEUTSCHLAND UND DEM TROPISCHEN ATLANTIK**

BONNER METEOROLOGISCHE ABHANDLUNGEN

Heft 92 (2021) (ISSN 0006-7156)

Herausgeber: Andreas Hense

Sebastian Brune

**DER WAVELET-BASIERTE ORGANISATIONSSINDEX
ALS MASS DER KONVEKTIVEN ORGANISATION
ÜBER DEUTSCHLAND UND DEM TROPISCHEN ATLANTIK**

Der Wavelet-basierte Organisationsindex als Maß der konvektiven Organisation über Deutschland und dem tropischen Atlantik

DISSERTATION
ZUR
ERLANGUNG DES DOKTORGRADES (DR. RER. NAT.)
DER
MATHEMATISCH-NATURWISSENSCHAFTLICHEN FAKULTÄT
DER
RHEINISCHEN FRIEDRICH-WILHELMS-UNIVERSITÄT BONN

vorgelegt von
M.Sc.
Sebastian Brune
aus
Papenburg

Bonn, Mai, 2021

Diese Arbeit ist die ungekürzte Fassung einer der Mathematisch-Naturwissenschaftlichen Fakultät der Rheinischen Friedrich-Wilhelms-Universität Bonn im Jahr 2021 vorgelegten Dissertation von Sebastian Brune aus Papenburg.

This paper is the unabridged version of a dissertation thesis submitted by Sebastian Brune born in Papenburg to the Faculty of Mathematical and Natural Sciences of the Rheinische Friedrich-Wilhelms-Universität Bonn in 2021.

Anschrift des Verfassers:

Address of the author:

Sebastian Brune
Institut für Geowissenschaften, Abt. Meteorologie
Universität Bonn
Auf dem Hügel 20
D-53121 Bonn

1. Gutachter: PD Dr. Petra Friederichs,
Rheinische Friedrich-Wilhelms-Universität Bonn
2. Gutachter: Prof. Dr. Andreas Hense,
Rheinische Friedrich-Wilhelms-Universität Bonn

Tag der Promotion: 06. Oktober 2021

Inhaltsverzeichnis

Zusammenfassung	3
1 Einleitung	7
2 Theoretische Grundlagen	11
2.1 Organisationsindexe	11
2.1.1 Simple Convective Aggregation Index (SCAI)	11
2.1.2 Organization Index (I_{org})	12
2.1.3 Convective Organization Potential (COP)	12
2.2 Wavelet-Transformation	13
2.2.1 Diskrete Wavelet-Transformation (DWT)	13
2.2.2 Dual-Tree Complex Wavelet Transformation (DTCWT)	14
3 Konvektive Organisation über Deutschland	17
3.1 Einleitende Worte zu den Zielen und zur Vorgehensweise	17
3.2 Der Wavelet-basierte Organisationsindex (WOI)	17
3.3 Zusammenfassung der Ergebnisse	18
4 Konvektive Organisation über dem tropischen Atlantik	21
4.1 Einleitende Worte zu den Zielen und zur Vorgehensweise	21
4.2 Der modifizierte WOI	22
4.3 Der lokal berechnete WOI (LWOI)	22
4.4 Zusammenfassung der Ergebnisse	23
5 Konvektive Organisation besonderer Ereignisse anhand von Radar- und Satellitendaten	27
5.1 Einleitende Worte zu den Zielen und zur Vorgehensweise	27
5.2 Der Dual-Tree LWOI (LW)	28
5.3 Zusammenfassung der Ergebnisse	29
6 Software-Paket zur Berechnung von WOI, LWOI und LW	31
6.1 Einleitung	31
6.2 Zusammenfassung der wesentlichen Funktionen	31
6.2.1 Die Funktion WOI	31
6.2.2 Die Funktion LW	32
7 Weitere Arbeiten im Rahmen dieser Dissertation	33
7.1 Artikel Kapp et al. (2018)	33
7.2 Artikel Stevens et al. (2020)	33

8 Fazit und Ausblick	35
Symbol- und Abkürzungsverzeichnis	37
Literaturverzeichnis	41
Danksagung	47
Liste aller Publikationen und Zuständigkeiten der Autoren	49

Zusammenfassung

In dieser Arbeit wird die konvektive Organisation mithilfe von zweidimensionalen Wavelet-Transformationen der Regenrate und der Helligkeitstemperatur analysiert. Aus dem Wavelet-Spektrum lassen sich Informationen über die Skala der Konvektion, deren Intensität und deren Orientierung ableiten. Jede der drei Größen bildet eine Komponente des neu eingeführten Wavelet-basierten Organisationsindex (WOI).

In einer ersten Studie wird der WOI benutzt, um zwischen sehr unorganisierter Konvektion und organisierten konvektiven Strukturen (Multizellen, Squall-Line) zu unterscheiden. Grundlage dafür bilden drei Fallstudien mit hochauflösenden ICON-Simulationen über Deutschland. Die berechneten Wavelet-Spektren der Regenraten zeigen, dass unorganisierte Konvektion kleinskaliger ist und eine geringere Intensität aufweist als organisierte Konvektion in Form von Multizellen und Squall-Lines. Letztere zeichnen sich zusätzlich durch eine Richtungsabhängigkeit im Wavelet-Spektrum aus. Ein Vergleich mit Wavelet-Spektren aus Radarbeobachtungen liefern ein ähnliches Bild. Die dynamischen und konvektiven Variablen wie Windscherung, Helizität, CIN und CAPE aus dem ICON-Modell offenbaren derweil zwei unterschiedliche Cluster: Wenig organisierte Konvektion tritt in Verbindung mit schwachen Höhenwinden und einer damit einhergehenden geringen vertikalen Windscherung auf, während sich die organisierte Konvektion durch ein stärkeres Forcing entwickeln kann. Vor Ausbruch der organisierten Konvektion kann sich im Tagesverlauf mehr CAPE aufbauen, da die Luftmasse durch erhöhtes CIN anfangs gedeckelt ist. Neben WOI werden auch drei in der Literatur etablierte konvektive Organisationsindexe berechnet. Es stellt sich heraus, dass WOI in dieser Fallstudie unorganisierte Konvektion von organisierten Strukturen unterscheiden kann, während die anderen Indexe nur 90 % aller Zeitschritte richtig zuordnen können.

Die drei WOI-Komponenten sind untereinander nicht direkt vergleichbar, sodass im nächsten Schritt eine Normierung eingeführt wird. Weiterhin stellt sich heraus, dass durch die Wahl eines alternativen Wavelets die Struktur des Niederschlags besser erfasst werden kann. Durch diese Anpassungen wird es möglich, die konvektive Organisation erstmals auf einer Karte zu lokalisieren (LWOI) und somit Regionen unterschiedlicher konvektiver Organisation zu identifizieren. Diese Erweiterung von WOI in zwei Dimensionen wird auf ICON-Simulationen über dem tropischen Atlantik angewendet. Im Vergleich zu den maritimen konvektiven Umlagerungen ist die Konvektion über dem afrikanischen Festland großskaliger und intensiver. Ähnliche Erkenntnisse liefert LWOI für Niederschlagsabschätzungen via Satelliten im Mikrowellen- und Infrarotbereich. Ein Vergleich mit den dynamischen und konvektiven Variablen zeigt auch hier klare Unterschiede zwischen den unterschiedlichen Graden der konvektiven Organisation über dem Festland und dem benachbarten Atlantik.

Im dritten Schritt wird die Struktur von Schauern und Gewittern sowie bei Hagelereignissen oder Starkniederschlägen mit dem finalen Index LW untersucht. Eine abschließende Optimierung sorgt dafür, dass der LW frei von Schwellenwerten ist und auf einer belie-

bigen zweidimensionalen Variable flexibel anwendbar ist. Während zuvor Regenraten als Grundlage für das Wavelet-Spektrum dienten, wird der Index LW auch auf Helligkeitstemperaturen angewendet. Es zeigt sich, dass Hagel- und Starkregenereignisse mit intensiven Niederschlägen und niedrigen Helligkeitstemperaturen einhergehen. Die Skala der intensiven Konvektion ist dabei sehr klein, d. h., dass das Ereignis auf einen sehr engen Raum begrenzt ist. Darüber hinaus ist es sogar möglich, mithilfe von LW_{sc} , LW_{in} und LW_{ai} zwischen Schauern, Gewittern und Hagel-/Starkregenereignissen zu klassifizieren.

Abstract

Convective organization is analyzed with help of a two-dimensional wavelet transform of rain rate and brightness temperature. From the wavelet spectrum, information about the scale of convection, its intensity and its orientation can be derived. Each of the three quantities forms a component of the so-called wavelet-based organization index (WOI).

First, WOI is used to distinguish between scattered convection and a linearly organized squall line in the midlatitudes. A comparison with dynamic and convective variables within three case studies shows that WOI differentiates better between unorganized structures and linear convection than ordinary organization indices from literature.

However, the original definition of WOI still has some weaknesses. Through normalization and the choice of a different wavelet, all three components become more comparable. Thus, convective organization can be localized on a map for the first time (LWOI). It turns out that the organization of squall lines over Africa differs from the maritime convection over the tropical Atlantic in scale and intensity. A comparison with the dynamic and convective variables also shows clear differences between the different degrees of convective organization.

In the third and final step, the structure of showers and thunderstorms as well as in the area of hail or heavy precipitation is examined with the final index LW. A final optimization ensures that LW is also free of threshold values and can be flexibly applied to any two-dimensional variable. The index LW is also applied to brightness temperatures instead of rain rates. It turns out that hail and heavy rain events are associated with intense rainfall and low brightness temperatures. The scale of the intense convection is very small, i.e. the events local phenomena. Furthermore, it is even possible to classify between showers, thunderstorms and hail/heavy rain events using LW_{sc} , LW_{in} and LW_{ai} .

1 Einleitung

In den letzten Jahren hat sich die Auflösung verschiedener Wetter- und Klimavorhersagemodelle immer weiter verbessert, sodass regionale hochauflösende Simulationen mit Gitterabständen von 150 m oder globale Simulationen mit Gitterabständen von 5 km möglich werden. Neben der besseren Beschreibung von turbulenten Wirbeln und einer verbesserten Repräsentation orografischer sowie anderer lokaler Effekte sorgt die höhere Modellauflösung auch dafür, dass verschiedene konvektive Prozesse nicht mehr subgitterskalig parametrisiert werden müssen, sondern teils explizit aufgelöst werden können. In dieser Dissertation wird in verschiedenen Simulationen und Beobachtungsdatensätzen untersucht, wie sich die äußeren Bedingungen wie Windscherung oder CAPE auf die Organisation von Konvektion auswirken. Darüber hinaus wird der Grad der konvektiven Organisation in Schauern und Gewittern bzw. während Hagel- und Starkregenereignissen analysiert.

Diese Arbeit entstand in der zweiten Phase des vom Bundesministerium für Bildung und Forschung geförderten Projektes "High Definition Clouds and Precipitation for Advancing Climate Prediction" (HD(CP)²). Ziel des Projektes war es, ein genaueres Verständnis der Zusammenhänge zwischen Wolken- und Niederschlagsbildung zu erlangen und die Repräsentation der verschiedenen Prozesse im Klima- und Wettervorhersagmodellen zu verbessern. Dafür wurden hochauflösende Simulationen durchgeführt, die von den Projektpartnern unter verschiedenen Gesichtspunkten ausgewertet wurden. Im Teilbereich S5 (Convective Organization) wurde schwerpunktmäßig die Wechselwirkung von der konvektiven Organisation und der synoptischen Skala untersucht.

Grundlage dafür ist eine akkurate Bestimmung der konvektiven Organisation. In der Literatur haben sich einige konvektive Organisationsindexe etabliert, die von unterschiedlichen Schwellenwerten und Variablen abhängen. Zumeist handelt es sich dabei um Variablen wie Helligkeitstemperaturen oder Niederschläge, die mittels Satelliten oder Radaren gemessen werden können. Die Indexe haben gemeinsam, dass sie auf objekt-basierten Clusteranalysen beruhen und den Grad der mittleren konvektiven Organisation über einer beliebig großen Domain messen. Dadurch ist keine Lokalisierung von stark organisierten Zellen und unorganisierten Zellen möglich. Stärken und Schwächen einzelner Indexe werden in Kapitel 2.1 diskutiert.

Um regionale Variation der konvektiven Organisation zu erfassen, werden in dieser Arbeit zweidimensionale Wavelet-Transformationen von Regenraten und Helligkeitstemperaturen interpretiert. Details zu den Wavelet-Transformationen sind in Kapitel 2.2 zu finden. In einer vorherigen Studie (Kapp et al., 2018) konnten wir mithilfe der Wavelet-Spektren die simulierten Niederschläge eines Ensembles mit 20 Membern der korrekten Beobachtung bzw. Reanalyse zuordnen (Kapitel 7.1). Dabei unterscheiden sich besonders die konvektiven Tage von Situationen mit frontalem Niederschlag. Der konvektive Niederschlag ist kleinskaliger, während der frontale Niederschlag eine starke Richtungsabhängigkeit aufweist, d. h. Fronten sind linear orientiert. Ähnliche Ergebnisse liefert die spektrale

Analyse von linear organisierter Konvektion wie im Falle einer Squall-Line. Squall-Lines sind größer in der Skala und linear, während beispielsweise Schauer hinter einer Kaltfront eher kleinskalig und isotrop sind. Neben der Skala der Konvektion und der Anisotropie beinhaltet das Wavelet-Spektrum auch Informationen über die Intensität, die durch die gesamte spektrale Energie beschrieben werden kann. Die drei Komponenten Skala, Intensität und Anisotropie bilden die Grundlage für den Wavelet-basierten Organisationsindex (WOI), der im Rahmen dieser Dissertation definiert und erweitert wird.

Konvektion tritt in vielen Regionen der Welt in unterschiedlichsten Formen auf. In den mittleren Breiten erstreckt sich Konvektion auf einer horizontale Skala von 10 – 100 m für einzelne Kumuli bzw. Shallow Convection über Einzelzellen von etwa 10 km bis hin zu großen konvektiven Systemen, die problemlos eine Größe von mehreren Hundert Kilometer erreichen können (Orlanski, 1975). Dementsprechend variiert auch die Lebensdauer der verschiedenen Zelltypen. Shallow Convection lebt auf Zeitskalen von wenigen Minuten, Einzelzellen haben einen Zyklus von bis zu 50 Minuten (Weisman & Klemp, 1986). Mit über drei Stunden handelt es sich bei Superzellen und Mesoskalige Konvektive Systeme bzw. Mesoskaligen Konvektiven Clustern um sehr langlebige Konvektionstypen (Parker & Johnson, 2000; Houze, 2004). Diese verschiedenen Strukturen werden in ICON-Simulationen mit einem Gitterabstand von rund 150 m und Radarbeobachtungen dreier unterschiedlicher Fallbeispiele (kurzlebige, kleinskalige Konvektion durch Höhenkaltluft; lokale Einzel-/Superzellen; Durchzug einer markanten Squall-Line) untersucht. Details dazu sind in Kapitel 3, welches die wesentlichen Ergebnisse aus Brune et al. (2018) zusammenfasst, zu finden.

In den Tropen existieren noch weitaus größere Systeme wie Hurrikane, African Easterly Waves (AEWs) oder die Madden-Julian-Oszillation (Petersen & Rutledge, 2001). Speziell die AEWs, bei denen es sich um westwärts propagierende Wellen in der unteren Troposphäre über Afrika handelt, nehmen großen Einfluss auf die Entwicklung von Konvektion über dem afrikanischen Festland und dem tropischen Atlantik (Carlson, 1969; Duvel, 1990; Fink & Reiner, 2003; Mekonnen et al., 2006; Crétat et al., 2015; Mekonnen & Rossow, 2018; Tomassini, 2018). Mit ihrer Periode von 2,5 bis 5 Tagen (Burpee, 1972; Lubis & Jacobi, 2015), einer Phasengeschwindigkeit von 8 – 10 m/s (Reed et al., 1977; Price et al., 2007) und einer Wellenlänge von 2000 – 5000 km (Diedhiou et al., 1999; Kiladis et al., 2006) sorgen sie für regelmäßiges Auftreten organisierter Konvektion in Form von mesoskaligen Systemen (Mathon & Laurent, 2001; Jackson et al., 2009; Rickenbach et al., 2009). Über dem tropischen Atlantik spielt neben dem Forcing aus der mittleren und oberen Atmosphäre vor allem die Oberflächentemperatur des Ozeans eine große Rolle (Xie & Carton, 2004). Dadurch zeichnet sich die Konvektion über dem tropischen Atlantik generell durch schwächere Regenraten und größere stratiforme Anteile aus (Schumacher & Houze Jr, 2006; Futyan & Del Genio, 2007; Liu et al., 2007; Janiga & Thorncroft, 2014; Janiga & Thorncroft, 2016). Diese regionalen Unterschiede der konvektiven Organisation über dem afrikanischen Kontinent und dem tropischen Atlantik wurden in Brune et al. (2020a) untersucht. Eine Zusammenfassung der Studie wird in Kapitel 4 gegeben.

Je nach Art der Konvektion kann es zu Begleiterscheinungen wie Großhagel, Starkwind, Extremniederschlag oder auch Tornados kommen. In dem Artikel von Brune et al. (2021) wird daher der Zusammenhang zwischen konvektiver Organisation und der Art des konvektiven Ereignisses untersucht (Kapitel 5 dieser Arbeit). Als Grundlage dienen zum einen die SYNOP-Meldungen aus dem Messnetz des Deutschen Wetterdienstes (DWD),

zum anderen Schadensmeldungen aus der European Severe Weather Database (Dotzek et al., 2009, ESWD). Wird von einer Wetterwarte ein Schauer oder ein Gewitter gemeldet oder liegt eine Meldung über Starkniederschlag oder Großhagel vor, so wird die Struktur des zugehörigen Radar- und Satellitenbildes analysiert. Neben Helligkeitstemperaturen (Auflösung: $4 \text{ km} \times 4 \text{ km}$) werden auch hochaufgelöste, korrigierte Radardaten (Winterrath et al., 2018, RADKLIM) benutzt, um die konvektive Organisation zu bestimmen. Es stellt sich heraus, dass es möglich ist, nur anhand der drei LWOI-Komponenten Skala, Intensität und Anisotropie zwischen Schauern, Gewittern und Ereignissen mit Großhagel bzw. Starkniederschlag zu unterscheiden. Zudem können Strukturen wie das Hook-Echo in Superzellen erkannt werden.

Diese kumulative Dissertation fasst die drei erwähnten Studien in den Kapiteln 3, 4 und 5 zusammen. Die einzelnen Kapitel bestehen jeweils aus einer Einleitung, in der die Ziele und die Vorgehensweise vorgestellt werden. Daran schließt sich ein Theorienteil an, in dem detailliert auf den WOI bzw. dessen Weiterentwicklung eingegangen wird. Es folgt die Vorstellung der wesentlichen Ergebnisse. Ebenfalls Teil der kumulativen Dissertation ist die Entwicklung und Veröffentlichung eines Software-Pakets zur Berechnung des Wavelet-basierten Organisationsindexes (Kapitel 6). Im Rahmen dieser Dissertation wurde an zwei weiteren Studien anteilig mitgewirkt. Details dazu sind in Kapitel 7 zu finden. Zum Abschluss dieser Arbeit wird ein umfassendes Fazit gezogen und ein kurzer Ausblick gewagt.

2 Theoretische Grundlagen

In allen drei veröffentlichten Artikeln steht die Beschreibung der Organisation von Konvektion mittels des Wavelet-basierten Organisationsindexes im Vordergrund. Deshalb wird im folgenden Abschnitt 2.1 zunächst auf die in der Literatur verwendeten Indexe zur Beschreibung der konvektiven Organisation eingegangen. Der zweite Teil (Abschnitt 2.2) beschäftigt sich mit der zweidimensionalen Wavelet-Transformation, die die Grundlage des neu entwickelten Organisationsindexes bildet.

2.1 Organisationsindexe

Um den Grad der Organisation von Konvektion zu bestimmen, sind in den letzten Jahren mehr als 20 verschiedene Indexe in der Literatur präsentiert worden (Brune et al., 2021). Fast alle Kennzahlen geben die mittlere Organisation über der gewählten Domain an. Sie zeigen oft große Abhängigkeiten von der Gitterstruktur oder den gewählten Schwellenwerten, die bei der Anwendung von Cluster-Algorithmen benötigt werden. Oft werden Variablen wie Strahlung, Oberflächentemperatur, Wasserdampfgehalt oder Niederschlag, die mittels Satellit oder Radar beobachtet werden können. Manche Maßzahlen analysieren die Vertikalgeschwindigkeit und sind somit nur auf numerische Klima- oder Wettermodelle anwendbar. Es gibt also kein Organisationsmaß, welches allgemein anwendbar ist und konvektive Organisation im Raum lokalisieren kann. Die Organisationsmaße SCAI, L_{org} und COP) werden nachfolgend näher beschrieben, um sie später mit dem Wavelet-basierten Organisationsindex zu vergleichen.

2.1.1 Simple Convective Aggregation Index (SCAI)

Der SCAI (Tobin et al., 2012) zählt die Anzahl der konvektiven Cluster über einer Domain mit $N_x \times N_y$ Gitterpunkten und vergleicht diese mit dem Abstand der Cluster. Zur Bestimmung der konvektiven Cluster werden Gitterpunkte mit einer Helligkeitstemperatur kleiner als 240 K als konvektiv markiert. Ein Cluster-Algorithmus mit vier Verbindungen ermittelt die Anzahl der Cluster N , die mit der Anzahl der maximal verfügbaren Cluster $N_{max} = (N_x \cdot N_y)/2$ normalisiert wird. $n = N \cdot (N - 1)/2$ ist die Anzahl der Cluster-Paare und d_s gibt den Abstand zwischen zwei Clustern an. Die n -te Wurzel aus dem Produkt der Abstände für alle Cluster-Paare lautet

$$D_0 = \sqrt[n]{\prod_{s=1}^n d_s}. \quad (2.1)$$

Je kleiner D_0 , desto näher sind die Cluster zusammen. D_0 wird mit einer charakteristischen Länge L (hier $L = 1000$ km) skaliert, sodass SCAI definiert ist als

$$\text{SCAI} = \frac{N}{N_{max}} \frac{D_0}{L} \cdot 1000. \quad (2.2)$$

SCAI misst die inverse Organisation, d. h., dass der SCAI für eine feste Anzahl von Clustern N direkt proportional zum Abstand der Cluster ist. Liegen die Cluster nah zusammen (organisiert), nimmt SCAI geringe Werte an. Entfernen sich die Zellen voneinander, so erhöht sich der SCAI. Neben der Einführung der charakteristischen Länge L hängt der SCAI von der Anzahl der Gitterpunkte und der Auflösung ab.

2.1.2 Organization Index (I_{org})

I_{org} (Tompkins & Semie, 2017) unterscheidet zwischen regulärer, zufälliger und organisierter Konvektion. Gitterpunkte, an denen die Vertikalgeschwindigkeit in 730 hPa größer als 1 m/s ist, werden als konvektiv markiert. Benachbarte konvektive Punkte werden zu einem Updraft zusammengefasst und der Abstand d_s zum räumlich nächsten Updraft bestimmt. Die kumulative Verteilungsfunktion der Abstände wird dann mit der Weibull Verteilung

$$W = 1 - \exp\left(\frac{N}{A}\pi d^2\right) \quad (2.3)$$

verglichen. N ist die Anzahl der Updrafts (Cluster) und A die Fläche der gesamten Domain. Ist Konvektion zufällig, dann kann die Organisation durch einen Poisson-Prozess mit der Weibull Verteilung W beschrieben werden und im Diagramm mit W auf der x-Achse und N auf der y-Achse würde eine Diagonale zeigen. I_{org} ist als die Fläche unterhalb dieses Integrals definiert und wäre in dem Fall $I_{org} = 0.5$. Liegt die Kurve oberhalb der Diagonalen ($I_{org} > 0.5$), so sind die Abstände zwischen den Updrafts gering und I_{org} zeigt organisierte Konvektion an.

2.1.3 Convective Organization Potential (COP)

Das COP (White et al., 2018) basiert auf den Überlegungen des Potentials zwischen zwei Punktladungen und beruht auf der langwelligen Ausstrahlung. Das Interaktionspotential zwischen zwei konvektiven Zellen a und b lässt sich schreiben als

$$V(a, b) = \frac{\sqrt{A_a} + \sqrt{A_b}}{d(a, b)\sqrt{\pi}}. \quad (2.4)$$

A_a (A_b) ist die Fläche des Clusters a (b), $d(a, b)$ gibt den Abstand zwischen beiden Clustern an. Das gesamte COP einer Domain mit N Clustern errechnet sich aus der Summe der einzelnen Potentiale

$$\text{COP} = \frac{\sum_{a=1}^N \sum_{b=a+1}^N V(a, b)}{\frac{1}{2}N \cdot (N - 1)} \quad \text{für } N > 1. \quad (2.5)$$

Das COP steigt, wenn die Objekte größer werden und sich der Abstand der Cluster verringert. Um COP zu berechnen, müssen mindestens zwei Cluster vorhanden sein.

2.2 Wavelet-Transformation

Zur Analyse des Grades der konvektiven Organisation wird die Wavelet-Transformation von Regenraten und Helligkeitstemperaturen genutzt. Wavelets habe ihren Ursprung in der Signal- und Bildverarbeitung, aber auch in der Meteorologie kommen sie häufig als nützliches Tool zur Erkennung von Strukturen zum Einsatz (Weniger et al., 2017). In diesem Abschnitt wird die diskrete Wavelet-Transformation (DWT) und die Dual-Tree Complex Wavelet Transformation (DTCWT) inklusive der notwendigen Bias-Korrektur nach Eckley et al. (2010) beschrieben. Eine allgemeine Einführung in die Wavelet-Theorie und vertiefende Grundlagen sind beispielsweise in Daubechies (1992), Vidakovic & Mueller (1994), Kumar & Foufoula-Georgiou (1997), Torrence & Compo (1998) oder Nason (2008) zu finden.

2.2.1 Diskrete Wavelet-Transformation (DWT)

Für die DWT wird eine zweidimensionale Variable (z. B. Regenrate, Helligkeitstemperatur) mit $2^K \times 2^K$, $K \in \mathbb{N}$, Gitterpunkten in einen Raum mit neuen Basisfunktionen projiziert. Die neuen Basisfunktionen, die sogenannten Tochter-Wavelets $\psi_{k,d,\mathbf{u}}(\mathbf{r})$ mit $\mathbf{r} \in \mathbb{Z}^2$, haben einen kompakten Support in Raum und Frequenz und werden durch Skalieren (Skala k), Drehen (Orientierung d) und Verschieben (Shift \mathbf{u}) aus dem sogenannten Mutter-Wavelet $\psi(\mathbf{r})$ generiert. Im Gegensatz zur Fourier-Transformation lassen sich mithilfe der DWT auch nicht-stationäre Signale erfassen, da die Basisfunktionen im Raum lokalisiert sind.

Als Mutter-Wavelet, welches auch als Hochpassfilter interpretiert werden kann (Vidakovic & Mueller, 1994), können verschiedene Wavelets fungieren. In dieser Arbeit wird sowohl das Haar-Wavelet (Haar, 1910) als auch das Daubechies 4 Wavelet (DB4, Daubechies, 1992) benutzt. Das Haar-Wavelet gilt als einfaches Wavelet mit einem verschwindenden Moment und besteht aus zwei Rechteckfunktionen, die eine Unstetigkeit aufweisen. Das DB4-Wavelet ist dagegen glatter, besitzt zwei verschwindende Momente und hat einen viermal größeren Support, was eine weniger genaue Lokalisation im Vergleich zum Haar-Wavelet zur Folge hat.

Die Tochter-Wavelets werden nun über die gesamte Domain verschoben. Für jede Skala k ($k = 1, \dots, K$) und jede der $D = 3$ Orientierungen ($d = 1$ entspricht vertikal, $d = 2$ horizontal, $d = 3$ diagonal) erhält man ein zweidimensionales Feld der Ausgangsgröße $2^K \times 2^K$. Die Information des zweidimensionalen Ursprungsfeldes wird also in ein neues Feld der Dimension $2^K \times 2^K \times K \times D$ überführt. Dadurch ist die Information aus dem Eingangsfeld auf allen Skalen und Orientierungen vorhanden, weshalb die Transformation auch als redundante DWT bezeichnet wird.

Eckley et al. (2010) erweitern den eindimensionalen Ansatz von Nason et al. (2000) und definieren den lokalen stationären zweidimensionalen Wavelet-Prozess als

$$X(\mathbf{r}) = \sum_{k=1}^K \sum_{d=1}^D \sum_{\mathbf{u}} w_{k,d,\mathbf{u}} \psi_{k,d,\mathbf{u}}(\mathbf{r}) \xi_{k,d,\mathbf{u}}, \quad (2.6)$$

wobei die Koeffizienten $w_{k,d,\mathbf{u}}$ als Wichtungen abhängig von der Art des Wavelets (hier Haar und DB4) gegeben sind und $\xi_{k,d,\mathbf{u}}$ ein zufälliges weißes Rauschen mit Mittelwert

null repräsentiert. Unter Annahme lokaler Stationarität, d. h. die Kovarianz von X ändert sich nur langsam mit \mathbf{r} , kann die Autokovarianz von X im Grenzfall einer unendlich großen Domain durch $|w_{k,d,\mathbf{u}}|^2$ dargestellt werden (Eckley et al., 2010). $|w_{k,d,\mathbf{u}}|^2$ wird als lokales Wavelet-Spektrum bezeichnet und kann aus dem Quadrat empirischen Wavelet-Koeffizienten $|\sum_{\mathbf{r}} X(\mathbf{r}) \psi_{k,d,\mathbf{u}}(\mathbf{r})|^2$ geschätzt werden. Allerdings ist dieser Schätzer aufgrund der hohen Redundanz verzerrt, was sich durch eine Dominanz der großen Skalen äußert. Um dem entgegenzuwirken, haben Eckley et al. (2010) eine Korrekturmatrixt \mathbf{A}_{ψ}^{-1} eingeführt. Die Matrix berücksichtigt die Korrelationen der Tochter-Wavelets $\psi_{k,d,\mathbf{u}}(\mathbf{r})$ und kann mithilfe des R-Pakets LS2W (Eckley & Nason, 2011) abhängig vom gewünschten Wavelet (Haar, DB4) und der Größe der Domain (z. B. 1024×1024 Gitterpunkte) berechnet werden. Für die detaillierte Herleitung sei an dieser Stelle auf Nason et al. (2000) und Eckley et al. (2010) verwiesen. Zusammenfassungen der technischen Details sowie anschauliche Beispiele sind in Kapp et al. (2018), Buschow et al. (2019) und Buschow & Friederichs (2020) zu finden.

Die Herleitung in Eckley et al. (2010) basiert auf der Annahme einer unendlich großen Domain. Im realen Fall ist die Domain begrenzt, sodass durch die Korrekturmatrixt \mathbf{A}_{ψ}^{-1} negative Werte im lokalen Wavelet-Spektrum auftreten können. Besonders anfällig für negative Werte ist das Haar-Wavelet (Buschow et al., 2019), welches durch seine kurze Supportlänge (zwei Pixel) hingegen eine gute Lokalisation ermöglicht. Als guter Kompromiss zwischen möglichst wenig “negativer Energie” im Wavelet-Spektrum und einer guten Lokalisation erwies sich das DB4-Wavelet. Der Rechenaufwand zur Bestimmung der Korrekturmatrixt \mathbf{A}_{ψ}^{-1} kann abhängig von der Länge des Wavelets und der Domain sehr groß werden, weshalb im R-Paket calcWOI die vorberechneten Matrizen bereits enthalten sind (Kapitel 6).

2.2.2 Dual-Tree Complex Wavelet Transformation (DTCWT)

Während der Entwicklung des Wavelet-basierten Organisationsindexes stellte sich heraus, dass mithilfe der drei Orientierungen aus den DWTs (ost-west, nord-süd und diagonal) die Ausrichtung der Squall-Lines nicht erfasst werden kann. Nord-süd und ost-west orientierte Objekte werden gut erfasst, da die Tochter-Wavelets um 90° zueinander rotiert sind. Allerdings ist die diagonale Richtung keine echte Rotation des Wavelets um 45° , sondern weist eine andere Struktur auf, die kleinskalige Features beinhaltet. Anschauliche Darstellung und weitere Details sind in Buschow & Friederichs (2021) und Brune et al. (2021) zu finden.

In Kapitel 5 wird deshalb statt der DWT die sogenannte Dual-Tree Complex Wavelet Transformation (DTCWT) nach Kingsbury (1999) verwendet. Eine Übersicht und tiefgehende Informationen zur DTCWT sind in Selesnick et al. (2005) zu finden. Im Gegensatz zu der DWT wird das Mutter-Wavelet ψ nun durch ein komplexes Wavelet der Form $\psi = \psi_r + i\psi_i$ ersetzt. ψ_r und ψ_i werden so gewählt, dass sie 90° phasenverschoben sind. Für den zweidimensionalen Fall ergeben sich so letztlich insgesamt sechs Tochter-Wavelets (Buschow & Friederichs, 2021), die die $D = 6$ Orientierungen $d = 15^\circ, 45^\circ, 75^\circ, 105^\circ, 135^\circ, 165^\circ$ haben. Die nahezu vollständige Rotationsinvarianz (Kingsbury, 2006) dieser sechs Tochter-Wavelets ermöglichen später eine bessere Beschreibung der konvektiven Organisation (Kapitel 5).

Auch für die DTCWT wird jedes Tochter-Wavelet über jeden Gitterpunkt der Domain

$2^K \times 2^K$, für jede Skala K und jede Orientierung D , verschoben. Demnach erhält man nach Anwendung dieser redundanten Transformation ein Feld der Größe $2^K \times 2^K \times K \times D$, welches ebenfalls der Bias-Korrektur unterzogen werden muss. Die zuvor diskutierte Korrektur nach Eckley et al. (2010) wurde von Nelson et al. (2018) für die DTCWT angewendet. Zur Berechnung der zweidimensionalen redundanten Dual-Tree Transformation inklusive der Bias-Korrektur wird das R-Paket **dualtrees** (Buschow et al., 2020) verwendet.

3 Konvektive Organisation über Deutschland

Eine ausführliche Version dieses Kapitels wurde veröffentlicht in:

Brune, S., F. Kapp & P. Friederichs (2018). „A wavelet-based analysis of convective organization in ICON large-eddy simulations“. *Quarterly Journal of the Royal Meteorological Society* 144 (717), S. 2812–2829.

3.1 Einleitende Worte zu den Zielen und zur Vorgehensweise

Im Gegensatz zu vielen anderen Studien, die einen objekt-basierten Ansatz wählen (Abschnitt 2.1), werden hier Wavelet-Spektren von Regenraten zur Beschreibung der konvektiven Organisation genutzt. In Kapp et al. (2018) konnte gezeigt werden, dass mithilfe von Wavelet-Spektren verschiedene räumliche Strukturen in Niederschlagsfeldern erfasst werden können und sich diese Spektren sogar dazu eignen, um Vorhersagen zu verifizieren.

Die Datengrundlage bilden ICON-Simulationen mit Gitterabständen von rund 150 m und Radarbeobachtungen. Die simulierten und beobachteten Regenraten werden auf ein reguläres Longitude-Latitude-Gitter mit $N_x \times N_y = 529 \times 626$ Gitterpunkten und einem Gitterpunktabstand von etwa 1,2 km interpoliert. Das Modellgebiet umfasst große Teile Deutschlands sowie Teile der Nachbarstaaten. Die drei gewählten Fallbeispiele decken sowohl unorganisierte Konvektion in Form von vielen, kurzlebigen Schauern (15.08.2014) als auch organisierte Multi- bzw. Superzellen (04.07.2015) und linear organisierte Konvektion (05.07.2015) ab. Untersucht wird, ob nur mithilfe der Wavelet-Spektren von Regenraten verschiedene Organisationsgrade erfasst werden können. Neben den Regenraten sind auch viele dynamische und konvektive Variablen aus den Simulationen verfügbar. Diese werden im zweiten Schritt dazu genutzt, um einen Zusammenhang zwischen Organisationsgrad und der Umgebung herzustellen.

3.2 Der Wavelet-basierte Organisationsindex (WOI)

Grundlage des Wavelet-basierten Organisationsindexes (WOI) ist die redundante DWT eines zweidimensionalen Eingangsfeldes (Abschnitt 2.2). Zur Berechnung der DWT wird aus dem 529×626 Gitterpunkte großen Modelldomain mittig ein Bereich von 512×512 Punkten ausgeschnitten. Damit die Ränder periodisch sind, wird das Feld zunächst am rechten Rand und dann am oberen Rand gespiegelt, bevor dann die DWT auf das Feld mit

1024×1024 Gitterpunkten angewendet wird. Als Mutter-Wavelet wird das Haar-Wavelet benutzt.

Die Transformation gibt Aussagen darüber, auf welcher räumlichen Skala k die größte spektrale Energie befindet und welche Orientierung d dominiert. Organisierte Konvektion führt generell zu großskaligen und intensiven Niederschlägen im Vergleich zu unorganisierter Konvektion wie beispielsweise rückseitig einer Kaltfront (Rückseitenwetter). Zudem kann sich organisierte Konvektion linear ausrichten. Aus DWT der Regenraten können genau diese Informationen gewonnen werden: Die Skala im Wavelet-Spektrum bildet als erste Komponente WOI_1 , WOI_2 beinhaltet die gesamte spektrale Energie und ist somit Indikator für die Intensität des Niederschlags und WOI_3 berücksichtigt die Orientierung.

Mathematisch lässt sich die Komponenten wie folgt schreiben:

$$\text{WOI}_1 = \frac{\bar{E}_l}{\bar{E}_s + \bar{E}_l} \quad (3.1)$$

$$\text{WOI}_2 = \frac{\bar{E}_l + \bar{E}_s}{r} \quad (3.2)$$

$$\text{WOI}_3 = \frac{1}{3} \sqrt{\sum_d \left(\left(\frac{E_s^d - \bar{E}_s}{\bar{E}_s} \right)^2 + \left(\frac{E_l^d - \bar{E}_l}{\bar{E}_l} \right)^2 \right)} \quad (3.3)$$

$$\text{WOI} = \sum_i \log(\text{WOI}_i) \quad (3.4)$$

Dabei beschreibt \bar{E}_s die spektrale Energie auf kleinen Skalen ($10 - 40$ km) und \bar{E}_l die großskalige spektrale Energie ($80 - 1280$ km), jeweils gemittelt über die Domain und die drei Orientierungen. r ist die Anzahl der Gitterpunkte mit Regenraten größer als 0 mm/h . E_s^d repräsentiert die kleinskalige und E_l^d die großskalige über die Domain gemittelte spektrale Energie für die Orientierung ost-west ($d = 1$), nord-süd ($d = 2$) bzw. diagonal ($d = 3$). Da die einzelnen Komponenten, insbesondere WOI_2 , nicht normiert sind, wird der Logarithmus auf die drei Anteile angewendet und anschließend addiert, um die konvektive Organisation in einer Zahl zusammenzufassen.

3.3 Zusammenfassung der Ergebnisse

Die Analyse der Wetterlage vom 14.08.2014 zeigt, dass aufgrund schwacher Höhenwinde und damit verbundener geringer vertikaler Windscherung die Voraussetzungen für kurzlebige, kleinskalige Einzelzellen gegeben war. CAPE betrug abseits der Zellen rund $200 - 500 \text{ J/kg}$, was bei verschwindend geringen CIN-Werten von unter 10 J/kg und jahreszeitbedingt starker solarer Einstrahlung rasch komplett abgerufen werden konnte. Ganz anders stellte sich die Situation am 04./05.07.2015 dar, als sich im Tagesverlauf unter einem starken Deckel (100 J/kg CIN) zunächst mehr als 2000 J/kg CAPE aufbauen konnten. Zudem sorgte die Höhenströmung für ein stärkeres Forcing, was mit einer Windscherung von rund 20 m/s einherging. Am 04.07.2015 lag ein Trog etwas westlich von Deutschland, sodass sich nur lokal konvektive Zellen im Norden und Osten bilden konnten. Diese Zellen profitierten allerdings von den konvektionsfördernden Bedingungen und entwickelten sich rasch zu Multi- oder Superzellen mit Regenraten von 100 mm/h . Als der

Trog am 05.07.2015 weiter nach Westen vorangekommen war, nahm die Windscherung, aber vor allem das Forcing aus dem Höhenfeld zu, sodass sich etwa ab Mittag bei erneut über 2000 J/kg CAPE linear organisierte Konvektion entwickelte. So erstreckte sich am Nachmittag über der Mitte Deutschlands eine markante Squall-Line von Nord nach Süd, die gegen Abend den Osten des Landes erreichte. Zwar lassen sich Unterschiede zwischen den simulierten Regenraten und den Radarbeobachtungen feststellen, allerdings spiegelt das Modell die Art und Struktur der Konvektion zufriedenstellend wider.

Die Wavelet-Spektren der drei simulierten Fallbeispiele zeigen demzufolge deutliche Unterschiede. Im Fall der unorganisierten Konvektion am 15.08.2014 verteilt sich die spektrale Energie gleichmäßig auf die drei verschiedenen Raumrichtungen. Ab ca. 08 UTC startet die Konvektion auf kleinsten Skalen (1,2 – 2,4 km). Im weiteren Tagesverlauf werden die Zellen mit 4,8 km nur minimal größer. Ab den frühen Abendstunden sinkt die konvektive Aktivität wieder rapide ab und kommt gegen 20 UTC komplett zum Erliegen. Die Wavelet-Spektren am 04.07.2015 zeigen einen komplett anderen Verlauf. Erst um kurz vor 18 UTC zeigt das Spektrum erste konvektive Zellen, die sehr rasch auf Skalen von 9,6 km bis zu 76,8 km anwachsen, was typisch für die Entwicklung von Multi- und Superzellen in gut gescherter Umgebung ist. Die Energie in nord-süd und diagonaler Richtung ist im Vergleich zur ost-west Ausdehnung erhöht, was für etwas mehr meridionale Orientierungen spricht. Noch deutlicher wird die Richtungsabhängigkeit für die Squall-Line am 05.07.2015. In allen spektralen Richtungen liegt die bevorzugte Skala bei 19,2 km bis 38,4 km, die spektrale Energie in nord-süd Ausrichtung ist jedoch so groß wie in ost-west und diagonaler Richtung zusammen. Auch die mittlere spektrale Energie ist um ein Vielfaches größer als in den beiden Fallbeispielen zuvor. Dabei setzt die Konvektion erst am späten Vormittag ein und verlässt den östlichen Rand des Modellgebiets gegen 18 UTC. Während am 15.08.2014 und am 04.07.2015 die gesamte spektrale Energie auf Skalen kleiner als 100 km liegt, enthält das Spektrum im Fall der Squall-Line am 05.07.2015 auch auf Skalen von 153,6 km und 307,2 km positive Werte. Dies entspricht der meridionalen Ausdehnung der Linie. Die Spektren der beobachteten Niederschlagsraten stimmen mit den simulierten Regenraten größtenteils überein, allerdings unterschätzt das Modell den Start der Konvektion am 04.07.2015 um rund drei Stunden und simuliert zu großskalige Objekte verglichen mit den Radarbeobachtungen. Die präferierte nord-süd Ausrichtung der Linie stimmt jedoch in Simulation und Beobachtung überein. Die Regenraten werden allgemein etwas zu schwach simuliert, d. h., dass die spektrale Energie in den Beobachtungen über der in den Simulationen liegt. Da es sich bei den hier analysierten Wavelet-Spektren um räumlich gemittelte Energien handelt, kann über die genaue Position der Squall-Line in Modell und Beobachtung keine Aussage getroffen werden.

Die unorganisierte Konvektion am 15.08.2014 unterscheidet sich in vielerlei Hinsicht von den organisierten Strukturen am 04./05.07.2015. Eine K-means Clusteranalyse basierend auf diversen dynamischen und konvektiven Variablen wie z. B. Windscherung, Helizität, Lifted Index, CAPE oder CIN unterscheidet zwischen zwei Clustern. Cluster A beinhaltet alle Zeitschritte vom 15.08.2014, ausgezeichnet u. a. durch wenig CAPE, sehr geringer Windscherung und Helizität sowie einem höheren Lifted Index. Organisierte Konvektion in Cluster B (alle Zeitschritte vom 04./05.07.2015) tritt in Verbindung mit viel CAPE, hoher Windscherung und erhöhter Helizität auf.

Berechnet man die konvektiven Organisationsmaße SCAI, I_{org} und COP basierend auf einem Schwellenwert von 2 mm/h für die drei Fallstudien, so deuten alle Indexe eine

schwächere Organisation am 15.08.2014 an. Vor allem zwischen 10 UTC und 20 UTC, also in der Hauptzeit der konvektiven Aktivität, stimmen SCAI, I_{org} und COP in Simulation und Beobachtung sehr gut überein. Am 04./05.07.2015 ist SCAI nahe 0, was auf eine sehr große Organisation hindeutet. I_{org} und COP nehmen im Vergleich zum ersten Fallbeispiel höhere Werte an, was die bisherigen Eindrücke der starken Organisation am 04./05.07.2015 bestätigt.

Der in dieser Studie neu eingeführte Wavelet-basierte Organisationsindex lässt sich ohne einen Schwellenwert direkt auf die Regenraten anwenden. Die erste Komponente WOI_1 zeigt, dass die Skala der Konvektion am 15.08.2014 sowohl in den Simulationen als auch in den Beobachtungen kleiner ist als für die Fälle im Juli 2015. Der Unterschied zwischen kleinskaliger Konvektion am 15.08.2014 und der großskaligen Konvektion im Juli 2015 fällt für die Radardaten allerdings etwas geringer aus. Die Intensität, gemessen anhand von WOI_2 , ist am 15.08.2014 um eine Größenordnung kleiner als am 04./05.07.2015. Wie bereits zuvor angedeutet, ist die Intensität aufgrund höherer Regenraten in den Beobachtungen stärker als in den Simulationen. Relativ vergleichbar ist die simulierte und gemessene Anisotropie (WOI_3). Die Konvektion am 15.08.2014 ist sehr isotrop, während die organisierten Strukturen linear ausgerichtet sind. Fasst man die drei WOI_i -Komponenten zum WOI zusammen, so lassen sich anhand des kombinierten Indexes die unorganisierte Konvektion vom 15.08.2014 und die organisierten Strukturen am 04./05.07.2015 perfekt trennen. Dies gilt sowohl für die simulierten als auch für die beobachteten Regenraten.

Die Vergleiche vom WOI mit SCAI, I_{org} und COP zeigen, dass einzig der WOI die beiden zuvor gefundenen Cluster A und B aus der Analyse dynamischer und konvektiver Variablen trennen kann. COP und SCAI sind in der Lage 92 % bzw. 88 % der Zeitschritte zu trennen, während I_{org} nur 55 % aller Zeitschritte korrekt zuordnet. Mit dem WOI ist also eine Alternative zu den objekt-basierten Indexen SCAI, I_{org} und COP gefunden worden. Der WOI benötigt im Gegensatz zu den konventionellen Indexen keinen Schwellenwert und keinen Cluster-Algorithmus. Allerdings muss gemäß der WOI-Definition bei der Berechnung zwischen klein- und großskaligen Wellenlängen unterschieden werden. Zudem sind die drei Komponenten nicht normiert oder begrenzt, was bei der Zusammenfassung durch die Addition der Logarithmen kompensiert werden soll. Denkbar wäre hier auch die Einführung verschiedener Wichtungen für die verschiedenen Komponenten.

In dieser Studie wurden räumliche Mittelwerte der spektralen Koeffizienten betrachtet. Dadurch wurde die Ortsinformation aus dem Wavelet-Spektrum eliminiert. Man hätte also eine ähnliche Analyse auch auf Basis von Fourier-Spektren durchführen können. Die hier vernachlässigte Ortsinformation im Wavelet-Spektrum wird in den folgenden beiden Studien dazu genutzt, einen ortsabhängigen Organisationsindex zu definieren. Dass die konvektive Organisation überhaupt mittels Wavelet-Spektren von Regenraten beschrieben werden kann, ist anhand der drei Fallbeispiele eindrucksvoll gezeigt worden.

4 Konvektive Organisation über dem tropischen Atlantik

Eine ausführliche Version dieses Kapitels wurde veröffentlicht in:

Brune, S., S. Buschow & P. Friederichs (2020). „Observations and high-resolution simulations of convective precipitation organization over the tropical Atlantic“. *Quarterly Journal of the Royal Meteorological Society* 146 (729), S. 1545–1563.

4.1 Einleitende Worte zu den Zielen und zur Vorgehensweise

Nachdem der Grad der konvektiven Organisation für ausgewählte Tage über Deutschland mithilfe vom WOI erfolgreich gemessen werden konnte, liegt der Fokus nun auf dem tropischen Atlantik. Im Bereich der innertropischen Konvergenzzone kommt es sehr oft zu teils lang anhaltenden konvektiven Umlagerungen. Neben der vornehmlich durch die Passatwinde angetriebene Konvektion spielen auch die sogenannten *African Easterly Waves* (AEWs) eine wichtige Rolle. Dabei handelt es sich um Störungen entlang der Konvergenzzone, die sich von Afrika westlich ausbreiten und großen Einfluss auf die Organisation von Konvektion haben. So kommt es mit Unterstützung starker diabatischer Effekte aufgrund der intensiven solaren Einstrahlung über dem afrikanischen Kontinent zu organisierten Clustern, vornehmlich Squall-Lines, die während des Nordsommers entlang bzw. knapp südlich der Sahelzone entstehen und auf den östlichen Atlantik zusteuern. Je nach Intensität der Welle breiten sich Squall-Lines auch über dem Atlantik aus und können durchaus tropische Wirbelstürme initiieren. Allerdings kommt es durch den durchgehend warmen Ozean vermehrt zu unorganisierter maritimer Konvektion, die wiederum Einfluss auf die AEWs hat. Das Untersuchungsgebiet erstreckt sich in einem 25° breiten Streifen von Afrika (15°O) über den Atlantik bis nach Südamerika (-65°O). Genutzt werden erneut hochauflöste ICON-Simulationen (Gitterabstand von rund 2,5 km), diesmal allerdings für einen Zeitraum von einem Monat (01.08.2016 – 31.08.2016). Verglichen wird der simulierte Niederschlag mit Regenraten, die aus Satellitenmessungen abgeleitet wurden. Für eine bessere Vergleichbarkeit werden die simulierten und beobachteten Niederschläge auf ein Longitude-Latitude-Gitter mit $N_x \times N_y = 820 \times 291$ Gitterpunkten und einem Gitterpunktabstand von etwa 10 km interpoliert. Da abgeleitete Niederschlagsabschätzungen sowohl im Mikrowellen-Kanal (MW) als auch im Infrarot-Bereich (IR) vorhanden sind, können die Simulationen mit beiden Beobachtungstechniken verglichen werden. So kann neben der Bestimmung der Organisation in beiden Beobachtungsdaten auch ein Vergleich mit der simulierten Organisation angestellt werden und die Simulation dahingehend verifiziert werden. Zusätzlich erhält man aus den Simulationen viele weitere Parameter wie

CAPE, Windscherung, Temperatur und Feuchte. Diese können dazu genutzt werden, um die Ursache für die unterschiedlich organisierten Strukturen zu finden. Dazu wird eine Korrelationsanalyse durchgeführt.

4.2 Der modifizierte WOI

Nach der Anwendung vom WOI auf andere Fallbeispiele und weitere Datensätze stellte sich heraus, dass einige Modifikationen am ursprünglichen WOI vorgenommen werden sollten. Aufgrund des zuvor gewählten Haar-Wavelets und der Bias-Korrektur nach (Eckley et al., 2010), kam es oft zu negativen Werten im Wavelet-Spektrum. Diese negativen spektralen Energien können sich in einem negativen oder sehr großen WOI_1 äußern. Zusätzlich kann für intensive Niederschläge WOI_2 sehr groß werden. WOI_3 hingegen zeigt recht geringe Variation, weshalb eine Normierung der Komponenten sinnvoll ist. Um die negative spektrale Energie zu reduzieren und gleichzeitig die Lokalisation nicht zu verlieren, wird auf das weniger scharfe DB4-Wavelet zurückgegriffen (Abschnitt 2.2). In WOI_2 wird eine Exponentialfunktion eingeführt und WOI_3 erhält einen normierenden Vorfaktor. Somit sind alle Komponenten zwischen 0 (unorganisiert) und 1 (organisiert) normiert. Die modifizierten WOI-Komponenten lauten demnach

$$WOI_{sc} = \frac{\bar{E}_l}{\bar{E}_s + \bar{E}_l}, \quad (4.1)$$

$$WOI_{in} = 1 - \exp\left(-\frac{\bar{E}}{\frac{r}{N_x \cdot N_y}}\right), \quad (4.2)$$

$$WOI_{ai} = \frac{1}{2\sqrt{3}} \sqrt{\sum_d \left(\left(\frac{E_s^d - \bar{E}_s}{\bar{E}_s} \right)^2 + \left(\frac{E_l^d - \bar{E}_l}{\bar{E}_l} \right)^2 \right)}. \quad (4.3)$$

\bar{E}_s steht für die kleinskalige Energie auf den Skalen 1 – 3 (10 – 40 km), \bar{E}_l beschreibt die großskalige Energie auf den Skalen 4 – 7 (80 – 1280 km), jeweils gemittelt über die Domain und alle drei Richtungen. Die modifizierte erste Komponente WOI_{sc} beschreibt weiterhin das Verhältnis großskaliger zu gesamter Energie und ist durch die Wahl des DB4-Wavelets zwischen 0 (kleinskalig) und 1 (großskalig) normiert. Die Intensitätskomponente WOI_{in} nimmt mit der gesamten spektralen Energie \bar{E} zu. Außerdem wird berücksichtigt, an wie vielen Gitterpunkten r der gesamten Domain ($N_x \cdot N_y$) der Niederschlag überhaupt fällt. WOI_{in} geht demnach gegen 1 für intensive Niederschläge, die nur an wenigen Gitterpunkten auftreten. Verteilt sich große spektrale Energie auf viele Gitterpunkte (z. B. an einer Front), so ist die Intensität gering ($WOI_{in} \rightarrow 0$). Die Anisotropie wird mit einem eingeführten Vorfaktor normiert, der dafür sorgt, dass WOI_{ai} ebenfalls zwischen 0 (alle Richtungen mit gleicher Energie) und 1 (Energie konzentriert auf eine Richtung) variieren kann.

4.3 Der lokal berechnete WOI (LWOI)

Mit den zuvor erläuterten Modifikationen ist es nun möglich, erstmals die konvektive Organisation innerhalb einer Domain zu lokalisieren. Dazu wird der modifizierte WOI an

jedem einzelnen Gitterpunkt (i, j) berechnet und die spektrale Energie nicht mehr über die Domain gemittelt. Im Vorfeld war dies noch zwingend notwendig, um die negative Energie über das räumliche Mittel zu verringern. Der lokale WOI (LWOI) lässt sich wie folgt berechnen

$$\text{LWOI}_{sc}(i, j) = \frac{E_l(i, j)}{E_s(i, j) + E_l(i, j)}, \quad (4.4)$$

$$\text{LWOI}_{in}(i, j) = 1 - \exp(-E(i, j)), \quad (4.5)$$

$$\text{LWOI}_{ai}(i, j) = \frac{1}{2\sqrt{3}} \sqrt{\sum_d \left(\left(\frac{E_s^d(i, j) - E_s(i, j)}{E_s(i, j)} \right)^2 + \left(\frac{E_l^d(i, j) - E_l(i, j)}{E_l(i, j)} \right)^2 \right)} \quad (4.6)$$

mit

$$E(i, j) = \frac{1}{3 \cdot 7} \sum_d \sum_k E_k^d(i, j), \quad (4.7)$$

$$E_l(i, j) = \frac{1}{3 \cdot 4} \sum_d \sum_{4 \leq k \leq 7} E_k^d(i, j), \quad E_l^d(i, j) = \frac{1}{4} \sum_{4 \leq k \leq 7} E_k^d(i, j), \quad (4.8)$$

$$E_s(i, j) = \frac{1}{3 \cdot 3} \sum_d \sum_{1 \leq k \leq 3} E_k^d(i, j), \quad E_s^d(i, j) = \frac{1}{3} \sum_{1 \leq k \leq 3} E_k^d(i, j). \quad (4.9)$$

$E_k^d(i, j)$ beschreibt das Wavelet-Spektrum am Gitterpunkt (i, j) für die Skala $k = 1, 2, \dots, 7$ und Richtung $d = 1, 2, 3$. Wie beim modifizierten WOI umfassen die Skalen 1 – 3 (10 – 40 km) die kleine Skala und 4 – 7 (80 – 1280 km) die große Skala.

Bei der Berechnung des modifizierten WOI und LWOI wird das Feld von 820×291 Gitterpunkte an den Rändern mit Nullen zu der Größe 1024×1024 aufgefüllt. An den Übergangsbereichen wird wie in Weniger et al. (2017) und Kapp et al. (2018) ein linearer Filter von 25 Gitterpunkten angewendet, um die Gradienten im Randbereich zu glätten. Nach der DWT werden die beiden größten Skalen $k = 9$ und $k = 10$ aufgrund der künstlich erzeugten Ränder nicht weiter beachtet. Die Länge des DB4-Wavelets der Skala $k = 8$ übersteigt zudem die Größe der ursprünglichen Domain, sodass nur die Skalen $k = 1, \dots, 7$ berücksichtigt wurden. Nach der DWT wird das ursprüngliche Feld von 820×291 Gitterpunkten ausgeschnitten und der modifizierte WOI bzw. LWOI gemäß der vorherigen Formeln berechnet.

4.4 Zusammenfassung der Ergebnisse

Als erstes wird in einer Fallstudie die Organisation einer Squall-Line über dem Westen Afrikas in den beiden Beobachtungsdatensätzen und der Simulation mithilfe der drei LWOI-Komponenten analysiert. Die Position der Squall-Line nahe der westafrikanischen Atlantikküste deckt sich in den Beobachtungen und der Simulation. Allerdings variiert die Ausdehnung und die Intensität, was sich auch in den LWOI-Komponenten zeigt. So ist die Squall-Line in der Simulation sehr schmal (niedriger LWOI_{sc}) und intensiv (hoher LWOI_{in}), während die Beobachtungen eine breitere Linie mit weniger starken Intensitäten zeigen. Besonders in der MW-Beobachtung identifiziert der LWOI südlich und südwestlich

der Squall-Line auf dem Atlantik sehr schwache, großskalige Objekte, die sowohl in den IR-Beobachtungen als auch in der Simulation fehlen. Im Vergleich zu den MW-Daten sind die IR-Beobachtungen intensiver und etwas kleinskaliger. Die dritte Komponente $LWOI_{ai}$ deutet vor allem in ICON die starke Linearität an, insgesamt ist $LWOI_{ai}$ deutlich verrauschter und deshalb schwieriger zu interpretieren. Die Organisationsmaße I_{org} , SCAI und COP, angewandt auf Regenraten $\geq 0.1 \text{ mm/h}$, decken sich weitestgehend mit dem räumlich gemittelten $LWOI_{sc}$. Die beiden Komponenten $LWOI_{in}$ und $LWOI_{ai}$ sind mit den konventionellen Größen nicht messbar, sodass $LWOI_{in}$ und $LWOI_{ai}$ eine Ergänzung darstellen. Der besondere Mehrwert vom LWOI ist jedoch die Lokalisierung der Organisation, während die anderen Maßzahlen nur die mittlere Organisation über die betrachtete Domain angeben.

Im nächsten Schritt wird das Monatsmittel der Regenrate und der LWOI-Komponenten berechnet, um regionale Unterschiede der konvektiven Organisation zu untersuchen. Es bestätigt sich der Eindruck des Fallbeispiels: ICON enthält besonders viele kleinskalige Features, MW-Beobachtungen sind großskaliger und IR-Beobachtungen sind intensiv. Aber auch regional unterscheiden sich die Beobachtungen teilweise deutlich von der ICON-Simulation. So sind die Niederschläge in den MW-Beobachtungen über dem Atlantik besonders großskalig, während IR und ICON die Niederschläge durch die Squall-Lines über dem afrikanischen Kontinent als großskalig charakterisieren. Der Unterschied zwischen den Beobachtungen ist mit den Messprinzipien zu erklären. Aus den Mikrowellen werden sehr häufig schwache, großskalige Niederschlagsfelder abgeleitet, während die Messungen im Infrarotbereich zu punktuellen, meist sehr intensiven Niederschlagsraten führen. Der Unterschied in der Intensität wird auch von $LWOI_{in}$ sehr gut beschrieben. Das Monatsmittel von $LWOI_{ai}$ variiert nur sehr schwach über der Domain. Dies ist zum einen durch das Auftreten hochgradig isotroper organisierter Strukturen wie Hurrikane zu erklären, zum anderen durch die Charakteristik des Wavelet-Spektrums. In dem Analysezeitraum kommt es häufig vor, dass meridional ausgerichtete Squall-Lines nach Westen ziehen und sich dabei etwas zonaler orientieren. Obwohl die Struktur der Squall-Lines weitestgehend gleich bleibt, verringert sich $LWOI_{ai}$ durch die leichte Drehung teils drastisch, da die verwendete Wavelet-Zerlegung nicht komplett rotationsinvariant ist. Als Alternative zu $LWOI_{ai}$ kann die bevorzugte Orientierung der Niederschlagsobjekte bestimmt werden, indem die Gesamtenergie der drei Richtungen ost-west, nord-süd und diagonal verglichen wird. Es stellt sich heraus, dass Konvektion über Afrika überwiegend nord-süd bzw. meridional ausgerichtet ist, während über dem tropischen Atlantik die ost-west bzw. zonale Orientierung dominiert. Die fehlende Rotationsinvarianz führt dazu, dass bei weniger als 10 % aller Objekte auf der diagonalen Orientierung die meiste Energie liegt.

Neben der Diskussion der Monatsmittel ist aufgrund der stündlichen Auflösung der Beobachtungen und der ICON-Simulation auch eine zeitliche Analyse der Niederschlagsraten möglich. Dazu werden zunächst Hovmöller-Diagramme der zwischen 2°N und 17°N gemittelten MW-, IR- und ICON-Regenraten betrachtet. Die Hovmöller-Diagramme zeigen allesamt acht von Afrika nach Westen propagierende Niederschlagsbänder. Durch das räumliche Mittel und der alle 24 Stunden neu initialisierten Simulation weicht die Simulation kaum von den beiden Beobachtungsdatensätzen ab. Lediglich die Intensität wird von ICON etwas unterschätzt. Zudem sind die Strukturen in den ICON-Simulationen feiner als in den IR- und speziell MW-Beobachtungen. Die acht westwärts propagierenden Cluster sind ebenfalls als zyklonale Anomalien in der simulierten 700 hPa Vorticity zu erkennen.

In der zweiten Monatshälfte lassen sich anhand des Niederschlags und der Vorticity die Entwicklung des tropischen Sturms Fiona und des Hurrikan Gaston nachverfolgen. Die anschließende Analyse mittels Wavelet-Transformationen in Raum und Zeit von Sebastian Buschow bestätigte, dass es sich bei den westwärts ausbreitenden Clustern um African Easterly Waves handelte.

Die hochauflösenden ICON-Simulationen erlauben es, einen Zusammenhang zwischen der Konvektion und dynamischen bzw. konvektiven Variablen herzustellen. Somit wird zum Schluss der Studie die Frage beantwortet, inwiefern $LWOI_{sc}$ und $LWOI_{ai}$ mit stündlichen Output-Variablen wie Windscherung, CAPE, Vertikalgeschwindigkeit oder bodennahen Änderungen der Temperatur, der Feuchte, des Drucks oder des Windes korrelieren. Dafür werden meridionale Mittelwerte der Modellvariablen und der beiden $LWOI$ -Komponenten gebildet und zeitliche Korrelationen berechnet. Die Unsicherheit wird durch ein 5-Tage-Block-Bootstrapping abgeschätzt. Dabei werden zufällig sechs Blöcke von fünf aufeinander folgenden Tagen mit Zurücklegen ausgewählt, um 200 Samples mit je $30 \times 24 \text{ h} = 720 \text{ h}$ zu generieren. $LWOI_{sc}$ ist positiv korreliert mit den Abbau von CAPE (0,27) und der 6 km Windscherung (0,24). Die Skala der Konvektion steigt also mit einem hohen Verbrauch von CAPE und einer starken Windscherung wie im Beispiel von Squall-Lines. Die Intensität $LWOI_{in}$ ist besonders positiv korreliert mit der maximalen (0,64) und mittleren Vertikalgeschwindigkeit (0,60), der mittleren Divergenz zwischen 8,5 km und 15,0 km (0,58) und der integrierten relativen Feuchte (0,53), was darauf schließen lässt, dass niederschlagsreiche Konvektion durch intensive Updrafts in einer feuchten Umgebung entstehen. Es gibt jedoch auch lokale Unterschiede, die wir ebenfalls dank des lokalen Organisationsindexes quantifizieren können. Der Abbau von CAPE ist entlang der ganzen Domain durchgehend signifikant positiv korreliert mit $LWOI_{sc}$. Allerdings liegt der CAPE-Abbau über den Kontinenten bei bis zu 1000 J/kg, während die maritime Konvektion nur rund 100 J/kg CAPE konsumiert, obwohl $LWOI_{sc}$ im Mittel auch über dem Ozean großskalige Konvektion misst. Ähnlich sieht das Muster von CAPE selbst aus. Über den Kontinenten, wo CAPE sogar teils signifikant negativ mit $LWOI_{sc}$ korreliert, aber auch über dem tropischen Atlantik ist ausreichend CAPE von 1000 J/kg oder mehr im Mittel verfügbar. Dennoch kommt es nicht in allen Regionen zu großskaliger Konvektion, weshalb CAPE alleine nicht über die Skala von Konvektion entscheidet. Vielmehr sorgt hohe 6 km Windscherung für großskalige Konvektion, was sich beim Vergleich der Monatsmittel von $LWOI_{sc}$ und der Scherung zeigt. Die zeitlichen Korrelationen von $LWOI_{in}$ und der Vertikalgeschwindigkeit, der Divergenz in der oberen Atmosphäre und der integrierten relativen Feuchte liegen über dem tropischen Atlantik bei 0,50 oder mehr. Dies lässt darauf schließen, dass die Updrafts über dem Meer unmittelbar mit der Intensität der Niederschläge zusammenhängen. Auch über den Kontinenten lässt sich dieser Zusammenhang erkennen, vor allem im Bereich der afrikanischen Squall-Lines decken sich die Mittelwerte von $LWOI_{in}$ und der Vertikalgeschwindigkeit sowie der Divergenz. Es lässt sich also festhalten, dass die Organisationsmaße $LWOI_{sc}$ und $LWOI_{in}$, die einzig auf der spektralen Analyse von Regenraten basieren, im Einklang mit den dynamischen und konvektiven Variablen sind und die regionalen Unterschiede im Grad der konvektiven Organisation erfassen können.

5 Konvektive Organisation besonderer Ereignisse anhand von Radar- und Satellitendaten

Eine ausführliche Version dieses Kapitels wurde veröffentlicht in:

Brune, S., S. Buschow & P. Friederichs (2021). „The local wavelet-based organization index – Quantification, localization and classification of convective organization from radar and satellite data“. *Quarterly Journal of the Royal Meteorological Society* 147 (736), S. 1853–1872.

5.1 Einleitende Worte zu den Zielen und zur Vorgehensweise

Um den Grad der konvektiven Organisation in verschiedenen Regionen einer Domain zu bestimmen, wurde der lokale Wavelet-basierte Organisationsindex LWOI eingeführt. Aufgrund der fehlenden Rotationsinvarianz des Wavelet-Spektrums, konnte die Anisotropie allerdings nicht korrekt bestimmt werden. Zudem muss für die Berechnung vom LWOI im Vorfeld die kleine und die große Skala definiert werden, was einen zusätzlichen Freiheitsgrad – ähnlich zum (willkürlichen) Schwellenwert in den diversen Cluster-Algorithmen – zur Folge hat. Um den Problemen der Rotationsinvarianz und der Skaleneinteilung entgegenzuwirken, wird der LWOI überarbeitet. Dazu werden komplexe 2D Dual-Tree Wavelets verwendet und die zentrale Skala (Buschow et al., 2020) eingeführt. Details zum überarbeiteten Index, der als LW bezeichnet wird, sind im anschließenden Abschnitt zu finden.

In dieser Studie wird der LW dazu benutzt, um beispielsweise den Grad der Organisation im Bereich von Großhagel und Starkniederschlägen sowie während Schauern und Gewittern zu bestimmen. Als Datengrundlage dient zum einen ein Datensatz vom European Severe Storms Laboratory (ESSL, Dotzek et al., 2009), zum anderen die Wettermeldungen der SYNOP Stationen im Netz des DWDs zwischen 2001 und 2018. Die konvektive Organisation wird auf Basis der kalibrierten Regenraten des RADKLIM Datensatzes vom DWD (Winterrath et al., 2018) bestimmt. Da der Wavelet-basierte Organisationsindex unabhängig von der Wahl der Variable ist, wird der LW auch für Satellitenbeobachtungen der Helligkeitstemperatur (Janowiak et al., 2017) berechnet. Die jeweiligen Komposita von LW_{sc} , LW_{in} und LW_{ai} enthalten interessante, signifikante Strukturen, die näher diskutiert werden. Abschließend wird gezeigt, dass Schauer, Gewitter und Ereignisse mit Hagel bzw. starkem Niederschlag anhand des LW klassifiziert werden können.

5.2 Der Dual-Tree LWOI (LW)

In der Studie der konvektiven Organisation über dem tropischen Atlantik (Kapitel 4) stellte sich LWOI_{ai} als ungeeignet für die Beschreibung der Linearität von Konvektion heraus, da die zugrundeliegende DWT mit den drei Orientierungen nicht rotationsinvariant ist. Um diesem Problem entgegenzuwirken, wird die DTCWT mit ihren $D = 6$ Orientierungen verwendet (Abschnitt 2.2).

Die gesamte spektrale Energie E aus dem Dual-Tree Wavelet-Spektrum am Ort (x, y) für alle Skalen $k = 1, \dots, K$ und Orientierungen $d = 1, \dots, D$ lässt sich wie folgt schreiben

$$E(x, y) = \sum_{k=1}^K \sum_{d=1}^D E_{k,d}(x, y) \quad (5.1)$$

mit $E_{k,d}(x, y)$ als spektraler Energie für die Skala k und die Richtung d am Ort (x, y) .

Die normalisierte Energie der Skala k ($e_k(x, y)$) und die normalisierte Energie der Richtung d ($e_d(x, y)$) sind somit wie folgt definiert:

$$e_k(x, y) = \frac{1}{D} \sum_{d=1}^6 E_{k,d}(x, y) / E(x, y) \quad (5.2)$$

$$e_d(x, y) = \frac{1}{K} \sum_{k=1}^K E_{k,d}(x, y) / E(x, y) \quad (5.3)$$

Zur Bestimmung der Anisotropie werden nun die sechs normalisierten Energien der Richtung $e_d(x, y)$ auf einem Kreis mit Radius 1 im gleichen Abstand voneinander angeordnet. Danach wird der Schwerpunkt dieses Sechsecks bestimmt, der durch die Komponenten $\text{LW}_u(x, y)$ und $\text{LW}_v(x, y)$ lokalisiert ist. Die Anisotropie ergibt sich aus der Distanz vom Schwerpunkt zum Mittelpunkt $\sqrt{\text{LW}_u^2 + \text{LW}_v^2}$. Die dominierende Orientierung am Ort (x, y) lässt sich durch den Winkel $\phi = \arctan 2(\text{LW}_v(x, y), \text{LW}_u(x, y))$ bestimmen.

Eine weitere Verbesserung in der Definition des Wavelet-basierten Organisationsindexes kann mit der Einführung der zentralen Skala (Buschow et al., 2019) als LWOI_{sc} -Ersatz erzielt werden. Zur Berechnung von LWOI_{sc} muss zwischen der kleinen und großen Skala unterschieden werden. Dieser Freiheitsgrad soll eliminiert werden, um LWOI_{sc} auch zwischen Daten mit unterschiedlicher räumlicher Auflösung vergleichbar zu machen. Es stellt sich heraus, dass bei den untersuchten Fällen in Brune et al. (2018) und Brune et al. (2020a) die mittlere Skala nahezu identische Ergebnisse wie LWOI_{sc} liefert. Die zentrale Skala lässt sich aus dem Schwerpunkt der normalisierten Energie auf den verschiedenen Skalen $e_k(x, y)$ berechnen, sodass sich die drei LWOI-Komponenten auf Basis der Dual-Tree Wavelets, namentlich LW_{sc} , LW_{in} und LW_{ai} , mathematisch wie folgt beschreiben lassen:

$$\text{LW}_{sc}(x, y) = \frac{1}{K-1} \left(-1 + \sum_{k=1}^K e_k(x, y) \cdot k \right) \quad (5.4)$$

$$\text{LW}_{in}(x, y) = 1 - \exp(-E(x, y)) \quad (5.5)$$

$$\text{LW}_{ai}(x, y) = \sqrt{\text{LW}_u(x, y)^2 + \text{LW}_v(x, y)^2} \quad (5.6)$$

Die drei Komponenten sind nun auf verschiedene Datensätze anwendbar, benötigen keine vorgeschaltete Skalenaufteilung und sind weitestgehend invariant bezüglich Rotation.

Da die Größe des Radar-Komposit $N_x \times N_y = 805 \times 1005$ Gitterpunkte beträgt, wird das Feld an den Rändern für die DTCWT mit Nullen auf 1024×1024 aufgefüllt. Da durch die einzelnen Radare an den Rändern kreisrunde Fehlwerte entstehen, die für die DTCWT auf Null gesetzt werden, wird auf die Glättung der Ränder verzichtet. Stattdessen werden nur Reports verwendet, die komplett innerhalb der Radarabdeckung liegen. Für die DTCWT der Helligkeitstemperatur wird ein 512×512 Gitterpunkte großer Ausschnitt über Mitteleuropa gewählt, dessen Ränder in der Folge abgeschnitten und nicht mehr berücksichtigt werden.

5.3 Zusammenfassung der Ergebnisse

Die einzelnen Komponenten vom LW werden zunächst anhand eines geometrischen Objekts diskutiert. Mit zunehmender Größe eines Quadrats wird die Skala größer, während die Intensität und die Anisotropie gleich bleibt. Betrachtet man verschiedene Quadrate mit der gleichen Seitenlänge und erhöht die Intensität, indem die Werte innerhalb des Quadrats erhöht werden, so steigt LW_{in} kontinuierlich an. Verkleinert man die Seite des Quadrats, sodass ein Rechteck und im Grenzfall eine Linie entsteht, so nimmt die Skala (LW_{sc}) ab, zeitgleich vergrößert sich aber wie gewünscht die Anisotropie (LW_{ai}). Ein anschließender Vergleich mit konstruierten Feldern aus den Studien von Tobin et al. (2012) und White et al. (2018) zeigt, dass der LW sich ähnlich wie SCAI und COP verhält. Allerdings beinhaltet der LW durch die drei verschiedenen Komponenten noch weitere Informationen, sodass der LW sogar zwischen Situationen unterscheiden kann, in denen SCAI und COP die gleiche Organisation messen, obwohl optisch ganz andere Strukturen ausgemacht werden können.

Die große Stärke vom LW gegenüber den anderen Indexen liegt jedoch in der Lokalisierung. So zeigt die Analyse zweier Fallbeispiele, dass im Bereich des Hook-Echos einer Superzelle sehr hohe Niederschlagsraten auftreten, während im Falle einer Squall-Line die stärksten Niederschläge entlang einer Linie fallen. Dies resultiert in einer großen Skala (hoher LW_{sc}), während die Superzelle und speziell der Niederschlag im Hook-Echo kleinräumige Strukturen aufweist. Die Intensität ist bei beiden hoch, jedoch sinkt LW_{in} im hinteren Teil der Squall-Line rasch ab. LW_{ai} folgt dem Hook-Echo der Superzelle, die Anisotropie ist jedoch gering. Die Linearität der Niederschläge entlang der Squall-Line führt zu sehr hoher Anisotropie und auch die Richtungskomponenten LW_u und LW_v zeigen eine eindeutige Ausrichtung senkrecht zur Windscherung.

Da sich die Strukturen innerhalb der konvektiven Zellen abhängig von der Zugrichtung ausbilden, werden für die folgende Analyse der LW-Kompositen die Zellen entlang der Windscherung zwischen dem 500 hPa Niveau und dem 10 m Wind ausgerichtet. Als Grundlage dafür dient die Reanalyse ERA-Interim (Dee et al., 2011). Besonders Gewitter, Starkniederschläge und Hagel treten in Zusammenhang mit intensiven Regenraten und kalten Wolkentops auf. Für Schauer sind die Niederschlagsraten geringer und die Helligkeitstemperaturen höher.

In der Analyse vom LW liegt der Fokus auf den besonders intensiven und schadensbringenden Kategorien Starkniederschlag und Hagel sowie Schauer und Gewitter. Es stellt sich

heraus, dass die Skala der Regenraten im Fall von Gewittern gemäß Student-T-Test signifikant größer ist als für Starkniederschläge und Hagel. Zudem nimmt für die beiden zuletzt genannten Kategorien LW_{sc} mit zunehmender Entfernung vom Beobachtungsort rasch ab, während Gewitter nur geringe räumliche Variationen im Umkreis von 25 km aufweisen. Dies ist dadurch zu erklären, dass Starkregen und Hagel nur sehr lokal in einem Gewitter auftreten. Im Fall von Hagelereignissen, die meist im Zusammenhang mit Superzellen stehen, wird links vom Schervektor großskaliger Niederschlag identifiziert. Die Intensität (LW_{in}) ist am größten für Hagel- und Niederschlagsereignisse und sinkt rasch mit Entfernung vom Beobachtungsort. Stärkere Anisotropie tritt im skaligen Niederschlag links vom Schervektor während Hagelereignissen auf. Die dominierende Richtung im Wavelet-Spektrum folgt ausgehend von dem skaligen Niederschlag ganz gut der Struktur eines Hook-Echos.

Führt man die Analyse auf Basis von den größer aufgelösten Satellitenbeobachtungen durch, so werden die Strukturen im Bereich von Starkniederschlägen und Hagel ebenfalls als kleinskalig eingeschätzt. Starker Niederschlag und Hagel tritt überwiegend im Bereich starker Updrafts auf, die in der Helligkeitstemperatur oft als Overshooting Tops zu erkennen sind. In diesem Bereich detektiert LW_{in} gleichzeitig hohe Intensitäten, also sehr niedrige Temperaturen. Da in den Helligkeitstemperaturen die Strukturen weniger linear ausgerichtet sind, sondern vielmehr kreisförmig um die Overshooting Tops herum, ist die Anisotropie nicht so stark ausgeprägt. Einzig im Bereich von Hagelereignissen deutet LW_{ai} auf erhöhte Anisotropie im Bereich der Inflow-Line hin.

Abschließend werden die Erkenntnisse aus der vorangehenden Analyse benutzt, um eine Klassifikation zwischen den verschiedenen Kategorien Schauer, Gewitter und Starkniederschlägen bzw. Hagel durchzuführen. Es stellt sich heraus, dass die Klassifikation mithilfe eines einfachen neuralen Netzes mit einer Ebene am besten abschneidet. So leben Gewitter auf größeren Skalen und sind etwas intensiver als Schauer, während Hagel und Starkregen sich nur in einer noch höheren Intensität von Schauern und Gewittern unterscheiden.

6 Software-Paket zur Berechnung von WOI, LWOI und LW

Zur Berechnung des Wavelet-basierten Organisationsindexes in seinen unterschiedlichen Fassungen (WOI, modifizierter WOI, LWOI, LW) wurde folgendes R-Paket veröffentlicht:

Brune, S., S. Buschow, F. Kapp & P. Friederichs (2020). *calcWOI: Calculates the Wavelet-Based Organization Index.* R package version 1.0.3. URL: <https://CRAN.R-project.org/package=calcWOI> (zuletzt abgerufen am 18.03.2021).

6.1 Einleitung

Im Rahmen dieser Dissertation wurde das Software-Paket `calcWOI` zur Verfügung gestellt, um den Wavelet-basierten Organisationsindex komfortabel berechnen zu können. `calcWOI` ist in der Programmiersprache R geschrieben und wurde in seiner ersten Fassung (Version 1.0.1) am 02.04.2019 im *Comprehensive R Archive Network* veröffentlicht. Zu diesem Zeitpunkt waren Berechnungen von WOI, dem modifizierten WOI und LWOI möglich. Am 04.04.2019 wurde das erste Update (1.0.2) hochgeladen, welches kleinere Bugs und Tippfehler behob. Die aktuelle Version 1.0.3 vom 28.03.2020 beinhaltet zusätzlich die Funktion `LW` zur Berechnung von LW auf Basis der Dual-Tree Wavelets.

6.2 Zusammenfassung der wesentlichen Funktionen

`calcWOI` besteht aus insgesamt sieben Funktionen und dem Datensatz `AICEN`. `AICEN` beinhaltet die konstanten Koeffizienten zur Berechnung der Bias-Korrektur nach Eckley et al. (2010) und der zentralen Skala für Felder der Größe 16×16 bis 4096×4096 Gitterpunkte. Die Hilfsfunktionen `blowup` (ergänzt Nullen am Rand), `buildperiodic` (spiegelt das Eingangsfeld und generiert dadurch ein periodisches Feld), `flatten` (glättet die Ränder) und `shiftmat` (verschiebt Elemente einer Matrix) werden hier nicht weiter diskutiert. Die Funktion `wavtra` erwartet ein bereits quadratisches zweidimensionales Eingangsfeld mit Seitenlänge 2^K , $K \in \mathbb{N}$ (z. B. generiert mit den Hilfsfunktionen) und führt die Wavelet-Transformation samt Bias-Korrektur mithilfe der Koeffizienten aus `AICEN` durch. Die beiden Hauptfunktionen `WOI` und `LW` werden im Folgenden vorgestellt.

6.2.1 Die Funktion WOI

Die zentrale Funktion in `calcWOI` zur Berechnung von WOI, dem modifizierten WOI und LWOI ist `WOI`. Das erste Argumente der Funktion ist ein beliebig großes zweidimensionale

Array, für welches die Indexe berechnet werden sollen. Zweites und drittes Argument ist die Vorauswahl der kleinen und großen Skala, welche für die Berechnung von WOI und LWOI benötigt wird. Um die Anzahl der Gitterpunkte mit Niederschlag oder unterschritten Helligkeitstemperatur zu identifizieren, kann ein Schwellenwert (z. B. 0.1 mm/h, 245 K) übergeben werden. Das fünfte Argument gibt an, wie viele Gitterpunkte am Rand geglättet werden sollen, bevor das Feld an den Rändern mit Nullen zu einer quadratischen Größe mit Seitenlänge 2^K , $K \in \mathbb{N}$, aufgefüllt wird. Zudem gibt es einen Schalter, der Meldungen der Funktion aus dem Bildschirm ausgibt. Mit dem siebten und letzten Argument der Funktion `WOI` kann man der Funktion mitteilen, ob das Eingangsfeld bereits periodische Ränder hat (z. B. globale Daten).

In der Funktion wird zunächst geprüft, ob das Eingangsfeld eine angemessene Dimension hat. Je nach Einstellung wird anschließend der Rand geglättet und mit Nullen aufgefüllt oder das Feld periodisch fortgesetzt. Für das nun quadratische Feld wird mit der Funktion `wavtra` die Wavelet-Transformation durchgeführt. `wavtra` basiert auf den R-Paketen `wavethresh` (Nason, 2016) und `LS2W` (Eckley & Nason, 2011). Die Wavelet-Koeffizienten an den zuvor künstlich generierten Rändern werden nach der Transformation abgeschnitten. Um die Rechenzeit möglichst gering zu halten, werden die Wavelet-Koeffizienten an eine Fortran-Subroutine übergeben, die den WOI, den modifizierten WOI und den LWOI gemäß der Gleichungen (3.4)-(3.3), (4.1)-(4.3) bzw. (4.4)-(4.6) berechnet. Ausgegeben wird von der Funktion neben den jeweiligen Komponenten vom WOI, dem modifizierten WOI und dem LWOI auch die gewählten Eingangsparameter und die Rechenzeit.

6.2.2 Die Funktion LW

Die Funktion `LW` nutzt zur Berechnung des Dual-Tree Wavelet-Spektrums die Funktion `f1d2dt` aus dem R-Paket `dualtrees` (Buschow et al., 2020). `LW` hat als Eingangsparameter das zweidimensionalen Eingangsfeld, den Schwellenwert und einen Schalter für die Bildschirmausgabe. Im Gegensatz zu `WOI` kann in `LW` die Größe des zu transformierenden Feldes sowie die Art der Randbedingungen bestimmt werden. Für nähere Details soll an dieser Stelle auf Buschow et al. (2020) verwiesen werden.

Die Funktion `LW` prüft zunächst ebenfalls, ob das Eingangsfeld die nötigen Eigenschaften zur Transformation besitzt. Dann wird die Dual-Tree Wavelet-Transformation durchgeführt, ehe die drei Komponenten LW_{sc} , LW_{in} und LW_{ai} gemäß der Gleichungen (5.4)-(5.6) berechnet werden. Zusätzlich zu den drei Komponenten werden die Komponenten LW_u , LW_v und deren Winkel ϕ ausgegeben, die mithilfe der Funktionen `dt2cen` und `cen2uv` aus dem `dualtrees`-Paket bestimmt werden.

7 Weitere Arbeiten im Rahmen dieser Dissertation

Zusätzlich wurde im Rahmen dieser Dissertation an zwei weiteren Artikeln mitgewirkt, die im Folgenden knapp zusammengefasst werden. Detaillierter wird auf die Passagen eingegangen, an denen ich maßgeblich beteiligt war.

7.1 Artikel Kapp et al. (2018)

Die Veröffentlichung Kapp et al. (2018) basiert auf der Masterarbeit von Kapp (2016), in der der Niederschlag des 20-Member-Ensembles COSMO-DE-EPS (Baldauf et al., 2011) mithilfe von Wavelets untersucht wurde. Insgesamt wurden 14 Fallbeispiele aus dem Jahr 2011 gewählt und die Vorhersage des Ensembles mit der regionalen Reanalyse COSMO-REA2 (Wahl et al., 2017) verglichen. Dafür wurde das Wavelet-Spektrum der Ensemble-Vorhersagen und der Reanalyse berechnet und über den Raum gemittelt, um nur die Struktur der Objekte und nicht deren Lokalisierung zu analysieren. Auf das Wavelet-Spektrum, welches aus $K = 6$ Skalen und $D = 3$ Orientierungen besteht, wurde eine lineare Diskriminanzanalyse (LDA) angewendet, um die Anzahl der Freiheitsgrade zu reduzieren. Es stellt sich heraus, dass allein auf Basis des räumlich gemittelten Wavelet-Spektrums und der anschließenden LDA die Reanalyse in über 80 % der Fälle dem korrekten Ensemble zugeordnet werden konnte. Generell war das Ensemble in der Lage, die räumlichen Strukturen des Niederschlagsfeldes in der Reanalyse gut vorherzusagen.

Die Berechnung der Wavelet-Spektren sowie das Anwenden der LDA wurden von Florian Kapp durchgeführt. Florian Kapp, Petra Friederichs und Michael Weniger haben gemeinsam die theoretischen Grundlagen erarbeitet und Methodik entwickelt. Der Artikel wurde überwiegend von Florian Kapp und Petra Friederichs geschrieben. Meine Beiträge bestanden in der Anfertigung der Abbildungen sowie dem Erstellen einzelner Textpassagen. Zudem konnte ich während der Mitarbeit an diesem Artikel grundlegende Kenntnisse über die Wavelet-Transformation und die technische Umsetzung erlangen, die ich im weiteren Verlauf dieser Dissertation an vielen Stellen einbringen konnte.

7.2 Artikel Stevens et al. (2020)

Im Rahmen der zweiten Phase des Projektes HD(CP)² wurde unter der Leitung von Bjorn Stevens ein umfangreicher Artikel veröffentlicht, der die wesentlichen Ergebnisse des Projektes zusammenfasst (Stevens et al., 2020). Dabei steht die Repräsentation von Wolken und Niederschlag in hochauflösenden Simulationen in unterschiedlichen klimatischen Regionen im Fokus. Neben den in dieser Dissertation schon betrachteten Simulationen über

Deutschland und dem tropischen Atlantik wurden beispielsweise auch Simulationen über dem Nordatlantik und Südostasien ausgewertet. Nach Beschreibung der Simulationen und verwendeten Beobachtungsdatensätze wird detailliert auf die Bereiche Niederschlag, Wolken und Parametrisierung wie Strahlung und Turbulenz eingegangen, ehe am Ende der Nutzen der hochauflösenden Simulationen diskutiert wird.

Um den Unterschied zwischen den hochauflösenden ICON-Simulationen und gängigen Wetter- und Klimamodellen wie ICON-NWP und ECHAM zu Beginn des Artikels zu visualisieren, wurden im Rahmen dieser Dissertation Energiespektren des horizontalen und vertikalen Windes angefertigt. Meine Aufgabe bestand darin, die Spektren der kinetischen Energie für den Wind in 500 hPa aus den verschiedenen Simulationen mit ICON, ICON-NWP und ECHAM zu berechnen, grafisch darzustellen und zu beschreiben (Abbildung 4 in Stevens et al., 2020). Die horizontale effektive Auflösung in den ICON-Simulationen liegt im Bereich von 1 km bis 10 km und ist damit um ein Hundertfaches höher als für das globale Wettermodell ICON-NWP (200 km) oder das Klimamodell ECHAM (500 km). Für die Untersuchung von Wolken- und Niederschlagsprozesse ist vor allem die Repräsentation der vertikalen Austauschprozesse von großer Bedeutung. Das Spektrum der vertikalen kinetischen Energie zeigt, dass in den Simulationen über Deutschland aus Kapitel 5 Prozesse von rund 1 km aufgelöst werden können. Dadurch sollten mithilfe dieser Simulationen die Wolken- und Niederschlagsbildung in den unterschiedlichen Simulationsgebieten gut abgebildet werden können und schlussendlich zu einem besseren Verständnis dieser Prozesse führen.

8 Fazit und Ausblick

Diese Dissertation fasst die Entwicklung und Anwendung des Wavelet-basierten Organisationsindexes zur Beschreibung der konvektiven Organisation zusammen. Die Information aus dem Wavelet-Spektrum bezüglich der Skala, der Intensität und der Richtung wurde genutzt, um die Organisation der Konvektion möglichst gut beschreiben zu können. In der ursprünglichen Fassung vom WOI (Kapitel 3) wurde das Haar-Wavelet benutzt und die einzelnen Komponenten waren nicht normiert. Bei der Weiterentwicklung vom WOI in Kapitel 4 wurden die Komponenten mit der Einführung des Daubechies 4 Wavelets und einer Normierung vergleichbarer. Zudem können die Komponenten seitdem auch im Raum berechnet werden (LWOI), sodass eine Lokalisierung der konvektiven Organisation innerhalb einer Domain möglich wurde. Es stellte sich jedoch heraus, dass die räumliche Orientierung der Konvektion, gemessen mittels der Anisotropiekomponente $LWOI_{ai}$, durch die fehlende Rotationsinvarianz des Wavelet-Spektrums nicht zufriedenstellend beschrieben werden kann. Deshalb wurde das rotationsinvariante Spektrum der Dual-Tree Wavelets eingeführt (Kapitel 5), um die finale Version des Indexes zu definieren. Zudem wurde der letzte Freiheitsgrad des LWOI, nämlich die vorherige Einteilung in kleine und große Skalen, mithilfe der Einführung der zentralen Skala eliminiert.

Im ersten Teil wurde die konvektive Organisation über Deutschland anhand der Regenraten für drei Fallbeispiele untersucht. Schon die ursprüngliche Version des Wavelet-basierten Organisationsindexes (WOI) konnte zwischen unorganisiertem Rückseitenwetter und linear organisierter Konvektion unterscheiden. Ein Vergleich mit konvektiven und dynamischen Variablen wie CAPE oder der Windscherung haben gezeigt, dass der WOI besser zwischen den beiden Organisationstypen unterscheiden kann als andere in der Literatur verwendeten Indexe.

In Kapitel 4 wurde der modifizierte WOI auf zwei Beobachtungsdatensätze und eine hochauflöste ICON-Simulation über dem tropischen Atlantik für den August 2016 angewendet. Es wurde gezeigt, dass sich die Struktur der Konvektion über dem afrikanischen Kontinent und dem tropischen Atlantik unterscheidet. Dabei wurden je nach Region unterschiedliche Korrelationen zwischen dem LWOI und den dynamischen und konvektiven Variablen aus dem ICON Modell gefunden.

Zuletzt wurden LW-Komposita um Hagel- und Starkregenereignisse sowie Schauer und Gewitter analysiert. Im Vergleich zu den beiden vorherigen Studien wurde der Index neben Regenraten erstmals auch auf Helligkeitstemperaturen angewendet. In den LW-Komposita beider Variablen waren signifikante Strukturen zu erkennen. Beispielsweise kann in den Regenraten die Struktur eines Hook-Echos mittels LW_{ai} detektiert werden, im Bereich starker Konvektion deuten räumlich begrenzte Signale in LW_{in} auf Overshooting-Tops hin. Zudem kann mithilfe der drei Komponenten LW_{sc} , LW_{ai} und LW_{in} zwischen Schauern, Gewitter und Ereignissen mit Hagel bzw. Starkregen klassifiziert werden.

Die Beschreibung der konvektiven Organisation funktioniert also nicht nur im Bereich von mittleren Breiten, sondern auch in anderen Regionen. Weiterhin ist der Index nicht

an Regenraten gebunden. Durch die Beschreibung über das Wavelet-Spektrum kann der Index auch dazu benutzt werden, um Organisation anhand von weiteren Variablen wie der Vertikalgeschwindigkeit oder dem Wasserdampfgehalt zu ermitteln. In seiner finalen Version ist der LW auch nicht mehr von Schwellenwerten abhängig. Der größte Vorteil gegenüber den gängigen Indexen aus der Literatur ist allerdings, dass mit dem LW die Organisation der Konvektion direkt auf einer Karte darstellbar ist. Somit können auch verschiedene räumliche Strukturen erkannt und die räumliche Variabilität der Organisation beschrieben werden. Durch die Bereitstellung des R-Pakets `calcWOI` (Kapitel 6) lassen sich die verschiedenen Versionen des Wavelet-basierten Organisationsindexes einfach berechnen.

Die Entwicklung des Indexes ist mit den hier präsentierten Studien abgeschlossen. In zukünftigen Studien könnte LW beispielsweise auf hochaufgelöste Reanalyse-Daten (COSMO-REA2, COSMO-REA6) angewendet werden, um die regionale und zeitliche Variabilität von konvektiver Organisation zu untersuchen und untereinander zu vergleichen. Dazu eignen sich prinzipiell auch Beobachtungen von Satellit und Radar. Im Vergleich zum homogenen Reanalyse-Output müssen in den Beobachtungen jedoch Fehlwerte und Messfehler herausgefiltert werden, um die Wavelet-Transformation anwenden zu können. Mithilfe einer Klimatologie basierend auf LW könnte die konvektive Organisation in Wetter- und Klimamodellen besser parametrisiert werden. Dadurch könnte auch die Wechselwirkung von organisierter Konvektion mit der synoptischen Skala besser erfasst und beschrieben werden.

Symbol- und Abkürzungsverzeichnis

A	Fläche der gesamten Domain
A_a	Fläche des Clusters a
A_b	Fläche des Clusters b
\mathbf{A}_ψ^{-1}	Korrekturmatrix für das Wavelet ψ
AEW	African Easterly Waves
calcWOI	R-Paket zur Berechnung des WOI, modifizierten WOI, LWOI und LW
CAPE	Convective Available Potential Energy
CIN	Convective Inhibition
COP	Convective Organization Potential
d	Orientierung im Wavelet-Spektrum
d_s	Abstand zweier Cluster
$d(a, b)$	Abstand zwischen Cluster a und Cluster b
D	Anzahl aller Orientierungen
D_0	Wurzel aus dem Produkt aller Abstände zwischen den Clustern
DB4	Daubechies 4 Wavelet
DTCWT	Dual-Tree Complex Wavelet Transformation
COSMO-DE-EPS	Ensemblevorhersage des DWDs mit 20 Membern
COSMO-REA2	Regionale Reanalyse des DWDs
DWT	Diskrete Wavelet-Transformation
DWD	Deutscher Wetterdienst
$e_d(x, y)$	Normalisierte Energie der Orientierung d aus dem Dual-Tree Wavelet-Spektrums am Gitterpunkt (x, y)
$e_k(x, y)$	Normalisierte Energie der Skala k aus dem Dual-Tree Wavelet-Spektrums am Gitterpunkt (x, y)
\bar{E}	Gesamte spektrale Energie
\bar{E}_l	Domain-gemittelte spektrale Energie auf großen Skalen
\bar{E}_s	Domain-gemittelte spektrale Energie auf kleinen Skalen
\bar{E}_l^d	Domain-gemittelte spektrale Energie auf großen Skalen für die Orientierung d
\bar{E}_s^d	Domain-gemittelte spektrale Energie auf kleinen Skalen für die Orientierung d
$E(i, j)$	Gesamte spektrale Energie am Gitterpunkt (i, j)
$E(x, y)$	Gesamte Energie aus dem Dual-Tree Wavelet-Spektrums am Gitterpunkt (x, y)
$E_{k,d}(x, y)$	Energie aus dem Dual-Tree Wavelet-Spektrums auf Skala k und Orientierung d am Gitterpunkt (x, y)

$E_k^d(i, j)$	Spektrale Energie auf Skala k und Orientierung d am Gitterpunkt (i, j)
$E_l(i, j)$	Spektrale Energie auf der großen Skala am Gitterpunkt (i, j)
$E_l^d(i, j)$	Spektrale Energie auf der großen Skala für die Orientierung d am Gitterpunkt (i, j)
$E_s(i, j)$	Spektrale Energie auf der kleinen Skala am Gitterpunkt (i, j)
$E_s^d(i, j)$	Spektrale Energie auf der kleinen Skala für die Orientierung d am Gitterpunkt (i, j)
ECHAM	Globales atmosphärisches Modell, Gitterpunktabstand von rund 100 km
ESWD	European Severe Weather Database
i	Gitterpunkt in x-Richtung
ICON	Icosahedral Nonhydrostatic, verwendetes Simulationsmodell
ICON-NWP	ICON mit einem Gitterpunktabstand von rund 40 km
I_{org}	Organization Index
IR	Infrarot-Kanal
j	Gitterpunkt in y-Richtung
k	Skala im Wavelet-Spektrum
K	Anzahl aller Skalen
L	Charakteristische Länge
LDA	Lineare Diskriminanzanalyse
LW	Lokaler Wavelet-basierter Organisationsindex, basierend auf der Dual-Tree Wavelet-Transformation
LW_{sc}	Komponente Skala des LW
LW_{in}	Komponente Intensität des LW
LW_{ai}	Komponente Anisotropie des LW
LW_u	Anisotropie in x-Richtung
LW_v	Anisotropie in y-Richtung
LWOI	Lokaler Wavelet-basierter Organisationsindex
$LWOI_{sc}$	Komponente Skala des LWOI
$LWOI_{in}$	Komponente Intensität des LWOI
$LWOI_{ai}$	Komponente Anisotropie des LWOI
MW	Mikrowellen-Kanal
n	Anzahl der Cluster-Paare
\mathbb{N}	Natürliche Zahlen (ohne Null)
N	Anzahl konvektiver Cluster
N_{max}	Anzahl maximal möglicher konvektiver Cluster
N_x	Anzahl Gitterpunkte in x-Richtung
N_y	Anzahl Gitterpunkte in y-Richtung
ϕ	Winkel der dominierenden Orientierung
ψ	Mutter-Wavelet
ψ_i	Imaginärer Part des Mutter-Wavelets
$\psi_{k,d,\mathbf{u}}$	Tochter-Wavelet zur Skala k , Orientierung d und Verschiebung \mathbf{u}
ψ_r	Reeller Part des Mutter-Wavelets
r	Anzahl Gitterpunkte mit Regenraten größer als 0 mm/h
\mathbf{r}	Ortsvektor im zweidimensionalen Raum

RADKLIM	Datensatz korrigierter Radardaten des DWD
SCAI	Simple Convective Aggregation Index
SYNOP	Meldung einer DWD Station
u	Shift
UTC	Coordinated Universal Time
$V(a, b)$	Interaktionspotential zwischen Cluster a und Cluster b
W	Weibull Verteilung
$w_{k,d,u}$	Wichtung im Wavelet-Prozess
WOI	Wavelet-basierter Organisationsindex
WOI_1	Komponente Skala des WOI
WOI_2	Komponente Intensität des WOI
WOI_3	Komponente Anisotropie des WOI
WOI_{sc}	Komponente Skala des modifizierten WOI
WOI_{in}	Komponente Intensität des modifizierten WOI
WOI_{ai}	Komponente Anisotropie des modifizierten WOI
x	Gitterpunkt in zonaler Richtung
X	Lokaler stationärer zweidimensionaler Wavelet-Prozess
$\xi_{k,d,u}$	Weißes Rauschen mit Mittelwert null
y	Gitterpunkt in meridionaler Richtung
\mathbb{Z}	Ganze Zahlen

Literaturverzeichnis

- Baldauf, M., A. Seifert, J. Förstner, D. Majewski, M. Raschendorfer & T. Reinhardt (2011). „Operational Convective-Scale Numerical Weather Prediction with the COSMO Model: Description and Sensitivities“. *Monthly Weather Review* 139 (12), S. 3887–3905.
- Brune, S., S. Buschow & P. Friederichs (2020a). „Observations and high-resolution simulations of convective precipitation organization over the tropical Atlantic“. *Quarterly Journal of the Royal Meteorological Society* 146 (729), S. 1545–1563.
- Brune, S., S. Buschow & P. Friederichs (2021). „The local wavelet-based organization index - Quantification, localization and classification of convective organization from radar and satellite data“. *Quarterly Journal of the Royal Meteorological Society* 147 (736), S. 1853–1872.
- Brune, S., S. Buschow, F. Kapp & P. Friederichs (2020b). *calcWOI: Calculates the Wavelet-Based Organization Index*. R package version 1.0.3.
- Brune, S., F. Kapp & P. Friederichs (2018). „A wavelet-based analysis of convective organization in ICON large-eddy simulations“. *Quarterly Journal of the Royal Meteorological Society* 144 (717), S. 2812–2829.
- Burpee, R. W. (1972). „The origin and structure of easterly waves in the lower troposphere of North Africa“. *Journal of the Atmospheric Sciences* 29 (1), S. 77–90.
- Buschow, S. & P. Friederichs (2020). „Using wavelets to verify the scale structure of precipitation forecasts“. *Advances in Statistical Climatology, Meteorology and Oceanography* 6 (1), S. 13–30.
- Buschow, S., J. Pidstrigach & P. Friederichs (2019). „Assessment of wavelet-based spatial verification by means of a stochastic precipitation model (wv_verif v0.1.0)“. *Geoscientific Model Development* 12 (8), S. 3401–3418.
- Buschow, S. & P. Friederichs (2021). „SAD: Verifying the scale, anisotropy and direction of precipitation forecasts“. *Quarterly Journal of the Royal Meteorological Society* 147 (735), S. 1150–1169.
- Buschow, S., N. Kingsbury & R. Wareham (2020). *dualtrees: Decimated and Undecimated 2D Complex Dual-Tree Wavelet Transform*. R package version 0.1.4.
- Carlson, T. N. (1969). „Some remarks on African disturbances and their progress over the tropical Atlantic“. *Monthly Weather Review* 97 (10), S. 716–726.
- Crétat, J., E. K. Vizy & K. H. Cook (2015). „The relationship between African easterly waves and daily rainfall over West Africa: observations and regional climate simulations“. *Climate dynamics* 44 (1-2), S. 385–404.
- Daubechies, I. (1992). *Ten lectures on wavelets*. Society for Industrial und Applied Mathematics, Philadelphia, PA, S. 357.
- Dee, D. P., S. Uppala, A. Simmons, P. Berrisford, P. Poli, S. Kobayashi, U. Andrae, M. Balmaseda, G. Balsamo, d. P. Bauer et al. (2011). „The ERA-Interim reanalysis:

- Configuration and performance of the data assimilation system“. *Quarterly Journal of the Royal Meteorological Society* 137 (656), S. 553–597.
- Diedhiou, A., S. Janicot, A. Viltard, P. De Felice & H. Laurent (1999). „Easterly wave regimes and associated convection over West Africa and tropical Atlantic: Results from the NCEP/NCAR and ECMWF reanalyses“. *Climate Dynamics* 15 (11), S. 795–822.
- Dotzek, N., P. Groenemeijer, B. Feuerstein & A. M. Holzer (2009). „Overview of ESSL’s severe convective storms research using the European Severe Weather Database ESS-WD“. *Atmospheric research* 93 (1-3), S. 575–586.
- Duvel, J. P. (1990). „Convection over tropical Africa and the Atlantic Ocean during northern summer. Part II: Modulation by easterly waves“. *Monthly Weather Review* 118 (9), S. 1855–1868.
- Eckley, I. A. & G. P. Nason (2011). „LS2W: Implementing the Locally Stationary 2D Wavelet Process Approach in R“. *Journal of Statistical Software* 43 (3), S. 1–23.
- Eckley, I. A., G. P. Nason & R. L. Treloar (2010). „Locally stationary wavelet fields with application to the modelling and analysis of image texture“. *Journal of the Royal Statistical Society, Series C* 59 (4), S. 595–616.
- Fink, A. H. & A. Reiner (2003). „Spatiotemporal variability of the relation between African easterly waves and West African squall lines in 1998 and 1999“. *Journal of Geophysical Research: Atmospheres* 108 (D11).
- Futyan, J. M. & A. D. Del Genio (2007). „Deep convective system evolution over Africa and the tropical Atlantic“. *Journal of Climate* 20 (20), S. 5041–5060.
- Haar, A. (1910). „Zur Theorie der orthogonalen Funktionensysteme“. *Mathematische Annalen* 69 (3), S. 331–371.
- Houze, R. A. (2004). „Mesoscale convective systems“. *Reviews of Geophysics* 42 (4).
- Jackson, B., S. E. Nicholson & D. Klotter (2009). „Mesoscale convective systems over western equatorial Africa and their relationship to large-scale circulation“. *Monthly Weather Review* 137 (4), S. 1272–1294.
- Janiga, M. A. & C. D. Thorncroft (2016). „The influence of African easterly waves on convection over tropical Africa and the east Atlantic“. *Monthly Weather Review* 144 (1), S. 171–192.
- Janiga, M. A. & C. D. Thorncroft (2014). „Convection over tropical Africa and the east Atlantic during the West African monsoon: Regional and diurnal variability“. *Journal of Climate* 27 (11), S. 4159–4188.
- Janowiak, J., B. Joyce & P. Xie (2017). „NCEP/CPC L3 Half Hourly 4km Global (60S - 60N) Merged IR V1“. Edited by Andrey Savtchenko, Greenbelt, MD, Goddard Earth Sciences Data and Information Services Center (GES DISC).
- Kapp, F. (2016). „Verification of COSMO-DE-EPS precipitation through wavelets“. Masterarbeit. Meteorologisches Institut der Rhein.-Friedr.-Wilh.-Universität.
- Kapp, F., P. Friederichs, S. Brune & M. Weniger (2018). „Spatial verification of high-resolution ensemble precipitation forecasts using local wavelet spectra“. *Meteorologische Zeitschrift* 27 (6), S. 467–480.
- Kiladis, G. N., C. D. Thorncroft & N. M. Hall (2006). „Three-dimensional structure and dynamics of African easterly waves. Part I: Observations“. *Journal of the Atmospheric Sciences* 63 (9), S. 2212–2230.

- Kingsbury, N. (1999). „Image processing with complex wavelets“. *Philosophical Transactions of the Royal Society of London. Series A: Mathematical, Physical and Engineering Sciences* 357 (1760), S. 2543–2560.
- Kingsbury, N. (2006). „Rotation-invariant local feature matching with complex wavelets“. *2006 14th European Signal Processing Conference*. IEEE, S. 1–5.
- Kumar, P. & E. Foufoula-Georgiou (1997). „Wavelet analysis for geophysical applications“. *Reviews of Geophysics* 35 (4), S. 385–412.
- Liu, C., E. J. Zipser & S. W. Nesbitt (2007). „Global distribution of tropical deep convection: Different perspectives from TRMM infrared and radar data“. *Journal of Climate* 20 (3), S. 489–503.
- Lubis, S. W. & C. Jacobi (2015). „The modulating influence of convectively coupled equatorial waves (CCEWs) on the variability of tropical precipitation“. *International Journal of Climatology* 35 (7), S. 1465–1483.
- Mathon, V. & H. Laurent (2001). „Life cycle of Sahelian mesoscale convective cloud systems“. *Quarterly Journal of the Royal Meteorological Society* 127 (572), S. 377–406.
- Mekonnen, A. & W. B. Rossow (2018). „The Interaction between Deep Convection and Easterly Wave Activity over Africa: Convective Transitions and Mechanisms“. *Monthly Weather Review* 146 (6), S. 1945–1961.
- Mekonnen, A., C. D. Thorncroft & A. R. Aiyyer (2006). „Analysis of convection and its association with African easterly waves“. *Journal of Climate* 19 (20), S. 5405–5421.
- Nason, G. (2008). *Wavelet methods in statistics with R*. Springer Science & Business Media.
- Nason, G. (2016). *wavethresh: Wavelets Statistics and Transforms*. R package version 4.6.8.
- Nason, G. P., R. Von Sachs & G. Kroisandt (2000). „Wavelet processes and adaptive estimation of the evolutionary wavelet spectrum“. *Journal of the Royal Statistical Society: Series B (Statistical Methodology)* 62 (2), S. 271–292.
- Nelson, J. D., A. J. Gibberd, C. Naifornita & N. Kingsbury (2018). „The locally stationary dual-tree complex wavelet model“. *Statistics and Computing* 28 (6), S. 1139–1154.
- Orlanski, I. (1975). „A rational subdivision of scales for atmospheric processes“. *Bulletin of the American Meteorological Society* 56, S. 527–530.
- Parker, M. D. & R. H. Johnson (2000). „Organizational modes of midlatitude mesoscale convective systems“. *Monthly Weather Review* 128 (10), S. 3413–3436.
- Petersen, W. A. & S. A. Rutledge (2001). „Regional variability in tropical convection: Observations from TRMM“. *Journal of climate* 14 (17), S. 3566–3586.
- Price, C., Y. Yair & M. Asfur (2007). „East African lightning as a precursor of Atlantic hurricane activity“. *Geophysical Research Letters* 34 (9).
- Reed, R. J., D. C. Norquist & E. E. Recker (1977). „The structure and properties of African wave disturbances as observed during Phase III of GATE“. *Monthly Weather Review* 105 (3), S. 317–333.
- Rickenbach, T., R. Nieto Ferreira, N. Guy & E. Williams (2009). „Radar-observed squall line propagation and the diurnal cycle of convection in Niamey, Niger, during the 2006 African Monsoon and Multidisciplinary Analyses Intensive Observing Period“. *Journal of Geophysical Research: Atmospheres* 114 (D3).

- Schumacher, C. & R. A. Houze Jr (2006). „Stratiform precipitation production over sub-Saharan Africa and the tropical East Atlantic as observed by TRMM“. *Quarterly Journal of the Royal Meteorological Society* 132 (620), S. 2235–2255.
- Selesnick, I. W., R. G. Baraniuk & N. C. Kingsbury (2005). „The dual-tree complex wavelet transform“. *IEEE signal processing magazine* 22 (6), S. 123–151.
- Stevens, B., C. Acquistapace, A. Hansen, R. Heinze, C. Klinger, D. Klocke, H. Rybka, W. Schubotz, J. Windmiller, P. Adamidis, I. Arka, V. Barlakas, J. Biercamp, M. Brueck, S. Brune, S. A. Buehler, U. Burkhardt, G. Cioni, M. Costa-Suros, S. Crewell, T. Crüger, H. Deneke, P. Friederichs, C. C. Henken, C. Hohenegger, M. Jacob, F. Jakub, N. Kalthoff, M. Köhler, T. W. v. Laar, P. Li, U. Löhnert, A. Macke, N. Madenach, B. Mayer, C. Nam, A. K. Naumann, K. Peters, S. Poll, J. Quaas, N. Röber, N. Rochetin, L. Scheck, V. Schemann, S. Schnitt, A. Seifert, F. Senf, M. Shapkaliyevski, C. Simmer, S. Singh, O. Sourdeval, D. Spickermann, J. Strandgren, O. Tessiot, N. Vercauteren, J. Vial, A. Voigt & G. Zängl (2020). „The Added Value of Large-Eddy and Storm-Resolving Models for Simulating Clouds and Precipitation“. *Journal of the Meteorological Society of Japan* 98 (2), S. 395–435.
- Tobin, I., S. Bony & R. Roca (2012). „Observational Evidence for Relationships between the Degree of Aggregation of Deep Convection, Water Vapor, Surface Fluxes, and Radiation“. *Journal of Climate* 25 (20), S. 6885–6904.
- Tomassini, L. (2018). „Mesoscale Circulations and Organized Convection in African Easterly Waves“. *Journal of the Atmospheric Sciences* 75 (12), S. 4357–4381.
- Tompkins, A. M. & A. G. Semie (2017). „Organization of tropical convection in low vertical wind shears: Role of updraft entrainment“. *Journal of Advances in Modeling Earth Systems* 9 (2), S. 1046–1068.
- Torrence, C. & G. P. Compo (1998). „A practical guide to wavelet analysis“. *Bulletin of the American Meteorological Society* 79 (1), S. 61–78.
- Vidakovic, B. & P. Mueller (1994). „Wavelets for kids“. *Instituto de Estadística, Universidad de Duke*.
- Wahl, S., C. Bollmeyer, S. Crewell, C. Figura, P. Friederichs, A. Hense, J. D. Keller & C. Ohlwein (2017). „A novel convective-scale regional reanalysis COSMO-REA2: Improving the representation of precipitation“. *Meteorologische Zeitschrift* 26 (4), S. 345–361.
- Weisman, M. L. & J. B. Klemp (1986). „Characteristics of Isolated Convective Storms“. *Mesoscale Meteorology and Forecasting*. Hrsg. von P. S. Ray. Boston, MA: American Meteorological Society, S. 331–358.
- Weniger, M., F. Kapp & P. Friederichs (2017). „Spatial verification using wavelet transforms: a review“. *Quarterly Journal of the Royal Meteorological Society* 143 (702), S. 120–136.
- White, B. A., A. M. Buchanan, C. E. Birch, P. Stier & K. J. Pearson (2018). „Quantifying the Effects of Horizontal Grid Length and Parameterized Convection on the Degree of Convective Organization Using a Metric of the Potential for Convective Interaction“. *Journal of the Atmospheric Sciences* 75 (2), S. 425–450.
- Winterrath, T., C. Brendel, M. Hafer, T. Junghänel, A. Klameth, K. Lengfeld, E. Wallender, E. Weigl & A. Becker (2018). *RADKLIM Version 2017.002: Reprocessed quasi gauge-adjusted radar data, 5-minute precipitation sums (YW)*.

- Xie, S.-P. & J. A. Carton (2004). „Tropical Atlantic variability: Patterns, mechanisms, and impacts“. *Earth Climate* 147, S. 121–142.

Danksagung

An dieser Stelle möchte ich mich bei allen bedanken, die mir in den letzten Jahren bei der Anfertigung der Dissertation zur Seite standen. Ohne eure Unterstützung wäre dies nicht möglich gewesen!

Mein besonderer Dank gilt PD Dr. Petra Friederichs, die mir überhaupt erst die Möglichkeit zur Promotion gegeben hat. Mit ihren Ideen und Anregungen hat sie einen sehr großen Anteil an dieser Arbeit.

Ebenfalls möchte ich Prof. Dr. Andreas Hense und seiner gesamten Arbeitsgruppe für den konstruktiven Austausch während unserer gemeinsamen Zeit danken. Hervorzuheben sind Sebastian Buschow und Florian Kapp, die als Co-Autoren der jeweiligen Publikationen immer wertvollen Input gegeben haben.

Diese Arbeit entstand während der zweiten Phase des Projektes “High Definition Clouds and Precipitation for Advancing Climate Prediction”. Neben der Finanzierung durch das Bundesministerium für Bildung und Forschung danke ich allen Projektmitgliedern, insbesondere dem Teilprojekt S5 (Convective Organization), für die gemeinsame erfolgreiche Zeit.

Abschließend möchte ich mich bei Nadine, meiner Familie und meinen Freunden bedanken, die mich in den letzten Jahren hervorragend unterstützt haben.

Liste aller Publikationen und Zuständigkeiten der Autoren

Die vorliegende kumulative Dissertation besteht aus den drei publizierten Artikeln Brune et al. (2018), Brune et al. (2020a) und Brune et al. (2021) und einem veröffentlichten Software-Paket Brune et al. (2020b). Es folgt eine Übersicht der Veröffentlichungen mit Hinweisen zu den Zuständigkeiten der Autoren.

- Brune, S., F. Kapp & P. Friederichs (2018). „A wavelet-based analysis of convective organization in ICON large-eddy simulations“. *Quarterly Journal of the Royal Meteorological Society* 144 (717), S. 2812–2829.
 - S. Brune: Konzept, Methodik, Datenverarbeitung, Berechnung der Wavelet-Spektren und Organisationsindexe, Anfertigen der Abbildungen, Erstellen des Manuskripts
 - F. Kapp: Unterstützung bei Berechnung der Wavelet-Spektren, Mitarbeit am Manuskript
 - P. Friederichs: Konzept, Methodik, Mitarbeit am Manuskript
- Brune, S., S. Buschow & P. Friederichs (2020). „Observations and high-resolution simulations of convective precipitation organization over the tropical Atlantic“. *Quarterly Journal of the Royal Meteorological Society* 146 (729), S. 1545–1563.
 - S. Brune: Konzept, Methodik, Datenbeschaffung und Datenverarbeitung, Berechnung der Wavelet-Spektren und Organisationsindexe, Erstellen des Manuskripts
 - S. Buschow: Theoretische Grundlagen, mathematischer Background, Mitarbeit am Manuskript
 - P. Friederichs: Konzept, Methodik, Mitarbeit am Manuskript
- Brune, S., S. Buschow & P. Friederichs (2021). „The local wavelet-based organization index – Quantification, localization and classification of convective organization from radar and satellite data“. *Quarterly Journal of the Royal Meteorological Society* 147 (736), S. 1853–1872.
 - S. Brune: Konzept, Methodik, Datenverarbeitung, Berechnungen, Erstellen des Manuskripts
 - S. Buschow: Konzept, Methodik, theoretische Grundlagen, mathematischer Background, Mitarbeit am Manuskript
 - P. Friederichs: Konzept, Methodik, Mitarbeit am Manuskript

- Brune, S., S. Buschow, F. Kapp & P. Friederichs (2020). *calcWOI: Calculates the Wavelet-Based Organization Index*. R package version 1.0.3. URL: <https://CRAN.R-project.org/package=calcWOI> (zuletzt abgerufen am 18.03.2021).
 - S. Brune: Erstellen und Entwickeln des Pakets, Schreiben des Manuals
 - S. Buschow: Mitarbeit an einzelnen Funktionen, Bereitstellung von **AICEN**
 - F. Kapp: Erstellen der Funktionen **blowup** und **flatten**
 - P. Friederichs: Idee, Unterstützung bei der Entwicklung des Pakets

Nachfolgend sind die drei Artikel sowie das Manual zum Software-Paket zu finden.

Received: 23 April 2018 | Revised: 16 August 2018 | Accepted: 20 September 2018 | Published on: 2 December 2018
DOI: 10.1002/qj.3409

RESEARCH ARTICLE

Quarterly Journal of the
Royal Meteorological Society 

A wavelet-based analysis of convective organization in ICON large-eddy simulations

Sebastian Brune  | Florian Kapp | Petra Friederichs

Meteorological Institute, University of Bonn,
Germany

Correspondence

Sebastian Brune, Meteorological Institute,
University of Bonn, Auf dem Hügel 20, 53121
Bonn, Germany.

Email: sbrune@uni-bonn.de

Funding information

German Ministry for Education and Research
(BMBF) grant FKZ01LK1507B,

Wavelet spectra of rain rates are used to characterize convective organization in high-resolution simulations (horizontal grid spacing 156 m) with the large-eddy model ICON-LEM over Germany. Scattered convection takes place on scales between 1.2 and 4.8 km, while organized structures like supercells or mesoscale convective systems act on scales above 4.8 km. Organization of convection within squall lines is visible in the spectra as spectral energy is increased in certain directions. We further investigate the dynamical properties that relate to convective organization, and highlight the role of parameters such as CAPE and wind shear. Preferred spatial scale, average convective rain rate and anisotropy as inferred from the wavelet spectra are important characteristics to quantify convective organization. They are used to introduce a wavelet-based organization index (WOI). Compared with other indices for convective organization, WOI does not require the definition of objects. Using the WOI we are able to distinguish organized from non-organized convection.

KEYWORDS

convective organization, ICON-LEM, wavelet transform, wavelet-based organization index

1 | INTRODUCTION

Convective processes play an important role in the generation of high-impact weather in Central Europe, especially during the summer months (van Delden, 2001). Observed convection ranges from small cumulus clouds up to large mesoscale convective systems (MCSs). Thus, the horizontal scale varies from about hundreds of metres for cumulus or shallow convection, over several kilometres for deep moist convection to more than 200 km in the case of mesoscale systems (Orlanski, 1975). The lifetime of shallow convection is about a few minutes, whereas single cell storms can last up to 50 min (Weisman and Klemp, 1986). MCSs even show a lifetime of more than three hours (Parker and Johnson, 2000).

In the literature, the term organized convection is often used for long-living and large-scale forced convection. Following the Rotunno–Klemp–Weisman (RKW) theory (Rotunno *et al.*, 1988; Weisman and Rotunno, 2004), environmental

quantities of a convective cell like low-level vertical wind shear or helicity (Droegemeier *et al.*, 1993) have crucial influence on the development of the storm. For example, strong vertical wind shear separates the up- and downdraughts of a cell, enhances its lifetime and increases the degree of convective organization (Houze, 2004). Storms in a strongly sheared environment develop quickly and can cause severe damage through strong wind gusts, hail, heavy rainfall with flash floods and sometimes also tornadoes (e.g. Gatzen, 2004; Barthlott *et al.*, 2017). Hence, synoptic characteristics and the large-scale forcing play an important role in convective organization.

Of widespread interest is a better understanding of mesoscale processes like convection and its organization, including their simulation and parametrization, and the synoptic-scale forcing on convection. Hence, the project *High-Definition Clouds and Precipitation for Advancing Climate Prediction* (HD(CP)²) developed a high-resolution large-eddy model (ICON-LEM) with grid point distances

of about 156 m (Heinze *et al.*, 2017). One central aim of the project is to understand the organization of convection and the feedback processes between convection and the environment in high-resolution simulations of real weather cases.

Because direct three-dimensional observations of (thermo-)dynamical variables like wind, temperature or moisture are generally not available, convective organization is often characterized on the basis of radar or satellite measurements using Hovmöller diagrams (Carbone *et al.*, 2002) or Fourier spectra (Wong and Skamarock, 2016). Other studies categorize convection using organization indexes like the simple convective aggregation index (SCAI; Tobin *et al.*, 2012) or the index of organization (I_{org} ; Tompkins and Semie, 2017). Both consist of a single number and summarize the organization of the cells in the domain. A disadvantage of SCAI is its strong dependence on the horizontal grid of the data. To reduce grid dependency, White *et al.* (2018) introduced the convective organization potential (COP). COP is comparable to SCAI, but it also includes the area of each convective cluster. A detailed discussion of SCAI, I_{org} and COP is given in the Appendix.

Here we employ a wavelet analysis to identify the degree of convective organization. With the help of wavelet energy spectra, it is possible to determine the scale and the orientation of the prevailing spatial pattern in the data (Weniger *et al.*, 2017; Kapp *et al.*, 2018), and may distinguish between e.g. meridionally orientated fronts and weakly forced convection without a preferred orientation. The former show spectral energy on large scales in the north–south direction, while the latter has energy on small scales without any preferred horizontal direction.

This study characterizes convective organization using simulation output of ICON-LEM. We investigate high-resolution dynamical variables together with simulated precipitation fields to answer the following questions:

- How do the dynamical variables relate to precipitation and the degree of convective organization?
- Are we able to characterize convective organization solely on the basis of precipitation via wavelet spectra?

We further develop an alternative convective organization index based on wavelet spectra, the so-called wavelet-based organization index (WOI).

The outline of this article is as follows. We first present the ICON-LEM together with the observables used in this study (section 2). Three selected weather cases are described in detail in section 3. We then give a short description of the theoretical background on our wavelet analysis in section 4, and compare the wavelet spectra for precipitation in the simulations and observations in section 5. We complete our study with a discussion of convective organization indices in section 6 and present our novel WOI. A summary with concluding remarks is given in section 7.

2 | MODEL AND DATA

All simulations are performed with a limited-area high-resolution version of the Icosahedral Non-hydrostatic model (ICON; Zängl *et al.*, 2015). ICON was jointly developed by DWD (German Meteorological Service, Offenbach, Germany) and MPI-M (Max Planck Institute for Meteorology, Hamburg, Germany), and at the beginning of 2015 replaced the global model GME as the operational global numerical weather prediction model at DWD.

Simulations of the large-eddy version ICON-LEM (Heinze *et al.*, 2017) are performed within the project HD(CP)², funded by the German Ministry for Education and Research. ICON-LEM is run with three different grid lengths $\Delta_x = 156, 312, 625$ m over a large region in Germany as displayed in Figure 1a. ICON-LEM uses a triangular grid, thus the grid distance is given by the square root of the mean triangle area (Dipankar *et al.*, 2015). The vertical direction is described using 150 full levels (151 half levels) up to a height of about 21 km (Figure 1b). The distance between the vertical model levels varies from 20 m at the ground to over 100 m in the middle troposphere and to more than 200 m in the stratosphere. The model levels close to the surface follow the orography. The influence of the orography vanishes with height. Above 16 km the model levels are flat. Initialization and boundary data are provided by COSMO-DE¹ analyses at the main synoptic times (0000, 0300, 0600, ..., 2100 UTC), and by COSMO-DE forecasts between these times.

The spin-up in ICON-LEM lasts around 6 h and the effective resolution is of about $8 \Delta_x = 1.2$ km for the finest grid spacing of 156 m (Heinze *et al.*, 2017). Other models like Weather Research and Forecasting (WRF) and COSMO have slightly higher effective resolutions with $7 \Delta_x$ in WRF (Skamarock, 2004) and $5 \Delta_x$ to $6 \Delta_x$ in COSMO-DE (Bierdel *et al.*, 2012). For more information on ICON, we refer to Wan *et al.* (2013), Dipankar *et al.* (2015), Reinert *et al.* (2016), and Heinze *et al.* (2017).

With a total of about 3 billion grid points, ICON-LEM produces an enormous amount of output. Therefore the model output is interpolated onto a coarser regular grid with a longitudinal extent from 4.500 to 14.496°E by steps of 0.017°, and 47.500 to 54.496°N by steps of 0.011°. This corresponds to a grid spacing of about 1.2 km. Due to output problems at the northern and eastern borders of the model domain, the outermost grid points are neglected. At the southern border a band of 11 grid points, and at the western border of 61 grid points are ignored because of missing values. Thus, the variables are given at 150 vertical levels with the coarsened dimension of 529×626 grid points. The variables we output are specific humidity q , zonal u and meridional v wind components, temperature T and pressure p . The vertical velocity w is provided

¹The regional numerical weather prediction model operated by DWD (Baldauf *et al.*, 2011) developed by the Consortium for Small Scale Modeling (COSMO; www.cosmo-model.org; accessed 5 November 2018).

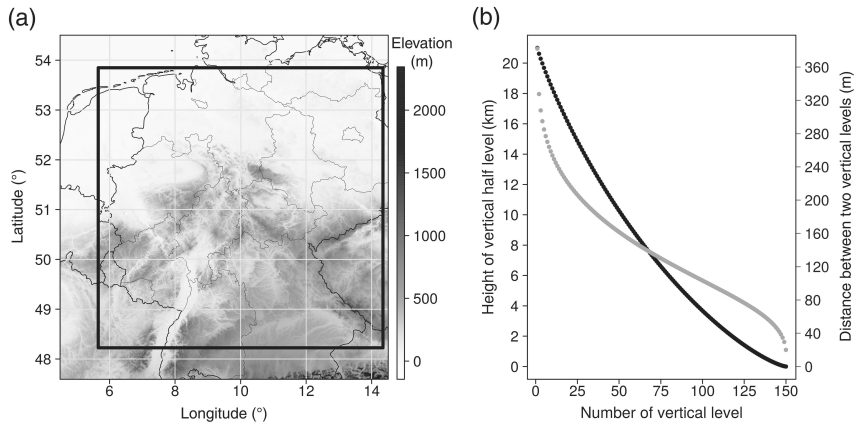


FIGURE 1 (a) Elevation and model area in ICON-LEM. Black framed area indicates the power of two 512×512 field for the wavelet decomposition. (b) Model level height (black dots, left axis) and layer thickness (grey dots, right axis) for every vertical level (bottom axis)

TABLE 1 ICON-LEM simulations used in this study

Date	Character	Remarks
15 August 2014	Scattered single cells	Randomly distributed strong thunderstorms during the day
04 July 2015	Severe convection	Organized cells in central and northern Germany in the afternoon
05 July 2015	Severe convection	Two convective lines in central and northern Germany during the day

on 151 half levels. The temporal resolution of the 3D output variables is 15 min.

We further calculate convective parameters such as mixed-layer CAPE (mixed layer about 50 hPa; Huntrieser *et al.*, 1997), mixed-layer convective inhibition (CIN), Showalter index (SI; Showalter, 1953), lifted index (LI; Galway, 1956), vertical wind shear of horizontal wind (Bunkers, 2002; Thompson *et al.*, 2007), storm-relative environmental helicity (SRH; Droegelemeier *et al.*, 1993) and convective time-scale τ_c (Done *et al.*, 2006; Craig *et al.*, 2012). τ_c can differentiate between situations where convection starts immediately in the presence of CAPE (*equilibrium convection* Emanuel, 1994), and situations with large CAPE, a capping inversion through high CIN and powerful convection after the cap is broken (*non-equilibrium convection* or *triggered convection*). τ_c can be interpreted as a ratio between CAPE and the precipitation rate. In several studies (Keil and Craig, 2011; Molini *et al.*, 2011; Craig *et al.*, 2012; Keil *et al.*, 2014) the threshold $\tau_c = 6$ h is chosen to differentiate between equilibrium ($\tau_c < 6$ h) and triggered convection ($\tau_c > 6$ h).

Because the wavelet transformation requires a power of two field with $2^n, n = 1, 2, 3, \dots$ grid points in longitudinal and latitudinal directions, we choose a 512×512 array in the centre of the 529×626 field (black framed area in Figure 1a). This selection reduces the influence of the boundary conditions and excludes regions without convection (e.g. North Sea) and the Alps.

In this study, we focus on an unorganized convection day (15 August 2014) and two strongly organized convection days (04 July 2015 (a few strong thunderstorms, likely supercells) and 05 July 2015 (linear thunderstorms, squall line)) in order

to investigate three different kinds of convective organization (Table 1).

For comparison with observations, we use precipitation estimates from the radar-based quantitative precipitation estimation products RADOLAN of DWD.² RADOLAN precipitation estimates are available on a grid with a 1 km grid spacing, and are interpolated on the ICON-LEM grid. The RADOLAN dataset covers Germany and is available every 5 min.

3 | WEATHER CASES

3.1 | Scattered convection; 15 August 2014

Figure 2 displays the convective situation on 15 August 2014 at 1500 UTC. A high number of randomly distributed cells is visible in the rain rate. Over southern Germany (Baden-Wuerttemberg and Bavaria), some multicell clusters develop, while Austria and the Czech Republic are influenced by large-scale rainfall. The rain rates vary between 0.1 and 0.5 mm h^{-1} in small showers, $2\text{--}5 \text{ mm h}^{-1}$ over Austria to about 50 mm h^{-1} in the stronger convective cells. The CAPE values range between 200 and 500 J kg^{-1} over the whole domain except in those regions where the convective cells have already consumed CAPE. Convection reduces CAPE to 0 almost immediately and stabilizes the atmosphere towards a convective equilibrium. Small CIN values below

²For more information see <http://www.dwd.de/RADOLAN>; accessed 5 November 2018.

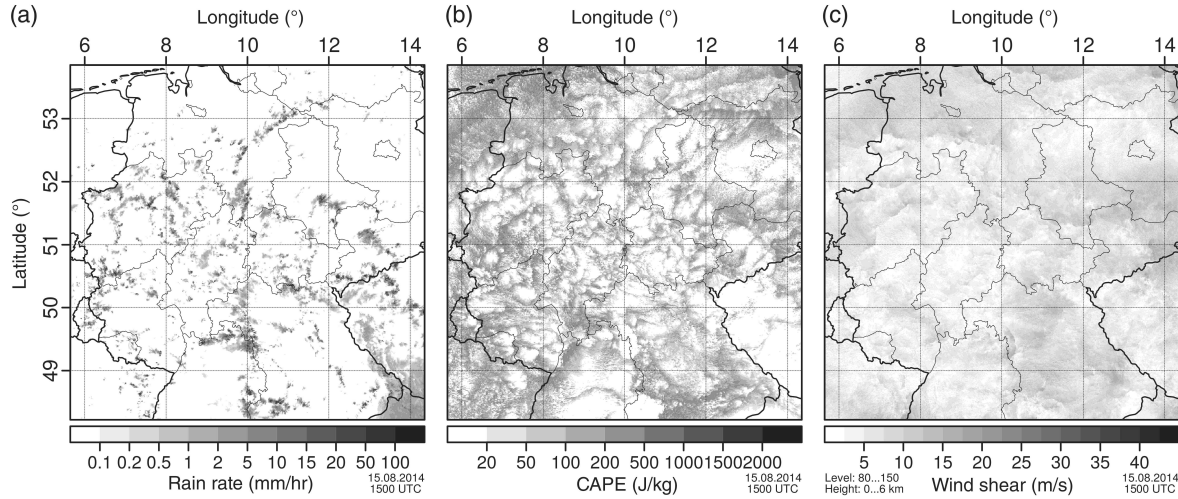


FIGURE 2 Snapshots of (a) rain rate, (b) CAPE and (c) vertical wind shear between surface and approximately 6 km height (model level 80) on 15 August 2014 at 1500 UTC

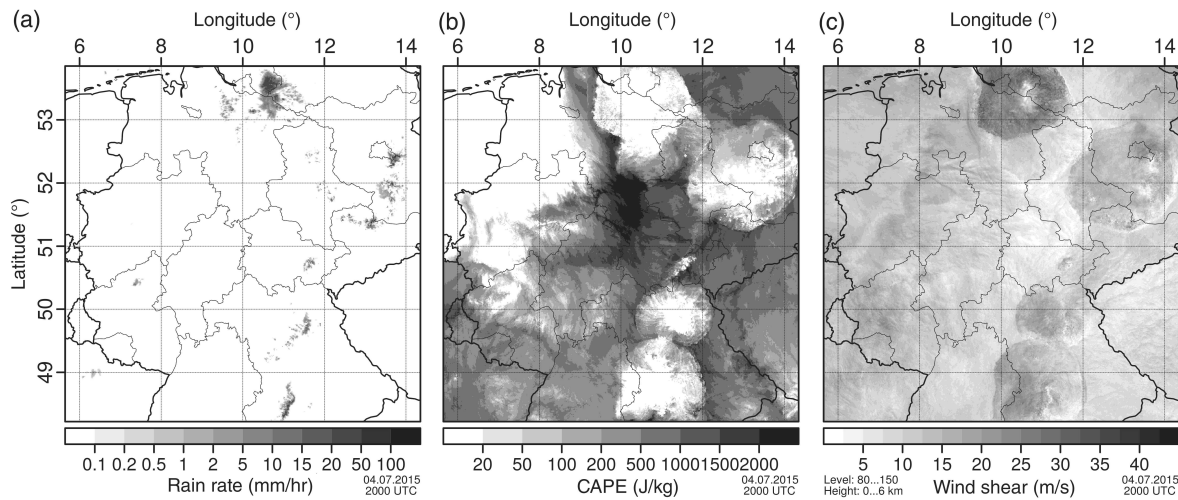


FIGURE 3 As Figure 2, but for 04 July 2015 at 2000 UTC

10 J kg^{-1} (not shown) and a weak dynamical forcing fosters the development of short-lived showers and thunderstorms. Dynamical forcing is small as seen in the 6 km vertical wind shear, where – due to an upper-level trough with low wind speeds at 6 km height – vertical wind shear is only about 5 m s^{-1} or below. ICON-LEM simulates shear values of about 10 m s^{-1} in locations over southeastern Germany and close to the North Sea. Due to small cold pools, the surface winds rise to 10 m s^{-1} with the consequence that the wind shear tends to 0.

3.2 | Strong single cells; 04 July 2015

In the evening of 04 July 2015 (Figure 3) ICON-LEM simulates a few severe thunderstorms, mostly supercells,

over northern and eastern Germany. The rain rates reach 50 mm h^{-1} in eastern Germany and up to 100 mm h^{-1} east of Hamburg. The rain patterns are mostly isotropic, although the cells located in northern and southern Germany have a slight north–south orientation. The supercells and severe thunderstorms are able to develop due to huge CAPE values of about 2000 J kg^{-1} . Elevated CIN of about 100 J kg^{-1} (not shown) persists until the evening. An upper-level trough in Western Europe (not shown) leads to stronger dynamical forcing than on 15 August 2014. Thus, the 6 km wind shear is enhanced with values of about $15\text{--}20 \text{ m s}^{-1}$ next to the region of developing convection and 30 m s^{-1} within the region near the cold pool. In contrast to 15 August 2014, the 04 July 2015 case may be classified as a forced convective day.

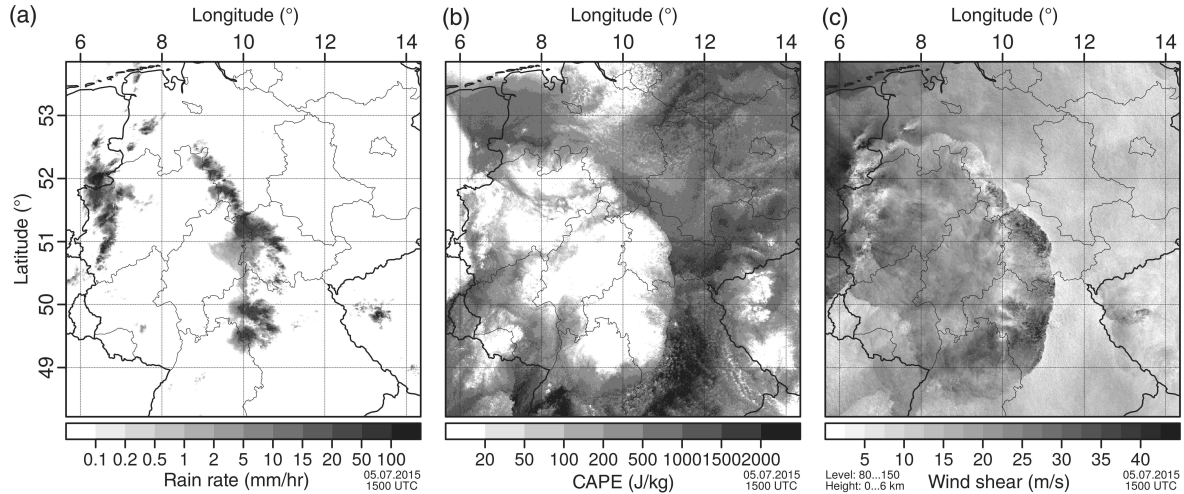


FIGURE 4 As Figure 2, but for 05 July 2015 at 1500 UTC

3.3 | Linearly organized convection; 05 July 2015

One day later on 05 July 2015 the dynamical configuration allows for the development of linearly organized structures (Figure 4). The first convective line over central Germany can be identified as a convergence line ahead of the cold front, which is just entering Germany from the west at 1500 UTC. Strong lifting overcomes CIN earlier on 05 July 2015 than on the previous day, and convection occurs before 1200 UTC. As on 04 July 2015, convection is characterized as forced convection. Along both the cold front and the convergence line, ICON-LEM simulates heavy rain rates exceeding 100 mm h^{-1} . Over the western Czech Republic single cells develop.

The values of CAPE rise in front of the convergence line to about 2500 J kg^{-1} (Figure 4b) and is thus as high as the day before. Behind the convergence line, CAPE is reduced to zero, so that convection along the cold front is weaker. The approaching trough forces the wind in the upper levels to speeds above 30 m s^{-1} (not shown) with a resulting bulk wind shear between the surface and 6 km of about $20\text{--}30 \text{ m s}^{-1}$ (Figure 4c). Thus, conditions for long-lived convection are fulfilled on 05 July 2015. The dynamical lifting by the trough is larger than the previous day, and the corresponding cold front along with the leading convergence line has a distinct linear structure.

4 | SPECTRAL WAVELET ANALYSIS

We use a decomposition via discrete wavelets to characterize the spatial structure of the precipitation fields. The wavelet filter is given by a set of redundant discrete wavelet transforms (DWTs). A comprehensive overview of the mathematical details regarding wavelets is given in Daubechies (1992). We use the Haar wavelet (Haar, 1910) as it might best cope with abrupt changes and areas with zeros in the precipitation fields.

While the Fourier transform assumes stationarity in space, wavelets allow for the evaluation of the signal not only on distinct scales but also at different locations. For a comprehensive overview of wavelets in meteorological verification applications, we refer to Weniger *et al.* (2017).

More specifically we resort to estimates of the locally stationary wavelet spectrum as introduced in Eckley *et al.* (2010). They use the spectral wavelet approach for texture analysis and provide the R Statistical Programming Language package LS2W (Eckley and Nason, 2011). A redundant DWT is chosen in Eckley *et al.* (2010), as it is shift invariant and robust against noise. The DWT results in an array of $1024 \times 1024 \times 30$ wavelet coefficients, one coefficient for each scale (1–10), direction (east–west, north–south, diagonal) and location (Fowler, 2005). The local wavelet spectrum is then given as the squared DWT coefficients. Due to the redundancy, the wavelet coefficients are not independent, which leads to a bias in the estimated wavelet spectrum. Eckley *et al.* (2010) introduce a bias correction, which may result in negative spectral energy values.

We further average the local spectrum over space to obtain spectral energy estimates for each scale and direction. For a short overview of the method, the reader is referred to Kapp *et al.* (2018), who use this approach for the verification of high-resolution ensemble precipitation forecasts. A detailed description of the estimation of the locally stationary wavelet spectrum in one dimension is given by Nason *et al.* (2000), and in two dimensions by Eckley *et al.* (2010).

Our wavelet decomposition requires periodic boundary conditions. In contrast to Weniger *et al.* (2017) and Kapp *et al.* (2018), who pad out the field with zeros around their data, we mirror the field at the eastern border and southern border to obtain a 1024×1024 field with periodic boundary conditions in both directions. While east–west and north–south oriented objects remain unaffected by this procedure, a pattern extending in a southwest to northeast orientation, or vice

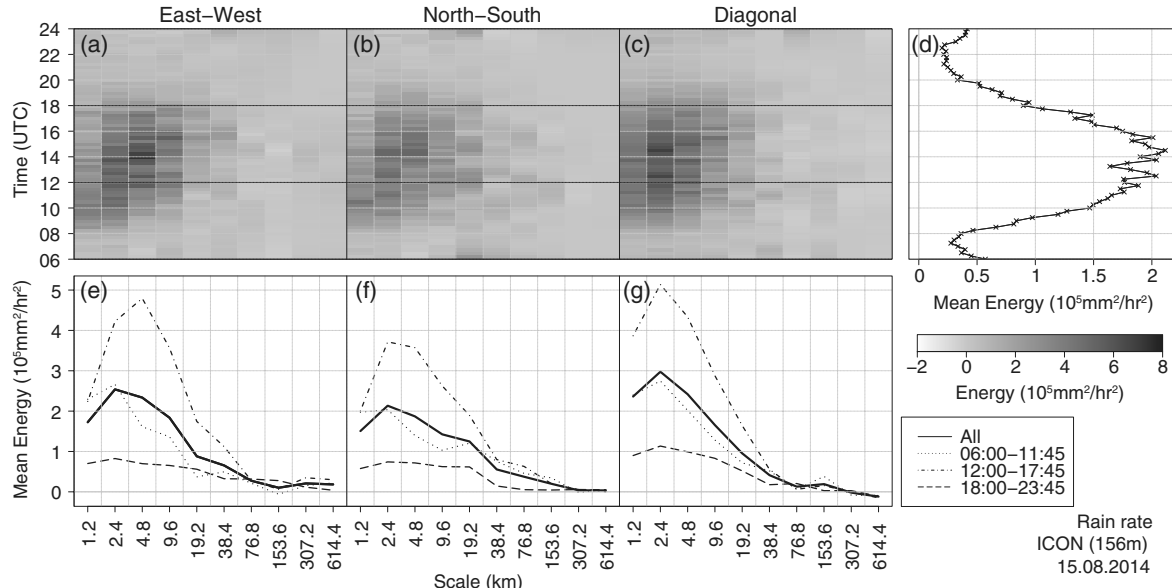


FIGURE 5 (a)–(c) Wavelet spectrum of ICON-LEM rain rates for every quarter hour between 0600 and 2400 UTC on 15 August 2014 (y-axis) for (a) east–west, (b) north–south and (c) diagonal directions on different scales (x-axis). Black horizontal lines separate morning (0600–1200 UTC), afternoon (1200–1800 UTC) and evening (1800–2400 UTC). (d) Mean spectral energy (black line) over all scales and directions for every quarter hour (y-axis). Crosses denote squared and domain-averaged rain rate. (e)–(g) Spectral energy averaged over the periods 0600–2345 UTC (solid line), 0600–1145 UTC (dotted line), 1200–1745 UTC (dot-dashed line) and 1800–2345 UTC (dashed line) for different scales and directions

versa, changes orientation in the mirrored part of the fields. Fortunately, this does not affect the diagonal component of the averaged wavelet spectrum. Due to the grid spacing of 1.2 km, the respective scale of the wavelets corresponds to $1.2 \text{ km} \times 2^{n-1}$, with $n = 1, 2, \dots, 10$.

5 | WAVELET SPECTRA OF SIMULATED AND OBSERVED PRECIPITATION

The wavelet spectrum on 15 August 2014 (Figure 5) reflects the evolution of the rain rate during the day. The onset of convection occurs around 0800 UTC producing small-scale rainfall at scales between 1.2 and 2.4 km in all directions without any preference. Until midday the cells grow and the horizontal extent of precipitating regions is about 9.6 km. After 1800 UTC convective activity rapidly drops due to decreasing diabatic heating. The averaged spectral energy reflects this behaviour with strongest convective activity and maximal spectral energy between 1200 and 1600 UTC.

The averaged wavelet energy equals the averaged squared rain rate (Figure 5d), with maximal differences of about 1%, and proves that the averaged wavelet energy is indeed unbiased. Figures 5e–g display the averaged spectral energy with respect to scale and direction. Most spectral energy on 15 August 2014 is located at scales between 1.2 and 9.6 km without a preferred direction.

On 04 July 2015 ICON-LEM simulates nearly no precipitation in the morning and afternoon. As a consequence, the

resulting wavelet spectrum contains almost no energy until 1800 UTC (Figure 6). At 1800 UTC the first cells arise and the spectral energy increases rapidly, especially at larger scales between 9.6 and 76.8 km, which corresponds to the extent of strong single-cell storms like supercells. The shape of the objects becomes more anisotropic, as the amount of spectral energy varies with the direction. At scales below 9.6 km the diagonal scale is preferred, and for scales above 9.6 km most energy is oriented in the north–south direction (also Figure 3a). In comparison to 15 August 2014 the wavelet spectra are less smooth, because the number of cells is much smaller. The total spectral energy is smaller, although the rain rates of the single cells are much higher than on the scattered convection day.

The wavelet spectrum of the cold front with the leading convergence line on 05 July 2015 produces the heaviest rain rates of all three cases (Figure 4a). The majority of convective precipitation is simulated in the afternoon. In the morning and in the evening the wavelet spectrum shows only small energy on all scales. The cold front and especially the convergence line produce strong rain rates located along a north–south line as seen in Figure 4a. The corresponding wavelet spectrum shows a clear preferred direction (Figure 7). The energy in the north–south direction is twice as large as that in the east–west or diagonal directions. The dominant scales in the north–south direction are 19.2–76.8 km, while the maximal energy for the other two directions is located on scales between 9.6 and 38.4 km. Compared to 15 August 2014 and 04 July 2015, the rain rates on 05 July

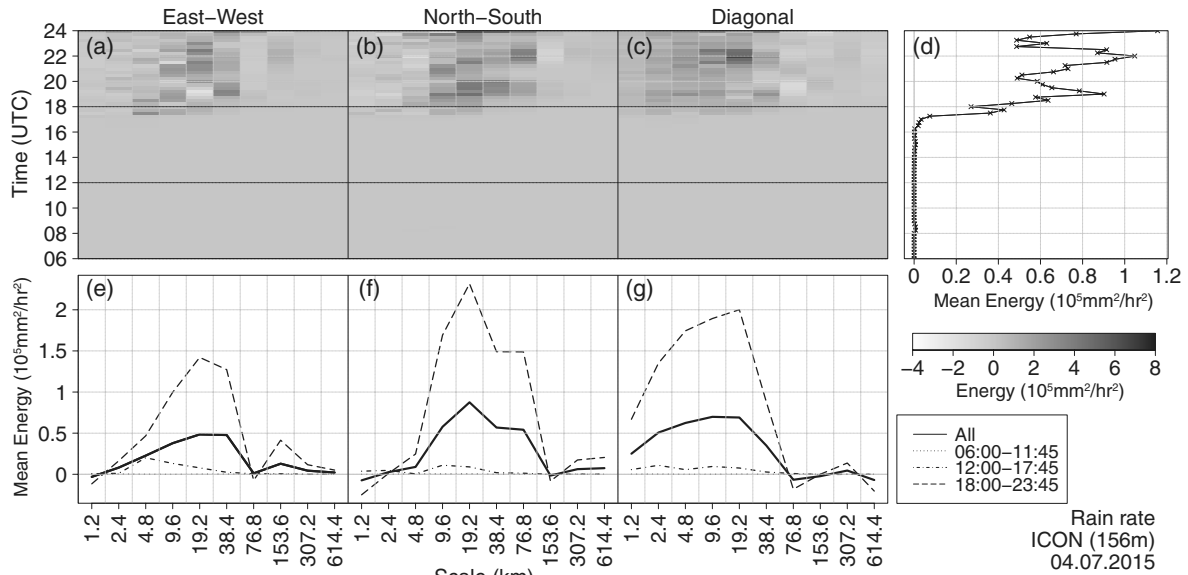


FIGURE 6 As Figure 5, but for 04 July 2015

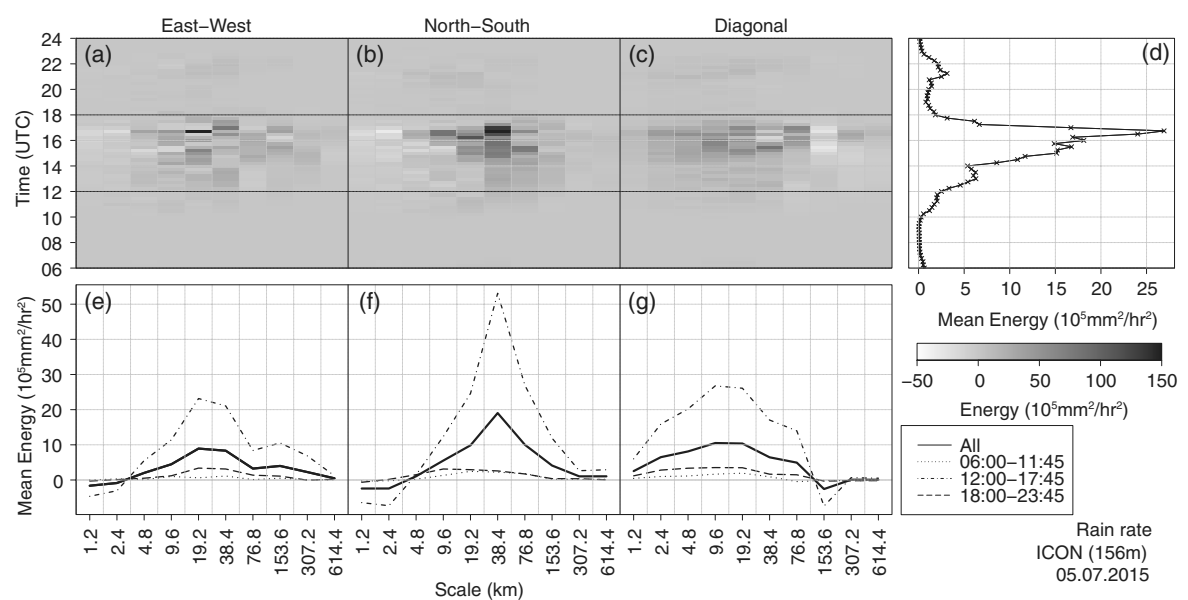


FIGURE 7 As Figure 5, but for 05 July 2015

2015 are stronger and the north–south direction is clearly preferred.

Figure 8a displays the RADOLAN rain rate on 15 August 2014 at 1500 UTC. In accordance with the ICON-LEM simulations, the observed precipitation is very scattered and occurs over the complete domain. The large-scale precipitation over Austria as simulated by ICON-LEM is missing in the radar data, as Austria lies outside the area observed in RADOLAN. Due to the fact that accumulation time in RADOLAN is longer than in ICON-LEM, the size of the

rain cell in RADOLAN is larger. Further, while ICON-LEM simulates convective activity mainly over central Germany, RADOLAN also shows short-lived cells over northern and eastern Germany.

The wavelet spectrum of RADOLAN precipitation (Figure 9) agrees well with the spectrum derived from ICON-LEM simulations on 15 August 2014. Total rainfall is slightly greater in RADOLAN than in ICON-LEM, but the temporal evolution and the spectral patterns are in accordance with the simulations. In contrast to the simulations, scale 1

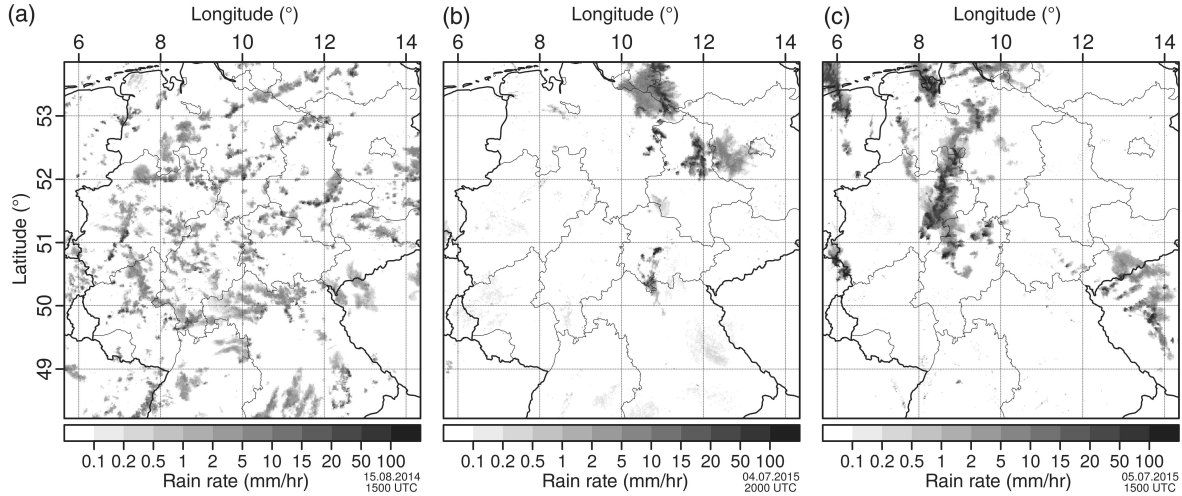


FIGURE 8 Observed rain rate estimates from RADOLAN at (a) 1500 UTC on 15 August 2014, (b) 2000 UTC on 04 July 2015 and (c) 1500 UTC on 05 July 2015

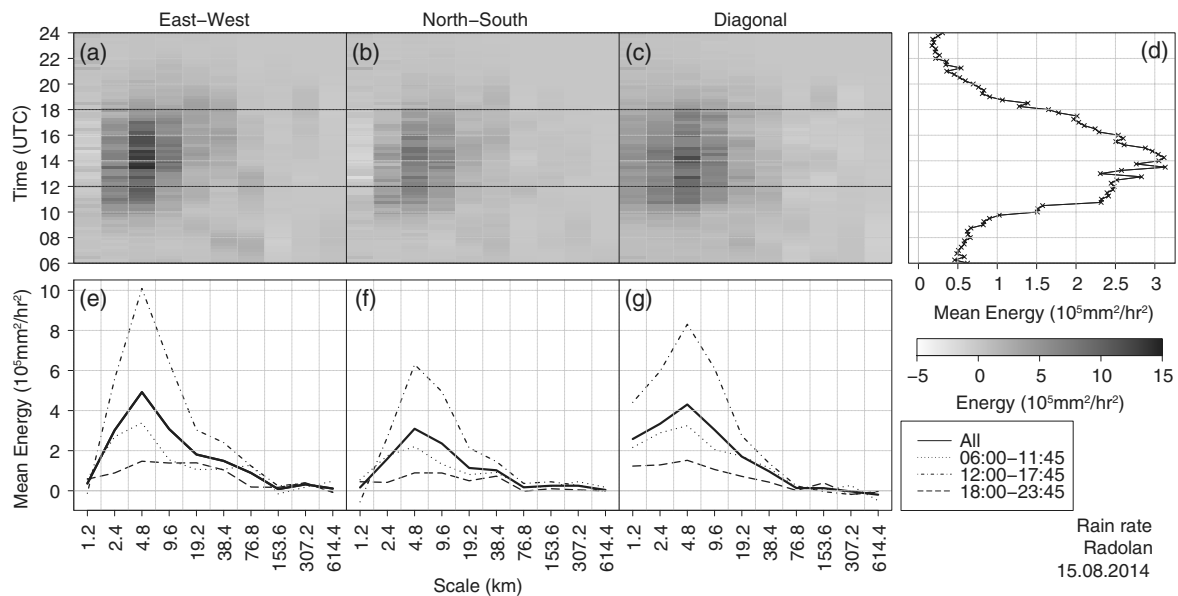


FIGURE 9 As Figure 5 for 15 August 2014, but based on RADOLAN rain rates

(1.2 km) contains no energy in RADOLAN. Scale 3 (4.8 km) dominates the spectrum and most energy is observed in the east–west direction, but the temporal evolution of convection in RADOLAN is very similar to the one in the ICON-LEM simulations on 15 August 2014.

On 04 July 2015 ICON-LEM and RADOLAN agree on the position and intensity of the Hamburg supercell, although the extent is much larger in RADOLAN (cf. Figures 3a and 8b). RADOLAN also observes convective cells located east of Berlin, which are not captured by the model simulation. Convection starts about two hours earlier in RADOLAN than in the simulation (Figure 10). In the morning, weak convection takes place over the North Sea and produces some spectral

energy until 1000 UTC. The ICON simulation underestimates the morning precipitation as well as the convective activity in the afternoon. Maximum spectral energy in RADOLAN is reached at around 1700 UTC with more than $10^6 \text{ mm}^2 \text{ h}^{-2}$ and therefore one order of magnitude higher than in ICON-LEM. The daily averaged spectral energy in RADOLAN shows no preferred direction. In the afternoon the energy is maximal in the north–south direction, and comparable to the evening period on 04 July 2015 in ICON-LEM. For all three directions the scale with maximal energy is smaller than in ICON-LEM, but in the evening the observed cell size increases.

On 05 July 2015, RADOLAN observes convective activity along a convergence line over the northern part of western

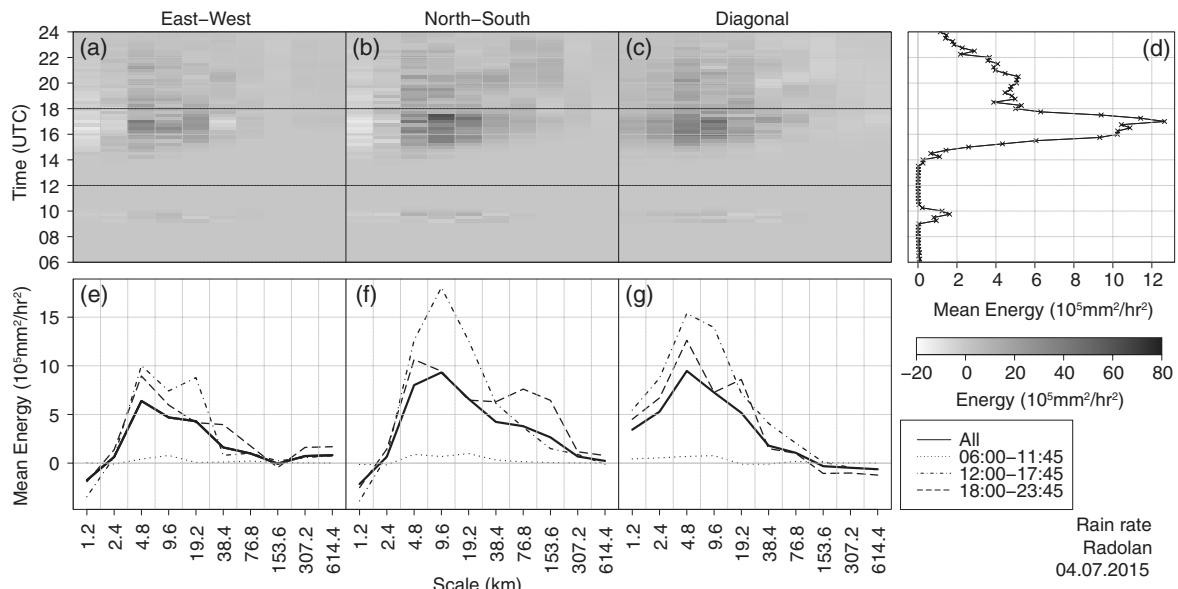


FIGURE 10 As Figure 6 for 04 July 2015, but based on RADOLAN rain rates

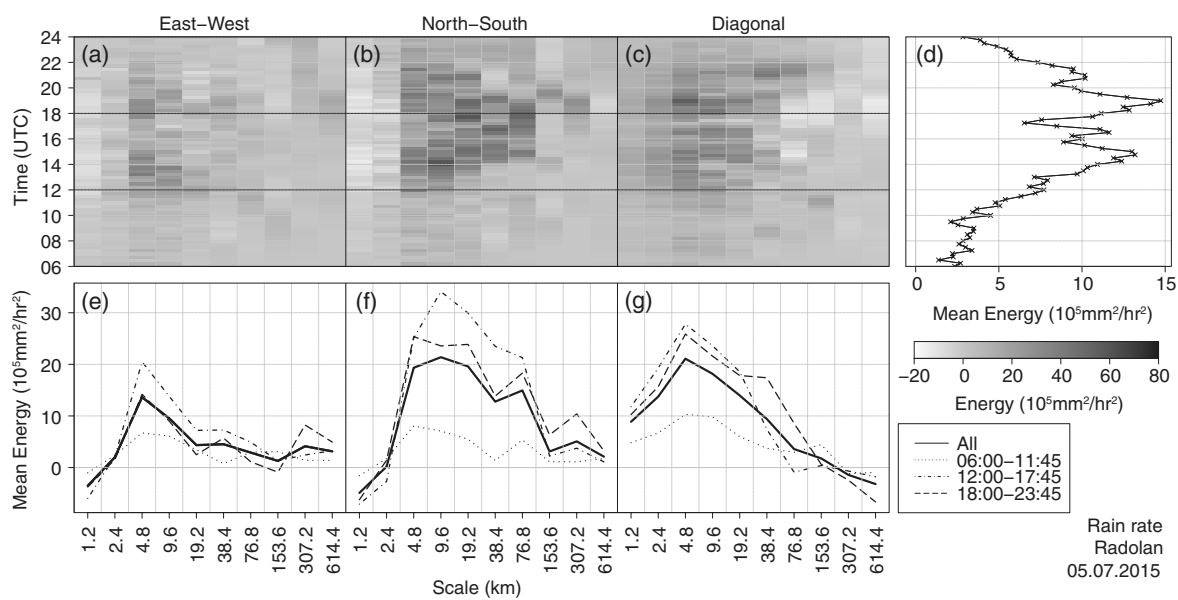


FIGURE 11 As Figure 7 for 05 July 2015, but based on RADOLAN rain rates

Germany (Figure 8c). Compared to RADOLAN, the simulated convergence line over central Germany is shifted approximately 100 km further east and 300 km further south (Figure 4a). The position of the cold front is simulated correctly, but the convective regions strongly differ. The observed cells in the Czech Republic are present in the simulations, while cells in the Erz Mountains are observed but not simulated. Nevertheless, the structure of the cells is simulated satisfactorily.

The wavelet spectra observed by RADOLAN (Figure 11) strongly differ from the simulation on 05 July 2015. During

the entire day, RADOLAN observes large rain rates. In the morning the spectral energy is concentrated on scales 9.6 km and below without any directional preference. When convection intensifies, spectral energy is largest in the north-south direction. In the east-west and diagonal directions the energy is substantially lower and the preferred scales of the convective cells are smaller than in north-south direction. The objects in the north-south direction show horizontal extents between 4.8 and 76.8 km, but especially in the evening large-scale elements (153.6 and 307.2 km) are observed. Thus, both north-south orientated convective lines are active

at the large mesoscale, whereas in the east–west direction their extent is only around 10 km.

6 | DYNAMICAL PROPERTIES AND CONVECTIVE ORGANIZATION

6.1 | Dynamical variables

We now turn to the dynamical properties of the atmosphere during convection and display in Figure 12 the temporal evolution of domain averages of CAPE, CIN, SI, LI, helicity, SRH, vertical wind shear, precipitation rate and τ_c . On 15 August 2014, domain-averaged CIN is below 10 J kg^{-1} . Hence, CAPE is directly reduced by convection, which is forced by diabatic heating after sunrise. The corresponding SI varies between 2 and 3 K, while LI becomes slightly negative between morning and late afternoon. Thus, both indices indicate moderate instability over Germany, because active cells reduce instability and increase the domain-averaged SI and LI. Helicity as well as SRH are not present until the evening, when diabatic heating and convection decay. Low wind speeds in the middle and upper levels prevent any stronger vertical wind shear and suppress the development of long-lived convection. The consequence is scattered convection with convective time-scales around or even below 1 h. Thus, the convection type is characterized as equilibrium convection. The simulated rain rate shows maximal values of up to 0.5 mm h^{-1} in the afternoon.

The 04 July 2015 case is characterized by enhanced CAPE values above 1000 J kg^{-1} . During the morning CAPE increases rapidly until 1200 UTC and drops after 1800 UTC when convection starts. Simultaneously, CIN decreases; after a huge blocking CIN of 400 J kg^{-1} in the morning, CIN is below 100 J kg^{-1} in the afternoon. To overcome CIN, diabatic heating and local surface convergence are necessary. Because the trough is far away from Germany, upper-level forcing is missing. Subsequently, local convection takes place in the form of single severe thunderstorms and supercells. The corresponding SI and LI are strongly negative. Helicity is not present on 04 July 2015, but SRH rises up to $20 \text{ m}^2 \text{s}^{-2}$ in the evening, when convection starts. Also vertical wind shear increases, because upper-level winds become stronger. Combined with high CAPE values, the favoured storm types are strong single cells and even supercells. The corresponding convective time-scale is longer than one day, which is typical for forced convection. Because only a few cells develop, domain-averaged rain rates are below 0.2 mm h^{-1} . Comparison with 15 August 2014, the instability and inhibition are stronger and SRH and vertical wind shear are increased. Thus, the “loaded gun” situation (high instability, but CIN suppresses convective initiation) on 04 July 2015 ends up in only a few severe thunderstorms contrasting with the scattered convection on 15 August 2014.

On 05 July 2015 CAPE increases rapidly during the morning with values of about 800 J kg^{-1} at 1200 UTC. Again,

CIN is large with values of about $100\text{--}150 \text{ J kg}^{-1}$ and suppresses convection in the morning. SI and especially LI are strongly negative until the afternoon. Both indices increase during the evening, while CAPE tends to 0 at midnight. CIN is overcome by the upper-level trough with its cold front and leading convergence line. Helicity between the surface and 1 km is around $20 \text{ m}^2 \text{s}^{-2}$ and becomes negative in the late afternoon. Helicity at 3 km is even stronger with $60 \text{ m}^2 \text{s}^{-2}$. SRH is increased and reaches $40 \text{ m}^2 \text{s}^{-2}$ at 1 km and $50 \text{ m}^2 \text{s}^{-2}$ at 3 km at 1500 UTC. At the same time the vertical wind shear reaches its maximum at more than 15 m s^{-1} for mid-level and 8 m s^{-1} for low-level wind shear. In accordance with the RWK theory, long-lived forced convection (squall line) develops with convective time-scales up to 10 h. The cold front and the leading convergence line as well as cells in the Czech Republic produce strong domain-average rain rates of around 1.5 mm h^{-1} . Increased wind shear and helicity as well as large-scale forcing by the cold front and convergence line lead to linearly organized structures. Although CAPE on 05 July 2015 is smaller than on 04 July, convective organization is stronger.

Thus, for our cases, strong convective organization in the ICON-LEM is determined by large CAPE and moderate CIN, occurring at the same time as positive SRH and large vertical wind shear. In order to investigate whether the weather situations can be classified as a few distinct convection types, we perform a cluster analysis based on the standardized time series of CAPE, CIN, SRH (1, 3 km), helicity (1, 3 km), wind shear (1, 3, 6 km), SI, LI, and heights of level of free convection (LFC) and lifted condensation level (LCL). For 04 July 2015 only seven hours (1700–2300 UTC) are used, since no rain is simulated before 1700 UTC. We use K-means clustering based on the silhouettes method (Rousseeuw, 1987). The cluster analysis suggests the existence of two significantly distinct clusters. Cluster A comprises the weather situation on 15 August 2014 with low wind shear, low helicity and high LI (Figure 13), while cluster B is characterized by higher instability and stronger dynamical forcing. Cluster B comprises both July cases, and the K-mean method is not able to differentiate between the dynamical conditions on 04 and 05 July 2015. If we fix the number of clusters to three, the first cluster remains unchanged, whereas cluster B splits into timesteps with moderate instability in the evenings of 04 and 05 July 2015 in one cluster and high instability and very large CAPE in the afternoon of both days in the other.

6.2 | Convective organization indices

Object-based convective organization indices like SCAI (Tobin *et al.*, 2012), I_{org} (Tompkins and Semie, 2017) and COP (White *et al.*, 2018) are introduced to distinguish between scattered and organized convection. Their calculation is relatively simple and generally based on the definition of rain clusters. These studies use brightness temperatures (Tobin *et al.*, 2012), vertical wind velocity at 730 hPa

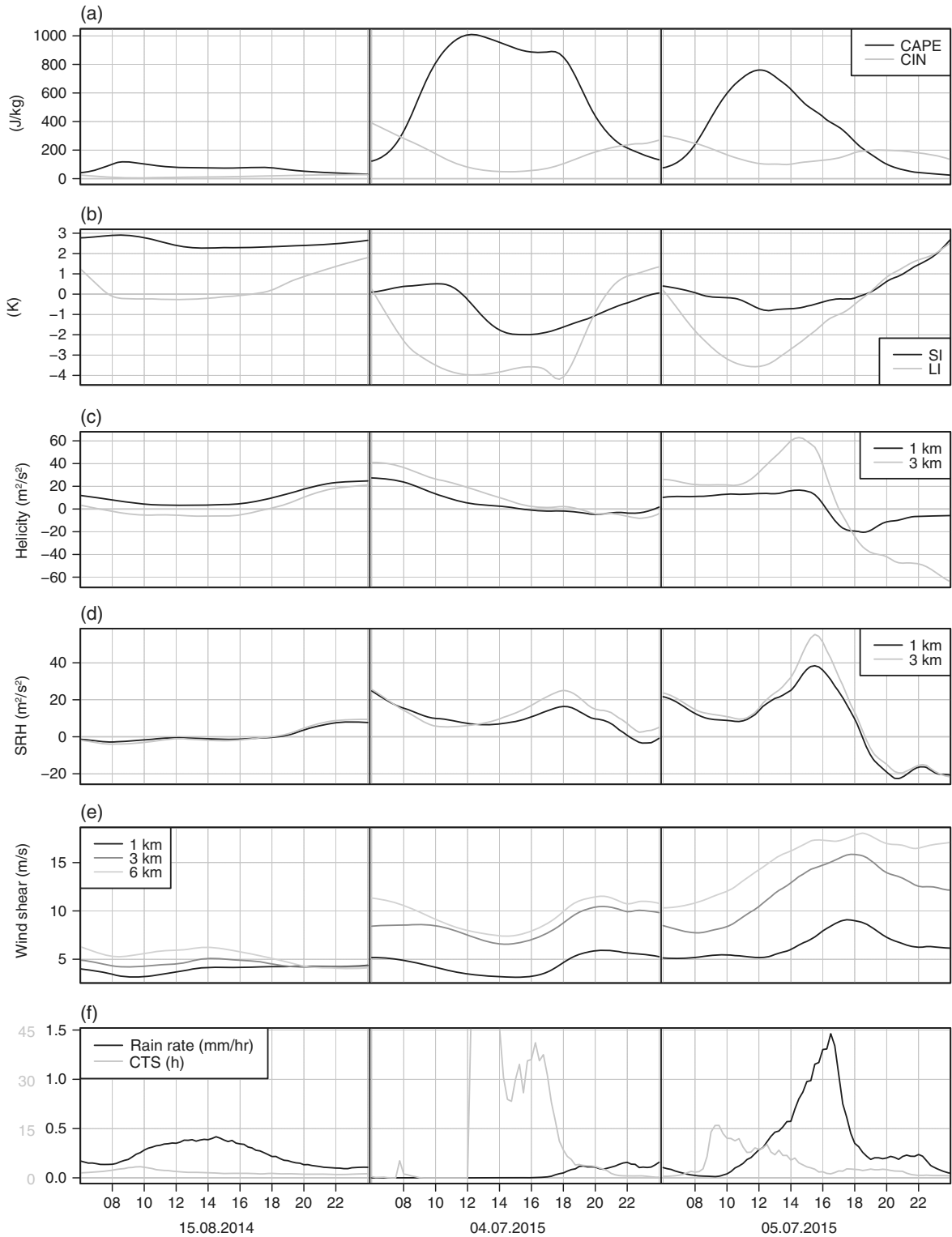


FIGURE 12 Time series of domain-averaged simulated (a) CAPE and CIN, (b) Showalter index (SI) and lifted index (LI), (c) helicity in the lowest 1 km and 3 km, (d) storm relative helicity in the lowest 1 km and 3 km with respect to wind velocity at 3 km height, (e) vertical wind shear between the surface and 1, 3 and 6 km, and (f) simulated rain rate (black y-axis) and convective time-scale τ_c (grey y-axis) on 15 August 2014 (left column), 04 July 2015 (middle column) and 05 July 2015 (right column)

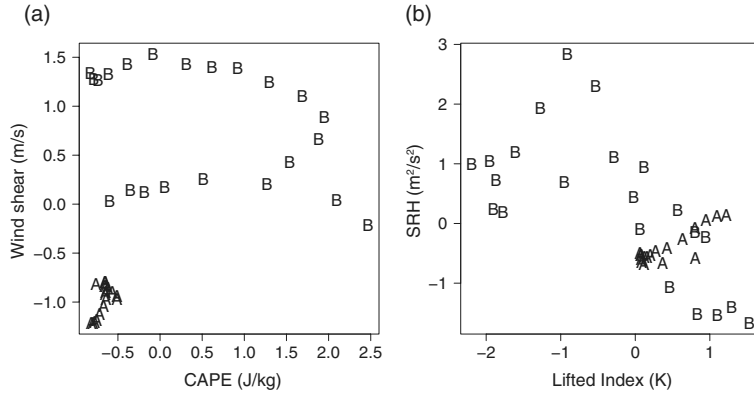


FIGURE 13 (a) K-means clustering for two clusters A and B based on standardized CAPE, CIN, SRH (1, 3 km), helicity (1, 3 km), wind shear (1, 3, 6 km), SI, LI, height of LFC and LCL. The x-axis shows CAPE and y-axis the 6 km wind shear. (b) is as (a), but for lifted index and 3 km storm relative helicity

(Tompkins and Semie, 2017) or outgoing long-wave radiation (White *et al.*, 2018).

In this study we define a rain cluster when at least four neighbouring points with rain rates above 2 mm h^{-1} exist. On the basis of this rain cluster analysis, we calculate SCAI, I_{org} and COP. Their definitions can be found in the Appendix. The time series of the indices are displayed in Figure 14.

On 15 August 2014 SCAI has a maximum of 0.7 around 1400 UTC for simulated precipitation, while SCAI for the RADOLAN data maximizes at 1200 UTC (0.85). The major contribution to SCAI is the number of clusters N , because the order-zero diameter D_0 , which can be interpreted as the degree of clumping (the definition of D_0 is given in the Appendix), is almost constant during the day. The number of clusters and therefore SCAI are slightly higher for radar precipitation, while evolution and timing are well captured by the simulations. This is consistent with the wavelet analysis in Figures 5 and 9. I_{org} is above 0.5 for all times on 15 August 2014, thus convection is more organized than random in the sense of Tompkins and Semie (2017). The large values of I_{org} occur because we use rain rates instead of vertical wind velocity for its calculation. Thus, we avoid using terms like regular, random or clustered here and just compare the values of I_{org} for the different cases. The minimum at 1400 UTC is caused by the presence of many small cells, which covered the whole domain. In the morning and in the evening smaller areas are affected by convection and the distance between the objects is smaller.

In general, COP is low with values below 0.05 before noon and a slight increase in the evening. All three indices indicate weakly organized storms during the day, with a minimum in convective organization around noon.

For 04 and 05 July 2015 the number of clusters is small and, as a consequence, SCAI is also small. I_{org} is very noisy, but generally larger than on 15 August 2014 during highest convective activity (1000–2000 UTC) and suggests more organized storms than on 15 August 2014. Although noisy, COP clearly suggests stronger organization during 04 and 05 July 2015.

The general tendencies with increased SCAI for weak organization on 15 August 2014 and larger values of I_{org} and COP for strong organization on 04 and 05 July 2015 are in agreement with results of Tobin *et al.* (2012), Tompkins and Semie (2017), Bao *et al.* (2017), Holloway (2017), Cronin and Wing (2017), Wing *et al.* (2018), and White *et al.* (2018). Although convective organization is reflected in the indices, SCAI is strongly dominated by the number of clusters, whereas I_{org} is very noisy and hard to interpret if the number of clusters is small. COP assumes circular elements, an assumption which is not met for the convective structures on 05 July 2015.

6.3 | Wavelet-based organization index (WOI)

We propose a wavelet-based convective organization index (WOI). As discussed in section 5, wavelet spectra provide information on the dominant scales of convection, total energy and anisotropy. Hence, our index will make use of these three characteristics of organization.

The first component (WOI_1) aims at the characterization of the dominant scale of convection and is defined as the ratio of large-scale to small-scale energy. Due to the horizontal grid spacing of 1.2 km, the wavelet spectrum includes ten scales, namely $1.2 \text{ km} \times 2^{n-1}$, $n = 1, 2, \dots, 10$. Single cell storms (e.g. pulse storms) produce rain rates on horizontal scales around 5 km and below, whereas organized structures like multicells or mesoscale convective systems act mostly on scales above 5 km. We thus define the first three scales 1–3 (1.2–4.8 km) as small scales (s) and the scales 4–7 (9.6–76.8 km) as large scales (l) of convection. We ignore the largest scales, 8–10 (153.6–614.4 km), as they are above the convective scale, and potentially influenced by the boundary conditions. WOI_1 is then given as the ratio of the averaged large-scale spectral energy \bar{E}_l to the total energy $\bar{E}_l + \bar{E}_s$ on the convective scales:

$$\text{WOI}_1 = \frac{\bar{E}_l}{\bar{E}_s + \bar{E}_l}. \quad (1)$$

The bar denotes the average over all three directions. WOI_1 is dimensionless and ranges between 1 and 0.

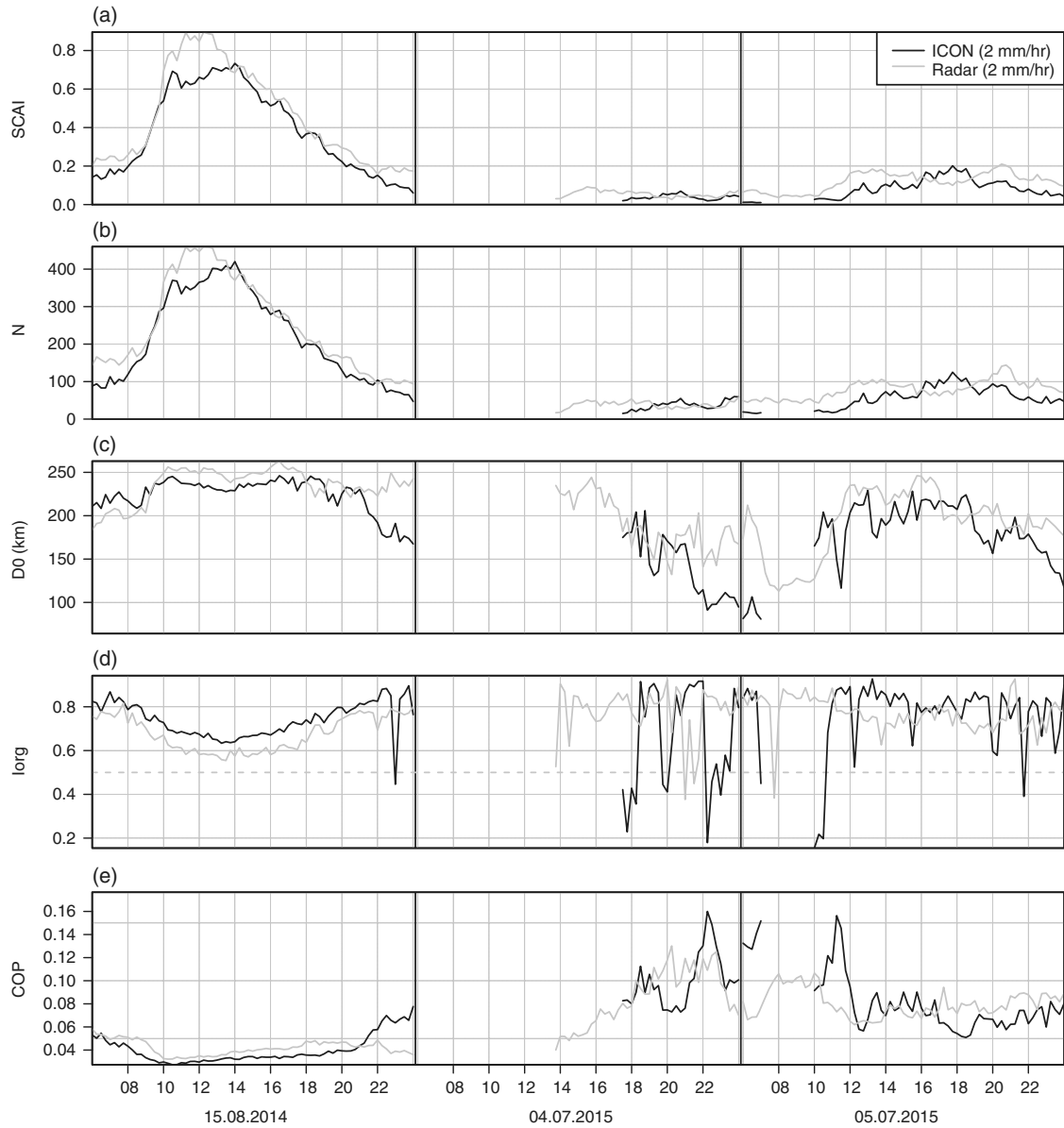


FIGURE 14 Time series of (a) SCAI, (b) number of convective clusters N , (c) order-zero diameter D_0 , (d) I_{org} , (e) COP calculated from simulated rain rate (black) and measured rain rate (grey) on 15 August 2014 (left column), 04 July 2015 (middle column) and 05 July 2015 (right column). A threshold of 2 mm h^{-1} is used and only timesteps with more than 15 cells are shown

The second index represents the total energy on the convective scales (1.2–76.8 km) scaled with the number of grid points r with rain rates above zero. This weighting is done in order to better differentiate between cases with many low-intensity rain cells (low WOI_2) and cases with few intense rain cells (high WOI_2):

$$\text{WOI}_2 = \frac{\overline{E}_l + \overline{E}_s}{r}. \quad (2)$$

The third component, WOI_3 , assesses anisotropy and uses the directional information of the wavelet spectrum. WOI_3

measures the deviation from an isotropic spectrum and is defined as the root-mean-square error between the energy E_i^d for each direction $d \in \{1, 2, 3\}$ and the energy averaged over all directions \overline{E}_i for both scales $i = s, l$. WOI_3 is defined as

$$\text{WOI}_3 = \frac{1}{3} \sqrt{\sum_d \left(\left(\frac{E_s^d - \overline{E}_s}{\overline{E}_s} \right)^2 + \left(\frac{E_l^d - \overline{E}_l}{\overline{E}_l} \right)^2 \right)}. \quad (3)$$

WOI_3 is a positive measure, where $\text{WOI}_3 = 0$ indicates that spectral energy is equal in all directions east–west ($d = 1$), north–south ($d = 2$) and diagonal ($d = 3$).

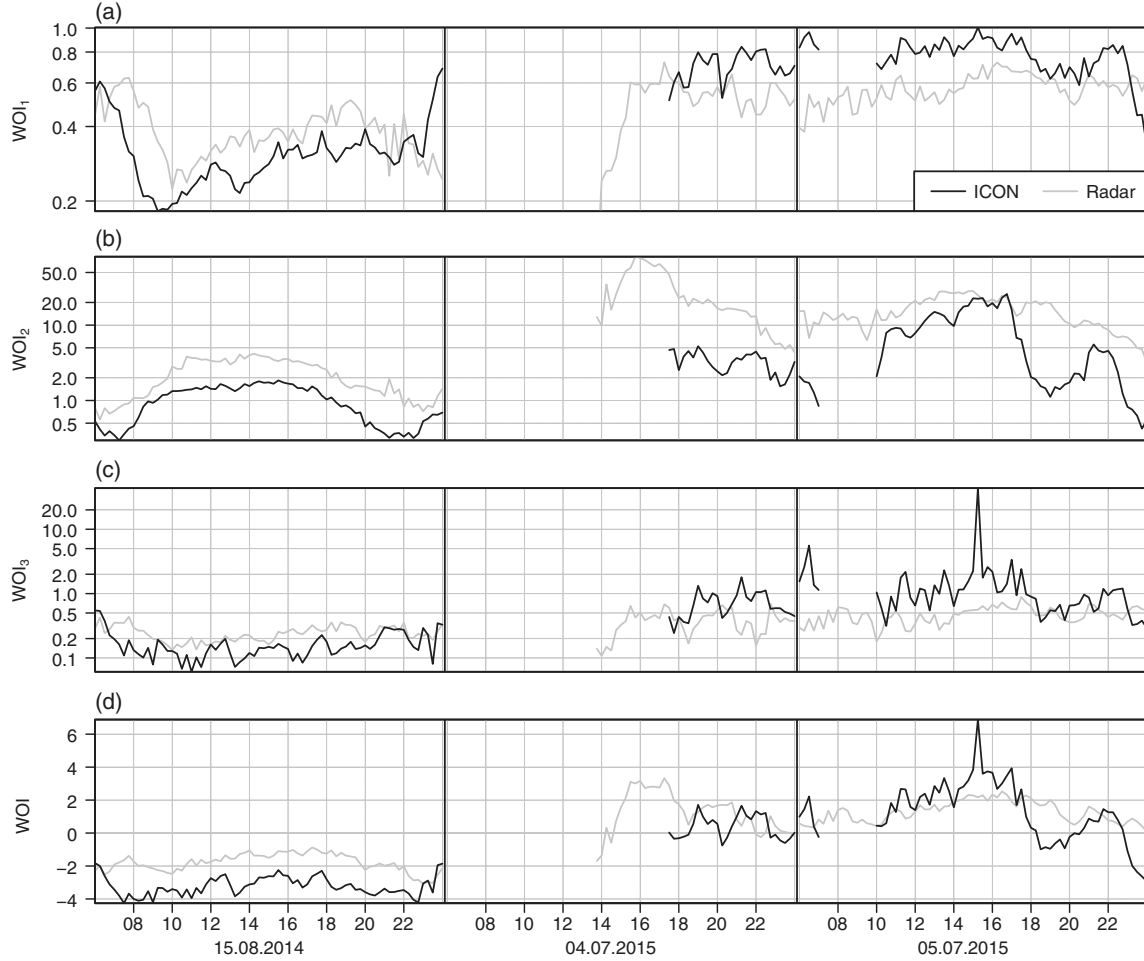


FIGURE 15 Time series of (a) WOI₁, (b) WOI₂, (c) WOI₃ and (d) WOI on 15 August 2014 (left column), 04 July 2015 (middle column) and 05 July 2015 (right column) for simulated rain rates (black) and measured rain rates (grey). The y-axis in (a)–(c) is logarithmic

As a summary measure, we propose the sum over the logarithm of the three components $WOI_i, i \in \{1, 2, 3\}$

$$WOI = \sum_i \log_e(WOI_i). \quad (4)$$

Since all components WOI_i are non-negative, WOI is defined for spectral energy \bar{E}_l larger than zero. A large WOI indicates strong convective organization (i.e. large rain rates, preference for larger scales, and anisotropy in the precipitation structures).

Time series of the WOI components are displayed in Figure 15a–c. On 15 August 2014 during most of the day the WOI_1 for the simulated rain rates ranges between 0.2 and 0.4, since most energy is present at small scales. In the morning hours, convective activity is relatively small; larger-scale stratiform rainfall is simulated with the consequence that $WOI_1 > 0.5$. WOI_2 has a maximum of 2.0 between 1400 and 1600 UTC, while WOI_3 is below 0.4 during the day. Thus, the three WOI components categorize 15 August 2014 as a day with isotropic small-scale convection.

On 04 July 2015 almost no rain is simulated before 1700 UTC, at which time convection starts in the model and the organization increases directly because of the strong wind shear. As a consequence, WOI_1 is above 0.5 until midnight. After 1800 UTC WOI_3 shows increased anisotropy. On 05 July 2015 relatively large-scale precipitation structures lead to a WOI_1 of about 0.8. WOI_1 is only weaker in the evening with values of about 0.6 and below. As already seen in section 5, the most total energy is simulated on 05 July 2015 around 1700 UTC. Strong anisotropy at the same time leads to WOI_3 between 1 and 2 with a peak above 20 at 1500 UTC and indicates strong organization.

On 15 August 2014 the radar-based values of WOI_1 , WOI_2 and WOI_3 are similar to the simulated ones. For the organized convection days, simulated precipitation has a stronger tendency toward larger-scale convection with a larger WOI_1 in the simulation than in the radar estimates, while the total spectral energy is generally smaller. On 04 July 2015 the radar-based WOI_2 is much higher and convection starts two

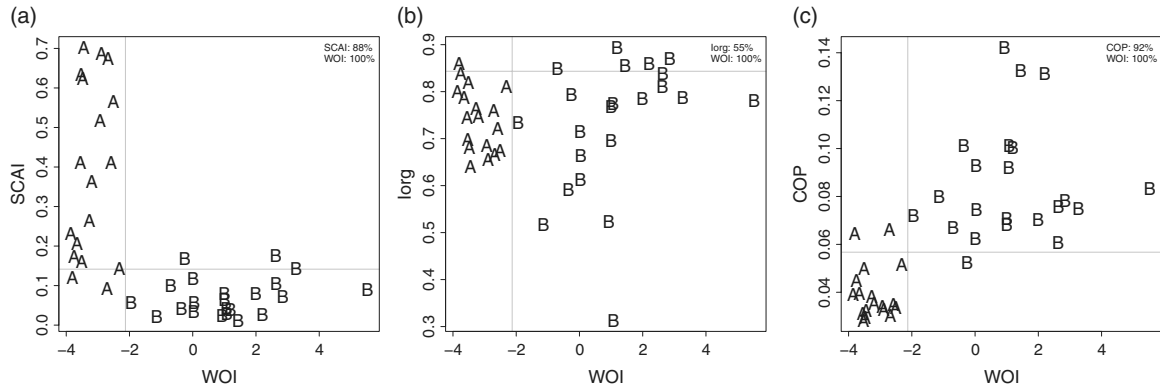


FIGURE 16 Comparison of WOI (x-axis) and (a) SCAI, (b) I_{org} and (c) COP (y-axes). Letters A and B represent the same clusters found via K-means in Figure 13. Vertical and horizontal lines separate the two clusters given by the best odds ratio of each index. The percentage of correctly assigned timesteps is shown at top right

hours earlier. The anisotropy in the radar estimates is lower than in the simulations for both days in July 2015. Additionally, WOI_3 derived from observations shows less variability for both July days.

The WOI is displayed in Figure 15d. WOI is small for both simulated and observed rain rates on 15 August 2014 with values around -3 and -1 , respectively, whereas stronger convective organization on 04 and 05 July 2015 leads to a positive WOI of up to 2. In the afternoon of 05 July 2015, when convection is organized along two lines, WOI becomes even more positive.

Figure 16 displays SCAI, I_{org} and COP against WOI, and assesses the ability of the each index to differentiate between the weakly organized cluster A, and the organized convection of cluster B (cf. Figure 13). All cases in cluster A have WOI values below -2.1 , while all in cluster B have a WOI larger than -2.1 . The value $\text{WOI} = -2.1$ separates both clusters A and B completely, such that all 40 timesteps are correctly classified (i.e. a success rate of 100%). A slightly lower success rate of 92% is obtained using COP, whereas using SCAI it is only of about 88%. I_{org} as calculated from rain rates is not able to differentiate between clusters A and B. If we use three clusters instead of two, none of WOI, COP, SCAI or I_{org} are able to differentiate the two dynamical clusters on 04 and 05 July 2015 (not shown).

WOI and COP are positively correlated (0.69), as both increase with the degree of convective organization, whereas SCAI decreases with increasing COP. No correlation is found between WOI and I_{org} . In our study I_{org} is calculated on the basis of rain rates above 2 mm h^{-1} and seems unable to characterize convective organization. Increasing the threshold from 2 to 10 mm h^{-1} leads to similar results. As SCAI strongly depends on the grid and the number of clusters N , and as I_{org} is not optimized for rain rates, we prefer COP and WOI to describe convective organization.

7 | CONCLUSION

This study investigates three weather cases with different convective organization in simulations with the high-resolution ICON-LEM and in radar observations. On 15 August 2014, ICON-LEM simulates convective cells randomly distributed over Germany. CIN as well as the small vertical wind shear are small, and CAPE is immediately reduced by the cells (equilibrium convection). The convective time-scale is thus small. Much larger CAPE but also stronger CIN on 04 July 2015 leads to the development of a few strong supercells. An additional large-scale forcing on 05 July 2015 results in the formation of two convective lines, which move across Germany.

Convective organization is quantified using wavelet spectra of rain rates. In the case of 15 August 2014 the spectrum is isotropic. Most spectral energy is located at small scales with a maximum at about 2.4 km. A few supercells on 04 July 2015 lead to large spectral energy on scales between 9.6 and 76.8 km. On 05 July 2015 two convective lines produce a very anisotropic wavelet spectrum, with spectral energy in the north-south direction being twice as high as that in the east-west or diagonal directions. In the north-south direction most energy is found on scales between 19.2 and 76.8 km, while the preferred scales in the east-west and diagonal directions are smaller.

For an evaluation of the ICON-LEM simulations, we compare the wavelet spectra to spectra obtained with RADOLAN precipitation estimates. Simulations and observations on 15 August 2014 are in very good accordance. Larger differences occur on 04 July 2015 with regard to the onset of convection. Convection is observed by RADOLAN in the early afternoon. The spectral energy is one magnitude higher and the maximum spectral energy is located on smaller scales than in the simulations. On 05 July 2015 simulation and observation match only moderately. While convective activity becomes maximal in ICON at around 1600 UTC, RADOLAN indicates

strong convection all day. The wavelet spectra indicate that the orientation differs between the ICON-LEM simulations and RADOLAN observations.

Further, area averages of dynamical and convective variables such as vertical wind shear, helicity, instability quantities and convective time-scale are used to differentiate between different kinds of convective organization. A K-means clustering suggests two significantly distinct clusters, namely the scattered convection on 15 August 2014 and the organized convection on 04 and 05 July 2015. Compared to the unorganized convection day, both July days are mainly characterized by strong vertical wind shear, increased helicity and high instability. Unexpectedly, no significantly distinct clusters in terms of dynamical variables can be identified during 04 and 05 July 2015.

We introduce a wavelet-based organization index (WOI) as an alternative to object-based organization indices such as SCAI, I_{org} , and COP. WOI is built upon three components, characterizing the relation of large-scale to convective precipitation (WOI_1), the total rate of convective precipitation (WOI_2), and the anisotropy of the convective structures (WOI_3).

In our study, WOI perfectly differentiates between the two clusters of convective organization as defined by the dynamical variables (i.e. weakly organized convection on 15 August 2014 and organized convection on 04 and 05 July 2015), COP is slightly less robust, whereas SCAI and I_{org} fail to identify the two clusters. However, longer simulation studies are required to assess in detail the potential of the WOI in comparison to COP.

The great advantage of WOI is that it does not require a threshold-based object identification, and thus may be less sensitive to *a priori* assumptions. However, WOI is not free of assumptions, e.g. one has to define the cut-off between small- and large-scale convection. Another disadvantage of WOI is that much mathematical theory is hidden behind wavelet transformation and the estimation of the wavelet spectrum. However, a sophisticated pool of software is available, and may be used to estimate wavelet spectra without deep mathematical knowledge.

A similar index to WOI may be obtained using two-dimensional Fourier spectra (e.g. Wong and Skamarock, 2016). One major difference between Fourier and wavelet transforms is the localization of the latter. In this study we discard spatial non-stationarity in the estimated spectra by using averages over the complete domain. In principle it might be possible to account for non-stationarities and to construct local wavelet-based indices, or even construct new indices which incorporate information on the non-stationarity.

ACKNOWLEDGEMENTS

We gratefully acknowledge financial funding by the project High Definition Clouds and Precipitation for Advancing Climate Prediction HD(CP)², funded by the German

Ministry for Education and Research (BMBF) under grant FKZ01LK1507B. We are thankful to two anonymous reviewers for their constructive comments on an earlier version of the article.

ORCID

Sebastian Brune  <https://orcid.org/0000-0002-3742-4443>

REFERENCES

- Baldau, M., Seifert, A., Förstner, J., Majewski, D., Raschendorfer, M. and Reinhard, T. (2011) Operational convective-scale numerical weather prediction with the COSMO model: description and sensitivities. *Monthly Weather Review*, 139, 3887–3905.
- Bao, J., Sherwood, S.C., Colin, M. and Dixit, V. (2017) The robust relationship between extreme precipitation and convective organization in idealized numerical modeling simulations. *Journal of Advances in Modeling Earth Systems*, 9, 2291–2303.
- Barthlott, C., Mühr, B. and Hoose, C. (2017) Sensitivity of the 2014 Pentecost storms over Germany to different model grids and microphysics schemes. *Quarterly Journal of the Royal Meteorological Society*, 143, 1485–1503.
- Bierdel, L.B., Friederichs, P. and Bentzien, S. (2012) Spatial kinetic energy spectra in the convection-permitting limited-area NWP model COSMO-DE. *Meteorologische Zeitschrift*, 21, 245–258.
- Bunkers, M.J. (2002) Vertical wind shear associated with left-moving supercells. *Weather and Forecasting*, 17, 845–855.
- Carbone, R.E., Tuttle, J.D., Ahijevych, D.A. and Trier, S.B. (2002) Inferences of predictability associated with warm season precipitation episodes. *Journal of the Atmospheric Sciences*, 59, 2033–2056.
- Craig, G.C., Keil, C. and Leuenberger, D. (2012) Constraints on the impact of radar rainfall data assimilation on forecasts of cumulus convection. *Quarterly Journal of the Royal Meteorological Society*, 138, 340–352.
- Cronin, T.W. and Wing, A.A. (2017) Clouds, circulation, and climate sensitivity in a radiative-convective equilibrium channel model. *Journal of Advances in Modeling Earth Systems*, 9, 2883–2905.
- Daubechies, I. (1992) *Ten Lectures on Wavelets*. Philadelphia, PA: Society for Industrial and Applied Mathematics.
- Dipankar, A., Stevens, B., Heinze, R., Moseley, C., Zängl, G., Giorgetta, M. and Brdar, S. (2015) Large-eddy simulation using the general circulation model ICON. *Journal of Advances in Modeling Earth Systems*, 7, 963–986.
- Done, J., Craig, G., Gray, S., Clark, P.A. and Gray, M. (2006) Mesoscale simulations of organized convection: importance of convective equilibrium. *Quarterly Journal of the Royal Meteorological Society*, 132, 737–756.
- Droegemeier, K.K., Lazarus, S.M. and Davies-Jones, R. (1993) The influence of helicity on numerically simulated convective storms. *Monthly Weather Review*, 121, 2005–2029.
- Eckley, I.A. and Nason, G.P. (2011) LS2W: implementing the locally stationary 2D wavelet process approach in R. *Journal of Statistical Software*, 43, 1–23.
- Eckley, I.A., Nason, G.P. and Treloar, R.L. (2010) Locally stationary wavelet fields with application to the modelling and analysis of image texture. *Journal of the Royal Statistical Society Series C (Applied Statistics)*, 59, 595–616.
- Emanuel, K.A. (1994) *Atmospheric Convection*. Oxford: Oxford University Press.
- Fowler, J.E. (2005) The redundant discrete wavelet transform and additive noise. *IEEE Signal Processing Letters*, 12, 629–632.
- Galway, J.G. (1956) The lifted index as a predictor of latent instability. *Bulletin of the American Meteorological Society*, 37, 528–529.
- Gatzen, C. (2004) A derecho in Europe: Berlin, 10 July 2002. *Weather and Forecasting*, 19, 639–645.
- Haar, A. (1910) Zur Theorie der orthogonalen Funktionensysteme. *Mathematische Annalen*, 69, 331–371.
- Heinze, R., Dipankar, A., Carbajal Henken, C., Moseley, C., Sourdeval, O., Trömel, S., Xie, X., Adamidis, P., Ament, F., Baars, H., Barthlott, C., Behrendt, A., Blahak, U., Bley, S., Brdar, S., Brueck, M., Crewell, S., Deneke, H., Di Girolamo, P., Evaristo, R., Fischer, J., Frank, C., Friederichs, P., Göcke, T., Gorges, K., Hande, L., Hanke, M., Hansen, A., Hege, H.-C., Hoose, C., Jahns, T., Kalthoff, N., Klocke, D., Kneifel, S., Knippertz, P., Kuhn, A., van Laar, T., Macke, A., Maurer, V., Meyer, B., Meyer, C.I., Muppa, S.K.,

- Neggers, R.A.J., Orlandi, E., Pantillon, F., Pospichal, B., Röber, N., Scheck, L., Seifert, A., Seifert, P., Senf, F., Siilagam, P., Simmer, C., Steinke, S., Stevens, B., Wapler, K., Weniger, M., Wulfmeyer, V., Zängl, G., Zhang, D. and Quaas, J. (2017) Large-eddy simulations over Germany using ICON: a comprehensive evaluation. *Quarterly Journal of the Royal Meteorological Society*, 143, 69–100.
- Holloway, C.E. (2017) Convective aggregation in realistic convective-scale simulations. *Journal of Advances in Modeling Earth Systems*, 9, 1450–1472.
- Houze, R.A. (2004) Mesoscale convective systems. *Reviews of Geophysics*, 42, RG4003. <https://doi.org/10.1029/2004RG000150>.
- Huntrieser, H., Schiesser, H., Schmid, W. and Waldvogel, A. (1997) Comparison of traditional and newly developed thunderstorm indices for Switzerland. *Weather and Forecasting*, 12, 108–125.
- Kapp, F., Friederichs, P., Brune, S. and Weniger, M. (2018) Spatial verification of high-resolution ensemble precipitation forecasts using local wavelet spectra. *Meteorologische Zeitschrift*. <https://doi.org/10.1127/metz/2018/0903>.
- Keil, C. and Craig, G.C. (2011) Regime-dependent forecast uncertainty of convective precipitation. *Meteorologische Zeitschrift*, 20, 145–151.
- Keil, C., Heinlein, F. and Craig, G.C. (2014) The convective adjustment time-scale as indicator of predictability of convective precipitation. *Quarterly Journal of the Royal Meteorological Society*, 140, 480–490.
- Molini, L., Parodi, A., Rebora, N. and Craig, G. (2011) Classifying severe rainfall events over Italy by hydrometeorological and dynamical criteria. *Quarterly Journal of the Royal Meteorological Society*, 137, 148–154.
- Nason, G.P., Von Sachs, R. and Kroisandt, G. (2000) Wavelet processes and adaptive estimation of the evolutionary wavelet spectrum. *Journal of the Royal Statistical Society: Series B (Statistical Methodology)*, 62, 271–292.
- Orlanski, I. (1975) A rational subdivision of scales for atmospheric processes. *Bulletin of the American Meteorological Society*, 56, 527–530.
- Parker, M.D. and Johnson, R.H. (2000) Organizational modes of midlatitude mesoscale convective systems. *Monthly Weather Review*, 128, 3413–3436.
- Reinert, D., Prill, F., Frank, H. and Zängl, G. (2016) *ICON Database Reference Manual; Research and Development at DWD*. Offenbach: DWD.
- Rotunno, R., Klemp, J.B. and Weisman, M.L. (1988) A theory for strong, long-lived squall lines. *Journal of the Atmospheric Sciences*, 45, 463–485.
- Rousseeuw, P.J. (1987) Silhouettes: a graphical aid to the interpretation and validation of cluster analysis. *Journal of Computational and Applied Mathematics*, 20, 53–65.
- Showalter, A.K. (1953) A stability index for thunderstorm forecasting. *Bulletin of the American Meteorological Society*, 34, 250–252.
- Skamarock, W.C. (2004) Evaluating mesoscale NWP models using kinetic energy spectra. *Monthly Weather Review*, 132, 3019–3032.
- Thompson, R.L., Mead, C.M. and Edwards, R. (2007) Effective storm-relative helicity and bulk shear in supercell thunderstorm environments. *Weather and Forecasting*, 22, 102–115.
- Tobin, I., Bony, S. and Roca, R. (2012) Observational evidence for relationships between the degree of aggregation of deep convection, water vapor, surface fluxes, and radiation. *Journal of Climate*, 25, 6885–6904.
- Tompkins, A.M. and Semie, A.G. (2017) Organization of tropical convection in low vertical wind shears: role of updraft entrainment. *Journal of Advances in Modeling Earth Systems*, 9, 1046–1068.
- van Delden, A. (2001) The synoptic setting of thunderstorms in western Europe. *Atmospheric Research*, 56, 89–110.
- Wan, H., Giorgetta, M.A., Zängl, G., Restelli, M., Majewski, D., Bonaventura, L., Fröhlich, K., Reinert, D., Rpodas, P., Kornbluh, L. and Förstner, J. (2013) The ICON-1.2 hydrostatic atmospheric dynamical core on triangular grids, Part I: formulation and performance of the baseline version. *Geoscientific Model Development*, 6, 735–763.
- Weisman, M.L. and Klemp, J.B. (1986) Characteristics of isolated convective storms. Ray, P. (Ed.) *Mesoscale Meteorology and Forecasting*, Chapter 15. Boston, MA: American Meteorological Society, pp. 331–358.
- Weisman, M.L. and Rotunno, R. (2004) A theory for strong long-lived squall lines? Revisited. *Journal of the Atmospheric Sciences*, 61, 361–382.
- Weniger, M., Kapp, F. and Friederichs, P. (2017) Spatial verification using wavelet transforms: a review. *Quarterly Journal of the Royal Meteorological Society*, 143, 120–136.
- White, B.A., Buchanan, A.M., Birch, C.E., Stier, P. and Pearson, K.J. (2018) Quantifying the effects of horizontal grid length and parameterized convection on the degree of convective organization using a metric of the potential for convective interaction. *Journal of the Atmospheric Sciences*, 75, 425–450.
- Wing, A.A., Reed, K.A., Satoh, M., Stevens, B., Bony, S. and Ohno, T. (2018) Radiative-convective equilibrium model intercomparison project. *Geoscientific Model Development*, 11, 793–813. <https://doi.org/10.5194/gmd-11-793-2018>.
- Wong, M. and Skamarock, W.C. (2016) Spectral characteristics of convective-scale precipitation observations and forecasts. *Monthly Weather Review*, 144, 4183–4196.
- Zängl, G., Reinert, D., Rpodas, P. and Baldauf, M. (2015) The ICON (ICOahedral Non-hydrostatic) modelling framework of DWD and MPI-M: description of the non-hydrostatic dynamical core. *Quarterly Journal of the Royal Meteorological Society*, 141, 563–579.

How to cite this article: Brune S, Kapp F, Friederichs P. A wavelet-based analysis of convective organization in ICON large-eddy simulations. *Q J R Meteorol Soc*. 2018;144:2812–2829. <https://doi.org/10.1002/qj.3409>

APPENDIX: CONVECTIVE ORGANIZATION INDICES

A.1 | Simple convective aggregation index (SCAI)

The simple convective aggregation index (SCAI; Tobin *et al.*, 2012) combines the number of convective clusters N and clumping of the clusters measured by the order-zero diameter D_0 . To detect the number of convective clusters, Tobin *et al.* (2012) use the four-connectivity clustering algorithm. N scales with the size of the grid, therefore N is normalized with $N_{\max} = (N_x N_y)/2$. N_x and N_y are the number of grid points in longitude and latitude directions, respectively. The order-zero diameter is given by

$$D_0 = \sqrt[n]{\prod_{i=1}^n d_i}$$

with n the number of pairs in clusters $n = N(N - 1)/2$ and d_i the distance between two clusters. A smaller D_0 means a higher clumping of the clusters. D_0 is normalized by a characteristic length L . SCAI is defined as the product of cluster number and clumping

$$\text{SCAI} = \frac{N}{N_{\max}} \frac{D_0}{L} \cdot 1000. \quad (\text{A1})$$

The factor 1000 is only introduced to get values of $\mathcal{O}(10)$. In this study the characteristic length is $L = 1000 \text{ km}$ and $N_{\max} = 131072$.

Thus, SCAI gives the inverse convective aggregation compared to a maximal disaggregation. In cases of organized convection, we expect a lower SCAI than for scattered, unorganized convection. Tobin *et al.* (2012) use brightness temperatures below 240 K to indicate convective regions. Other studies (e.g. Bao *et al.*, 2017; Holloway, 2017) distinguish between convective and non-convective grid points on the basis of precipitation.

A.2 | Organization index (I_{org})

Tompkins and Semie (2017) introduce the organization index (I_{org}) as a tool to distinguish between regular, random and clustered convection. Their calculations are based on the vertical wind velocity w at 730 hPa. All grid points with $w > 1 \text{ m s}^{-1}$ are characterized as convective. Neighbouring convective points are pooled to an updraught i . Then the distance of each updraught centroid d_i to the nearest neighbour assuming periodic boundaries is calculated. The cumulative density function of the nearest neighbour distances N can be compared to the Weibull distribution

$$W = 1 - \exp\left(\frac{N}{A}\pi d^2\right),$$

with number of updraughts N and the area of the whole domain A . If convection is random, convection can be described as a Poisson point process with the resulting Weibull distribution above. In this case, a diagonal line is expected in a diagram with W on the x -axis and N on the y -axis. The organization index I_{org} is defined as the integral below the curve. Thus, for clustered (regular) convection, the curve is above (below) the diagonal and $I_{\text{org}} > 0.5$ ($I_{\text{org}} < 0.5$). In other studies I_{org} is calculated on the basis of outgoing long-wave radiation (Wing *et al.*, 2018) and cloud-top temperatures (Cronin and Wing, 2017).

A.3 | Convective organization potential (COP)

Another index to analyse convective organization is given by the convective organization potential (COP; White *et al.*,

2018). COP includes the total number of objects N , the area of every object A_i and the distance d between the objects. Based on outgoing long-wave radiation thresholds, convective clusters are identified. For each cluster i the area A_i is calculated from the grid. The distance $d(i,j)$ between two clusters i and j is given by the distances of their centroids. From this, the interaction potential V between two convective clusters can be written as

$$V(i,j) = \frac{\sqrt{A_i} + \sqrt{A_j}}{d(i,j)\sqrt{\pi}}. \quad (\text{A2})$$

If the distance between their centres is small or their areas become large, the potential between two convective objects is large. To get the convective organization potential over the whole domain, the single potentials are summed and normalized by the total number of connections

$$\text{COP} = \frac{\sum_{i=1}^N \sum_{j=i+1}^N V(i,j)}{\frac{1}{2}N(N-1)}. \quad (\text{A3})$$

A higher organization potential means larger and closer objects. For $N = 1$, no interaction between two clusters is possible and COP is undefined.

Received: 12 June 2019 | Revised: 20 December 2019 | Accepted: 21 January 2020 | Published on: 18 February 2020
DOI: 10.1002/qj.3751

Quarterly Journal of the
Royal Meteorological Society 

RESEARCH ARTICLE

Observations and high-resolution simulations of convective precipitation organization over the tropical Atlantic

Sebastian Brune  | Sebastian Buschow | Petra Friederichs

Institute of Geosciences, University of Bonn, Germany

Correspondence

S. Brune, Institute of Geosciences,
University of Bonn, Auf dem Hügel 20,
53121 Bonn, Germany.
Email: sbrune@uni-bonn.de

Funding information

German Ministry for Education and Research (BMBF) for the HD(CP)2, FKZ01LK1507B

Abstract

High-resolution simulations (grid spacing 2.5 km) are performed with ICON-LEM to characterize convective organization in the Tropics during August 2016 over a large domain ranging from northeastern South America, along the tropical Atlantic to Africa (8,000×3,000 km). The degree of organization is measured by a refined version of the wavelet-based organization index (WOI), which is able to characterize the scale, the intensity and anisotropy of convection based on rain rates alone. Exploiting the localization of wavelets both in space and time, we define a localized version of the convective organization index (LWOI). We compare convection observed in satellite-derived rain rates with the corresponding processes simulated by ICON-LEM. Model and observations indicate three regions with different kinds of convective organization. Continental convection over West Africa has a predominantly meridional orientation and is more organized than over South America, because it acts on larger scales and is more intense. Convection over the tropical Atlantic is zonally oriented along the ITCZ and less intense. ICON and observations agree on the number and intensity of the African easterly waves during the simulation period. The waves are associated with strong vorticity anomalies and are clearly visible in a spatiotemporal wavelet analysis. The central speed and the wavelength of the waves is simulated well. Both the scale and intensity components of LWOI in ICON are significantly correlated with environmental variables. The scale of precipitation is related to wind shear, CAPE and its tendency, while the intensity strongly correlates with column-integrated humidity, upper-level divergence and maximum vertical wind speed. This demonstrates that the LWOI components capture important characteristics of convective precipitation.

KEY WORDS

convective organization, ICON-LEM, IMERG, LWOI, tropical convection, wavelet-based organization index, WOI

This is an open access article under the terms of the Creative Commons Attribution License, which permits use, distribution and reproduction in any medium, provided the original work is properly cited.

© 2020 The Authors. *Quarterly Journal of the Royal Meteorological Society* published by John Wiley & Sons Ltd on behalf of the Royal Meteorological Society.

1 | INTRODUCTION

Convection and its organization play an essential role in the dynamics of the climate system. For instance, around 70% of the total global precipitation over land is caused by deep convection (Xu and Zipser, 2012). Besides moisture fluxes through condensation and rainfall, it has crucial influence on the energy and momentum transport in the global circulation (Stevens and Bony, 2013). Convective processes interact with the global circulation and are driven by large-scale forcing due to waves, fronts and convergence lines (Duda and Gallus Jr. 2013). Different forcing mechanisms and environmental quantities such as wind shear or instability lead to weakly (e.g. pulse storms, scattered convection) or strongly (e.g. squall-lines, mesoscale convective systems) organized convection. Phenomena in the latter category live on larger spatial and temporal scales and are linked to strong forcing and increased wind shear (Moncrieff, 2010). Supercells, squall-lines and other mesoscale convective systems (MCSs) are associated with e.g. large hail, severe winds, tornadoes and/or heavy rainfalls (Groenemeijer *et al.*, 2017). Thus, the correct representation of convection and its degree of organization in numerical weather and climate prediction systems is vitally important.

In recent years the resolution of numerical weather prediction models has increased rapidly (grid spacing \approx 1–10 km) and many convective processes are resolved explicitly. However, in climate simulations with general circulation models (grid spacing \approx 10–100 km), convection still needs to be parametrized to describe organized features like the Madden-Julian oscillation satisfactorily (Peters *et al.*, 2017). Convective parametrizations are responsible for large uncertainties in climate prediction models and are still under vital debate (e.g., Birch *et al.*, 2015; Badlan *et al.*, 2017; Holloway *et al.*, 2017; Moncrieff *et al.*, 2017; Wing *et al.*, 2017). One major aspect in current research is the question of whether and how convective organization should be parametrized (e.g., Mapes and Neale, 2011). Therefore different degrees of convective organization need to be quantified.

Especially in the Tropics, where convection acts on very different scales ranging from cumulus convection and pulse storms up to hurricanes or the Madden-Julian oscillation (Petersen and Rutledge, 2001), a correct representation of convective organization is important. Most tropical convection is driven by the intertropical convergence zone (ITCZ), but heterogeneous continental landmasses (e.g., Africa and South America) greatly influence its initiation and organization as well. Current general circulation models are not able to predict the exact position of the ITCZ correctly (Möbis and Stevens,

2012; Nolan *et al.*, 2016), with the consequence that convection and its degree of organization are represented inadequately.

In our study, we focus on the tropical Atlantic including the adjacent parts of South America and Africa in August 2016 to investigate convective processes over three different regions: the northeastern coast of South America including the Amazon and Tocantins delta, the tropical Atlantic along the ITCZ, and West Africa including western parts of Sahel, Guinea Highlands and Gulf of Guinea. Earlier studies have shown that the types of convection, its organization and the forcing mechanisms are fundamentally different within these regions. Garstang *et al.* (1994), Rickenbach (2004) and Romatschke and Houze Jr. (2010) have shown that convection over northeastern South America is initiated by convergence lines along the coastline due to the easterlies. Intense long-living MCSs (mostly squall-lines) develop, move inland and benefit from the relatively flat terrain and high moisture in the Amazon and Tocantins delta. Over Africa, convection is driven by the African easterly waves (AEWs). AEWs modulate organized convection over Africa (Duvel, 1990; Mekonnen and Rossow, 2018; Tomassini, 2018) and initiate strong squall-lines with heavy rainfall (e.g., Carlson, 1969; Fink and Reiner, 2003; Mekonnen *et al.*, 2006; Crétat *et al.*, 2015). AEWs, defined as westward propagating lower-tropospheric disturbances over Africa, have a period of 2.5–5 days (Burpee, 1972; Lubis and Jacobi, 2015) and a phase speed of 8–10 m·s⁻¹ (Reed *et al.*, 1977; Price *et al.*, 2007). The wavelength of AEWs ranges from 2,000 km (e.g., Burpee, 1974) up to 5,000 km (Diedhiou *et al.*, 1999; Kiladis *et al.*, 2006), which correspond to zonal wavenumbers between 8 and 19. Thus, strongly organized MCSs, frequently organized into squall-lines (Mathon and Laurent, 2001; Jackson *et al.*, 2009; Rickenbach *et al.*, 2009), move westward across the tropical Atlantic. The large-scale forcing over the tropical Atlantic is weaker than over Africa (Xie and Carton, 2004). In general there are fundamental differences between convection over land and ocean (Zipser *et al.*, 2006; Janiga and Thorncroft, 2013). Convection over the tropical Atlantic shows lower cloud tops and less intense rain rates, but more stratiform rainfall than over Africa (Schumacher and Houze Jr. 2006; Futyan and Del Genio, 2007; Liu *et al.*, 2007; Janiga and Thorncroft, 2014; 2016).

To characterize these regions of different convective organization, we use high-resolution convection-permitting simulations and compare them to two kinds of satellite-derived rain rate estimations, namely passive microwave radiometers and infrared measurements.

Senf *et al.* (2018), using the same dataset as the present study, evaluated brightness temperatures simulated by

the ICOsahedral Non-hydrostatic model (ICON) against satellite observations over the tropical Atlantic using a histogram matching technique. Their object-based analysis shows that ICON simulates convection more realistically over continental regions than over the ocean, but contains more small-scale features and overestimates shallow cumulus clouds.

Convective organization is generally measured by indices such as the simple convective aggregation index (SCAI; Tobin *et al.*, 2012), the organization index (I_{org} ; Tompkins and Semie, 2017) or the convective organization potential (COP; White *et al.*, 2018). These conventional indices are based on cluster algorithms of brightness temperatures, vertical wind velocity and outgoing long-wave radiation, respectively. A comparison of the different convective organization indices is presented in Pscheidt *et al.* (2019).

Local convective organization has previously been investigated by Li *et al.* (2018) calculating the information entropy (Shannon, 1948) from satellite observations. They find that information entropy shows only small variances between weak and strong convective organization. Thus, defining convective organization locally is still challenging.

In meteorology, wavelets are used to verify precipitation or cloud fields (e.g., Casati *et al.*, 2004; Yano and Jakubiak, 2016; Weniger *et al.*, 2017; Kapp *et al.*, 2018; Buschow *et al.*, 2019) or to characterize the structure of convection (e.g., Yano *et al.*, 2001a; Yano *et al.*, 2001b; Klein *et al.*, 2018). Brune *et al.* (2018) developed the wavelet-based organization index (WOI) to differentiate between non-organized and organized convection over Germany based on rain rates. Typically, convective organization measurements (SCAI, I_{org} , COP) are directly applied to satellite measurements (e.g., Tobin *et al.*, 2012; Stein *et al.*, 2017; Senf *et al.*, 2018). In recent studies the indices are also used for radar data (Moseley *et al.*, 2019; Pscheidt *et al.*, 2019) or even satellite-derived rainfall (Holloway, 2017). Because the rain rate-based WOI is not yet tested for other variables such as outgoing long-wave radiation or brightness temperature, and has performed well for midlatitude rain rates, we analyze the structure of rain rates over the tropical Atlantic to characterize convective organization in this study. We refine WOI and exploit the wavelet's inherent power of localization in order to answer the following questions:

- How is convection organized over northeastern South America, tropical Atlantic and West Africa?
- Does ICON simulate convective organization correctly?
- How do environmental variables influence convective organization?

In order to explicitly quantify the role of AEWs with regard to these questions, we furthermore complement our spatial wavelet analysis with a spatiotemporal wavelet transform following Kikuchi and Wang (2010).

This article is structured as follows. Section 2 gives an overview of the ICON simulations and the observations. In Section 3 we present the WOI modifications including the extension to the local WOI (LWOI) and briefly introduce spatiotemporal wavelet transforms. After analyzing convective organization using the LWOI components, we turn to the temporal evolution of convection and link environmental quantities to the LWOI components in Section 4. We conclude the article with a summary in Section 5.

2 | MODEL AND DATA

Simulations for August 2016 are performed with a limited-area high-resolution version of the ICON model (Zängl *et al.*, 2015) within the High Definition Clouds and Precipitation for Advancing Climate Prediction (HD(CP)²) project, funded by the German Ministry for Education and Research. For detailed information on ICON we refer to Wan *et al.* (2013), Dipankar *et al.* (2015), Reinert *et al.* (2016), and Heinze *et al.* (2017).

In this study, we use ICON simulations over the tropical Atlantic with a horizontal grid spacing of $\Delta_x \approx 2.5$ km and 75 terrain following full levels (76 half levels) up to a height of about 30 km. Simulations over 36 hr were initialized with analyses from the European Centre for Medium-Range Weather Forecasts (ECMWF) at 0000 UTC and were performed for each day in August 2016. Boundary data were provided by ECMWF every 3 hr. Because spin-up takes at least 6 hr (Heinze *et al.*, 2017), we neglected the first 12 hr and chose the last 24 hr of each simulation to fully cover August 2016. This guarantees that the model physics can evolve and, although the simulations are not continuous, they are close to the observations.

The simulations include lots of interesting features such as shallow cumulus clouds, hurricanes, squall-lines and vortex streets during August 2016 and cover the tropical Atlantic as well as parts of the South American and African continents (Klocke *et al.*, 2017). Due to the high resolution, the long simulation period and persistent convective activity over the domain, the simulations are a good basis to investigate convective organization in the Tropics. However, ICON overestimates shallow cumulus and low-level clouds, which produce weak small-scale drizzle and an increased number of small-scale features (Senf *et al.*, 2018).

The ICON output is interpolated from the original triangular model grid on to a coarser regular grid with a longitudinal extent from 67.45°W to 14.45°E and 9.55°S to

19.45°N by steps of 0.10° in both directions. This corresponds to a horizontal grid spacing of about 10 km, which is close to the effective resolution of the used ICON ($7\Delta_x - 8\Delta_z$; Heinze *et al.*, 2017). The temporal resolution of the 2D output variables is 30 min, and 3D output is available every hour.

In contrast to the object-based study with satellite data by Senf *et al.* (2018), we characterize convective organization on the basis of simulated rain rates. To compare convective organization in ICON with observations, high-resolution rain rate measurements in space and time are required. In the absence of a sufficiently dense rain-gauge network or radar observations, we rely on satellite-derived rain estimations from the Integrated Multi-satellite Retrievals for Global precipitation measurement (IMERG; Huffman *et al.*, 2015) project¹ to assess the observed state of convective organization. Our primary data sources are passive microwave (MW) radiometers from low earth orbit satellites, which constitute the most direct measurements of precipitation available. Over water bodies, emissions from falling hydrometeors near the surface can easily be separated from surface emissions due to the difference in temperature. Over land, MW measurements are mainly determined by scattering from frozen-phase hydrometeors. Both kinds of data are intercalibrated using the global precipitation measurement core satellite's active MW radiometer – essentially a space-borne radar. Over land, the data undergo further calibration to rain-gauge-derived climatologies to create the final IMERG product.

While this procedure yields the overall most trustworthy available information, it may suffer from spatial and temporal inconsistencies. The satellites used to obtain the rain fields change perpetually and the measurement principle differs over land and sea. In addition, the temporal resolution is limited to the frequency of over-passing satellites. The Goddard profiling algorithm employed in IMERG therefore uses sophisticated time interpolation and auxiliary data from infrared (IR) images to create the half-hourly dataset we use. How strongly these processing steps alter the spatial structure of the resulting rain fields remains to be seen. In order to address this uncertainty in the observations, we therefore include the IR-derived rain rates as a secondary source of information. These images are based on a single instrument on a geostationary satellite, which always covers the complete domain and delivers half-hourly data. These data are less trustworthy since precipitation is inferred indirectly from cloud-top temperatures. For example, low warm precipitating clouds

may not be detected by the IR measurement, while high cirrus clouds can potentially be mis-interpreted as rain.

We aim at a more complete comparison using two observation datasets both to one another and to the simulations. Aside from model validation, the intercomparison of different satellite observations with respect to their spectral characteristics holds some interest in itself.

3 | METHODS

3.1 | Discrete wavelet transforms

To describe spatial structures in the precipitation fields, we decompose the rain rates with a redundant discrete wavelet transform. For a comprehensive overview of wavelets and their mathematical background, we refer to Daubechies (1992).

We compute the estimated locally stationary wavelet spectrum following Eckley *et al.* (2010) with help of the R Statistical Programming Language package LS2W (Eckley and Nason, 2011). The decomposition of a $2^J \times 2^J$ field leads to a set of $2^J \times 2^J \times J \times D$ wavelet coefficients with J scales ($1, \dots, J$) and $D = 3$ directions (east–west, north–south, diagonal). Here, the j th scale corresponds to features with a spatial extent of approximately 2^j grid-points. Since the wavelet coefficients are not independent, the spectral energy is biased towards large scales where most of the information in the local spectra is redundant. The correction of this bias following Eckley and Nason (2011) may lead to negative energy values at some locations. We discuss the ramifications of this phenomenon in Section 3.3.

The wavelet analysis requires a quadratic domain with $2^n \times 2^n$, $n \in \mathbb{N}$, grid points and periodic boundaries. Thus, we pad our original output field (820×291) with zeros to obtain a field of size 1024×1024 . To reduce the gradients between the original precipitation field and the synthetic zero-precipitation regions, we follow Weniger *et al.* (2017) and Kapp *et al.* (2018) and smooth the outer 25 grid points with a linearly decreasing filter. Both largest scales (9–10; 2,560–5,120 km) are strongly influenced by the formulation of the boundary conditions. Scale 8 (1,280 km) is smaller than the domain size, but the support length of the D4 wavelet exceeded the domain size. Due to these technical issues, we focus on scales 1–7 (10–640 km) in the 2D wavelet analysis, although convection may be organized into AEWs, which act on even larger scales.

In contrast to Brune *et al.* (2018), who only studied the spatially averaged wavelet spectra, we now intend to analyze the local spectra at every grid point. The location at which we store the respective wavelet coefficient therefore

¹<https://pmm.nasa.gov/category/keywords/imerg>; accessed 1 February 2020

becomes relevant. Since the Daubechies basis functions used by Eckley *et al.* (2010) can exhibit complicated structures within a large support area, it is not entirely obvious to which grid point should be attributed an individual projection. As an *ad hoc* solution, we store each coefficient at the corresponding centre of mass of the wavelet. This guarantees that spectral energy corresponding to any individual precipitation feature is located close to the feature itself, and leads to local spectra which are relatively straightforward to interpret.

3.2 | Wavelet-based organization index (WOI)

The wavelet-based organization index (WOI) was introduced by Brune *et al.* (2018) to differentiate between organized convective structures (e.g., squall-lines, supercells, clustered multicells, MCSs) and unorganized convection (e.g., pulse storms, scattered convection). The WOI consists of three components describing the horizontal scale of precipitation (WOI_1), its intensity (WOI_2) and anisotropy (WOI_3). They are defined as

$$\text{WOI}_1 = \frac{\bar{E}_l}{\bar{E}_s + \bar{E}_l}, \quad (1)$$

$$\text{WOI}_2 = \frac{\bar{E}_s + \bar{E}_l}{r}, \quad (2)$$

$$\text{WOI}_3 = \frac{1}{3} \sqrt{\sum_d \left(\left(\frac{E_s^d - \bar{E}_s}{\bar{E}_s} \right)^2 + \left(\frac{E_l^d - \bar{E}_l}{\bar{E}_l} \right)^2 \right)}. \quad (3)$$

\bar{E}_s represents the small-scale energy on scales 1–3 (10–40 km), while \bar{E}_l represents the large-scale energy on scales 4–7 (80–1,280 km) in the wavelet spectrum, averaged over the domain and each direction. r is the number of grid points with rain rates above zero. E_s^d stands for the small-scale and E_l^d for the large-scale domain-averaged energy in the east–west ($d = 1$), north–south ($d = 2$) and diagonal ($d = 3$) directions.

3.3 | Modified wavelet-based organization index

Negative energy induced by the bias correction of the spectral coefficients may result in a $\text{WOI}_1 > 1$ and a noisy

WOI_3 . Previous studies (Weniger *et al.*, 2017; Brune *et al.*, 2018; Kapp *et al.*, 2018) used the sharp Haar wavelet (Haar, 1910), which is also known as the first member of the Daubechies family (D1; Daubechies, 1992). Preliminary investigations have shown that negative energy is reduced drastically for higher orders of Daubechies wavelets. However, the support length of Daubechies wavelets increases with their order, resulting in less sharp localization. As a compromise between good localization and less negative energy, we choose the extremal phase D4 wavelet for all the following calculations. Remaining negative energy is set to 0 before calculating the indices.

In order to render all three components comparable, we scale WOI_3 with the factor of maximal anisotropy $(3/2\sqrt{3})$. Strong convective precipitation results in high mean spectral energy \bar{E} and is concentrated on a small number of grid points r of the total domain $N_x \cdot N_y$. To ensure that intense rain rates lead to a $\text{WOI}_2 \rightarrow 1$, we multiply the total energy by -1 and subtract the exponential term from 1. Thus, for less intense rain over larger parts of the domain, WOI_2 is 0, because

$$\exp\left(-\frac{\bar{E}}{r/(N_x \cdot N_y)}\right) \rightarrow 1.$$

The resulting WOI components describe scale (sc), intensity (in) and anisotropy (ai) of convection and are defined as

$$\text{WOI}_{\text{sc}} = \frac{\bar{E}_l}{\bar{E}_s + \bar{E}_l}, \quad (4)$$

$$\text{WOI}_{\text{in}} = 1 - \exp\left(-\frac{\bar{E}}{r/(N_x \cdot N_y)}\right), \quad (5)$$

$$\text{WOI}_{\text{ai}} = \frac{1}{2\sqrt{3}} \sqrt{\sum_d \left(\left(\frac{E_s^d - \bar{E}_s}{\bar{E}_s} \right)^2 + \left(\frac{E_l^d - \bar{E}_l}{\bar{E}_l} \right)^2 \right)}. \quad (6)$$

3.4 | Local wavelet-based organization index

For the localized analysis of convective organization, we calculate WOI_{sc} , WOI_{in} and WOI_{ai} at each rainy grid point (i, j) using

$$\text{LWOI}_{\text{sc}}(i, j) = \frac{E_l(i, j)}{E_s(i, j) + E_l(i, j)}, \quad (7)$$

$$\text{LWOI}_{\text{in}}(i, j) = 1 - \exp(-E(i, j)), \quad (8)$$

$$\text{LWOI}_{\text{ai}}(i,j) = \frac{1}{2\sqrt{3}} \sqrt{\sum_d \left\{ \left[\frac{E_s^d(i,j) - E_s(i,j)}{E_s(i,j)} \right]^2 + \left[\frac{E_l^d(i,j) - E_l(i,j)}{E_l(i,j)} \right]^2 \right\}}, \quad (9)$$

with

$$E(i,j) = \frac{1}{3 \cdot 7} \sum_d \sum_k E_k^d(i,j), \quad (10)$$

$$E_l(i,j) = \frac{1}{3 \cdot 4} \sum_d \sum_{4 \leq k \leq 7} E_k^d(i,j), \quad E_l^d(i,j) = \frac{1}{4} \sum_{4 \leq k \leq 7} E_k^d(i,j), \quad (11)$$

$$E_s(i,j) = \frac{1}{3 \cdot 3} \sum_d \sum_{1 \leq k \leq 3} E_k^d(i,j), \quad E_s^d(i,j) = \frac{1}{3} \sum_{1 \leq k \leq 3} E_k^d(i,j), \quad (12)$$

where $E_k^d(i,j)$ describes the wavelet spectrum at grid point (i,j) for scale $k = 1, 2, \dots, 7$ and direction $d = 1, 2, 3$. Note that the LWOI_{in} is not identical to the rain intensity, rather it denotes the total local variance integrated over all scales and directions. LWOI_{in} becomes large if there are sharp gradients in the precipitation field, as is the case for squall-lines.

The code to calculate WOI and LWOI is available as an R package *calcWOI* (Brune et al., 2019), which computes the original WOI as defined in Brune et al. (2018), the modified WOI components defined in Section 3.3 and LWOI components of an arbitrary 2D array.

3.5 | Theory of spatiotemporal wavelet transforms

Apart from its effect on the spatial patterns of precipitation, convective organization manifests itself in the movement and life cycle of thunderstorms. Since tropical weather systems are known to propagate predominantly in zonal directions, in our case westward across the Atlantic, we can infer their spatiotemporal characteristics from the meridional mean as a function of longitude and time. To quantify and compare the size and speed of the various moving systems present in this kind of data, we employ a spatiotemporal wavelet transform (STWT) which was first applied to the analysis of tropical waves by Kikuchi and Wang (2010). Following these authors, we use the complex Morlet mother wavelet given by

$$\psi(x,t) = e^{i(k_0 x + \omega_0 t)} e^{-(x^2 + t^2)/2}. \quad (13)$$

This function of space (here longitude) x and time t is a plane wave with frequency $\omega_0 = 6$ and wave number $k_0 = \pm 6$, localized by a Gaussian envelope. Here, the sign of k_0 determines the direction of propagation. The daughter wavelets of the STWT are given by

$$\psi_{a,c,\tau,b} = \frac{1}{a} \psi \left(\frac{x-b}{a \cdot \sqrt{c}}, \frac{t-\tau}{a/\sqrt{c}} \right), \quad (14)$$

where τ denotes shift in time and b shift in space; $a > 0$ is a common scaling parameter for both directions, and the parameter $c > 0$ corresponds to the phase speed of the daughter wavelet. The power P related to one of these basis functions is given by

$$P(a, c, \tau, b) = \frac{1}{a^3 c} \left| \int_{\mathbb{R}} \int_{\mathbb{R}} f(x, t) \psi_{a,c,\tau,b}^*(x, t) dx dt \right|^2, \quad (15)$$

where the normalization $1/(a^3 c)$ guarantees that the total power integrated over all daughters equals the variance of the original data (up to a further normalization dependent only on the choice of mother wavelet). Before applying the transform given by Equation (15) to the meridional means, we add zeros around the data to get a square field of $2^{11} \times 2^{11}$, thereby avoiding aliasing while speeding up the fast Fourier transformation used to perform the convolutions.

Kikuchi and Wang (2010) demonstrate how the parameters a and c can be related to the frequency ω and wavenumber k of the corresponding Fourier transform. While c is exactly the usual phase speed ω/k , the interpretation of a , which scales time and space alike, is less straightforward. To facilitate the interpretation of our results, we therefore replace a by the wavelength

$$\lambda = \frac{2\pi}{k} = 4\pi a \frac{\sqrt{c}}{\left(k_0 + \sqrt{k_0^2 + 2} \right)}.$$

For a derivation of this identity, as well as further technical details, the reader is referred to Kikuchi and Wang (2010) and references therein. Lastly, a natural way to represent the direction of the daughter wavelets, originally determined by k_0 , is to attach the sign of k_0 to the phase speed, meaning that the daughter denoted by $c = -10$ corresponds to $k_0 = -6, c = 10$.

In principle, we could apply the same discrete two-dimensional wavelet transform to the longitude–time diagrams. For two reasons, we use the STWT basis described above. Firstly, we expect the meridional means to exhibit inherently wave-like behaviour (Figure 4). The complex Morlet wavelet, which is simply a localized plane wave, therefore seems appropriate. Secondly, the spatial

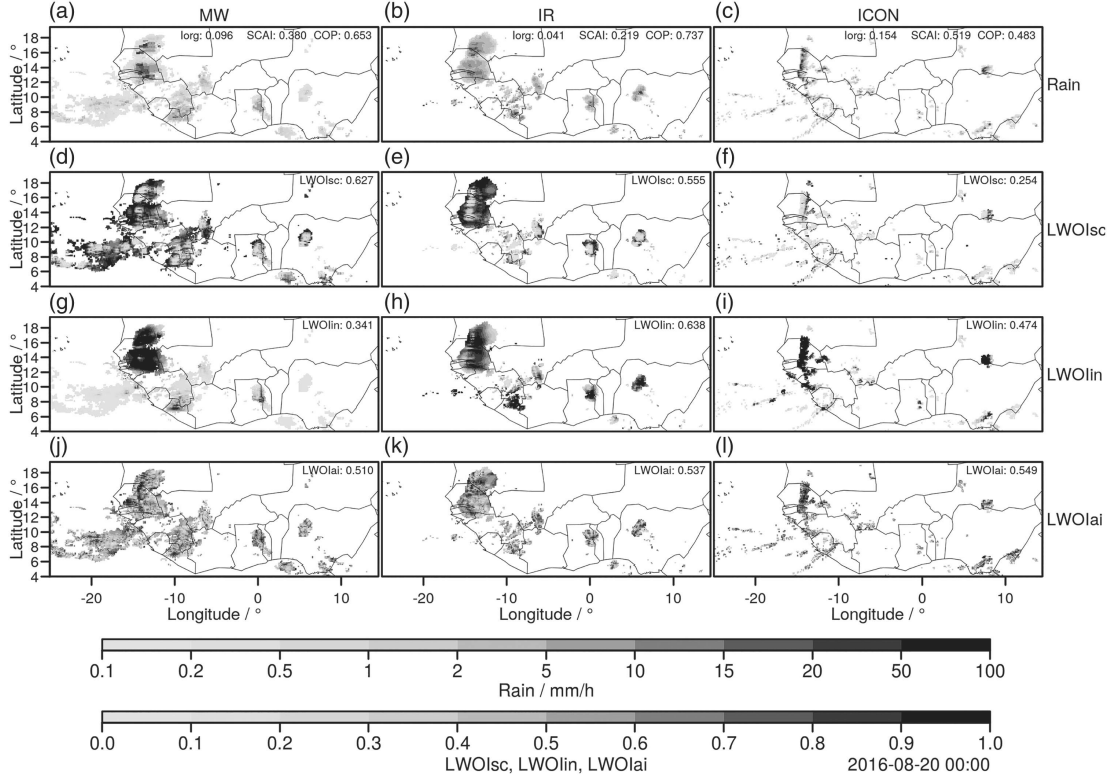


FIGURE 1 Snapshot of (a–c) rain rate in mm hr^{-1} , (d–f) LWOI_{sc} , (g–i) LWOI_{in} and (j–l) LWOI_{ai} of a West African squall-line at 0000 UTC on 20 August 2016 represented in (a, d, g, j) microwave observations, (b, e, h, k) infrared observations, and (c, f, i, l) ICON simulations. Only grid points with rain rates $\geq 0.1 \text{ mm hr}^{-1}$ are displayed. In (a–c) the organization index (I_{org} ; Tompkins and Semie, 2017), the simple convective aggregation index (SCAI; Tobin *et al.* 2012) and the convective organization potential (COP; White *et al.* 2018) are shown for the same threshold (0.1 mm hr^{-1}). In (d–l), the spatial average of LWOI_{sc} , LWOI_{in} and LWOI_{ai} are shown at top right

transform is limited to three directions, allows only scales which are powers of 2, and neglects the important larger scales. For spatiotemporal data, the basis functions correspond to exactly three distinct phase speeds, combined with periods of half a month, a quarter of a month and so on. The continuous STWT entails basis functions which are directly related to any desired combination of speed and scale, making it far more convenient for this purpose.

4 | RESULTS

4.1 | Convective organization of an African squall-line

To illustrate the different representations of convective organization in MW observations, IR observations, and ICON simulations, we show rain rates and the LWOI components on 20 August 2016 at 0000 UTC in Figure 1. A westward-moving squall-line developed during 19 August

2016 and travelled to West Africa. The position of the squall-line is similar in both observations and ICON, but the intensity and its east–west extent differ. In the observations there are two local precipitation maxima in the squall-line, while ICON simulates a more uniform, meridionally oriented precipitation line. The horizontal extent of the squall-lines is largest in the MW observations and slightly smaller in the IR observations. ICON simulates much finer structures and a narrow squall-line. In addition to the heavy precipitation event in West Africa, the MW observations include lots of weak and large-scale precipitation over the Eastern Atlantic, which is almost completely missing in the IR observations. ICON simulates more maritime rainfall than IR, but the precipitation features are smaller and more intense than in MW observations. ICON fails to simulate correctly the location of the single-cell storms over the African continent, but their structure and intensity is represented more satisfactorily.

LWOI_{sc} indicates that most precipitation features in the MW observations act on large scales. In IR only

the squall-line is characterized as a large-scale feature ($LWOI_{sc} > 0.9$), while other continental cells are of small scale ($LWOI_{sc} < 0.2$). In the ICON simulation $LWOI_{sc}$ is larger than 0.5 only for some pixels within the squall-line and over Central Africa, while otherwise rainfall in ICON acts mostly on small scales. Both observations and ICON agree that the squall-line is intense ($LWOI_{in} \approx 1$). The continental cells are less intense in MW than in IR or ICON. Although $LWOI_{ai}$ is generally noisy, anisotropy along the squall-line seems slightly increased. Especially in ICON, the north-south oriented squall-line is characterized as a linearly organized structure with $LWOI_{ai} > 0.9$.

In Figure 1a–c we provide values of I_{org} , SCAI and COP based on rain rates $\geq 0.1 \text{ mm}\cdot\text{hr}^{-1}$ for MW, IR and ICON. Note that all three indices are not tuned for rain rates and were originally based on vertical wind velocity (I_{org}), brightness temperatures (SCAI) and outgoing long-wave radiation (COP). I_{org} suggests that organization is higher in ICON than in MW and IR, while both COP and SCAI (lower value for SCAI means higher degree of organization) indicate that MW and IR rainfall is more organized than in the ICON simulations. The spatial average of $LWOI_{sc}$ is consistent with SCAI and COP and suggests that the scale of precipitation structures in ICON is much smaller than in both observations, which results in a high number of small objects. Note that SCAI and COP are sensitive to the number of cells and the area (Pscheidt *et al.*, 2019). The reason why I_{org} characterizes ICON rain rates as most organized is because the small-scale objects are close together. Intensity ($LWOI_{in}$) and anisotropy ($LWOI_{ai}$) are not assessed by I_{org} , SCAI or COP. The LWOI components provide additional information on the spatial structure of convection. None of the other convective organization indices provide localized maps of convective organization.

4.2 | Convective organization during August 2016

Figure 2a–c display the averaged rain rates in August 2016 observed by the MW observations, the IR observations and simulated by ICON. All three datasets show intense rainfall along the ITCZ, over northern parts of South America and over West Africa. ICON underestimates precipitation along the ITCZ compared to observations and fails to reproduce strong precipitation over the mountains of northern South America and West Africa. IR and ICON precipitation show finer structures than the MW observations. The analysis of snapshots (Figure 1) demonstrates that precipitation derived from MW observations includes frequent large-scale stratiform precipitation over the Atlantic, which is completely missing in IR and underestimated in ICON. These huge discrepancies between

both observations are based on the different measuring methods. Note that the IR and MW rain rates are estimated from satellite images and may include large uncertainties because of the issues discussed in Section 3.

We calculate temporal averages of $LWOI_{sc}$, $LWOI_{in}$ and $LWOI_{ai}$ at each location to provide an averaged characterization of local convective organization as displayed in Figure 2d–l. For this climatology we use the same mask for both observations and ICON. Only grid points with rain rates $\geq 0.1 \text{ mm}\cdot\text{hr}^{-1}$ for at least 2% of all 31×48 timesteps in MW, IR and ICON were taken into account to focus on the main precipitation regions and to exclude the incorrectly simulated drizzle in ICON. ICON reveals much smaller scales ($LWOI_{sc}$ in Figure 2d–f) compared to both observations due to the missing large-scale stratiform precipitation. In MW observations, the stratiform rainfall over the tropical Atlantic seems much larger in scale. In ICON and IR observations, African convection acts on the largest scales. This mismatch may be caused by the different satellite measurement method over ocean and land. However, ICON and both observations suggest that convection over the western tropical Atlantic and South America is of smaller scale than over Africa and eastern parts of the tropical Atlantic. Convection over South America is very localized. The large-scale features over Africa are associated with westward-propagating MCSs.

ICON and IR observations agree on the existence of intense West African rainfall caused by MCSs, but show differences over the ocean and South America, where ICON simulates weaker precipitation (Figure 2g–i). There are five local $LWOI_{in}$ maxima in MW observations, namely over the Guiana Shield, central tropical Atlantic, West African coast along the Guinea Highlands, Ghana and Gulf of Guinea west of Mount Cameroon. Especially over the eastern half of the tropical Atlantic, the $LWOI_{in}$ is low, although MW-derived precipitation is high (Figure 2a). Thus, in the MW observations rainfall from the large-scaled systems is less intense and more persistent. In contrast, rainfall estimated from IR satellite images is very intense over the tropical Atlantic (high $LWOI_{in}$), but smaller in scale as seen before. These contrary results are due to the different measurement methods discussed in Section 2.

Anisotropy (Figure 2j–k) is slightly lower over South America and parts of West Africa in the MW observations than in ICON simulations and IR observations, but generally the ICON simulations and observations agree well in this respect. The variability of the $LWOI_{ai}$ over the complete domain is relatively small, mainly due to two reasons. Firstly, due to a missing rotational invariance of the two-dimensional wavelets used here, the $LWOI_{ai}$ is not completely invariant with respect to rotation, that is $LWOI_{ai}$ changes when a squall-lines changes

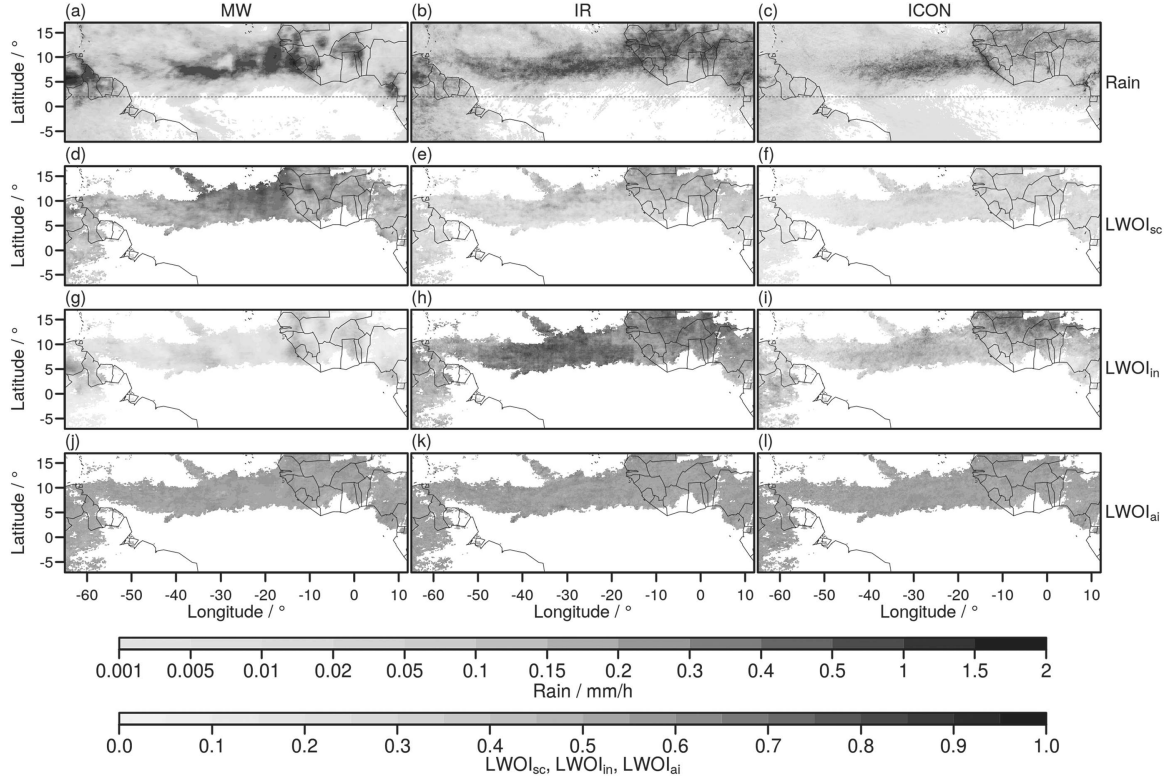


FIGURE 2 Monthly averaged (a–c) rain rates, (d–f) scale $LWOI_{sc}$, (g–i) intensity $LWOI_{in}$ and (j–l) anisotropy $LWOI_{ai}$ of precipitation during August 2016 in (a, d, g, j) MW, (b, e, h, k) IR and (c, f, i, l) ICON. $LWOI_{sc}$, $LWOI_{in}$ and $LWOI_{ai}$ are only shown for grid points with rain rates $\geq 0.1 \text{ mm}\cdot\text{hr}^{-1}$ for at least 2% of all timesteps in both observations and ICON. Dashed lines in (a–c) indicate latitude 2°N

its orientation. This may be relevant since meridionally oriented squall-lines over northern West Africa often propagate southwestwards at the end of their life cycle and change their orientation from north–south to diagonal. Secondly, convection over the tropical Atlantic may also organize into highly isotropic structures such as hurricanes. Thus although $LWOI_{in}$ is large, this results in a low $LWOI_{ai}$. $LWOI_{ai}$ as a single indicator thus may miss highly organized structures, but can be useful to differentiate a squall-line from a highly organized isotropic cluster, which both have a large $LWOI_{in}$. Because of the rotation issue and the noise in $LWOI_{ai}$, we concentrate on $LWOI_{sc}$ and $LWOI_{in}$ in the remainder of the article.

Nevertheless, to investigate the preferred orientation of precipitation patterns, we compare the scale-averaged spectral energy for each direction and show the percentage of east–west and north–south oriented objects during August 2016 in Figure 3. The orientation of each rain pixel is given as the direction of maximal energy. East–west (Figure 3a–c), north–south (Figure 3d–f) and diagonal (not shown) sum up to 1. East–west and north–south oriented objects are dominating. Only less than 10% of the objects

have a diagonal orientation, which is mainly due to the missing rotational invariance of the wavelet transform. Observations and ICON both show that convection is more zonally (east–west) oriented over the tropical Atlantic along and south of the ITCZ, while continental convection over Africa is mostly organized into meridionally (north–south) oriented squall-lines. Interestingly, MW, IR and ICON indicate that convection is also north–south oriented north of the ITCZ over the tropical Atlantic. This signal in orientation may be caused by eastward-moving squall-lines. Convection over South America shows no preferred direction.

4.3 | Temporal evolution of convection

Figure 4a–c present Hovmöller diagrams of the observed and simulated rain rates. Because most convective activity is concentrated over the northern half of the domain (Figure 2), we average the rain rates between 2°N and 17°N . ICON reproduces the large-scaled rainfall over the tropical Atlantic and daily convection over West

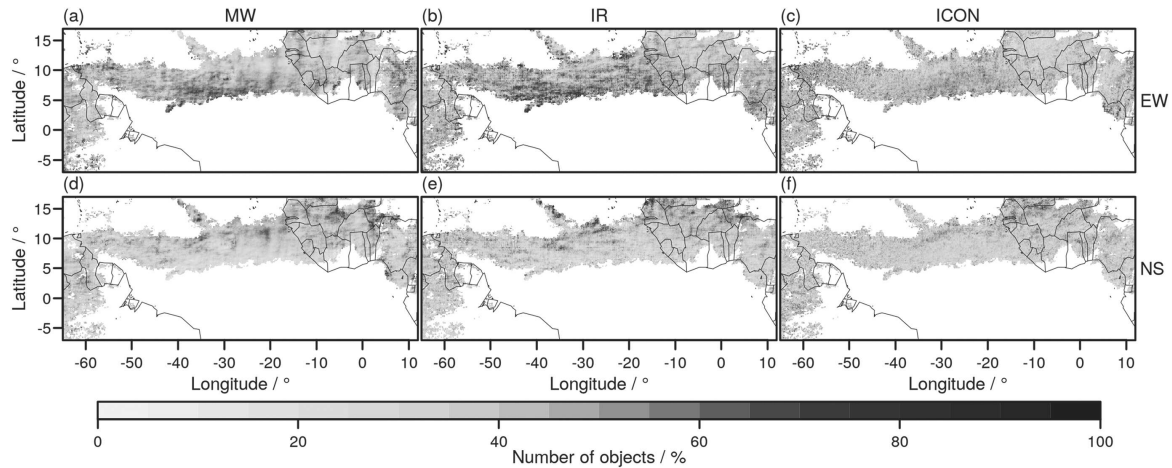


FIGURE 3 Preferred orientation of rain rate objects. Percentage of (a–c) east–west (EW) and (d–f) north–south (NS) oriented objects in (a, d) MW, (b, e) IR and (c, f) ICON

Africa very well. Only over South America and the Caribbean does ICON underestimate convective precipitation slightly. The close agreement between observations and simulations is mainly due to the initialization which takes place each 24 hr. During August 2016, approximately eight heavy precipitating clusters move from Africa to the west. All of them are clearly visible in the 700 hPa vorticity shown in Figure 4d. Especially the vorticity anomalies between 14 and 23 August 2016 are relatively strong and initiate the tropical storm *Fiona* and hurricane *Gaston* (Category 3).

Wavelets may be used to describe convective organization not only in space but also in time. The two-dimensional discrete wavelet investigates the time-averaged degree of convective organization in space, but ignores the longevity and propagation speed of the precipitating systems. Figure 4 has shown us that the central part of the domain is traversed by a number of large, westward-moving clusters with elevated degrees of spatial organization. In the light of the analyses presented by Schlueter *et al.* (2019), we expect that these large, intense, anisotropic features should be related to AEWs. To verify this hypothesis and to quantify the spatiotemporal variability of our three datasets, we apply the STWT as described in Section 3.5 to the meridionally averaged rain fields. Phase speeds are varied within a range of $10 \leq |c| \leq 100 \text{ km} \cdot \text{hr}^{-1}$ and the considered wavelengths range from 150 to 4,000 km.

Figure 5 shows the resulting wavelet spectra averaged over space and time. As expected, almost all spectral power is concentrated on the westward-moving side ($c < 0$). The largest values correspond to daily and sub-daily time-scales (i.e., small wavelengths and slow to moderate

speeds). IR has the overall greatest variability in this regime, while spectral energy in ICON is concentrated on the smallest scales ($\lambda < 250 \text{ km}$, $k > 20$). The two satellite datasets feature a notable increase in power at $T = 1$ day, which is not as pronounced in ICON. This decreased prominence of a diurnal cycle in the model is likely related to the overall weak simulated precipitation over South America which varies mostly on daily time-scales (cf. Figure 4).

As mentioned in Section 1, AEWs are characterized by periods of 2.5 to 5 days and zonal wavenumbers of 8 to 19, which roughly corresponds to wave numbers 1 to 5 in our domain. We recognize that all three datasets contain a distinct increase in power for $2.5 < T < 5$ days, with a common local maximum at the small-scale edge of the AEW regime ($c \approx -25 \text{ km} \cdot \text{hr}^{-1}$, $\lambda \approx 1,900 \text{ km}$).

Our wavelet approach makes it very straightforward to localize this AEW pattern in space and time. Instead of averaging over these two dimensions, we simply average the full spectra over all speeds and wavelengths corresponding to the features of interest (thick lines in Figure 5). In Figure 6, we have superimposed the resulting contours of AEW-related power on the original Hovmöller diagrams of rain (repeated from Figure 4). As expected, all local maxima correspond to the large, long-lived systems crossing the Atlantic with most power lying close to the African coast (20°W). Besides three dominant features persisting between 13 and 25 August 2016, we recognize one large system ending its life cycle near the beginning of the month and one beginning its westward journey near the end. While ICON has less power overall, related to generally lower intensities, the timing and locations are very similar to those of the satellite data.

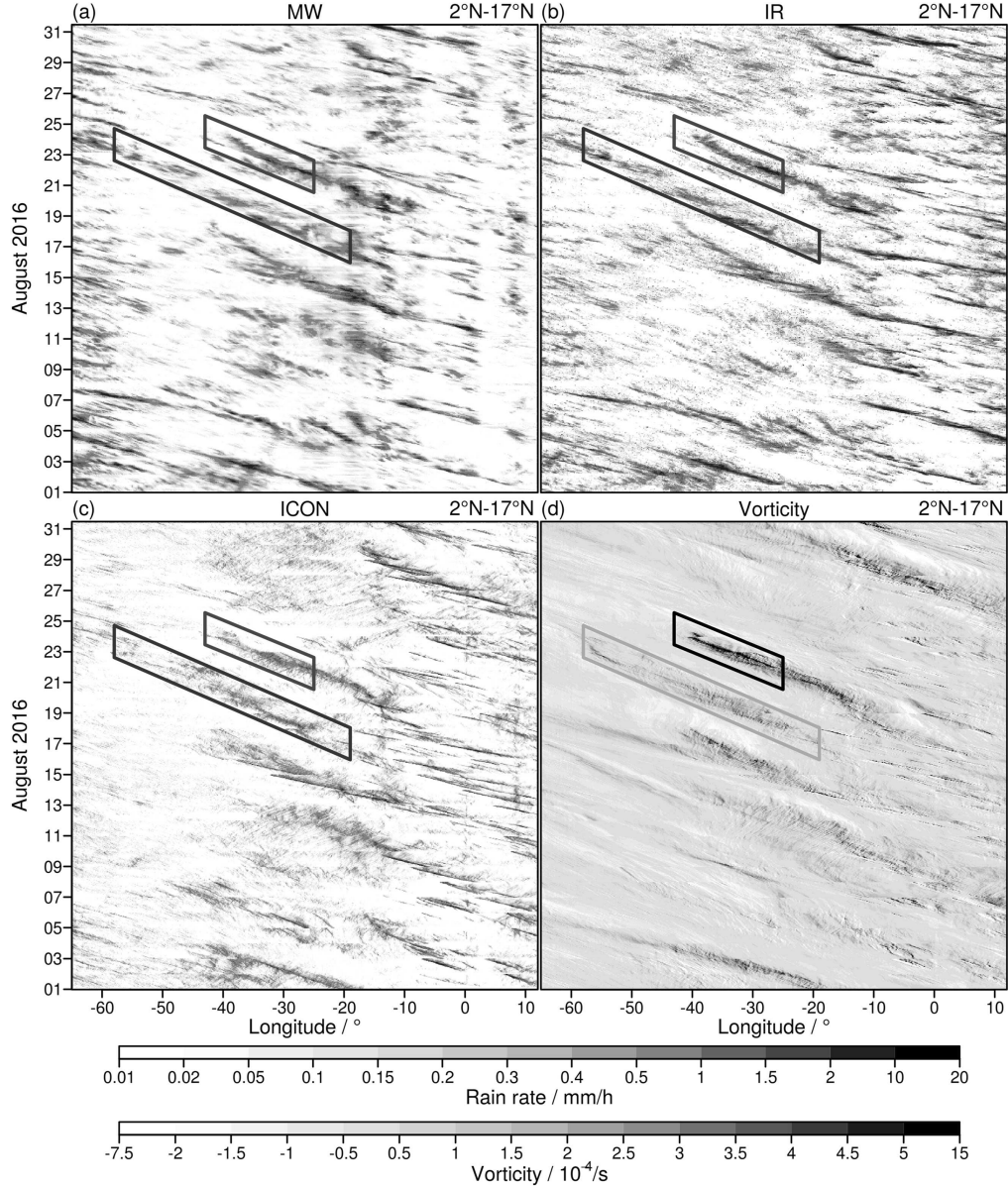


FIGURE 4 Hovmöller diagrams of (a) MW rain rate, (b) IR rain rate, (c) ICON rain rate and (d) height-averaged vorticity between model levels 51 and 53 (approximately 700 hPa). All variables are averaged between 2°N and 17°N (Figure 2). Boxes show the tropical storm Fiona (darkgray) and category 3 hurricane Gaston (black)

To enable a more direct comparison between model and observations, we summarize the time-averaged STWT spectra by calculating their barycentres in the λ - c plane, giving us one central speed and wavelength for every longitude. The resulting profiles (Figure 7) reveal the expected structure. Small, fast features dominate over the African continent and gain spatial extent while slowly losing speed over the ocean – the latter can be observed as a slight

upwards bend of the diagonal stripes in Figure 4. The characteristics over South America are similar to West Africa, albeit with a tendency towards even smaller scales. The three datasets are in fairly good agreement, particularly over the ocean where AEWs are most prevalent. Differences between model and observations are more pronounced over the continents. ICON simulates lower speeds over northwestern South America and smaller

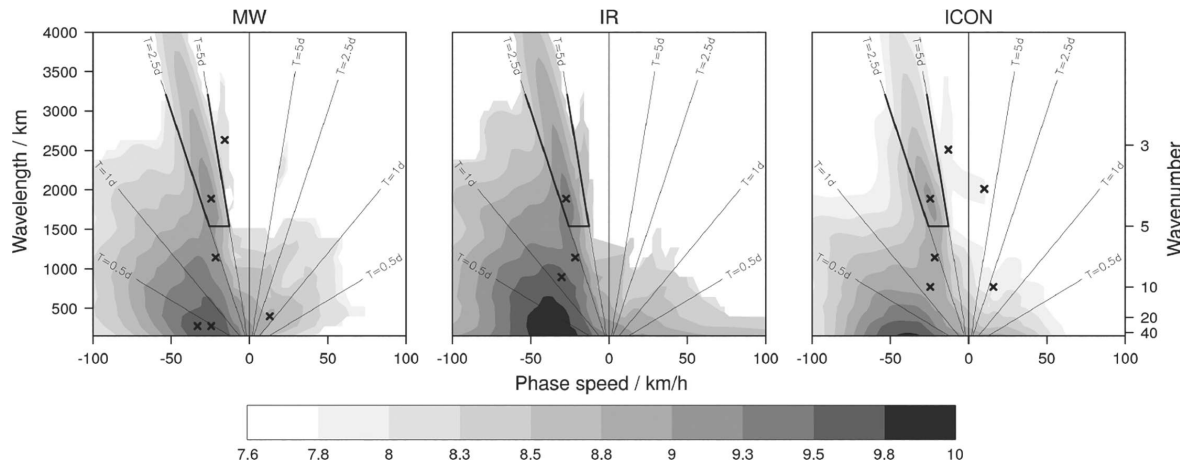


FIGURE 5 STWT spectrum (logarithmic colour levels) of the meridionally averaged rain fields as a function of phase speed and wavelength from (a) MW, (b) IR, and (c) ICON. Crosses mark all local extrema, and thick lines indicate the range of periods and wave numbers associated with AEWs. Values below the respective medians are shown in white

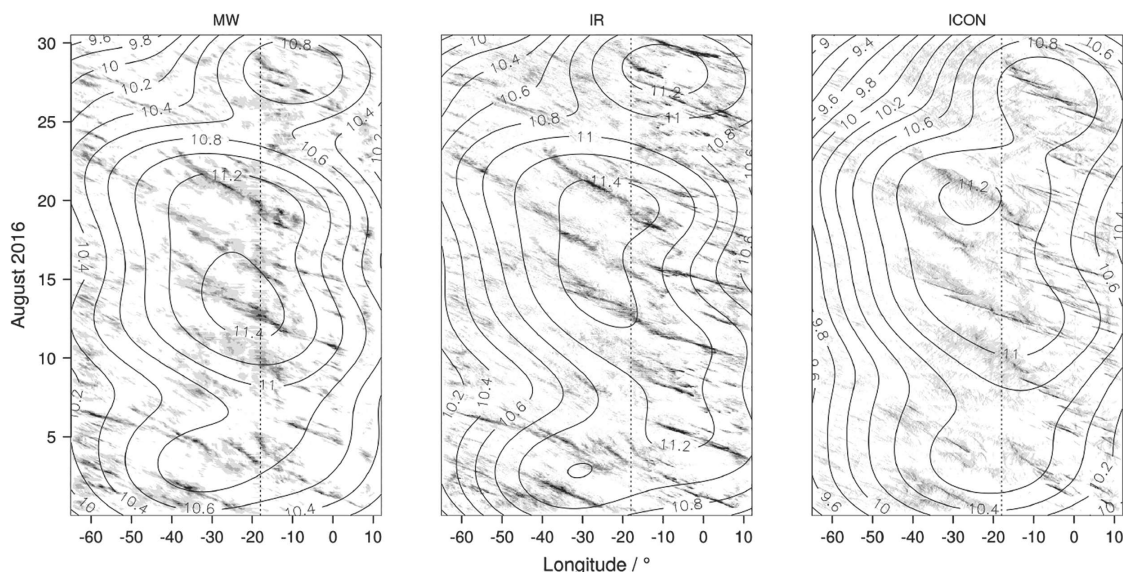


FIGURE 6 Hovmöller diagrams of precipitation (shading) and logarithm of power (contours) corresponding to AEWs from (a) MW, (b) IR and (c) ICON. The vertical dotted line indicates the West African coast

scales for West Africa, but the differences generally remain of the same order as the discrepancies between MW and IR.

4.4 | Link to environmental variables

The previous analysis suggests that tropical convection is organized into westward-moving squall-lines over West

Africa, while convection over the tropical Atlantic is more persistent and zonally oriented. Now we investigate convective organization over the tropical domain from a dynamical perspective using the ICON-simulated 2D and 3D variables.

To this end, we select a set of 30 environmental variables and additionally calculate hourly tendencies of nine variables such as the consumption of CAPE or changes in surface pressure within an hour before the onset of

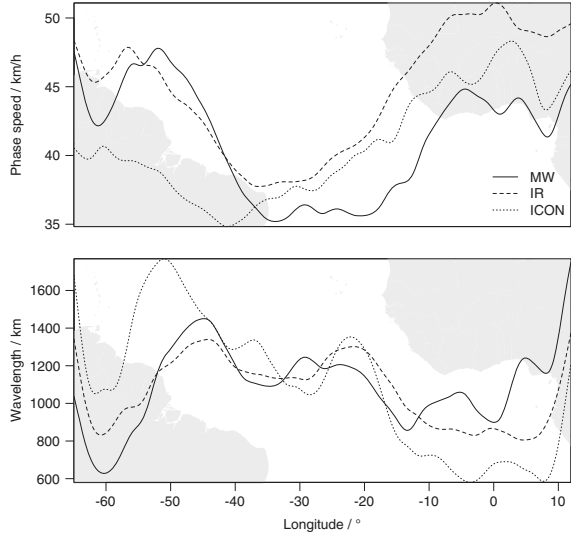


FIGURE 7 (a) Central speed and (b) wavelength as a function of longitude. A geographical map is added to the background for orientation

convection and during convection. Because most of the precipitation along the tropical Atlantic is convective, we assume convection if rain rates are above $0.1 \text{ mm}\cdot\text{hr}^{-1}$. We calculate the environmental variables for all rain pixels during August 2016. The temporal resolution of the 2D and 3D variables is 1 hr. To assess sampling uncertainty, we perform a five-day block bootstrapping. Six blocks of five running days are randomly chosen with replacement to generate 200 bootstrap samples each of $30 \times 24 = 720 \text{ hr}$. We calculate meridional averages of the environmental variables and the LWOI components for each sample, and compute the temporal correlations between the environmental variables and LWOI_{sc} and LWOI_{in} as shown in Table 1. The spread of the 95% sampling interval in Table 1 and Figure 8 indicates the null hypothesis that a correlation may be due to random chance. Correlations outside these intervals are significant.

LWOI_{sc} is positively correlated with the tendency of CAPE (0.27) and the 6 km wind shear (0.24). CAPE consumption and high wind shear leads to more large-scale rain rates such as are caused by squall-lines. Surprisingly, CAPE itself is negatively correlated with LWOI_{sc} (-0.25), meaning that precipitation acts on smaller scales when CAPE is high. However, this negative correlation is reversed over the central Tropical Atlantic, as seen in Figure 8e and discussed below. Correlations between LWOI_{in} and environmental quantities are higher than for LWOI_{sc}. Strong correlations between LWOI_{in} and maximum vertical wind velocity (0.64), mean vertical wind velocity (0.60), upper-level divergence (0.58) and

column-integrated relative humidity (0.53) indicate that rain rates are particularly intense with high LWOI_{in} in the case of powerful updraughts in a humid environment.

We describe the six best correlating environmental variables (Table 1) in more detail and discuss their regional variations. Figure 8c shows that the temporal correlations between meridionally averaged LWOI_{sc} and CAPE tendency are slightly positive (0.2) for all longitudes. The scale of convection gets larger when more CAPE is consumed by convection. The temporal average of CAPE tendency shows that the large-scaled African squall-lines consume up to $500\text{--}800 \text{ J kg}^{-1} \text{ hr}^{-1}$. Over the Atlantic and along the African coast, rainfall reduces CAPE by $100 \text{ J kg}^{-1} \text{ hr}^{-1}$ or less, although LWOI_{sc} is large. CAPE is also strongly reduced over South America and the Caribbean, where temporal averages of LWOI_{sc} indicate less organized rainfall. Thus, the tendency of CAPE does not directly determine the scale of convection.

Correlations between LWOI_{sc} and CAPE (Figure 8e) are even negative over both continents (-0.25) and maximal over the central tropical Atlantic (0.35). We conclude that high CAPE over the tropical Atlantic leads to large-scale precipitation, while the degree of organization over the South American and African continents does not depend on the amount of CAPE. The monthly averages show that CAPE is high over the West Atlantic ($1,500 \text{ J kg}^{-1}$) and below $1,000 \text{ J kg}^{-1}$ over central tropical Atlantic and Africa, although LWOI_{sc} indicates large-scale precipitation. This confirms that the influence of CAPE on LWOI_{sc} is relatively small over both continents.

Wind shear over 6 km is slightly positively correlated with LWOI_{sc} (Figure 8g). High wind shear fosters the evolution of large-scale systems such as squall-lines characterized by a large LWOI_{sc}. The averaged wind shear is large over most parts of Africa ($15 \text{ m}\cdot\text{s}^{-1}$), moderate over the West and Central Atlantic ($5\text{--}10 \text{ m}\cdot\text{s}^{-1}$) and low over the East Atlantic (below $5 \text{ m}\cdot\text{s}^{-1}$) and fits well to the LWOI_{sc} pattern shown in Figure 8a. Increased CAPE values in combination with moderate wind shear north of the ITCZ may be responsible for the north-south orientated convection in this region as observed in Figure 3.

Temporal correlations between LWOI_{in} and the maximum vertical wind, upper-level divergence and column-integrated relative humidity show a similar pattern. Between 65°W and 50°W , correlations are nearly constant, increase over the tropical Atlantic and maximize at 30°W , decrease slightly towards the West African coast and remain constant over West Africa. Correlations between the environmental variables and LWOI_{in} are much larger than for LWOI_{sc} and indicate that LWOI_{in} is directly linked to the updraught velocity, especially over the Atlantic and the African continent, and the column-integrated humidity. The maximum of the

TABLE 1 Correlations over time of LWOI_{sc} and LWOI_{in} with the 39 environmental variables at calculation height z and time t (B denotes the value 1 hr before onset of convection, D the value at the onset of convection, and BD the difference between values at onset of convection and at 1 hr before)

Variables	Description	z (km)	t	LWOI _{sc}	LWOI _{in}
CAPE	Conv. available pot. energy	—	B	**-0.25 (-0.20, -0.16)	-0.12 (-0.11, -0.06)
dCAPE	CAPE tendency	—	BD	** 0.27 (0.08, 0.13)	**-0.29 (-0.02, 0.03)
CIN	Convective inhibition	—	B	0.03 (-0.01, 0.04)	0.16 (0.01, 0.06)
dCIN	CIN tendency	—	BD	-0.06 (-0.06, -0.04)	0.02 (-0.03, 0.00)
CLCT	Total cloud cover	—	D	0.05 (0.10, 0.14)	** 0.35 (0.04, 0.10)
dCLCT	CLCT tendency	—	BD	-0.11 (-0.09, -0.06)	-0.04 (-0.04, -0.02)
COLRH	Column-integrated rel. hum.	0.0–30.0	B	0.05 (0.06, 0.14)	** 0.53 (0.02, 0.12)
DIVSURF	Divergence	0.0– 1.7	D	0.06 (-0.04, -0.00)	0.00 (-0.02, 0.02)
DIVTOP	Divergence	8.5–15.0	D	-0.09 (-0.00, 0.04)	** 0.58 (0.01, 0.10)
PMSL	Mean sea level pressure	surface	B	0.07 (0.02, 0.08)	-0.16 (-0.03, 0.03)
dPMSL	PMSL tendency	surface	BD	-0.09 (-0.04, -0.01)	** 0.21 (0.03, 0.06)
PVMID	Potential vorticity	1.7– 8.5	D	0.05 (0.01, 0.04)	0.11 (-0.01, 0.03)
PVTOP	Potential vorticity	8.5–15.0	D	-0.06 (-0.07, -0.02)	**-0.25 (-0.06, 0.01)
RH2M	Relative humidity	0.002	B	0.05 (0.07, 0.12)	0.16 (0.03, 0.08)
dRH2M	RH2M tendency	0.002	BD	-0.16 (-0.10, -0.07)	0.03 (-0.05, -0.01)
SHEARU3	Wind shear (u)	0.8–3.0	B	-0.12 (-0.11, -0.06)	0.06 (-0.05, 0.01)
SHEARU6	Wind shear (u)	0.8–6.0	B	-0.16 (-0.16, -0.10)	0.12 (-0.07, 0.01)
SHEARV3	Wind shear (v)	0.8–3.0	B	-0.17 (-0.15, -0.09)	-0.02 (-0.08, -0.01)
SHEARV6	Wind shear (v)	0.8–6.0	B	-0.13 (-0.12, -0.07)	0.08 (-0.06, 0.01)
SHEARWS3	Wind shear speed	0.8–3.0	B	0.19 (0.09, 0.17)	** 0.20 (0.01, 0.10)
SHEARWS6	Wind shear speed	0.8–6.0	B	** 0.24 (0.16, 0.21)	0.14 (0.04, 0.10)
T2M	Temperature	0.002	B	-0.13 (-0.13, -0.10)	-0.16 (-0.09, -0.05)
dT2M	T2M tendency	0.002	BD	** 0.20 (0.07, 0.11)	-0.18 (-0.01, 0.04)
TD2M	Dewpoint temperature	0.002	B	-0.12 (-0.07, -0.02)	-0.05 (-0.06, -0.02)
dTD2M	TD2M tendency	0.002	BD	0.13 (-0.01, 0.04)	**-0.33 (-0.06, 0.00)
THETAV	Virtual potential temp.	1.7–8.5	D	0.04 (-0.04, 0.02)	0.16 (-0.01, 0.06)
U10M	U wind	0.01	B	0.14 (0.13, 0.18)	0.09 (0.03, 0.09)
dU10M	U10M tendency	0.01	BD	0.04 (-0.02, 0.00)	-0.09 (-0.02, 0.01)
U300	U wind	9.4	B	0.00 (-0.11, 0.02)	0.12 (-0.04, 0.05)
U500	U wind	5.5	B	-0.01 (0.04, 0.11)	** 0.25 (-0.00, 0.09)
V10M	V wind	0.01	B	0.10 (0.09, 0.14)	-0.06 (0.00, 0.07)
dV10M	V10M tendency	0.01	BD	-0.03 (-0.04, -0.02)	-0.02 (-0.03, 0.00)
V300	V wind	9.4	B	-0.09 (-0.06, 0.01)	-0.09 (-0.06, 0.04)
V500	V wind	5.5	B	-0.04 (-0.04, 0.02)	-0.07 (-0.05, 0.05)
WMAX	Maximum vertical wind	1.7–8.5	D	**-0.23 (-0.03, 0.02)	** 0.64 (0.00, 0.11)
WMEAN	Mean vertical wind	1.7–8.5	D	**-0.23 (-0.04, 0.00)	** 0.52 (-0.01, 0.08)
WMIN	Minimum vertical wind	1.7–8.5	D	0.03 (-0.04, -0.00)	**-0.26 (-0.07, -0.02)
WS300	Wind speed	9.4	B	0.01 (-0.02, 0.09)	-0.07 (-0.03, 0.05)
WS500	Wind speed	5.5	B	0.10 (-0.06, 0.02)	-0.11 (-0.06, 0.03)

Note: Correlations $\geq \pm 0.20$ are marked **. Bold font denotes the three largest correlations for LWOI_{sc} and LWOI_{in}. 2.5 and 97.5%iles of the 200 samples are added in parentheses.

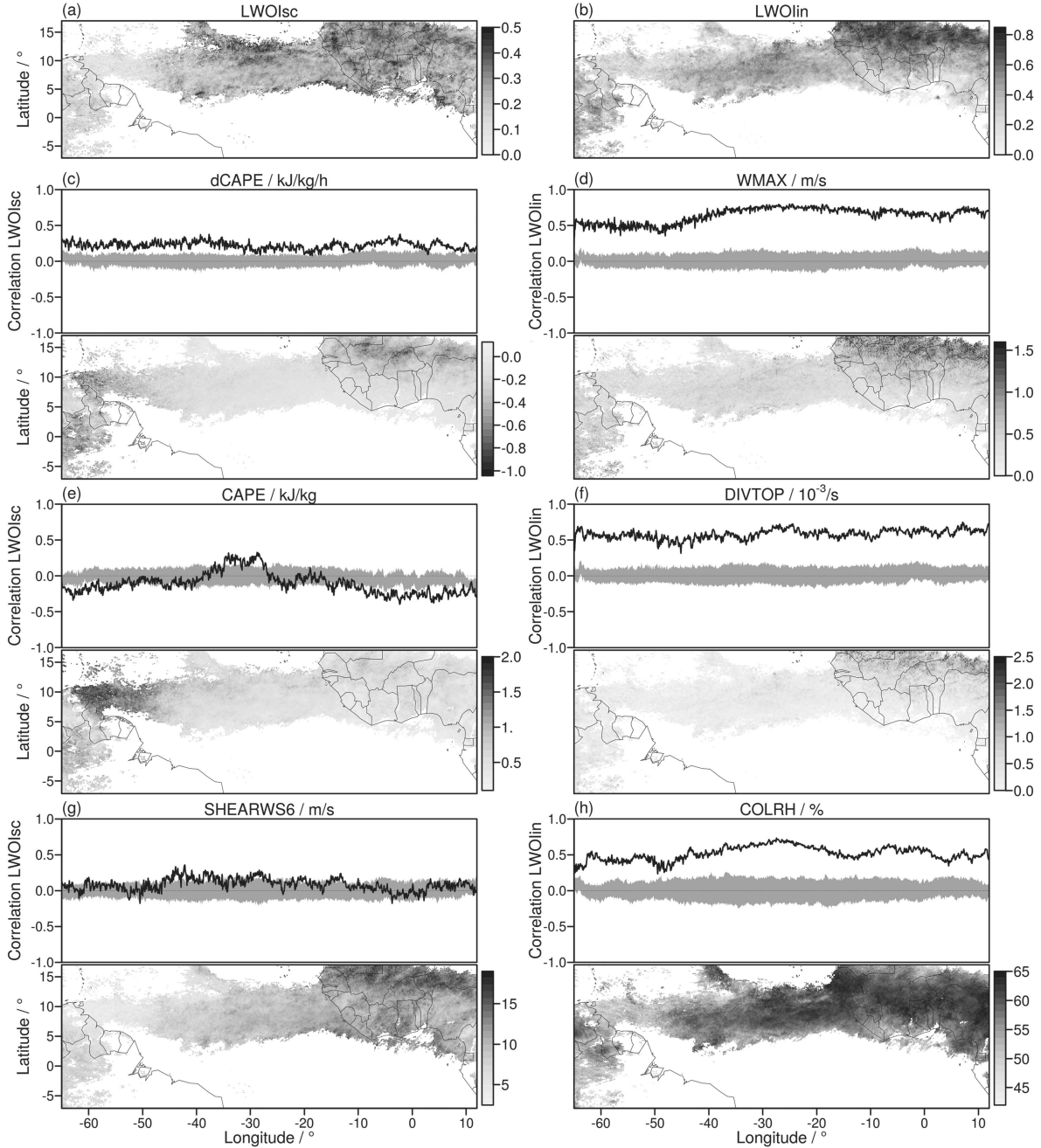


FIGURE 8 Monthly averages of (a) LWOI_{sc} and (b) LWOI_{in}. The upper plots in (c-h) show correlations (black) and 2.5–97.5%ile ranges (grey) for (c) dCAPE and LWOI_{sc}, (d) WMAX and LWOI_{in}, (e) CAPE and LWOI_{sc}, (f) DIVTOP and LWOI_{in}, (g) SHEARWS6 and LWOI_{sc}, and (h) COLRH and LWOI_{in}. The lower plots display temporal averages of the six selected environmental variables

vertical wind velocity and the upper-level divergence in Figure 8d,f show these strong updraughts over the northern parts of West Africa, where LWOI_{in} is maximal. Also over the Central Atlantic and over the South

American continent, increased updraught velocities are in accordance with an increased LWOI_{in}.

Our analysis demonstrates that LWOI_{sc} and LWOI_{in}, which are calculated only on the basis of rain rates, provide

useful information on convective organization. The LWOI components detect precipitation patterns of different kinds of convective storms.

5 | CONCLUSION

Especially along the Tropics, where intense and long-lived convective systems develop, numerical weather prediction and climate models often fail to represent the degree of organization successfully. To assess the degree of convective organization and to analyze the relevant processes in detail, we use half-hourly output of high-resolution ICON simulations (grid spacing 2.5 km) over the tropical Atlantic (domain size $8,000 \times 3,000$ km) and parts of South America and West Africa during August 2016. Comparisons are made with passive microwave radiometer observations (MW) and infrared measurements (IR) from the Integrated Multi-satellite Retrievals for Global precipitation measurement project (IMERG). ICON represents convective rainfall satisfactorily; the model contains even finer structures and produces small-scale drizzle over northern and southern parts of the tropical Atlantic. The IR measurements include strong precipitation inside deep convective cores and have potentially higher spatiotemporal consistency, but miss precipitation like stratiform rain outside the updraught regions.

To identify the degree of convective organization, we modified the wavelet-based organization index (WOI). We use the Daubechies 4 instead of the Daubechies 1 (Haar) wavelet, which results in less negative spectral energy. We furthermore normalize all three WOI components between 0 (non-organized convection) and 1 (organized convection). The resulting improved WOI allows us to study convective organization on scales ranging from the complete domain to individual grid-points without any further adjustments.

There are discrepancies between convective organization simulated by ICON and observed in MW- and IR-derived rain rates. Both observations and ICON show that convection over West Africa is more organized than over South America, because the scale of convection (LWOI_{sc}), its intensity (LWOI_{in}) and anisotropy (LWOI_{ai}) are higher. Due to the different measurement principles, the scale of rain rates in MW observations is higher than in the IR observations and ICON. IR observations show by far the greatest intensities ($\text{LWOI}_{\text{in}} \approx 1$). LWOI_{ai} indicates that convection over northern parts of West Africa is slightly more linearly organized than over South America. LWOI_{ai} is not completely invariant for similar but differently oriented squall-lines, and as a single index would not identify highly organized isotropic structures over the tropical Atlantic such as hurricanes. But in combination

with LWOI_{sc} and LWOI_{in} , the LWOI_{ai} index gives useful additional information on convective clusters. However, the issue of non-invariance with respect to rotation needs to be solved to fully exploit the anisotropy information. An analysis of the predominant orientation of the wavelet spectrum shows that convection over Africa is organized into meridional squall-lines while maritime convection is preferably zonally oriented.

Studying the temporal evolution using spatiotemporal wavelet transforms (STWT), we find that in ICON the small-scale variability is higher, but the diurnal cycle of convection, especially over South America, is less pronounced. However, the large-scale AEWs ($c \approx 25 \text{ km} \cdot \text{hr}^{-1}$, $\lambda \approx 1,900 \text{ km}$, $2.5 < T < 5$ days) are simulated satisfactorily in space and time. ICON and the observations agree on the central speed and wavelength of the AEWs. They include the fast westward-moving squall-lines ($|c| > 45 \text{ km} \cdot \text{hr}^{-1}$, $\lambda < 1,000 \text{ km}$) and more persistent, slow-moving meridionally oriented convection ($|c| < 40 \text{ km} \cdot \text{hr}^{-1}$, $\lambda \approx 1,200 \text{ km}$) over the Atlantic.

We use a set of 3D variables provided by ICON to relate convective organization to convective characteristics and the environmental forcing. The pattern of scale and intensity of convection measured by LWOI_{sc} and LWOI_{in} correlates with different environmental variables. It turns out that LWOI_{sc} is mainly modulated by wind shear. Large CAPE is not essential to simulate large-scale features, but the overlap of convective instability and strong wind shear is important. LWOI_{in} is controlled by vertical wind speed and upper-level divergence, which indicate strong updraughts.

In this study, we provide a promising approach to characterize convective organization locally. Compared to the entropy analysis by Li *et al.* (2018), the LWOI components vary over the domain and are in agreement with convective and environmental quantities. The LWOI components are tested over a large domain, but only for roughly 1,500 time steps. To get a long-lasting climatology of organization over the tropical Atlantic and its temporal variability during a year, this analysis could be extended to several years. It is also possible to study convection over other regions (e.g., North America, Europe or tropical Pacific) to improve the representation of convective organization in climate and weather prediction models.

This wavelet analysis could be directly applied to IR measurements such as outgoing long-wave radiation or other variables. However, the wavelet spectra may be more sensitive for low-variation cloud structures than for small-scale highly variable rain rates.

ACKNOWLEDGMENTS

We gratefully acknowledge financial support by the project High Definition Clouds and Precipitation for Advancing

Climate Prediction HD(CP)², funded by the German Ministry for Education and Research (BMBF) under grant FKZ01LK1507B (Sebastian Brune). Special thanks go to Velibor Pejcic for his advice on the IMERG satellite data. We are also very grateful to two anonymous reviewers for their constructive comments on an earlier version of the article.

ORCID

Sebastian Brune  <https://orcid.org/0000-0002-3742-4443>

REFERENCES

- Badlan, R.L., Lane, T.P., Moncrieff, M.W. and Jakob, C. (2017) Insights into convective momentum transport and its parametrization from idealized simulations of organized convection. *Quarterly Journal of the Royal Meteorological Society*, 143, 2687–2702
- Birch, C.E., Roberts, M.J., Garcia-Carreras, L., Ackerley, D., Reeder, M.J., Lock, A.P. and Schiemann, R. (2015) Sea-breeze dynamics and convection initiation: the influence of convective parametrization in weather and climate model biases. *Journal of Climate*, 28(20), 8093–8108
- Brune, S., Kapp, F. and Friederichs, P. (2018) A wavelet-based analysis of convective organization in ICON large-eddy simulations. *Quarterly Journal of the Royal Meteorological Society*, 717(144), 2812–2829
- Brune, S., Buschow, S., Kapp, F. and Friederichs, P. (2019) calcWOL: Calculates the Wavelet-based Organization Index. <https://cran.r-project.org/web/packages/calcWOL/calcWOL.pdf>; accessed 1 February 2020. R package version 1.0.2.
- Burpee, R.W. (1972) The origin and structure of easterly waves in the lower troposphere of North Africa. *Journal of the Atmospheric Sciences*, 29(1), 77–90
- Burpee, R.W. (1974) Characteristics of North African easterly waves during the summers of 1968 and 1969. *Journal of the Atmospheric Sciences*, 31(6), 1556–1570
- Buschow, S., Pidstrigach, J. and Friederichs, P. (2019) Assessment of wavelet-based spatial verification by means of a stochastic precipitation model (wv_verif v0.1.0). *Geoscientific Model Development*, 12, 3401–3418. <https://doi.org/10.5194/gmd-12-3401-2019>
- Carlson, T.N. (1969) Some remarks on African disturbances and their progress over the tropical Atlantic. *Monthly Weather Review*, 97(10), 716–726
- Casati, B., Ross, G. and Stephenson, D. (2004) A new intensity-scale approach for the verification of spatial precipitation forecasts. *Meteorological Applications*, 11(2), 141–154
- Crétat, J., Vizy, E.K. and Cook, K.H. (2015) The relationship between African easterly waves and daily rainfall over West Africa: observations and regional climate simulations. *Climate Dynamics*, 44(1–2), 385–404
- Daubechies, I. (1992) *Ten Lectures on Wavelets*, p. 357. Society for Industrial and Applied Mathematics, Philadelphia, PA.
- Diedhiou, A., Janicot, S., Viltard, A., De Felice, P. and Laurent, H. (1999) Easterly wave regimes and associated convection over West Africa and tropical Atlantic: Results from the NCEP/NCAR and ECMWF reanalyses. *Climate Dynamics*, 15(11), 795–822
- Dipankar, A., Stevens, B., Heinze, R., Moseley, C., Zängl, G., Giorgi, M. and Brdar, S. (2015) Large-eddy simulation using the general circulation model ICON. *Journal of Advances in Modeling Earth Systems*, 7(3), 963–986. <https://doi.org/10.1002/2015MS000431>
- Duda, J.D. and Gallus Jr, W.A. (2013) The impact of large-scale forcing on skill of simulated convective initiation and upscale evolution with convection-allowing grid spacings in the WRF. *Weather and Forecasting*, 28(4), 994–1018
- Duvel, J.P. (1990) Convection over tropical Africa and the Atlantic Ocean during northern summer. Part II: modulation by easterly waves. *Monthly Weather Review*, 118(9), 1855–1868
- Eckley, I.A. and Nason, G.P. (2011) LS2W: Implementing the locally stationary 2D wavelet process approach in R. *Journal of Statistical Software*, 43(3), 1–23. <https://doi.org/10.1863/jss.v043.i03>
- Eckley, I.A., Nason, G.P. and Treloar, R.L. (2010) Locally stationary wavelet fields with application to the modelling and analysis of image texture. *Journal of the Royal Statistical Society, Series C*, 59(4), 595–616. <https://doi.org/10.1111/j.1467-9876.2009.00721.x>
- Fink, A.H. and Reiner, A. (2003) Spatiotemporal variability of the relation between African easterly waves and West African squall lines in 1998 and 1999. *Journal of Geophysical Research: Atmospheres*, 108(D11)
- Futyan, J.M. and Del Genio, A.D. (2007) Deep convective system evolution over Africa and the tropical Atlantic. *Journal of Climate*, 20(20), 5041–5060
- Garstang, M., Massie Jr, H.L., Halverson, J., Greco, S. and Scala, J. (1994) Amazon coastal squall lines. Part I: structure and kinematics. *Monthly Weather Review*, 122(4), 608–622
- Groenemeijer, P., Ptčík, T., Holzer, A.M., Antonescu, B., Riemann-Campe, K., Schultz, D.M., Kühne, T., Feuerstein, B., Brooks, H.E., Doswell III, C.A., Koppert, H.-J. and Sausen, R. (2017) Severe convective storms in Europe: ten years of research and education at the European Severe Storms Laboratory. *Bulletin of the American Meteorological Society*, 98(12), 2641–2651
- Haar, A. (1910) Zur Theorie der orthogonalen Funktionensysteme. *Mathematische Annalen*, 69(3), 331–371. <https://doi.org/10.1007/BF01456326>
- Heinze, R., Dipankar, A., Henken, C.C., Moseley, C., Sourdeval, O., Träomel, S., Xie, X., Adamidis, P., Ament, F., Baars, H., Barthlott, C., Behrendt, A., Blahak, U., Bley, S., Brdar, S., Brueck, M., Crewell, S., Deneke, H., Di Girolamo, P., Evaristo, R., Fischer, J., Frank, C., Friederichs, P., Gäocke, T., Gorges, K., Hande, L., Hanke, M., Hansen, A., Hege, H.-C., Hoose, C., Jahns, T., Kalthoff, N., Klocke, D., Kneifel, S., Knippertz, P., Kuhn, A., van Laar, T., Macke, A., Maurer, V., Mayer, B., Meyer, C.I., Muppa, S.K., Neggers, R.A.J., Orlandi, E., Pantillon, F., Pospichal, B., Räöber, N., Scheck, L., Seifert, A., Seifert, P., Senf, F., Siligam, P., Simmer, C., Steinke, S., Stevens, B., Wapler, K., Weniger, M., Wulfmeyer, V., Zängl, G., Zhang, D. and Quaas, J. (2017) Large-eddy simulations over Germany using ICON: a comprehensive evaluation. *Quarterly Journal of the Royal Meteorological Society*, 143, 69–100. <https://doi.org/10.1002/qj.2947>
- Holloway, C.E. (2017) Convective aggregation in realistic convective-scale simulations. *Journal of Advances in Modeling Earth Systems*, 9(2), 1450–1472
- Holloway, C.E., Wing, A.A., Bony, S., Muller, C., Masunaga, H., L'Ecuyer, T.S., Turner, D.D. and Zuidema, P. (2017) Observing convective aggregation. *Surveys in Geophysics*, 38(6), 1199–1236
- Huffman, G.J., Bolvin, D.T. and Nelkin, E.J. (2015). Integrated Multi-satellite Retrievals for GPM (IMERG) Technical

- Documentation. https://pmm.nasa.gov/sites/default/files/document_files/IMERG_doc.pdf; accessed 1 February 2020.
- Jackson, B., Nicholson, S.E. and Klotter, D. (2009) Mesoscale convective systems over western equatorial Africa and their relationship to large-scale circulation. *Monthly Weather Review*, 137(4), 1272–1294
- Janiga, M.A. and Thorncroft, C.D. (2013) Regional differences in the kinematic and thermodynamic structure of African easterly waves. *Quarterly Journal of the Royal Meteorological Society*, 139, 1598–1614
- Janiga, M.A. and Thorncroft, C.D. (2014) Convection over tropical Africa and the East Atlantic during the West African monsoon: regional and diurnal variability. *Journal of Climate*, 27(11), 4159–4188
- Janiga, M.A. and Thorncroft, C.D. (2016) The influence of African easterly waves on convection over tropical Africa and the East Atlantic. *Monthly Weather Review*, 144(1), 171–192
- Kapp, F., Friederichs, P., Brune, S. and Weniger, M. (2018) Spatial verification of high-resolution ensemble precipitation forecasts using local wavelet spectra. *Meteorologische Zeitschrift*, 467–480
- Kikuchi, K. and Wang, B. (2010) Spatiotemporal wavelet transform and the multiscale behavior of the Madden-Julian oscillation. *Journal of Climate*, 23(14), 3814–3834
- Kiladis, G.N., Thorncroft, C.D. and Hall, N.M. (2006) Three-dimensional structure and dynamics of African easterly waves. Part i: observations. *Journal of the Atmospheric Sciences*, 63(9), 2212–2230
- Klein, C., Belušić, D. and Taylor, C.M. (2018) Wavelet scale analysis of mesoscale convective systems for detecting deep convection from infrared imagery. *Journal of Geophysical Research: Atmospheres*, 123(6), 3035–3050
- Klocke, D., Brueck, M., Hohenegger, C. and Stevens, B. (2017) Rediscovery of the doldrums in storm-resolving simulations over the tropical Atlantic. *Nature Geoscience*, 10(12), 891
- Li, Y., Yano, J.-I. and Lin, Y. (2018) Is atmospheric convection organised?: information entropy analysis. *Geophysical and Astrophysical Fluid Dynamics*, 113, 553–573. <https://doi.org/10.1080/03091929.2018.1506449>
- Liu, C., Zipser, E.J. and Nesbitt, S.W. (2007) Global distribution of tropical deep convection: different perspectives from TRMM infrared and radar data. *Journal of Climate*, 20(3), 489–503
- Lubis, S.W. and Jacobi, C. (2015) The modulating influence of convectively coupled equatorial waves (CCEWs) on the variability of tropical precipitation. *International Journal of Climatology*, 35(7), 1465–1483
- Mapes, B. and Neale, R. (2011) Parameterizing convective organization to escape the entrainment dilemma. *Journal of Advances in Modeling Earth Systems*, 3(2). <https://doi.org/10.1029/2011MS000042>
- Mathon, V. and Laurent, H. (2001) Life cycle of Sahelian mesoscale convective cloud systems. *Quarterly Journal of the Royal Meteorological Society*, 127, 377–406
- Mekonnen, A. and Rossow, W.B. (2018) The interaction between deep convection and easterly wave activity over Africa: convective transitions and mechanisms. *Monthly Weather Review*, 146(6), 1945–1961
- Mekonnen, A., Thorncroft, C.D. and Aiyer, A.R. (2006) Analysis of convection and its association with African easterly waves. *Journal of Climate*, 19(20), 5405–5421
- Möbis, B. and Stevens, B. (2012) Factors controlling the position of the intertropical convergence zone on an aquaplanet. *Journal of Advances in Modeling Earth Systems*, 4(4)
- Moncrieff, M.W. (2010) The multiscale organization of moist convection and the intersection of weather and climate. *Climate Dynamics*, 189, 3–26
- Moncrieff, M.W., Liu, C. and Bogenschutz, P. (2017) Simulation, modeling, and dynamically based parameterization of organized tropical convection for global climate models. *Journal of the Atmospheric Sciences*, 74(5), 1363–1380
- Moseley, C., Pscheidt, I., Cioni, G. and Heinze, R. (2019) Impact of resolution and air temperature on large-eddy simulation of mid-latitude summer time convection. *Atmospheric Chemistry and Physics Discussions*, 2019, 1–25. <https://doi.org/10.5194/acp-2019-638>
- Nolan, D.S., Tulich, S.N. and Blanco, J.E. (2016) ITCZ structure as determined by parameterized versus explicit convection in aquachannel and aquapatch simulations. *Journal of Advances in Modeling Earth Systems*, 8(1), 425–452
- Peters, K., Crueger, T., Jakob, C. and Möbis, B. (2017) Improved MJO-simulation in ECHAM 6.3 by coupling a stochastic multi-cloud model to the convection scheme. *Journal of Advances in Modeling Earth Systems*, 9(1), 193–219
- Petersen, W.A. and Rutledge, S.A. (2001) Regional variability in tropical convection: observations from TRMM. *Journal of Climate*, 14(17), 3566–3586
- Price, C., Yair, Y. and Asfur, M. (2007) East African lightning as a precursor of Atlantic hurricane activity. *Geophysical Research Letters*, 34(9)
- Pscheidt, I., Senf, F., Heinze, R., Deneke, H., Trömel, S. and Hohenegger, C. (2019) How organized is deep convection over Germany?. *Quarterly Journal of the Royal Meteorological Society*, 145, 2366–2384. <https://doi.org/10.1002/qj.3552>
- Reed, R.J., Norquist, D.C. and Recker, E.E. (1977) The structure and properties of African wave disturbances as observed during phase III of GATE. *Monthly Weather Review*, 105(3), 317–333
- Reinert, D., Prill, F., Frank, H. and Zängl, G. (2016) Database Reference Manual for ICON and ICON-EPS, version 1.1.9. Research and Development at DWD, Offenbach, Germany.
- Rickenbach, T.M. (2004) Nocturnal cloud systems and the diurnal variation of clouds and rainfall in southwestern Amazonia. *Monthly Weather Review*, 132(5), 1201–1219
- Rickenbach, T.M., Nieto Ferreira, R., Guy, N. and Williams, E. (2009) Radar-observed squall-line propagation and the diurnal cycle of convection in Niamey, Niger, during the 2006 African Monsoon and Multidisciplinary Analyses Intensive Observing Period. *Journal of Geophysical Research: Atmospheres*, 114(D3). <https://doi.org/10.1029/2008JD010871>
- Romatschke, U. and Houze Jr., R.A. (2010) Extreme summer convection in South America. *Journal of Climate*, 23(14), 3761–3791
- Schlüter, A., Fink, A.H., Knippertz, P. and Vogel, P. (2019) A systematic comparison of tropical waves over Northern Africa. Part I: influence on rainfall. *Journal of Climate*, 32(5), 1501–1523. <https://doi.org/10.1175/JCLI-D-18-0173.1>
- Schumacher, C. and Houze Jr., R.A. (2006) Stratiform precipitation production over sub-Saharan Africa and the tropical east Atlantic as observed by TRMM. *Quarterly Journal of the Royal Meteorological Society*, 132, 2235–2255

- Senf, F., Klocke, D. and Brueck, M. (2018) Size-resolved evaluation of simulated deep tropical convection. *Monthly Weather Review*, 146(7), 2161–2182
- Shannon, C.E. (1948) A mathematical theory of communication. *Bell System Technical Journal*, 27(3), 379–423
- Stein, T.H., Holloway, C.E., Tobin, I. and Bony, S. (2017) Observed relationships between cloud vertical structure and convective aggregation over tropical ocean. *Journal of Climate*, 30(6), 2187–2207
- Stevens, B. and Bony, S. (2013) What are climate models missing?. *Science*, 340(6136), 1053–1054
- Tobin, I., Bony, S. and Roca, R. (2012) Observational evidence for relationships between the degree of aggregation of deep convection, water vapor, surface fluxes, and radiation. *Journal of Climate*, 25(20), 6885–6904. <https://doi.org/10.1175/JCLI-D-11-00258.1>
- Tomassini, L. (2018) Mesoscale circulations and organized convection in African easterly waves. *Journal of the Atmospheric Sciences*, 75(12), 4357–4381
- Tompkins, A.M. and Semie, A.G. (2017) Organization of tropical convection in low vertical wind shears: role of updraft entrainment. *Journal of Advances in Modeling Earth Systems*, 9(2), 1046–1068. <https://doi.org/10.1002/2016MS000802>
- Wan, H., Giorgetta, M.A., Zängl, G., Restelli, M., Majewski, D., Bonaventura, L., Fröhlich, K., Reinert, D., Rípodas, P., Kornblueh, L. and Fürstner, J. (2013) The ICON-1.2 hydrostatic atmospheric dynamical core on triangular grids, part I: formulation and performance of the baseline version. *Geoscientific Model Development*, 6, 735–763. <https://doi.org/10.5194/gmd-6-735-2013>
- Weniger, M., Kapp, F. and Friederichs, P. (2017) Spatial verification using wavelet transforms: a review. *Quarterly Journal of the Royal Meteorological Society*, 143, 120–136. <https://doi.org/10.1002/qj.2881>
- White, B.A., Buchanan, A.M., Birch, C.E., Stier, P. and Pearson, K.J. (2018) Quantifying the effects of horizontal grid length and parameterized convection on the degree of convective organization using a metric of the potential for convective interaction. *Journal of the Atmospheric Sciences*, 75(2), 425–450. <https://doi.org/10.1175/JAS-D-16-0307.1>
- Wing, A.A., Emanuel, K.A., Holloway, C.E. and Muller, C. (2017) Convective self-aggregation in numerical simulations: a review. *Surveys in Geophysics*, 38, 1173–1197. <https://doi.org/10.1007/s10712-017-9408-4>
- Xie, S.-P. and Carton, J.A. (2004) Tropical Atlantic variability: patterns, mechanisms, and impacts. *Earth Climate*, 147, 121–142
- Xu, W. and Zipser, E.J. (2012) Properties of deep convection in tropical continental, monsoon, and oceanic rainfall regimes. *Geophysical Research Letters*, 39(7). <https://doi.org/10.1029/2012GL051242>
- Yano, J.-I. and Jakubiak, B. (2016) Wavelet-based verification of the quantitative precipitation forecast. *Dynamics of Atmospheres and Oceans*, 74, 14–29
- Yano, J.-I., Moncrieff, M.W. and Wu, X. (2001a) Wavelet analysis of simulated tropical convective cloud systems. Part II: decomposition of convective-scale and mesoscale structure. *Journal of the Atmospheric Sciences*, 58(8), 868–876
- Yano, J.-I., Moncrieff, M.W., Wu, X. and Yamada, M. (2001b) Wavelet analysis of simulated tropical convective cloud systems. Part I: basic analysis. *Journal of the Atmospheric Sciences*, 58(8), 850–867
- Zängl, G., Reinert, D., Rípodas, P. and Baldauf, M. (2015) The ICON (ICOsapherical Non-hydrostatic) modelling framework of DWD and MPI-M: description of the non-hydrostatic dynamical core. *Quarterly Journal of the Royal Meteorological Society*, 141, 563–579. <https://doi.org/10.1002/qj.2378>
- Zipser, E.J., Cecil, D.J., Liu, C., Nesbitt, S.W. and Yorty, D.P. (2006) Where are the most intense thunderstorms on earth?. *Bulletin of the American Meteorological Society*, 87(8), 1057–1072

How to cite this article: Brune S, Buschow S, Friederichs P. Observations and high-resolution simulations of convective precipitation organization over the tropical Atlantic. *Q.J.R. Meteorol. Soc.* 2020;146:1545–1563. <https://doi.org/10.1002/qj.3751>

The local wavelet-based organization index – Quantification, localization and classification of convective organization from radar and satellite data

Sebastian Brune[✉] | Sebastian Buschow[✉] | Petra Friederichs

Institute of Geosciences, University of Bonn, Bonn, Germany

Correspondence

S. Brune, Institute of Geosciences, University of Bonn, Auf dem Hügel 20, 53121 Bonn, Germany.
 Email: sbrune@uni-bonn.de

Funding information

Bundesministerium für Bildung und Forschung, Grant/Award Number: FKZ01LK1507B; Deutsche Forschungsgemeinschaft, Grant/Award Number: FR 2976/2-1

Abstract

We present a revised local wavelet-based organization index (LW), which is applied to both synthetic fields and meteorological fields of precipitation and brightness temperature for different types of convective organization. The LW consists of three components that describe the scale (LW_{sc}), quantify the intensity (LW_{in}), and analyze the anisotropy (LW_{ai}) of the convection. It is based solely on 2D wavelet decomposition and does not require a clustering algorithm or thresholding. The great advantages of LW are that it localizes the organization in space, is a universally applicable measure of organization and can be calculated with little effort. A comparison with other organizational metrics shows that LW better describes the structure and organization of convection. We analyze the LW components in the vicinity of severe weather reports related to single-cell storms, supercells or multi-cell storms. Composites thereof reveal that large hail and heavy precipitation are particularly local events that lead to small-scale and very intense precipitation. Especially in the case of hail, LW_{ai} shows the structure of a hook echo, which is expected, since hail events are usually associated with supercells. In relation to wind gusts, precipitation is rather large-scale and linearly oriented, since strong wind gusts are often a consequence of linearly organized systems such as squall lines or derechos. The brightness temperature analysis provides similar results to those of the rain rates. Structures like the typical radar hook echo are not visible in the satellite data, but overshooting tops caused by strong updraughts are recognized as small-scale, intense regions. The three LW components are used to classify showers, thunderstorms and precipitation/hail events with the help of a neural network, where showers are mainly classified by their scale characteristics, and precipitation/hail events by their pronounced intensity.

KEY WORDS

convective organization, radar composites, satellite composites, storm structure, wavelet-based organization index

This is an open access article under the terms of the Creative Commons Attribution License, which permits use, distribution and reproduction in any medium, provided the original work is properly cited.

© 2021 The Authors. *Quarterly Journal of the Royal Meteorological Society* published by John Wiley & Sons Ltd on behalf of the Royal Meteorological Society.

1 | INTRODUCTION

Convection and the degree of convective organization play an important role in the global circulation regarding moisture fluxes, energy and momentum transport (Stevens and Bony, 2013). In particular, the representation of convection and its organization in climate or weather prediction models is the subject of current research (e.g., Mapes and Neale, 2011; Birch *et al.*, 2015; Badlan *et al.*, 2017; Moncrieff *et al.*, 2017; Senf *et al.*, 2018; Senf *et al.*, 2019). Therefore the quantification of convective organization becomes important.

Convection may be organized into mesoscale structures by upper-level troughs, fronts or waves like the African Easterly Waves and Madden-Julian Oscillation (e.g., Ricard *et al.*, 2012; Cannon *et al.*, 2018; Xia *et al.*, 2018). Also orography (Imamovic *et al.*, 2019), surface heterogeneity (Lee *et al.*, 2019) and/or cold pools (Haerter *et al.*, 2019) influence the structure of convection. The interaction between convection and wind shear is well known (Rotunno–Klemp–Weisman theory; Rotunno and Klemp, 1982; Weisman and Rotunno, 2004) and leads to different convective storm types. Low-shear conditions result in less organized short-lived local storms such as pulse storms and single cells. Slightly increased wind shear may result in longer-lasting multicell storms, while strong wind shear fosters the evolution of long-lasting storm modes such as supercells or mesoscale convective systems (MCSs; Houze, 2004). All these storm types can become severe and damaging. Local, slow-moving single cells and multicells predominately produce strong precipitation, supercells are often responsible for large hail events, funnels or even tornadoes, and MCSs typically come along with severe wind gusts and/or heavy rainfall (Gallus *et al.*, 2008; Thompson *et al.*, 2012; Groenemeijer *et al.*, 2017).

To measure the aggregation and organization of convection, several convective aggregation/organization indices have been developed during recent years (Table 1). Most measurements have been based on clustering algorithms of different variables such as brightness temperature, outgoing long-wave radiation, vertical wind velocity, precipitation or integrated water vapour. Different (arbitrary) thresholds are used in the object-based analysis to distinguish between convective and non-convective pixels (Table 1). Since each individual index measures the organization in a different way (e.g., using the distance between the objects, their size or their form), Pscheidt *et al.* (2019) recommend the use of several convective organization indices. A few indices depend on the grid structure or are limited to specific regions. Especially the indices which are based on vertical wind velocity are not useful to diagnose convective organization from observable quantities such as satellite or radar data, because

convective updraughts are smaller in scale than their corresponding clouds and rain rates. All object-based indices measure only the averaged convective organization over the selected domain and are not able to localize different organization forms over different regions of the domain.

Recent studies show that spatial structures of clouds and precipitation fields can be successfully analyzed using wavelets (e.g., Yano *et al.*, 2001a; 2001b; Yano and Jakubiak, 2016; Weniger *et al.*, 2017; Kapp *et al.*, 2018; Klein *et al.*, 2018). A variety of properties, namely scale, total energy and direction, may be assessed with a wavelet-based organization index (WOI), which was introduced by Brune *et al.* (2018). The components of WOI characterize spatially averaged measures of scale, intensity and anisotropy. Brune *et al.* (2018) show that WOI performs well in a case-study and may be used to distinguish between unorganized and organized convection.

In Brune *et al.* (2020) a local WOI (LWOI) is used to investigate the scale ($LWOI_{sc}$) and intensity ($LWOI_{in}$) of convection over different parts of the tropical Atlantic. The great advantage of LWOI over convectional indices is the localization of different organization structures. One drawback of $LWOI_{sc}$ is that its definition requires the separation of scales into small and large scales, which introduces a certain arbitrariness. Another shortcoming of LWOI is that the discrete 2D wavelet decomposition is not invariant under rotation. This led to an anisotropy component $LWOI_{ai}$ which was too sensitive to small changes in rotation, and hence is not recommended as an indicator of convective organization.

Several approaches have recently been used in the literature to classify the type of weather event. Garcia *et al.* (2015) use a scattering wavelet transform to classify 1,239 images from a single radar into the hand-labelled classes “rain”, “shower”, “organized storm” and “unorganized storm”. A similarly hand-labelled set of 260 precipitation forecasts was used for pixel-by-pixel classification into “scattered” and “continuous” precipitation by Hamidi *et al.* (2020). These authors relied on texture indicators and a random forest algorithm. Jergensen *et al.* (2020) considered a very large dataset of 123,387 weather events observed in the contiguous United States. They fed up to 341 model variables into several machine-learning algorithms to predict supercells, disorganized precipitation and quasi-linear convective systems.

This study presents a revised version of the local wavelet-based organization index, denoted as LW. The shortcomings of WOI and LWOI have been addressed, and the index has been brought to a maturity that allows convective organization to be studied in terms of scale, intensity, and orientation. We demonstrate the performance of LW on synthetic fields and show the advantages of LW over the conventional object-based organization

TABLE 1 Overview of some convective organization measures and their references

Name		Variable and threshold	Reference
AF1	Ascending fraction	Vertical velocity at 500 hPa	Bao <i>et al.</i> (2017)
AF2	Ascending fraction	Upward mass-weighted vertical integral of vertical velocity	Bao <i>et al.</i> (2017)
ARH	Averaged relative humidity	Vertical-averaged relative humidity	Bao <i>et al.</i> (2017)
CAI	Convective Aggregation Index	>99th percentile precipitation	Pendergrass <i>et al.</i> (2016)
COP	Convective organization potential	Outgoing long-wave radiation	White <i>et al.</i> (2018)
H	Information entropy of convective occurrence	Brightness temperature <245 K and <205 K inside cores	Sullivan <i>et al.</i> (2019)
I _{org}	Organization Index	Vertical velocity >1 m·s ⁻¹ at 730 hPa	Tompkins and Semie (2017)
I _{org}	Organization Index	Hourly averaged vertical velocity >0.5 m·s ⁻¹ at 500 hPa	Cronin and Wing (2017)
I _{org}	Organization Index	Cloud-top temperature <235 K	Cronin and Wing (2017)
I _{org}	Organization Index	Outgoing long-wave radiation <173 W·m ⁻²	Wing <i>et al.</i> (2018)
I _{shape}	2D shape index	Radar reflectivity ≥30 dBZ	Pscheidt <i>et al.</i> (2019)
I _{shape}	2D shape index	Brightness temperature ≤240 K	Pscheidt <i>et al.</i> (2019)
LWOI	Local Wavelet-based Organization Index	Rain rate	Brune <i>et al.</i> (2020)
MICA	Morphological Index of Convective Aggregation	Brightness temperature <240 K	Kadoya and Masunaga (2018)
ROME	Radar Organization Metric	Radar reflectivity >40 dBZ	Retsch <i>et al.</i> (2020)
S _λ (P)	Zonal convective clustering	Precipitation between 6°S and 6°N	Popp and Bony (2019)
SCAI	Simple Convective Aggregation Index	Brightness temperature <240 K	Tobin <i>et al.</i> (2012; 2013)
SCAI	Simple Convective Aggregation Index	95th percentile daily precipitation	Bao <i>et al.</i> (2017)
SCAIP	Simple Convective Aggregation Index Precipitation	Precipitation >1.49 mm·day ⁻¹	Holloway (2017)
SF	Subsiding fraction	Large-scale vertical velocity at 500 hPa	Coppin and Bony (2015)
WOI	Wavelet-based Organization Index	Rain rate	Brune <i>et al.</i> (2018)
α	Degree of aggregation	Integrated water vapour variance	Lebsack <i>et al.</i> (2017)

indices. Then LW is used to study the local convective organization of showers and thunderstorms. We combine the convective organization from a dense radar network (RADKLIM) and high-resolution brightness temperatures with about 26,000 damaging severe weather reports and nearly 150,000 convective event reports over Germany over almost two decades (2001–2018) and investigate which degrees of convective organization are associated with

damage reports. We also apply LW to the brightness temperatures and show that the applicability of LW is not limited to rain rates. Finally, we classify the type of weather event based on LW via a neural network.

This article is structured as follows. In Section 2 we describe the radar and satellite data, as well as the reports on weather and severe weather. Section 3 gives an overview of the methods including Dual-tree complex

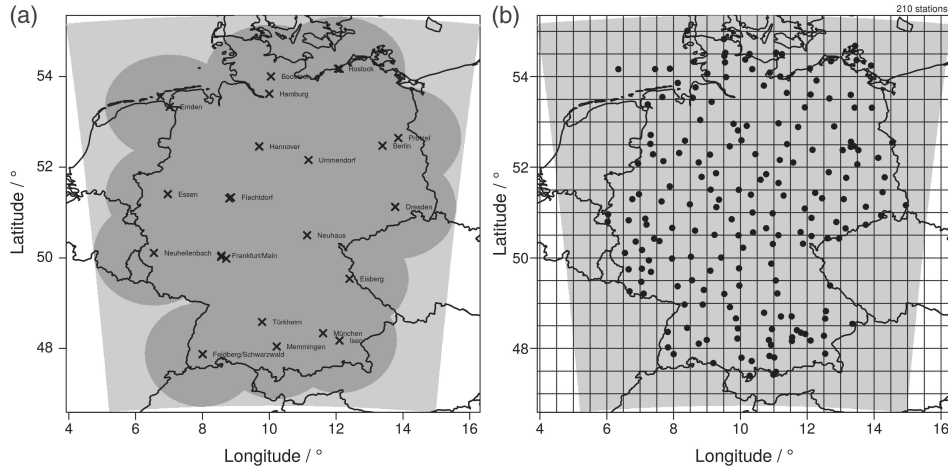


FIGURE 1 (a) Radar positions (black crosses), radar coverage (dark grey area) and $805 \times 1,005$ domain (light grey area). (b) 210 manned SYNOP stations (black dots) and ERA-Interim grid (black lines) over the domain (light grey area)

wavelet transforms and the revised LW. At the beginning of Section 4 we apply LW on constructed fields and compare LW to other convective organization indices. Then we study case-studies of a supercell and a squall line and analyze the general spatial structure of different convective weather events with help of LW composites. At the end of Section 4 we use machine learning to classify these events solely on the basis of LW. We conclude the study with a summary and additional remarks in Section 5.

2 | DATA

2.1 | RADKLIM dataset

The nationwide calibrated rain rate composite RADKLIM (Winterrath *et al.*, 2018) was published by the German meteorological service, Deutscher Wetterdienst (DWD), and is based on the RADOLAN method which combines radar data with rain gauge measurements. The reflectivity of all 17 C-band radars in Germany is corrected for radar-specific errors such as clutter, reduction effects, shading or increasing scan volumes (Winterrath *et al.*, 2019). The application of these climatological corrections ensures that RADKLIM is a consistent dataset of radar-based precipitation estimates. Figure 1(a) shows the radar positions between 2001 and 2018. The radar composite (dark grey area) covers Germany and surrounding countries on a 1×1 km grid and is available every 5 min from 01 January 2001 to 31 December 2018. Some radar locations changed during the period (e.g., Emden, Frankfurt, Flechtdorf). The domain we use consists of $805 \times 1,005$ grid points (light grey area in Figure 1a), which

is padded with zeros at the boundaries to obtain an array of size $1,024 \times 1,024$ for the wavelet transform (Section 3.3). RADKLIM contains missing values due to radar failure, maintenance and software updates or artefacts such as beam blockage. However, thanks to the quality control and high temporal and spatial resolution of the rain rates, the dataset should be suitable to study the convective organization over the last two decades.

2.2 | Satellite dataset

We also use half-hourly infrared brightness temperatures merged from the European (METEOSAT), Japanese (GMS, MT-Sat-1R, Himawari-8) and U.S. geostationary satellites (GOES) between 2001 and 2018. Details on the freely available dataset¹ are provided in Janowiak *et al.* (2017). The dataset covers the region between 60° S and 60° N with a horizontal resolution of approximately 4 km. The data contain missing values due to zenith angle corrections, especially at high latitudes. Beam blockages behind deep vertical clouds with high cloud tops in the Northern Hemisphere result in missing values north of the intense convection. These missing values are set to a distance-weighted average to get a complete dataset, which is required to perform the wavelet transform. Other issues such as the parallax effect are not considered in this study. Bieliński (2020) showed that the parallax effect is about 8–10 km in Northern Germany for deep convective clouds, which corresponds to a shift of only one or two pixels in

¹https://disc.gsfc.nasa.gov/datasets/GPM_MERGIR_1/summary;
accessed 12 February 2021.

TABLE 2 Total number of rain showers and thunderstorms reported by manned weather stations (SYNOP) and all severe weather reports of severe precipitation and hail events in ESWD between 01 January 2001 and 31 December 2018

Class	Controlled	Database	Description
Shower	169,371	SYNOP	Rain shower at SYNOP station of DWD
Thunderstorm	32,004	SYNOP	Audible thunder at SYNOP station of DWD
PRECIP	3,693	ESWD	Report of severe precipitation (e.g., flooding)
HAIL	1,987	ESWD	Report of large hail (≥ 2 cm) or hail accumulation
precip_hail	5,680	ESWD	PRECIP+HAIL

Note: Only quality- and time-controlled ESWD reports are listed. SYNOP reports are assumed to be exact in place and time. Precipitation and hail events together form the precip_hail class.

the satellite image. After downloading the data, we select a box covering longitudes 0.00–18.61 °E and latitudes 40.00–58.60 °N. The extracted domain of 512×512 grid points covers Central Europe and the wavelet transform can be directly applied to this quadratic domain.

2.3 | ERA-Interim

Convection in Central Europe is often embedded in a southwesterly flow, with the consequence that convective cells move to the northeast (e.g., Weijenborg *et al.*, 2015). For the analysis of cell composites, it is necessary to rotate the convective cells along the movement direction, which is often given by the main synoptic flow. We use the 10 m and 500 hPa wind field of the ERA-Interim reanalyses (Dee *et al.*, 2011) from the European Centre for Medium-Range Weather Forecasts (ECMWF) to adjust the cells along the wind shear vector between the 500 hPa level and the surface. ERA-Interim is freely available² and has a horizontal resolution of approximately 80 km ($0.75^\circ \times 0.75^\circ$). The global ERA-Interim dataset covers the complete period between 2001 and 2018 with a temporal resolution of six hours (0000, 0600, 1200, 1800 UTC). In between (0300, 0900, 1500, 2100 UTC), short-term forecasts are provided.

2.4 | SYNOP stations

The DWD observes the present weather every hour according to the convention of the World Meteorological Organization WMO (1992) at its synoptic stations in Germany. These so-called SYNOP reports report on the current weather situation and the weather within the last hour. Report of special events such as thunderstorms are

given immediately. We use SYNOP reports at 210 manned stations shown in Figure 1(b). Because these are official reports at fixed stations, we assume that the SYNOP reports have no errors in either place or time. Until the end of 2018, some of the manned stations were replaced by automatic stations. Reports of automatic stations are not considered due to different shower and thunderstorm criteria. Between 2001 and 2018 there were 169,371 showers reported at manned stations, and thunderstorms occurred 32,004 times (Table 2).

2.5 | European Severe Weather Database (ESWD)

Additionally, we use reports on convective storms from the quality-controlled European Severe Weather Database (ESWD)³. The ESWD database contains only those significant weather events that threaten people or may cause damage. Incoming reports are plausibility checked (QC0+), confirmed and documented by a reliable source such as storm spotters (QC1) or when extra work has been performed to validate the report (QC2). Details on the database are given in Dotzek *et al.* (2009) and Groenemeijer and Kühne (2014).

The database has been in existence since 2008, but many reports have been added retroactively. Our dataset consists of 23,790 reports over Germany until 31 December 2018 including 6,447 heavy precipitation events (PRECIP) and 4,111 hail events with hail diameter ≥ 2 cm (HAIL). Other reports such as severe wind or tornado reports do not necessarily come along with rainfall or low brightness temperatures and are discarded in this study. Each precipitation and hail report comprises information on the longitude, latitude and time, precisely to the minute. The reports may be displaced in space and/or time. Thus, most reports contain information on time uncertainty. To

²<https://www.ecmwf.int/en/forecasts/datasets/reanalysis-datasets/era-interim>; accessed 12 February 2021.

³<https://www.eswd.eu/>; accessed 12 February 2021.

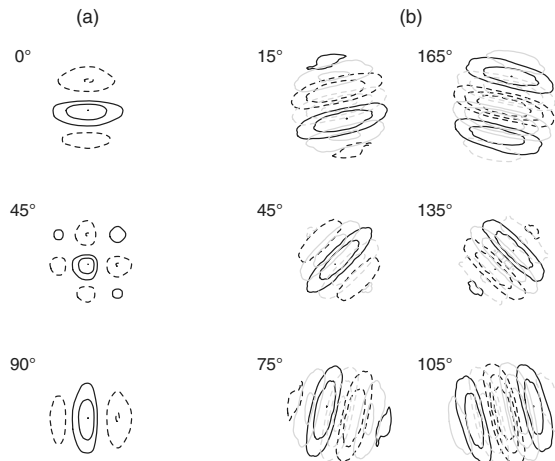


FIGURE 2 Directed daughter wavelets for (a) the Daubechies 4 DWT used in Brune *et al.* (2020) and (b) the DTWCT used in this paper. Solid and dashed contours mark the positive and negative phase; grey lines in (b) show the imaginary part

exclude events which are relatively uncertain in time and not completely reliable, we use only reports with a time uncertainty of less than one hour and quality-checked data with QC1 or QC2. About half of the reports meet these criteria (Table 2).

3 | METHODS

3.1 | Dual-tree complex wavelet transforms (DTCWT)

The essential improvement of the LW compared to the LWOI results from the change of the wavelet transformation, which for LW is the so-called Dual-tree complex wavelet transforms (DTCWT). Like the discrete wavelet transform (DWT) used for LWOI, the DTWCT consists of projecting a two-dimensional field onto a series of new basis functions with limited support in space and frequency. These so-called daughter wavelets are obtained from a single mother wavelet $\psi(x, y)$ via shifts ($\psi_u(x, y) = \psi(x - u_x, y - u_y)$), scaling ($\psi_j(x, y) = \psi(2^{-j}x, 2^{-j}y)$) and changes in orientation. The DWT's poor directional properties stem from its use of only three distinct orientations, namely 0° , 90° and $\pm 45^\circ$ (Figure 2a). We therefore replace the real-valued ψ by a complex function $\psi_c = \psi_r + i\psi_i$ according to Kingsbury (1999), where ψ_r and ψ_i are essentially phase-shifted versions of each other. As shown in Figure 2b, the resulting daughter wavelets have six well-defined directions $\{15^\circ, 45^\circ, 75^\circ, 105^\circ, 135^\circ, 165^\circ\}$. Combined with the slightly modified treatment of the

diagonal directions as introduced by Kingsbury (2006), the wavelet transform is almost invariant to rotation. For an introduction and a comprehensive discussion of the benefits of the DTCWT, the reader is referred to Selesnick *et al.* (2005).

We use the redundant version of the DTCWT, where the daughter wavelets are shifted to any discrete location (x, y) for all directions $d \in \{1, \dots, 6\}$ and scales $j \in \{1, \dots, J\}$, since we want to analyze the local degree of convective organization at each grid point. We denote the squared modulus of the corresponding complex coefficient as local spectral energy $E_{j,d}(x, y)$. Nelson *et al.* (2018) extended the theory of locally stationary wavelet processes (Eckley *et al.*, 2010) to the case of the DTCWT and formulated the necessary bias correction for the local energies, which removes unwanted overemphasis on the very large scales. The complete redundant DTCWT including the bias correction is implemented in the `dualtrees` R-package (Buschow *et al.*, 2020).

3.2 | The revised local wavelet-based organization index (LW)

Like its predecessor, LW has three components representing the dominant scale, LW_{sc} , the intensity, LW_{in} , and the anisotropy, LW_{ai} . Let $E(x, y) = \sum_{j,d=1}^{J,6} E_{j,d}(x, y)$ be the total bias-corrected energy at a given grid point. We define the normalized energy of scale j as $e_j(x, y) = \frac{1}{6} \sum_{d=1}^6 E_{j,d}(x, y)/E(x, y)$. Analogously, the normalized energy of direction d is $e_d(x, y) = \frac{1}{J} \sum_{j=1}^J E_{j,d}(x, y)/E(x, y)$.

To define the index of local scales LW_{sc} , we place e_j along a line so that the position of the energy of the j th scale is j , and calculate the centre of mass. With the use of the so-called central scale, as introduced by Buschow *et al.* (2019), it is no longer necessary to define in advance which scales are considered large or small. By using the central scale, LW_{sc} now also reacts to the redistribution of energy within the small or large scales, which was not the case with $LWOI_{sc}$.

Let us now extend the idea of a central scale to two dimensions and define an index for the anisotropy $LW_{ai}(x, y)$. We place the energy of the six directions $e_d(x, y)$ at equal distances along a circle with radius 1 (Figure 3). The vector pointing from the centre of the circle to the centre of mass has two components, $LW_u(x, y)$ and $LW_v(x, y)$. The degree of anisotropy at location (x, y) is defined by the distance to the centre $\sqrt{LW_u^2 + LW_v^2}$. The angle $\theta = \arctan 2(LW_v, LW_u)$ allows us to estimate the dominant direction at the location.

The intensity component $LW_{in}(x, y)$ is based on the total spectral energy $E(x, y)$ and mainly related to the total variability of the variable in space. Its definition is the same

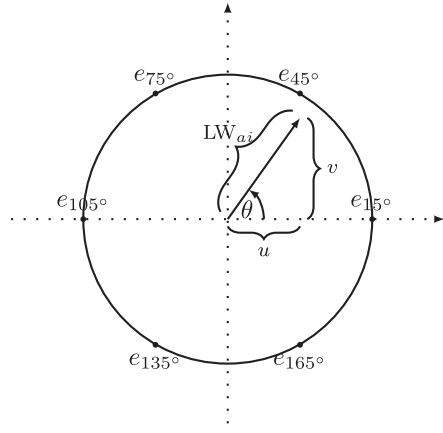


FIGURE 3 Calculation of LW_{ai}

as in Brune *et al.* (2020). In summary, the components of LW are defined as follows:

$$LW_{sc}(x, y) = \frac{1}{J-1} \left(-1 + \sum_{j=1}^J e_j(x, y) \cdot j \right), \quad (1)$$

$$LW_{in}(x, y) = 1 - \exp \{ -E(x, y) \}, \quad (2)$$

$$LW_{ai}(x, y) = \sqrt{LW_u(x, y)^2 + LW_v(x, y)^2}. \quad (3)$$

All three LW components are normalized to the interval $[0, 1]$. Their calculation is included in the latest version of the `calcWOI` R-package (Brune *et al.*, 2019).

3.3 | LW calculation of RADKLIM and satellite data

The two-dimensional wavelet transformation is applied to quadratic fields of $2^n \times 2^n$, $n \in \mathbb{N}$ with periodic boundaries. The non-rectangular domain of the radar composite (Figure 1a) allows neither mirroring of the data at the boundaries as done in Brune *et al.* (2018) nor a linear filtering at the boundaries as used in Brune *et al.* (2020).

For RADKLIM, we add zeros around the $805 \times 1,005$ grid point domain to obtain a $1,024 \times 1,024$ field. Missing values in RADKLIM are set to 0. This may introduce additional gradients in the rain rates at the edge of a radar or around regions with missing data and, since wavelet transformation is sensitive to such gradients, the results may be distorted at the boundaries. For this reason, reports that are close to the edge of the radar composite are not

considered in the later analysis. We calculate LW over the complete domain at each time step with a shower or thunderstorm at a SYNOP station or a precipitation or hail report in the ESWD data. In regions where rain rates are below $0.1 \text{ mm}\cdot\text{hr}^{-1}$, the components of LW are set to ‘not available’. To ensure that the radar image is directly linked to the report, we select the closest radar time step. Since RADKLIM is available every 5 min, the time shift between the reports is not more than 3 min.

For brightness temperatures we calculate LW directly on a square grid with 512×512 points. The region relevant for us is located at the centre of the domain and is therefore surrounded by many grid points, so the influence of the boundaries is small. In the absence of clouds, the brightness temperature essentially measures the temperature of the ground. This leads to strong signals from regions with high surface temperature gradients, for example, in the Alps or between land and sea. We therefore follow Sullivan *et al.* (2019) and introduce a threshold of 245 K to remove the higher surface temperatures, that is, brightness temperatures above 245 K are set to 245 K before applying the wavelet transform. After applying the wavelet transform, pixels with a brightness temperature of 245 K are marked as ‘not available’ and are not used for further analysis. Similar to RADKLIM, we choose the closest time step of the satellite data, resulting in a time offset of at most 15 min.

3.4 | Composites

The composites are calculated for an environment of 25 grid points in each direction from the location of the SYNOP or severe weather report. The resulting cell composites consist of 51×51 grid points (i.e., approximately 51×51 km for the radar composites and 204×204 km for the satellite composites) with the report location centred in the middle. This area should cover the region of main convective activity, for example, strong updraughts with heavy rainfall or deep convective clouds with overshooting tops. Situations where not all surrounding 25 grid points are within the radar coverage are not included in the analysis. We rotate the individual images along the wind shear vector between 500 hPa and 10 m at the central grid point. We assume that the convective storms are embedded in the mean synoptic flow, which is represented by the direction of the wind shear (Kirkpatrick *et al.*, 2007). Thus the images are rotated so that the wind shear vector points from left to right. Note that the direction of movement of a convective cell may be rotated by up to 20° – 30° with respect to the direction of the wind shear. Maddox (1976) and Davies and Johns (1993) noted that supercells, in particular, have their own dynamics and their direction of motion can deviate to the right as well as to the left from

the direction of the shear vector. Deviations from our simple assumption that the cells move along the direction of the 500 hPa wind shear will introduce noise into the composites, which will only reduce the significance in the statistical tests.

We test the hypothesis that the mean value of the time series at a particular pixel is equal to the mean over all pixels and all 12 classes shown in Table 2. Thus Student *t*-tests were performed at each location individually; regions where the null hypothesis was not rejected at $p=1\%$ are marked accordingly in the plots of our composites (Section 4.3). For LW_{in} , which has a strongly non-normal distribution due to the point-mass at 1, the tests were preformed on the logarithm of the time series.

LW_{ai} represents a special case; because we are primarily interested in the existence of coherent directional structures in the data, we first average the two directional components LW_u and LW_v (cf. Figure 3) over time and then calculate the composite of LW_{ai} according to Equation (3). Due to the quadratic form of the definition, the result is not identical to the average over the instantaneous values of LW_{ai} . By first averaging LW_u and LW_v , we allow randomly oriented objects to average out, leaving us with a composite representing the degree to which a *specific* direction dominates the local structure. This is perfectly analogous to the difference between the average absolute wind speed and the absolute value of the average wind vector. These directions are well defined due to the shear-based rotation of the individual images. To assess significance, we test LW_u and LW_v individually and visually mark regions where one or both of the hypothesis tests rejected the null hypothesis at $p=1\%$.

4 | RESULTS

4.1 | LW for idealized fields

We start with an investigation of the behaviour of the three LW components – scale (LW_{sc}), intensity (LW_{in}) and anisotropy (LW_{ai}) – for idealized images. Figure 4 shows different constructed objects that represent changes in size, intensity and anisotropy. All images have a size of 64×64 grid points. The images are padded with zeros to obtain an array of size 512×512 . The LW components as shown in Figure 4d,h,l are spatial averages over the grid points with rain.

A single pixel with rain is the smallest possible object in the domain and is characterized by $LW_{sc} \approx 0$. LW_{sc} increases with the size of the object and is around 0.5 for an object of size 16×16 . For an object that covers a quarter of the total domain, LW_{sc} reaches 0.7. The intensity is around 0.15 for all different object sizes, because the rain rates are

a constant $10 \text{ mm}\cdot\text{hr}^{-1}$ inside the squares and $0 \text{ mm}\cdot\text{hr}^{-1}$ outside. Anisotropy is close to 0 for a very small square, since the object is almost circular. The horizontal and vertical gradients along the sides of larger squares induce a slight increase in the anisotropy index LW_{ai} .

If we increase the rain rates for all pixels inside the square from 1 to $32 \text{ mm}\cdot\text{hr}^{-1}$, the intensity component LW_{in} increases monotonically from 0 for weak intensities up to 0.8 for strong rainfall. The reason for this increase is that LW_{in} is sensitive to spatial gradients, not the strength of the rainfall itself. Scale and anisotropy remain constant, if the size of the squares does not change.

To investigate the behaviour of LW_{ai} , we reduce the width of the object continuously from 32 to 1 grid point. The intensity remains at $10 \text{ mm}\cdot\text{hr}^{-1}$. The scale in the *x*-direction changes from large to very small, which results in a decreasing LW_{sc} . The gradients between no rain and $10 \text{ mm}\cdot\text{hr}^{-1}$ along the left and right side of the objects remain the same, so that LW_{in} is almost constant. The anisotropy component LW_{ai} for the large square is relatively small (below 0.2). Reducing the extent in the *x*-direction leads to higher anisotropy. For a rectangle of size 16×32 , LW_{ai} is around 0.4; the anisotropy of a sharp line is even higher (0.6).

Conventional convection indices such as the simple convective aggregation index (SCAI; Tobin *et al.*, 2012) or the convective organization potential (COP; White *et al.*, 2018) cannot characterize individual objects as shown in Figure 4. Nevertheless, in order to be able to compare LW with SCAI and COP, we have calculated spatial averages of the LW components for eight different cases from Tobin *et al.* (2012) and White *et al.* (2018). The information from the different LW components turns out to be very useful, because LW allows us to distinguish between different structures that have the same SCAI and COP. Details of this comparison are given in the Appendix. On the basis of these encouraging findings, the convective organization of real cases using LW is analyzed in detail below.

4.2 | LW of a supercell and a squall line

We now analyze the spatial structure of convection and its organization during two cases: an isolated supercell west of Bonn in western Germany on 09 June 2014 at 1240 UTC, and a powerful squall line in northwestern Germany on 12 July 2010 at 1230 UTC (Figure 5). The supercell developed within a high-energy air mass and a heavily sheared environment ahead of the 2014 Pentecostal storm over western Germany (Barthlott *et al.*, 2017; Mathias *et al.*, 2017). Details of the squall line and its development can be found in Uebel and Bott (2015).

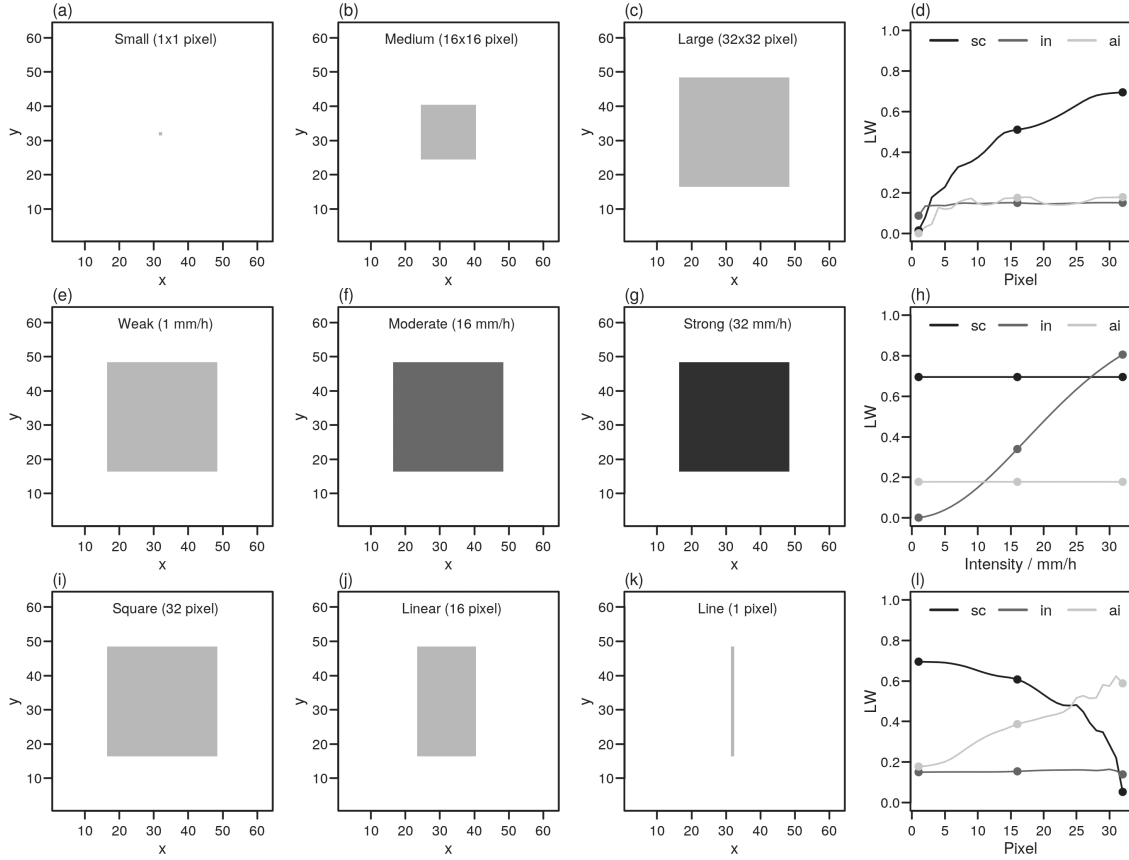


FIGURE 4 (a)–(c) Images of idealized rain images with a small (1×1 pixel), medium (16×16 pixels) and large (32×32 pixels) raining object in a 64×64 plane. All pixels within the squares have the same intensity ($10 \text{ mm} \cdot \text{hr}^{-1}$), and outside the square the intensity is $0 \text{ mm} \cdot \text{hr}^{-1}$. (d) LW components scale (black), intensity (dark grey) and anisotropy (light grey) as a function of the object length. The dots represent LW for the three cases shown in (a)–(c). (e)–(g) Images with equally sized squares with weak ($1 \text{ mm} \cdot \text{hr}^{-1}$), moderate ($16 \text{ mm} \cdot \text{hr}^{-1}$) and strong ($32 \text{ mm} \cdot \text{hr}^{-1}$) rain rates. (h) shows LW components as a function of rain intensity. The dots represent LW for the three cases shown in (e)–(g). (i) Images with 32 pixels of rain in x - and y -directions, (j) a rectangle with 16×32 pixels and (k) a line with 1×32 pixels of the same intensity ($10 \text{ mm} \cdot \text{hr}^{-1}$). (l) shows LW components as a function of object width. The dots represent LW for the three cases shown in (i)–(k)

The supercell on 09 June 2014 is characterized by a sharp and intense hook echo with rain rates above $150 \text{ mm} \cdot \text{hr}^{-1}$. Markowski (2002) provided a review on hook echo structures in radar observations. The hail report was located inside the hook in the region with the strongest rainfall. Rain intensity decreased rapidly from the location of the report to a distance of $10\text{--}15$ km, where rain rates became more uniform and were only about $10 \text{ mm} \cdot \text{hr}^{-1}$. LW_{sc} is about 0.30 around the hook echo and indicates a large amount of small-scale variability in the rain field near the hook. Outside the area with strongest precipitation the scale increases to about 0.55 at the outer bound of the supercell, because rainfall there was more stratiform. The supercell produced very intense rain rates, which results in a high LW_{in} of nearly 1. Slightly less intense precipitation was identified only $20\text{--}25$ km away

from the report with $LW_{in} \approx 0.90$, since the spatial gradients between no rain and rain rates of about $10 \text{ mm} \cdot \text{hr}^{-1}$ were smaller than inside the hook. LW_{ai} increases with the distance from the hook, because small-scale structures in the centre lead to a more isotropic pattern ($LW_{ai} \approx 0.25$). The stratiform rainfall at the edge of the supercell was more orientated with $LW_{ai} \approx 0.50$. The direction follows the hook echo and is parallel to the shear vector in the stratiform region and crosses the wind vector in the centre.

The intensity of the precipitation along the squall line was slightly weaker ($100 \text{ mm} \cdot \text{hr}^{-1}$) than in the supercell. The highest intensities were located along a line perpendicular to the shear vector. The rainfall behind the squall line was less intense and more uniform (high LW_{sc}). Local precipitation maxima along the squall line are characterized as smaller in scale, because the spatial variation was

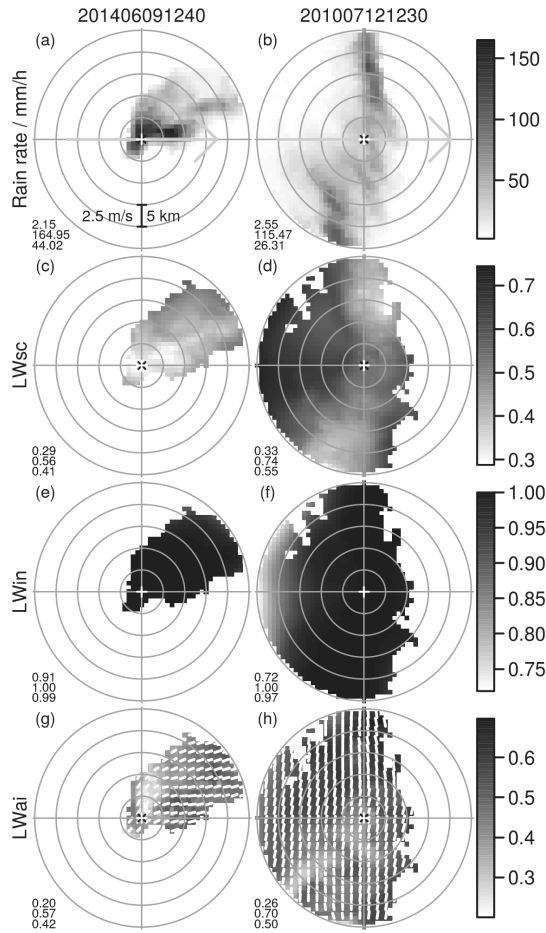


FIGURE 5 (a, b) Observed rain rate by RADKLIM, (c, d) LW_{sc} , (e, f) LW_{in} and (g, h) LW_{ai} of (a, c, e, g) an isolated supercell west of Bonn in western Germany on 09 June 2014 at 1240 UTC and (b, d, f, h) a squall line in northwestern Germany on 12 July 2010 at 1230 UTC. The images are centred around a large hail report in the supercell case and a severe wind gust in the squall line case. Grey circles represent the distance from the centre every 5 km. All the images contain 51×51 pixels, which correspond to $51 \times 51 \text{ km}^2$. The images are rotated along the wind shear vector between 500 hPa and surface from the ERA-Interim reanalyses (grey arrow in (a, b); the distance between two circles corresponds to 2.5 m s^{-1}). Numbers at bottom left show minimum, maximum and spatial mean of the variables. White lines in (g, h) represent the preferred direction obtained from the wavelet spectrum at every second pixel

particularly large in this area. LW_{in} is maximal along the squall line due to the strong gradients between no rainfall in front of the squall line and very high intensities at the leading edge. In the region 20 to 25 km behind the squall line, the stratiform precipitation was weaker and characterized by LW_{in} of about 0.75. We find a distinct

orientation along the squall line perpendicular to the wind shear. LW_{ai} of up to 0.65 detects the most linear segments at the leading edge.

4.3 | Composites of weather events

Figure 6 shows the composites of LW calculated from radar data for SYNOP showers and SYNOP thunderstorms as well as ESWD PRECIP and ESWD HAIL events. All plots are oriented such that the direction of the wind shear is from left to right (arrows in Figure 5). We find that the scale of the rain rates is generally smallest near the report for all LW_{sc} composites. This is in line with the results presented in Steiner *et al.* (1995); in the small-scale convective core (i.e., the centre of the SYNOP shower or thunderstorm) the spatial gradient in precipitation intensity is very large, while outside, in the stratiform area, the precipitation echoes are larger in scale and spatially more homogeneous.

For SYNOP showers and thunderstorms, the area with minimum scale is slightly shifted towards the wind shear. Thus, assuming that the shear vector roughly indicates the direction of cell motion, the spatial scale of a shower or thunderstorm event is smallest right at the beginning of the event. After the onset of the first precipitation, the structures in the radar image become somewhat larger (left region of the composite). SYNOP showers and thunderstorms reveal larger scales than ESWD HAIL and PRECIP with weaker gradients over the area. Thus rain rates related to SYNOP shower and thunderstorm reports act on larger scales and are more uniform in a range of 25 km around the report. This pattern is possibly due to the fact that SYNOP showers and thunderstorms usually come along with relatively uniform rain rates.

In contrast, LW_{sc} is much smaller near the ESWD HAIL and PRECIP events and increases strongly with distance from the observation point. Large hailstones and heavy precipitation usually develop only locally in a severe thunderstorm, for example in a prominent hook echo of a supercell (Figure 5) or within a powerful updraught of a multicell. Another indicator for the occurrence of hail in the vicinity of a supercell is the large-scale precipitation field to the left of the shear vector at a distance of 10 to 20 km from the report (e.g., Kumjian, 2011).

The intensity of rain rates (LW_{in}) is of course highest in the immediate vicinity of ESWD HAIL and PRECIP events. With increasing distance from the event, the rain rate decreases evenly in all directions. This is consistent with the results of Lochbihler *et al.* (2017). They also found that precipitation intensities rapidly decrease radially from the centre of the event. Since the significance tests were performed against all four classes and thus also against the

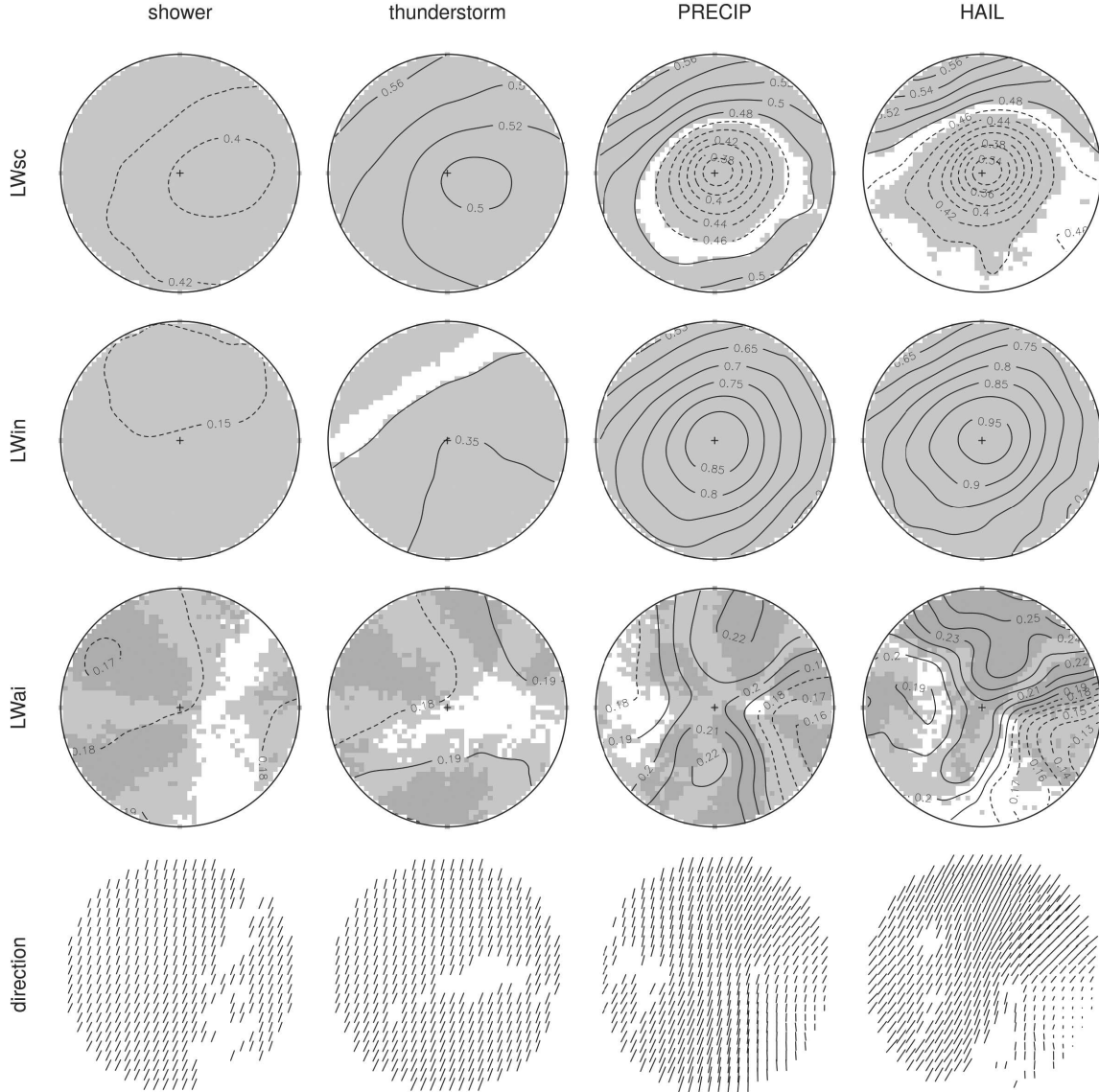


FIGURE 6 From top to bottom, composites of LW_{sc}, LW_{in}, LW_{ai} and the preferred local direction calculated from radar data for shower and thunderstorms of SYNOP stations, and damage reports of precipitation (PRECIP) and hail events (HAIL) in ESWD. The centre of each composite is marked by a black cross and the radius of each circle is 25 km. Solid and dashed contours correspond to values above and below the overall average of the respective variable. The hypothesis that the local values differ from this overall average was rejected at $p = 1\%$ in the grey regions. For LW_{ai}, the light grey region indicates that at least one directional component was significant; both were significant in the dark grey zone (Section 3.4)

many showers (Table 2), the rain rates are also significant for thunderstorms.

The strong anisotropy (LW_{ai}) in the ESWD HAIL composite extends from the large-scale precipitation area to approximately the observation site and somewhat beyond. The predominant direction is from large-scale precipitation to the hail observation site. Although the complete

hook curvature cannot be traced exactly, the anisotropy pattern is significant and fits to the structures described in Markowski (2002). For SYNOP thunderstorms and showers, the anisotropy is lower, so the directional information in the wavelet spectrum is less meaningful. Low anisotropy suggests that the rain rates related to SYNOP showers and thunderstorms have a more rounded shape

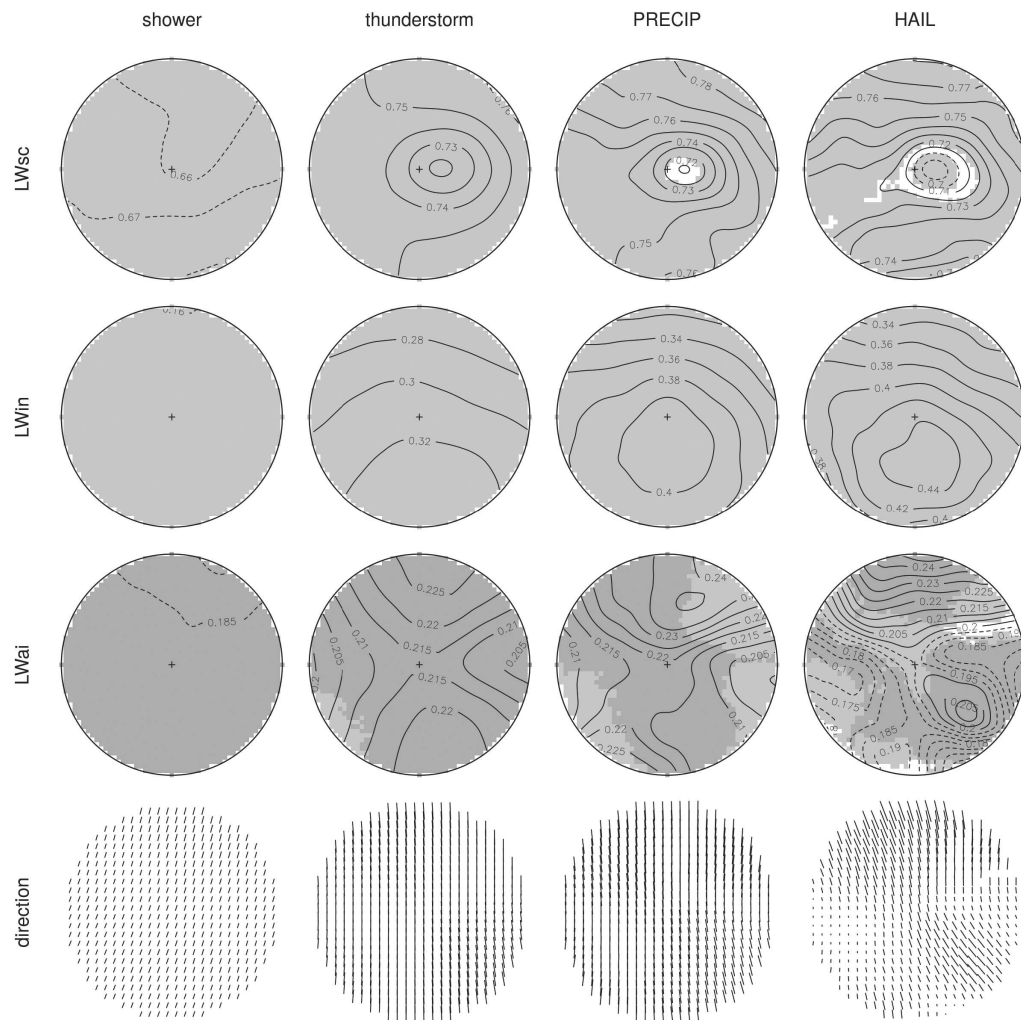


FIGURE 7 As Figure 6, but calculated from brightness temperatures. Circles here have a radius of 100 km, whereas the radius in Figure 6 is 25 km

and, accordingly, rainfall rates do not have a specific direction (case-study in Brune *et al.*, 2018).

The satellite-based composites in Figure 7, which represent both a larger area (100 km versus 25 km) and a different physical quantity (clouds instead of precipitation), reveal a number of interesting differences and similarities. LW_{sc} shows, as with precipitation rates, that the brightness temperature structures around ESWD PRECIP and especially HAIL reports are lower than for SYNOP thunderstorms. We attribute this to the fact that some precipitation and most hail events are associated with strong updraughts, which can be seen in satellite images as overshooting convective cloud tops (e.g., Bedka, 2011; Punge *et al.*, 2017). The overshooting tops lead to small-scale temperature variations at the upper edge of the

cloud, which are detected by LW_{sc}. Showers are generally smaller in scale and show almost no spatial variance in LW_{sc}, because the corresponding satellite images consist of isolated pixels with brightness temperatures below the defined 245 K threshold.

The highest LW_{in} values occur in the case of ESWD PRECIP and HAIL when the brightness temperatures are particularly low. The maxima are shifted about 20 to 30 km from the centre to the right, seen from the shear vector. The shifted position of the LW_{in} maximum could detect the inflow line, which is typically found in this region (Weaver *et al.*, 1994; Mazur *et al.*, 2009; Bedka *et al.*, 2010). For SYNOP thunderstorms and especially showers, LW_{in} does not vary in space. This could be related to the fact that in showers the threshold value of 245 K is only

slightly undercut (Pscheidt *et al.*, 2019) and therefore the spatial variance in brightness temperature is lower than for hail events.

The most striking structures in anisotropy can be found in the brightness temperatures of the powerful updraughts for ESWD HAIL events. As in the rain rate analysis, LW_{ai} is largest to the left of the shear vector. In the case of satellite data, the typical radar hook echo is of course not visible, instead we find a tongue with significantly increased LW_{ai} values extending from the centre to the right side of the shear vector. This tongue is also clearly visible in the direction of the wavelet spectrum. Responsible for this pattern could be the already mentioned inflow line, which is more linear in its orientation at the top compared to the circular and therefore rather isotropic overshoot.

4.4 | Classification of shower and thunderstorms using machine learning

In order to quantify the link between LW and the occurrence of reported weather events, we now attempt to predict the class of the observed event based on the three LW components, averaged over the circular environments shown in Figures 6 and 7. Due to their relatively small number of cases, as well as similarities in the respective LW composites, we combine the two ESWD classes HAIL and PRECIP into a single “precip_hail” class.

The caret R-package (Kuhn, 2020) allows us to easily implement and test a variety of classifier algorithms. In a first step, the labelled dataset is separated into 70% training data, 15% test data for model selection and 15% validation data which is used to assess the final model. Each model is fitted to the training data for a range of appropriate meta parameters in a ten-fold cross-validation procedure. The best version of each model is selected based on the optimal value of the Cohen’s Kappa (Cohen, 1960), that is, the improvement in accuracy over a random classification. Next, each optimized model predicts the probabilities of the three classes in the test data.

Based on these preliminary tests with a variety of linear and nonlinear classifiers (including random forests, linear and quadratic discriminant analysis and others), we select a simple feed-forward neural network with nine nodes in a single hidden layer as the best algorithm for our task. In this simple nonlinear model, nine different intermediate values are computed as linear combinations of the input variables and normalized to unit sum via a soft-max activation function. These nine “nodes” are again linearly re-combined and transformed in the same way to produce probabilities for the three classes. In our case, the optimal weights are found via the Broyden–Fletcher–Goldfarb–Shanno algorithm.

TABLE 3 Brier skill scores of the neural network classifier

	BSS
Everything (radar)	0.44
Everything (satellite)	0.21
No intensity	0.18
No scale	0.34
No anisotropy	0.43

Note: The top two rows corresponds to models using all three indicators from radar or satellite data. The following three rows are based on radar data, where one of the three LW components was left out.

The performance of our selected classifier is summarized by Brier skill scores in Table 3; the climatological frequencies of the classes in the test data serve as the reference forecasts. When all three radar-based LW components are used as input, the model achieves a 44% improvement over the climatology. The skill decreases by roughly 50% when the satellite-based LW is used instead. An even more severe drop in performance occurs when the intensity information is withheld. The scale component appears to be the second most relevant predictor; anisotropy contributes only very little to the overall skill.

Figure 8 shows the predicted class probabilities, averaged over (a) all LW_{ai} and (b) all LW_{in} , together with the occurrence of the three classes in the validation dataset. We find that SYNOP thunderstorms live on larger scales than SYNOP showers, the predicted division line sloping towards smaller scales at higher intensities. Damaging precipitation and hail (ESWD precip_hail) are exclusively predicted in a small region of intermediate scales and extreme intensities ($LW_{in} > 0.75$), although some instances of this class are scattered across the entire point cloud. Larger values of LW_{ai} lead to a preference for showers even at larger scales.

In order to quantify the impact of each individual predictor, we construct partial dependency plots (Figure 9). This simplified visualization confirms that SYNOP showers and thunderstorms are well separated by both intensity and scale while the ESWD “precip_hail” class can only be detected by its intensity. As expected, the anisotropy has only marginal influence on the class probabilities.

For a more detailed look at the final model’s behaviour, we consider several scalar forecast attributes for each of the three classes (Table 4). Unsurprisingly, the majority class “SYNOP shower” was slightly over-forecast (Bias > 1) while having the best hit rate as well as the fewest false alarms. The “ESWD precip_hail” class has the best overall proportion correct due to many correct negatives. Conversely, SYNOP thunderstorms appear to be hardest to classify and exhibits the worst performance metrics.

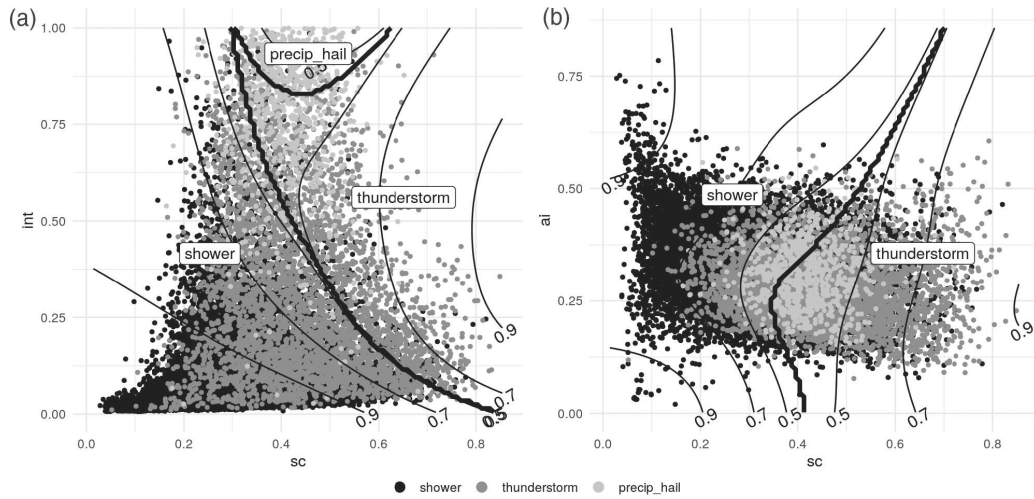


FIGURE 8 Distribution of SYNOP shower, SYNOP thunderstorm and ESWD precipitation or hail events in (a) scale-intensity space and (b) scale-anisotropy space. Thin contours indicate the predicted probabilities of the three classes (starting at $p=0.5$), and thick lines mark the decision boundaries of the neural network classifier

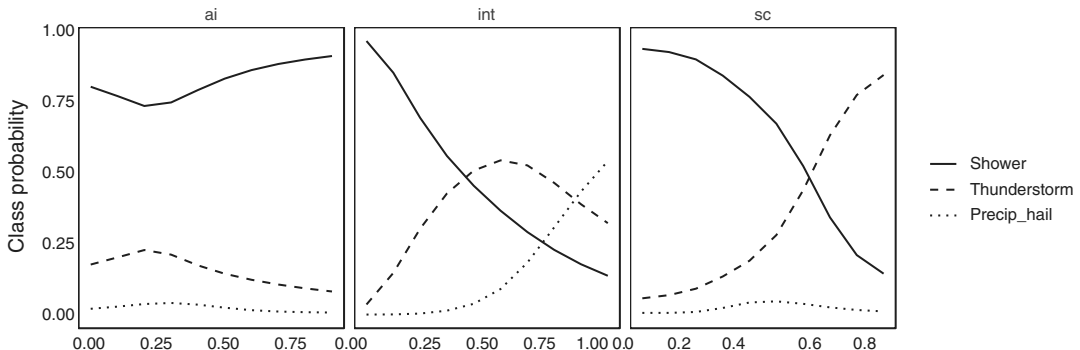


FIGURE 9 Partial dependency plots for the neural network classifier. Each predictor is set to a series of fixed values, leaving the remaining test data unchanged. The predicted class probabilities are averaged over all samples and plotted as a function of the fixed predictor value

	PC	CSI	Bias	FAR	Hit-rate	ETS
Shower	0.88	0.85	1.06	0.10	0.95	0.48
Thunderstorm	0.85	0.44	0.83	0.32	0.56	0.35
Precip_hail	0.97	0.45	0.85	0.33	0.57	0.43

TABLE 4 Proportion correct (PC), critical success index (CSI), bias, false alarm ratio (FAR), hit-rate and equitable threat score (ETS) of the neural network classifier

5 | SUMMARY AND CONCLUDING REMARKS

In this study the convective organization was investigated with the revised local wavelet-based organization index, LW. First, the performance of LW was tested for different types of objects such as squares and lines of different sizes

and intensities. The three components LW_{sc} , LW_{in} and LW_{ai} , which describe the scale, intensity and anisotropy of convection, are able to recognize the structure of the tested forms. A comparison of the spatially averaged LW with the conventional organization indices SCAI (Tobin *et al.*, 2012) and COP (White *et al.*, 2018) shows that LW, thanks to its manifold information, is able to distinguish between forms

of organization that look the same in the eyes of SCAI and COP.

After these first encouraging results, LW was applied to real cases. The databases for our analysis are 1×1 km radar data and 4×4 km satellite observations of brightness temperatures between 2001 and 2018 over Germany. We relate them to convective reports such as showers or thunderstorms reported by weather stations and to severe weather reports such as precipitation or hail provided by the European Severe Weather Database.

Snapshots of two case-studies show that the structures of a supercell are much smaller, can sometimes be more intense and are more isotropic than squall lines. LW is able to identify the small region with hail. LW also detects the larger scale and stronger anisotropy in the stratiform part of the supercell in contrast to the small scale and very intense hook echo. The linear structure of the squall line is characterized by large anisotropy, which is also clearly found in the direction of the wavelet spectrum.

The analysis of cell composites of the radar-based rain rates confirmed the results from the snapshots: hail events, which mostly occur in combination with supercells, as well as heavy precipitation are very local phenomena (small scale, low LW_{sc}). Both types show very large spatial variability as they are very intense (high LW_{in}) and isotropic (higher LW_{ai}). For hail reports the wavelet spectrum follows the direction of the hook echo.

Since our LW analysis is not based on any threshold values and the only requirement is a complete spatial field of any variable, LW is universally applicable. To illustrate this, we have also investigated the structure of brightness temperatures. The LW analysis led to similar results. In particular, the small-scale overshooting tops in the region of the large anvil could be identified on the basis of scale, intensity and isotropy.

In a final step, we used the organization and structure metrics LW_{sc} , LW_{in} and LW_{ai} to classify showers, thunderstorms and severe precipitation/hail events. We averaged the LW components for each single composite and fitted a variety of classifier algorithms to our data. In cross-validation, a neural network using all three radar-based LW components delivers the best results ($BSS \approx 0.44$ compared to climatology). The winning classifier has learned that showers and thunderstorms act on small and large scales, respectively, whereas precipitation/hail events are mainly distinguished by their extreme intensity. Anisotropy has very little influence on the classification. The skill for the satellite-based LW decreases by almost 50%, indicating that the structure of different precipitation events is more easily discerned based on radar data.

LW also has some limitations: for the calculation of the wavelet spectrum some technical requirements have to be met. The domain should preferably be a square, have a size

of $2^n \times 2^n$, $n \in \mathbb{N}$ with periodic boundary conditions, and should not contain missing values. These criteria are usually not all met at the same time, so compromises have to be made. The boundary conditions for the radar data had no effect in this study, because the observations were mostly far enough inside the domain. More problematic were the missing values in the brightness temperatures due to beam blockage, which were given a spatial average value. These problems could be avoided, for example, by choosing a model area near the Equator or calculating LW for the model output of numerical weather forecasting systems or reanalyses. However, missing values are also a problem for other organization indices.

The mathematical background of the wavelet transformation is not trivial. Therefore, this paper does not deal with wavelet theory in detail, but rather aims to show the benefits of wavelet spectra. Information on scale, intensity, and anisotropy can be obtained from any two-dimensional field with a single wavelet transformation. To provide easy access to LW and to apply LW to your own datasets, the R-package `calcWOI` is provided free.

LW is not only a supplement to the many different organizational indices, but combines many features of the individual metrics in the literature. We do not need cluster analysis or well-considered thresholds, but can apply LW directly to two-dimensional fields of any variable. This makes LW universally applicable. The strength of LW, which distinguishes it from all others, is the exact localization of the organization. LW is the first index that displays convective organization on a 2D map.

In this study we identified significant patterns in the radar and satellite observations using LW such as hook echoes, inflow lines, overshooting tops or linear structures. It would be interesting to see whether these results could be confirmed in other studies based on larger datasets and in other regions. LW offers a great opportunity to study climatologies of convective organization. This could lead to new parametrizations of convection and its organization to improve representation in weather and climate prediction models.

ACKNOWLEDGMENTS

We gratefully acknowledge financial funding by the project High Definition Clouds and Precipitation for Advancing Climate Prediction HD(CP)², funded by the German Ministry for Education and Research (BMBF) under the grant FKZ01LK1507B (Sebastian Brune). Sebastian Buschow was supported by the DFG under grant no. FR 2976/2-1. Open Access funding was enabled and organized by Projekt DEAL via the Rheinische Friedrich-Wilhelms-Universität Bonn. We would like to thank the European Severe Storms Laboratory (ESSL) for providing the severe weather reports. We are also very

grateful to two anonymous reviewers for their constructive comments on an earlier version of the article. Open Access funding enabled and organized by Projekt DEAL.

ORCID

Sebastian Brune  <https://orcid.org/0000-0002-3742-4443>
 Sebastian Buschow  <https://orcid.org/0000-0003-4750-361X>

REFERENCES

- Badlan, R.L., Lane, T.P., Moncrieff, M.W. and Jakob, C. (2017) Insights into convective momentum transport and its parametrization from idealized simulations of organized convection. *Quarterly Journal of the Royal Meteorological Society*, 143, 2687–2702.
- Bao, J., Sherwood, S.C., Colin, M. and Dixit, V. (2017) The robust relationship between extreme precipitation and convective organization in idealized numerical modeling simulations. *Journal of Advances in Modeling Earth Systems*, 9, 2291–2303.
- Barthlott, C., Mühr, B. and Hoose, C. (2017) Sensitivity of the 2014 Pentecost storms over Germany to different model grids and microphysics schemes. *Quarterly Journal of the Royal Meteorological Society*, 143, 1485–1503.
- Bedka, K., Brunner, J., Dworak, R., Feltz, W., Otkin, J. and Greenwald, T. (2010) Objective satellite-based detection of overshooting tops using infrared window channel brightness temperature gradients. *Journal of Applied Meteorology and Climatology*, 49, 181–202. <https://doi.org/10.1175/2009JAMC2286.1>.
- Bedka, K.M. (2011) Overshooting cloud-top detections using MSG SEVIRI infrared brightness temperatures and their relationship to severe weather over Europe. *Atmospheric Research*, 99, 175–189.
- Bielinski, T. (2020) A parallax shift effect correction based on cloud height for geostationary satellites and radar observations. *Remote Sensing*, 12, 365.
- Birch, C.E., Roberts, M.J., Garcia-Carreras, L., Ackerley, D., Reeder, M.J., Lock, A.P. and Schiemann, R. (2015) Sea-breeze dynamics and convection initiation: the influence of convective parameterization in weather and climate model biases. *Journal of Climate*, 28, 8093–8108.
- Brune, S., Kapp, F. and Friederichs, P. (2018) A wavelet-based analysis of convective organization in ICON large-eddy simulations. *Quarterly Journal of the Royal Meteorological Society*, 144, 2812–2829.
- Brune, S., Buschow, S., Kapp, F. and Friederichs, P. (2019) calcWOI-package: calculates the wavelet-based organization index. <https://rdrr.io/cran/calcWOI/man/calcWOI-package.html>; accessed 12 February 2021.
- Brune, S., Buschow, S. and Friederichs, P. (2020) Observations and high-resolution simulations of convective precipitation organization over the tropical Atlantic. *Quarterly Journal of the Royal Meteorological Society*, 146, 1545–1563. <https://doi.org/10.1002/qj.3751>.
- Buschow, S., Pidstrigach, J. and Friederichs, P. (2019) Assessment of wavelet-based spatial verification by means of a stochastic precipitation model (wv_verif v0.1.0). *Geoscientific Model Development*, 12(8), 3401–3418. <https://doi.org/10.5194/gmd-12-3401-2019>.
- Buschow, S., Kingsbury, N. and Wareham, R. (2020) dualtrees: decimated and undecimated 2D complex dual-tree wavelet transform. <https://cran.r-project.org/web/packages/dualtrees/index.html>; accessed 12 February 2021.
- Cannon, F., Hecht, C.W., Cordeira, J.M. and Ralph, F.M. (2018) Synoptic and mesoscale forcing of southern California extreme precipitation. *Journal of Geophysical Research: Atmospheres*, 123, 13–714.
- Cohen, J. (1960) A coefficient of agreement for nominal scales. *Educational and Psychological Measurement*, 20(1), 37–46. <https://doi.org/10.1177/001316446002000104>.
- Coppin, D. and Bony, S. (2015) Physical mechanisms controlling the initiation of convective self-aggregation in a general circulation model. *Journal of Advances in Modeling Earth Systems*, 7, 2060–2078.
- Cronin, T.W. and Wing, A.A. (2017) Clouds, circulation, and climate sensitivity in a radiative-convective equilibrium channel model. *Journal of Advances in Modeling Earth Systems*, 9, 2883–2905.
- Davies, J.M. and Johns, R.H. (1993) Some wind and instability parameters associated with strong and violent tornadoes: 1. Wind shear and helicity. In: *The Tornado: its structure, dynamics, prediction, and hazards*, Washington, DC: American Geophysical Union, pp. 573–582.
- Dee, D.P., Uppala, S.M., Simmons, A.J., Berrisford, P., Poli, P., Kobayashi, S., Andrae, U., Balmaseda, M.A., Balsamo, G., Bauer, P., Bechtold, P., Beljaars, A.C.M., van de Berg, L., Bidlot, J., Bormann, N., Delsol, C., Dragani, R., Fuentes, M., Geer, A.J., Haimberger, L., Healy, S.B., Hersbach, H., Holm, E.V., Isaksen, L., Källberg, P., Köhler, M., Matricardi, M., McNally, A.P., Monge-Sanz, B.M., Morcrette, J.-J., Park, B.-K., Peubey, C., de Rosnay, P., Tavolato, C., Thépaut, J.-N. and Vitart, F. (2011) The ERA-Interim reanalysis: configuration and performance of the data assimilation system. *Quarterly Journal of the Royal Meteorological Society*, 137, 553–597.
- Dotzek, N., Groenemeijer, P., Feuerstein, B. and Holzer, A.M. (2009) Overview of ESSL's severe convective storms research using the European Severe Weather Database, ESWD. *Atmospheric Research*, 93, 575–586.
- Eckley, I.A., Nason, G.P. and Treloar, R.L. (2010) Locally stationary wavelet fields with application to the modelling and analysis of image texture. *Journal of the Royal Statistical Society, Series C*, 59, 595–616.
- Gallus, W.A.Jr., Snook, N.A. and Johnson, E.V. (2008) Spring and summer severe weather reports over the Midwest as a function of convective mode: a preliminary study. *Weather and Forecasting*, 23, 101–113.
- Garcia, G.B., Lagrange, M., Emmanuel, I. and Andrieu, H. (2015) Classification of rainfall radar images using the scattering transform, In: *23rd European Signal Processing Conference (EUSIPCO)*, Piscataway, NJ: IEEE, pp. 1940–1944.
- Groenemeijer, P. and Kühne, T. (2014) A climatology of tornadoes in Europe: results from the European Severe Weather Database. *Monthly Weather Review*, 142(12), 4775–4790. <https://doi.org/10.1175/MWR-D-14-00107.1>.
- Groenemeijer, P., Pucik, T., Holzer, A.M., Antonescu, B., Riemann-Campe, K., Schultz, D.M., Khne, T., Feuerstein, B., Brooks, H.E., Doswell, C.A.III., Koppert, H.-J. and Sausen, R. (2017) Severe convective storms in Europe: ten years of research and education at the European Severe Storms Laboratory. *Bulletin of the American Meteorological Society*, 98, 2641–2651.

- Haerter, J.O., Böing, S.J., Henneberg, O. and Nissen, S.B. (2019) Circling in on convective organization. *Geophysical Research Letters*, 46, 7024–7034.
- Hamidi, Y., Raynaud, L., Rottner, L. and Arbogast, P. (2020) Texture-based classification of high-resolution precipitation forecasts with machine-learning methods. *Quarterly Journal of the Royal Meteorological Society*, 146, 3014–3028. <https://doi.org/10.1002/qj.3823>.
- Holloway, C.E. (2017) Convective aggregation in realistic convective-scale simulations. *Journal of Advances in Modeling Earth Systems*, 9, 1450–1472. <https://doi.org/10.1002/2017MS000980>.
- Houze, R.A. (2004) Mesoscale convective systems. *Reviews of Geophysics*, 42(4). <https://doi.org/10.1029/2004RG000150>.
- Imamovic, A., Schlemmer, L. and Schär, C. (2019) Mountain volume control on deep-convective rain amount during episodes of weak synoptic forcing. *Journal of the Atmospheric Sciences*, 76, 605–626.
- Janowiak, J., Joyce, B. and Xie, P. (2017) *NCEP/CPC L3 half hourly 4 km global (60S–60N) merged IR v1*. Savtchenko, A. (Ed.) Greenbelt, MD: Goddard Earth Sciences Data and Information Services Center. <https://doi.org/10.5067/P4HZB9N27EKU>.
- Jergensen, G.E., McGovern, A., Lagerquist, R. and Smith, T. (2020) Classifying convective storms using machine learning. *Weather and Forecasting*, 35, 537–559.
- Kadoya, T. and Masunaga, H. (2018) New observational metrics of convective self-aggregation: methodology and a case study. *Journal of the Meteorological Society of Japan*, 96, 535–548.
- Kapp, F., Friederichs, P., Brune, S. and Weniger, M. (2018) Spatial verification of high-resolution ensemble precipitation forecasts using local wavelet spectra. *Meteorologische Zeitschrift*, 467–480.
- Kingsbury, N. (1999) Image processing with complex wavelets. *Philosophical Transactions of the Royal Society of London. Series A*, 357, 2543–2560.
- Kingsbury, N. (2006) Rotation-invariant local feature matching with complex wavelets, In: *14th European Signal Processing Conference*, Piscataway, NJ: IEEE, pp. 1–5.
- Kirkpatrick, J.C., McCaul Jr, E.W. and Cohen, C. (2007) The motion of simulated convective storms as a function of basic environmental parameters. *Monthly Weather Review*, 135, 3033–3051.
- Klein, C., Belušić, D. and Taylor, C.M. (2018) Wavelet scale analysis of mesoscale convective systems for detecting deep convection from infrared imagery. *Journal of Geophysical Research: Atmospheres*, 123, 3035–3050.
- Kuhn, M. (2020). caret: Classification and regression training. <https://rdrr.io/cran/caret/>; accessed 12 February 2021.
- Kumjian, M. (2011) Precipitation properties of supercell hook echoes. *E-Journal of Severe Storms Meteorology*, 6(5). <https://ejssm.org/ojs/index.php/ejssm/article/viewArticle/93>; accessed 12 February 2021.
- Lebsack, M.D., L'Ecuyer, T.S. and Pincus, R. (2017) An observational view of relationships between moisture aggregation, cloud, and radiative heating profiles. *Surveys in Geophysics*, 38, 1237–1254.
- Lee, J.M., Zhang, Y. and Klein, S.A. (2019) The effect of land surface heterogeneity and background wind on shallow cumulus clouds and the transition to deeper convection. *Journal of the Atmospheric Sciences*, 76, 401–419.
- Lochbihler, K., Lentink, G. and Siebesma, A.P. (2017) The spatial extent of rainfall events and its relation to precipitation scaling. *Geophysical Research Letters*, 44, 88629–88636. <https://doi.org/10.1002/2017GL074857>.
- Maddox, R.A. (1976) An evaluation of tornado proximity wind and stability data. *Monthly Weather Review*, 104, 133–142.
- Mapes, B. and Neale, R. (2011) Parameterizing convective organization to escape the entrainment dilemma. *Journal of Advances in Modeling Earth Systems*, 3(2). <https://doi.org/10.1029/2011MS000042>.
- Markowski, P.M. (2002) Hook echoes and rear-flank downdrafts: a review. *Monthly Weather Review*, 130, 852–876.
- Mathias, L., Ermert, V., Kelemen, F.D., Ludwig, P. and Pinto, J.G. (2017) *Weather and Forecasting*, 32(3), 1121–1141. <https://doi.org/10.1175/WAF-D-16-0192.1>.
- Mazur, R.J., Weaver, J.F. and Vonder Haar, T.H. (2009) A preliminary statistical study of correlations between inflow feeder clouds, supercell or multicell thunderstorms, and severe weather. *Weather and Forecasting*, 24, 921–934.
- Moncrieff, M.W., Liu, C. and Bogenschutz, P. (2017) Simulation, modeling, and dynamically based parameterization of organized tropical convection for global climate models. *Journal of the Atmospheric Sciences*, 74, 1363–1380.
- Nelson, J.D., Gibberd, A.J., Naofornita, C. and Kingsbury, N. (2018) The locally stationary dual-tree complex wavelet model. *Statistics and Computing*, 28, 1139–1154.
- Pendergrass, A.G., Reed, K.A. and Medeiros, B. (2016) The link between extreme precipitation and convective organization in a warming climate: global radiative-convective equilibrium simulations. *Geophysical Research Letters*, 43, 11–445.
- Popp, M. and Bony, S. (2019) Stronger zonal convective clustering associated with a wider tropical rain belt. *Nature Communications*, 10, 1–12.
- Pscheidt, I., Senf, F., Heinze, R., Deneke, H., Trömel, S. and Hohenegger, C. (2019) How organized is deep convection over Germany? *Quarterly Journal of the Royal Meteorological Society*, 145, 2366–2384. <https://doi.org/10.1002/qj.3552>.
- Punge, H., Bedka, K., Kunz, M. and Reinbold, A. (2017) Hail frequency estimation across Europe based on a combination of overshooting top detections and the ERA-Interim reanalysis. *Atmospheric Research*, 198, 34–43.
- Retsch, M.H., Jakob, C. and Singh, M.S. (2020) Assessing convective organization in tropical radar observations. *Journal of Geophysical Research: Atmospheres*, 125(7). <https://doi.org/10.1029/2019JD031801>.
- Ricard, D., Ducrocq, V. and Auger, L. (2012) A climatology of the mesoscale environment associated with heavily precipitating events over a northwestern Mediterranean area. *Journal of Applied Meteorology and Climatology*, 51, 468–488.
- Rotunno, R. and Klemp, J.B. (1982) The influence of the shear-induced pressure gradient on thunderstorm motion. *Monthly Weather Review*, 110, 136–151.
- Selesnick, I.W., Baraniuk, R.G. and Kingsbury, N.C. (2005) The dual-tree complex wavelet transform. *IEEE Signal Processing Magazine*, 22, 123–151.
- Senf, F., Klocke, D. and Brueck, M. (2018) Size-resolved evaluation of simulated deep tropical convection. *Monthly Weather Review*, 146, 2161–2182.
- Senf, F., Brueck, M. and Klocke, D. (2019) Pair correlations and spatial statistics of deep convection over the tropical Atlantic. *Journal of the Atmospheric Sciences*, 76, 3211–3228.
- Steiner, M., Houze, R.A. and Yuter, S.E. (1995) Climatological characterization of three-dimensional storm structure

- from operational radar and rain gauge data. *Journal of Applied Meteorology and Climatology*, 34(9), 1978–2007. [https://doi.org/10.1175/1520-0450\(1995\)034<1978:CCOTDS>2.0.CO;2](https://doi.org/10.1175/1520-0450(1995)034<1978:CCOTDS>2.0.CO;2).
- Stevens, B. and Bony, S. (2013) What are climate models missing?. *Science*, 340, 1053–1054.
- Sullivan, S.C., Schiro, K.A., Stubenrauch, C. and Gentine, P. (2019) The response of tropical organized convection to El Niño warming. *Journal of Geophysical Research: Atmospheres*, 124, 8481–8500.
- Thompson, R.L., Smith, B.T., Grams, J.S., Dean, A.R. and Broyles, C. (2012) Convective modes for significant severe thunderstorms in the contiguous United States. Part II: supercell and QLCS tornado environments. *Weather and Forecasting*, 27, 1136–1154.
- Tobin, I., Bony, S. and Roca, R. (2012) Observational evidence for relationships between the degree of aggregation of deep convection, water vapor, surface fluxes and radiation. *Journal of Climate*, 25, 6885–6904.
- Tobin, I., Bony, S., Holloway, C.E., Grandpeix, J.-Y., Seze, G., Coppin, D., Woolnough, S.J. and Roca, R. (2013) Does convective aggregation need to be represented in cumulus parameterizations?. *Journal of Advances in Modeling Earth Systems*, 5, 692–703.
- Tompkins, A.M. and Semie, A.G. (2017) Organization of tropical convection in low vertical wind shears: role of updraft entrainment. *Journal of Advances in Modeling Earth Systems*, 9, 1046–1068. <https://doi.org/10.1002/2016MS000802>.
- Uebel, M. and Bott, A. (2015) Mesoscale air transport at a midlatitude squall line in Europe – a numerical analysis. *Quarterly Journal of the Royal Meteorological Society*, 141, 3297–3311.
- Weaver, J.F., Purdom, J.F. and Szoke, E.J. (1994) Some mesoscale aspects of the 6 June 1990 Limon, Colorado, tornado case. *Weather and Forecasting*, 9, 45–61.
- Weijenborg, C., Friederichs, P. and Hense, A. (2015) Organisation of potential vorticity on the mesoscale during deep moist convection. *Tellus A: Dynamic Meteorology and Oceanography*, 67(1). <https://doi.org/10.3402/tellusa.v67.25705>.
- Weisman, M.L. and Rotunno, R. (2004) ‘A theory for strong long-lived squall lines’ revisited. *Journal of the Atmospheric Sciences*, 61, 361–382.
- Weniger, M., Kapp, F. and Friederichs, P. (2017) Spatial verification using wavelet transforms: a review. *Quarterly Journal of the Royal Meteorological Society*, 143, 120–136. <https://doi.org/10.1002/qj.2881>.
- White, B.A., Buchanan, A.M., Birch, C.E., Stier, P. and Pearson, K.J. (2018) Quantifying the effects of horizontal grid length and parameterized convection on the degree of convective organization using a metric of the potential for convective interaction. *Journal of the Atmospheric Sciences*, 75, 425–450. <https://doi.org/10.1175/JAS-D-16-0307.1>.
- Wing, A.A., Reed, K.A., Satoh, M., Stevens, B., Bony, S. and Ohno, T. (2018) Radiative-convective equilibrium model intercomparison project. *Geoscientific Model Development*, 11(2), 793–813. <https://doi.org/10.5194/gmd-11-793-2018>.
- Winterrath, T., Brendel, C., Hafer, M., Junghänel, T., Klameth, A., Lengfeld, K., Walawender, E., Weigl, E. and Becker, A. (2018) RADKLIM Version 2017.002: reprocessed quasi-gauge-adjusted radar data, 5-minute precipitation sums (YW). https://doi.org/10.5676/DWD/RADKLIM_YW_V2017.002.
- Winterrath, T., Brendel, C., Junghänel, T., Klameth, A., Lengfeld, K., Walawender, E., Weigl, E., Hafer, M. and Becker, A. (2019) An overview of the new radar-based precipitation climatology of the Deutscher Wetterdienst – data, methods, products. In: *Rainfall Monitoring, Modelling and Forecasting in Urban Environment. UrbanRain18: 11th International Workshop on Precipitation in Urban Areas Conference Proceedings*, ETH Zurich, Switzerland: Institute of Environmental Engineering, pp. 132–137.
- WMO (1992) *International Meteorological Vocabulary*, WMO-No. 182. Geneva, Switzerland: World Meteorological Organization.
- Xia, R., Zhang, D.-L., Zhang, C. and Wang, Y. (2018) Synoptic control of convective rainfall rates and cloud-to-ground lightning frequencies in warm-season mesoscale convective systems over North China. *Monthly Weather Review*, 146, 813–831.
- Yano, J.-I. and Jakubiak, B. (2016) Wavelet-based verification of the quantitative precipitation forecast. *Dynamics of Atmospheres and Oceans*, 74, 14–29.
- Yano, J.-I., Moncrieff, M.W., Wu, X. and Yamada, M. (2001a) Wavelet analysis of simulated tropical convective cloud systems. Part I: basic analysis. *Journal of the Atmospheric Sciences*, 58, 850–867.
- Yano, J.-I., Moncrieff, M.W. and Wu, X. (2001b) Wavelet analysis of simulated tropical convective cloud systems. Part II: decomposition of convective-scale and mesoscale structure. *Journal of the Atmospheric Sciences*, 58, 868–876.

How to cite this article: Brune S, Buschow S, Friederichs P. The local wavelet-based organization index – Quantification, localization and classification of convective organization from radar and satellite data. *QJR Meteorol. Soc.* 2021;147:1853–1872. <https://doi.org/10.1002/qj.3998>

APPENDIX A

COMPARISON: LW VERSUS SCAI AND COP

The results for the idealized images are encouraging in the sense that the index behaves as one would expect. We are extending our investigation to more realistic and compare LW with the organization indices SCAI and COP. In Figure A1 we reproduce four snapshots of different organization obtained from brightness temperatures in Tobin *et al.* (2012) (their figure 2) and four constructed snapshots from White *et al.* (2018) (their figure 4). All grey pixels in Figure A1 represent deep convective clouds, defined by brightness temperatures below 240 K. White pixels are assigned to the non-convective environment. SCAI and COP suggests the highest degree of convective aggregation (SCAI = 5.42, COP = 0.52) in situation (a). Higher SCAI values and a lower COP indicate lower convective organization in (d) and (c). The scattered cells in scene (b) are unorganized (SCAI = 16.42, COP = 0.19). All four synthetic fields in Figure A1e–h are not distinguishable in

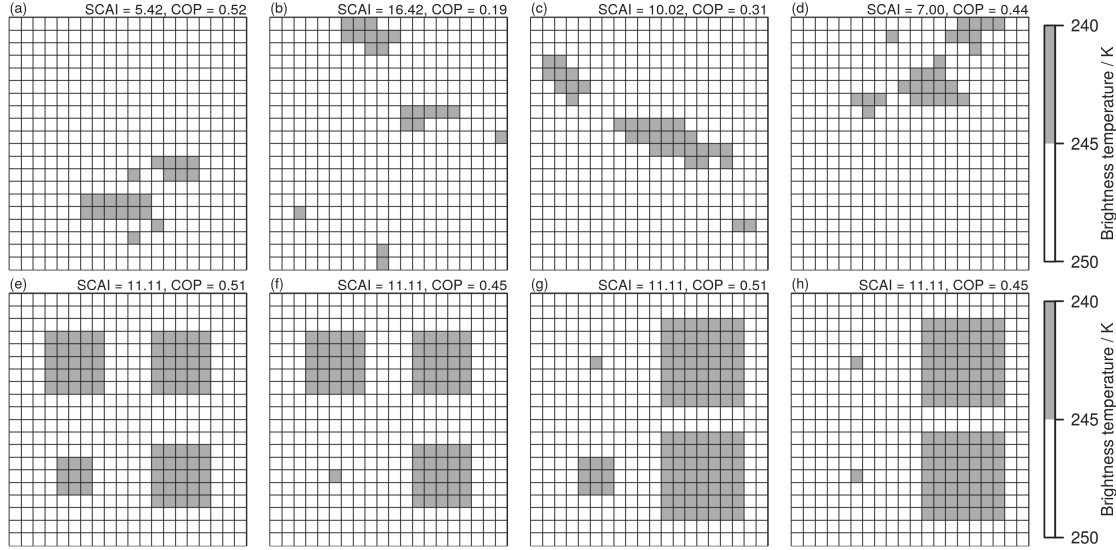


FIGURE A1 Snapshots of (a)–(d) segmented domains, reproduced from figure 2 in Tobin *et al.* (2012), and (e)–(h) four synthetic fields, reproduced from figure 5e–h in White *et al.* (2018). Corresponding SCAI and COP values are shown above each scene

TABLE A1 Number of pixels colder than 240 K, SCAI, COP and spatial means of the LW components for scenes (a)–(h) in Figure A1

	(a)	(b)	(c)	(d)	(e)	(f)	(g)	(h)
Pixels	22	21	33	27	84	76	108	100
SCAI	5.42	16.42	10.02	7.00	11.11	11.11	11.11	11.11
COP	0.52	0.19	0.31	0.44	0.51	0.45	0.51	0.45
LW _{sc}	0.35	0.36	0.36	0.32	0.44	0.45	0.47	0.47
LW _{in}	0.27	0.24	0.28	0.26	0.23	0.23	0.21	0.21
LW _{ai}	0.34	0.25	0.34	0.32	0.15	0.17	0.22	0.22
LW _u	-0.05	0.00	-0.14	0.01	0.05	0.05	-0.03	-0.00
LW _v	0.07	0.12	0.11	0.16	0.09	0.11	0.16	0.15

Note: Bold numbers represent maxima (minima for SCAI), italic numbers represent minima (maxima for SCAI) over all eight scenes.

the eyes of SCAI. COP is not able to capture the organization forms in scenes (e) and (g) as well as in scenes (f) and (h).

We calculate LW for the satellite images shown in Figure A1, where we set all convective pixels to 240 K and the environmental non-convective grid points to 250 K. This introduces realistic gradients of 10 K between convective and non-convective pixels. Higher gradients would only increase the absolute values of LW_{in}, while its spatial pattern as well as LW_{sc} and LW_{ai} would remain unchanged (not shown). The 20 × 20 snapshots are padded with zeros to obtain an array of the size 128 × 128. This is large enough to reduce the effect of the boundaries, since for larger arrays (256 × 256, 512 × 512, ...) the LW values are very similar (not shown).

Table A1 compares SCAI and COP with spatial averages of LW for the eight different scenes. Scenes (a)–(d) are generally characterized as smaller in scale, more intense and more anisotropic than the constructed images (e)–(h). Obviously, the absolute number of connected convective pixels in scenes (a)–(d) is much smaller than in (e)–(h) with resulting lower LW_{sc}. The intensity LW_{in} measures the horizontal gradients of brightness temperature. The spatial variance in scenes (a)–(d) is higher, due to the higher number of edges in relation to the total number of convective pixels. In contrast, there is no spatial variance inside the constructed squares in (e)–(h) with consequential smaller LW_{in} values. In the real world we expect high spatial variance in the radar and satellite data. In comparison to SCAI and COP, LW_{ai} considers

the spatial structures and needs no thresholding. The anisotropy in the constructed cases (e)–(h) is lower than in (a)–(d), because the spatial extent in zonal and meridional directions of the squares is equal.

SCAI and COP reveal no differences between scenes (e) and (g), although there are two big objects in (g), while the size of the squares in (e) is similar. Only the LW index is able to differentiate between these scenes. Large objects

in (g) lead to higher LW_{sc} values and the regular structured squares in (e) are more isotropic, while both large squares in the right half of scene (g) could be interpreted as an interrupted meridional squall line. The north–south orientation can also be seen in the increased LW_v component. LW indicates larger and more anisotropic objects in scene (h) compared to scene (f), while the degree of convective organization is the same in the eyes of SCAI and COP.

Package ‘calcWOI’

March 28, 2020

Type Package

Title Calculates the Wavelet-Based Organization Index

Version 1.0.3

Date 2020-03-24

Author Sebastian Brune, Sebastian Buschow, Florian Kapp, Petra Friederichs

Maintainer Sebastian Brune <sbrune@uni-bonn.de>

Depends R (>= 3.5.0), wavethresh (>= 4.5), LS2W (>= 1.3.4), dualtrees
(>= 0.1.4)

Description Calculates the wavelet-based organization index following Brune et al (2018) (<doi:10.1002/qj.3409>), the modified wavelet-based organization index and the local wavelet-based organization index of an arbitrary 2D array using Wavelet Transforms of the LS2W package by Eckley et al (2010) (<doi:10.1111/j.1467-9876.2009.00721.x>) and Eckley and Nason (2011) (<doi:10.18637/jss.v043.i03>). In Version 1.0.3 the calculation of LW is added.

License GPL-3

LazyData true

NeedsCompilation yes

Repository CRAN

Date/Publication 2020-03-28 08:20:17 UTC

R topics documented:

calcWOI-package	2
AICEN	3
blowup	4
buildperiodic	5
flatten	5
LW	6
shiftmat	8
wavtra	9
WOI	10

Index

13

calcWOI-package*Calculates the Wavelet-Based Organization Index***Description**

Calculates the original wavelet-based organization index, the modified wavelet-based organization index and the local wavelet-based organization index of an arbitrary 2D array. Since version 1.0.3 the function LW is added, which calculates the local wavelet-based organization index with help of Dual-tree wavelets.

Details

This package provides all functions and tools to calculate the wavelet-based organization index (Brune et al., 2018). The central function within the calcWOI package is WOI. This function calculates the original WOI, the modified WOI and the local WOI (Brune et al., 2020a). All these indexes based on wavelet transforms (DaubExPhase4) done with the function wavtra, where we use parts of the cddews function within the package LS2W to create the function wavtra and constant data like the inverse correction matrix AI and the centre of mass matrix.

Other functions in calcWOI like flatten, blowup and buildperiodic are used to ensure that the incoming field is quadratic and periodic.

The function LW allows the calculation of the revised LWOI, namely LW, of an arbitrary array. Details on the new LW will be published in Brune et al (2020b).

Author(s)

Sebastian Brune, Sebastian Buschow, Florian Kapp, Petra Friederichs. Maintainer: Sebastian Brune <sbrune@uni-bonn.de>

References

- Eckley, I.A., Nason, G.P. and Treloar, R.L. (2010) Locally stationary wavelet fields with application to the modelling and analysis of image texture. *Journal of the Royal Statistical Society (Series C)*, 59, 595–616.
- Eckley, I.A. and Nason, G.P. (2011). LS2W: Implementing the Locally Stationary 2D Wavelet Process Approach in R, *Journal of Statistical Software*, 43(3), 1-23.
- Brune, S., Kapp, F., & Friederichs, P. (2018). A wavelet-based analysis of convective organization in ICON large-eddy simulations. *Quarterly Journal of the Royal Meteorological Society*, 144(717), 2812–2829.
- Brune, S., Buschow, S., & Friederichs, P. (2020a). Observations and high-resolution simulations of convective precipitation organization over the tropical Atlantic. *Quarterly Journal of the Royal Meteorological Society*.
- Brune, S., Buschow, S., & Friederichs, P. (2020b). The Local Wavelet-based Organization Index - Quantification, Localization and Classification of Convective Organization from Radar and Satellite Data. In preparation.

Examples

```

# Calculate WOI, modified WOI and LWOI for a random precipitation
# field using an 230x200 array with
# random positive numbers
x <- array(5 + rnorm(230*200), dim = c(230, 200))
s <- c(1,2)
l <- c(3,4)
thres <- 0.1
flat <- 5
WOIres <- WOI (x = x, s = s, l = l, thres = thres, flat = flat,
verbose = TRUE)
# original WOI (Brune et al., 2018)
WOIorig <- WOIres$WOIorig
print(paste("Original WOI:", WOIorig))
# modified WOI
WOI <- WOIres$WOI
print(paste("Modified WOI:", WOI))
# local WOI
LWOI <- WOIres$LWOI
par(mfrow = c(2, 2))
image(LWOI, main = "LWOI")

# Calculate the three components of the
# local wavelet-based organization index with Dual-tree wavelets
LW <- LW(x, thres = thres, Nx = 2^ceiling(log2(max(dim(x)))),
Ny = 2^ceiling(log2(max(dim(x)))), boundaries = "pad")
image(LW$LWsc, main = "LWsc", zlim = 0:1)
image(LW$LWin, main = "LWin", zlim = 0:1)
image(LW$LWai, main = "LWai", zlim = 0:1)

```

Description

This file includes the lists AIx and CENx for $x = 16, 32, 64, 128, 256, 512, 1024, 2048$ or 4096 . AIx is the inverse matrix calculated by Eckley et al. (2010). CENx includes the centre of mass for DaubExPhase4, calculated with help of the LS2W package by Eckley and Nason (2011).

Usage

```
data(AICEN)
```

Format

List of 18 elements (9 AIx and 9 CENx). CENx include lists for x and y direction.

Author(s)

Sebastian Buschow, Sebastian Brune

References

- Eckley, I.A., Nason, G.P. and Treloar, R.L. (2010) Locally stationary wavelet fields with application to the modelling and analysis of image texture. *Journal of the Royal Statistical Society (Series C)*, 59, 595-616.
- Eckley, I.A. and Nason, G.P. (2011). LS2W: Implementing the Locally Stationary 2D Wavelet Process Approach in R, *Journal of Statistical Software*, 43(3), 1-23.

Examples

```
data(AICEN)
image(AICEN$AI256)
str(AICEN)
```

blowup	<i>Adds zeros around 2D array</i>
--------	-----------------------------------

Description

This function adds zeros around a 2D array to get a M x M field.

Usage

```
blowup(x, M, number = 0)
```

Arguments

- | | |
|--------|--|
| x | 2D array, which should be blown up to a M x M array. |
| M | Dimension of new array including zeros at boundaries. M should be larger than max(dim(x)). |
| number | Number, that should be added to the incoming array. Default is 0. |

Value

Returns the M x M array with the original field in the centre.

Author(s)

Florian Kapp

Examples

```
# Add zeros around a 3x3 matrix to generate a 8x8 matrix.
x <- matrix(1:9, nrow = 3)
new <- blowup(x = x, M = 8, number = 0)
new
```

buildperiodic

5

buildperiodic	<i>Builds periodic array by mirroring at side and top</i>
----------------------	---

Description

This function generates periodic boundaries by mirroring at side and top. The resulting array is four times larger than the incoming array.

Usage

```
buildperiodic(x)
```

Arguments

x	2D quadratic array.
---	---------------------

Value

Returns a 2D array, which is four times larger than the incoming array.

Author(s)

Sebastian Brune

Examples

```
x <- matrix(1:12, nrow = 4)
out <- buildperiodic(x = x)
out
```

flatten	<i>Reduces the boundary gradients</i>
----------------	---------------------------------------

Description

This function smoothes the boundaries with a linear filter.

Usage

```
flatten(x, filter)
```

Arguments

x	2D array, which boundaries should be smoothed.
filter	The smoothing vector with increasing elements from 0...1. The length of the vector corresponds to the number of smoothed points at each side.

Value

Returns the incoming field with smoothed boundaries.

Author(s)

Florian Kapp

Examples

```
# Smooth outer 25 grid points
x <- array(10, dim = c(100, 200))
xflat <- flatten(x = x, filter = seq(0, 1, , 25))
par(mfrow = c(1, 2))
image(x, main = "Original")
image(xflat, main = "Smoothed Bound")
```

LW

Calculates the wavelet-based organization index with the dualtree wavelet transform

Description

This function calculates the locally wavelet-based organization index (LW) as defined in Brune et al. (2020) based on the dualtree complex wavelet transform.

Usage

```
LW(x, thres = 0.1, Nx = 2^ceiling(log2(max(dim(x)))),  
Ny = 2^ceiling(log2(max(dim(x)))), boundaries = "pad", verbose = FALSE)
```

Arguments

x	2D numeric array with dimensions larger than 16 x 16. dim(x)[1] has not to be equal to dim(x)[1], but NA and/or NaN are not allowed.
thres	0 or a positive number. Threshold for rain rate. Default is 0.1 mm/h, because we calculate LWOI only for grid points, where rain rate is ≥ 0.1 mm/h. For brightness temperatures we use 245 K.
Nx	The number of grid points in x direction of the array, which is put into the dualtree wavelet transform. The default is the log2 of maximum dimension of the ingoing array. Nx must be equal or larger than the first dimension of x.
Ny	The number of grid points in y direction of the array, which is put into the dualtree wavelet transform. The default is the log2 of maximum dimension of the ingoing array. Ny must be equal or larger than the second dimension of x.
boundaries	Handles the boundary conditions, either "pad", "mirror" or "periodic".
verbose	Default FALSE. Set TRUE for print statements.

LW

7

Value

This functions returns a list with follwing elements:

<i>LWsc</i>	LWOI scale calculated with dualtrees. The array is masked with thres. The dimension of <i>LWsc</i> is equal to the dimension of <i>x</i> , if the boundaries are only padded with zeros.
<i>LWin</i>	LWOI intensity calculated with dualtrees. The array is masked with thres. The dimension of <i>LWsc</i> is equal to the dimension of <i>x</i> , if the boundaries are only padded with zeros.
<i>LWai</i>	LWOI anisotropy calculated with dualtrees. The array is masked with thres. The dimension of <i>LWsc</i> is equal to the dimension of <i>x</i> , if the boundaries are only padded with zeros.
<i>LWuu</i>	LWOI u component calculated with dualtrees. The array is masked with thres. The dimension of <i>LWsc</i> is equal to the dimension of <i>x</i> , if the boundaries are only padded with zeros.
<i>LWvv</i>	LWOI v component with dualtrees. The array is masked with thres. The dimension of <i>LWsc</i> is equal to the dimension of <i>x</i> , if the boundaries are only padded with zeros.
<i>angle</i>	Angle of spectrum. The array is masked with thres. The dimension of <i>angle</i> is equal to the dimension of <i>x</i> , if the boundaries are only padded with zeros. Angle ranges between 0 degree and 180 degree.
<i>thres</i>	Threshold of LW calculation.
<i>mask</i>	Mask defined by <i>thres</i> .
<i>x</i>	Ingoing array.
<i>ts</i>	Computation time in seconds.

Warning

The input array must be numeric without NA or NaN and maximal of size 1024 x 1024.

Note

This function calculates the locally wavelet-based organization on the basis of dualtree wavelet spectra. To calculate the WOI, modified WOI or LWOI as presented in Brune et al (2020), use the function WOI.

Author(s)

Sebastian Brune

References

- Brune, S., Kapp, F., & Friederichs, P. (2018). A wavelet-based analysis of convective organization in ICON large-eddy simulations. Quarterly Journal of the Royal Meteorological Society, 144(717), 2812-2829. Brune, S., Buschow, S., & Friederichs, P. (2020). Observations and high-resolution simulations of convective precipitation organization over the tropical Atlantic. Quarterly Journal

of the Royal Meteorological Society. Brune, S., Buschow, S., & Friederichs, P. (2020). The Local Wavelet-based Organization Index - Quantification, Localization and Classification of Convective Organization from Radar and Satellite Data.

Examples

```
# Random array of dim 230 x 200
x <- array((rnorm(230*200)), dim = c (230, 200))
thres <- 0.1
LWres <- LW(x, thres = thres, Nx = 2^ceiling(log2(max(dim(x)))), 
Ny = 2^ceiling(log2(max(dim(x)))), boundaries = "pad")
print(paste("The LWOI calculation took", LWres$ts, "seconds."))
# plot data
par(mfrow = c(3, 2))
# original data
image(LWres$x, main = "Original data", zlim = 0:1)
# scale component
image(LWres$LWsc, main = "Scale", zlim = 0:1)
# intensity component
image(LWres$LWin, main = "Intensity", zlim = 0:1)
# anisotropy component
image(LWres$LWai, main = "Anisotropy", zlim = 0:1)
# u component
image(LWres$LWuu, main = "u direction", zlim = 0:1)
# v component
image(LWres$LWvv, main = "v direction", zlim = 0:1)
```

shiftmat

Shifts the elements of a matrix

Description

This function shifts the elements of an array to the right and the top.

Usage

```
shiftmat(x, dx = 0, dy = 0)
```

Arguments

x	2D array.
dx	Integer number. Number of grid points to shift the array to the north. Should be smaller than dim(x). Default is 0.
dy	Integer number. Number of grid points to shift the array to the west. Should be smaller than dim(x). Default is 0.

Value

Returns an array with shifted elements.

wavtra

9

Author(s)

Sebastian Brune

Examples

```
# shift the matrix dx = 1 and dy = 2 grid points
x <- array(1:48, dim = c(6, 8))
xshift <- shiftmat(x = x, dx = 1, dy = 2)
```

wavtra

Performs the wavelet transform

Description

This function uses parts the wavelet transform of Eckley et al. (2010). We use the DaubExPhase4 wavelet for all calculations. The inverse A matrix is loaded from constants.rda. The resulting value of each transform is written to the centre of mass of the spectrum, which is also saved in constants.rda due to computation time.

Usage

```
wavtra(x)
```

Arguments

x	2D array of dimension $2^n \times 2^n$ with $n = 4, 5, \dots$ or 12. Periodic boundaries are assumed.
---	---

Value

Returns a 3D array with $2^n \times 2^n \times 3^n$ wavelet coefficients. The third dimension includes the wavelet coefficients of North-South scales 1-n, East-West scales 1-n and Diagonal scales 1-n.

Author(s)

Sebastian Brune, Sebastian Buschow

References

Eckley, I.A., Nason, G.P. and Treloar, R.L. (2010) Locally stationary wavelet fields with application to the modelling and analysis of image texture. Journal of the Royal Statistical Society (Series C), 59, 595-616.

Eckley, I.A. and Nason, G.P. (2011). LS2W: Implementing the Locally Stationary 2D Wavelet Process Approach in R, Journal of Statistical Software, 43(3), 1-23.

Examples

```
x <- array(1:(2^12), dim = c(2^6, 2^6))
print(dim(x))
```

WOI

*Calculates WOI, modified WOI and LWOI***Description**

This function calculates the wavelet-based organization index (WOI) as defined in Brune et al. (2018), a modified version of WOI and the local WOI using DaubExPhase4 wavelet.

Usage

```
WOI(x = x, s = c(1, 3), l = c(4, 7), thres = 0.1, flat = 25,
verbose = FALSE, periodic = FALSE)
```

Arguments

- x 2D numeric array with dimensions larger than 16 x 16. dim(x)[1] has not to be equal to dim(x)[1], but NA and/or NaN are not allowed.
- s Vector (length 2) of smallest small convective scale and largest small convective scale. Default: s = c(1, 3).
- l Vector (length 2) of smallest large convective scale and largest large convective scale. Default: l = c(4, 7).
- thres 0 or a positive number. Threshold for rain rate. Default is 0.1 mm/h, because we calculate LWOI only for grid points, where rain rate is >= 0.1 mm/h.
- flat The number of grid points at each side, which should be smoothed linearly. Default is 25. For quadratic arrays with dimension $2^n \times 2^n$ boundaries are not smoothed and flat is a dummy variable.
- verbose If TRUE, the function prints progress statements and calculation time. Default is FALSE.
- periodic If TRUE, the field x is already of size $2^n \times 2^n$ and has peridodic boundaries. Default is FALSE.

Value

This functions returns a list with follwing elements:

- WOI1orig Original WOI1 (but calculated with DaubExPhase4).
- WOI2orig Original WOI2 (but calculated with DaubExPhase4).
- WOI3orig Original WOI3 (but calculated with DaubExPhase4).
- WOIorig Original WOI (but calculated with DaubExPhase4).
- WOI1 Modified WOI1.
- WOI2 Modified WOI2.
- WOI3 Modified WOI3.
- WOI Modified WOI.

WOI

11

LWOI1	2D array of LWOI1.
LWOI2	2D array of LWOI2.
LWOI3	2D array of LWOI3.
LWOI	2D array of LWOI.
s	Smallest and largest small convective scale.
l	Smallest and largest large convective scale.
flat	The number of grid points at each side, which are smoothed.
quad	TRUE or FALSE, if the ingoing array is quadratic and $2^n \times 2^n$.
thres	Threshold of LWOI calculation.
RR	Ingoing array.
ts	Computation time in seconds.

Warning

This function calculates WOI/LWOI only for arrays up to 2048 x 2048. Minimum size is 16 x 16.

Note

This function preprocesses the ingoing array. If x is quadratic with dimension 2^n , the function generates periodic boundaries by mirroring. If x is not $2^n \times 2^n$, the boundaries are smoothed regarding flat and 0 are added. In this case, the dimensions of the LWOI arrays are 2^n smaller than dim(x).

Author(s)

Sebastian Brune

References

Brune, S., Kapp, F., & Friederichs, P. (2018). A wavelet-based analysis of convective organization in ICON large-eddy simulations. Quarterly Journal of the Royal Meteorological Society, 144(717), 2812-2829.

Examples

```
# Random array of dim 350 x 300
x <- array(rnorm(350*300), dim = c(350, 300))
s <- c(1, 2)
l <- c(3, 4)
thres <- 0.1
flat <- 25
WOIres <- WOI(x = x, s = s, l = l, thres = thres, flat = flat,
                 verbose = TRUE)
# original WOI (Brune et al., 2018)
WOIorig <- WOIres$WOIorig
print(paste("Original WOI:", WOIorig))
# modified WOI
WOI <- WOIres$WOI
```

```
print(paste("Modified WOI:", WOI))
# local WOI
LWOI <- WOIres$LWOI
par(mfrow = c(1, 2))
image(WOIres$RR, main = "Rain")
image(LWOI, main = "LWOI")
```

Index

*Topic **datasets**

AICEN, 3

AICEN, 3

blowup, 4

buildperiodic, 5

calcWOI (calcWOI-package), 2

calcWOI-package, 2

flatten, 5

LW, 6

shiftmat, 8

wavtra, 9

WOI, 10

BONNER METEOROLOGISCHE ABHANDLUNGEN

Herausgegeben vom Institut für Geowissenschaften der Universität Bonn, Abteilung Meteorologie, durch Prof. Dr. H. FLOHN (Hefte 1-25), Prof. Dr. M. HANTEL (Hefte 26-35), Prof. Dr. H.-D. SCHILLING (Hefte 36-39), Prof. Dr. H. KRAUS (Hefte 40-49), ab Heft 50 durch Prof. Dr. A. HENSE.

Heft 1-69: siehe <https://www.ifgeo.uni-bonn.de/abteilungen/meteorologie/bibliothek/bonner-meteorologische-abhandlungen-bma>

70-92: open access, verfügbar unter <https://bonndoc.ulb.uni-bonn.de/xmlui/handle/20.500.11811/1627>



Heft 70: **A S M Mostaqimur Rahman**: Influence of subsurface hydrodynamics on the lower atmosphere at the catchment scale, 2015, 98 S. + XVI.

Heft 71: **Sabrina Wahl**: Uncertainty in mesoscale numerical weather prediction: probabilistic forecasting of precipitation, 2015, 108 S.

Heft 72: **Markus Übel**: Simulation of mesoscale patterns and diurnal variations of atmospheric CO₂ mixing ratios with the model system TerrSysMP-CO₂, 2015, [erschienen] 2016, 158 S. + II

Heft 73: **Christian Bernardus Maria Weijenborg**: Characteristics of Potential Vorticity anomalies associated with mesoscale extremes in the extratropical troposphere, 2015, [erschienen] 2016, 151 S. + XI

Heft 74: **Muhammad Kaleem**: A sensitivity study of decadal climate prediction to aerosol variability using ECHAM6-HAM (GCM), 2016, 98 S. + XII

Heft 75: **Theresa Bick**: 3D Radar reflectivity assimilation with an ensemble Kalman filter on the convective scale, 2016, [erschienen] 2017, 96 S. + IX

Heft 76: **Zied Ben Bouallegue**: Verification and post-processing of ensemble weather forecasts for renewable energy applications, 2017, 119 S.

Heft 77: **Julia Lutz**: Improvements and application of the Statistical Analogue Resampling Scheme STARS, 2016, [erschienen] 2017, 103 S.

Heft 78: **Benno Michael Thoma**: Palaeoclimate Reconstruction in the Levant and on the Balkans, 2016, [erschienen] 2017, XVI, 266 S.

Heft 79: **Ieda Pscheidt**: Generating high resolution precipitation conditional on rainfall observations and satellite data, 2017, V, 173 S.

- Heft 80: **Tanja Zerenner**: Atmospheric downscaling using multi-objective genetic programming, 2016, [erschienen] 2017, X, 191 S.
- Heft 81: **Sophie Stolzenberger**: On the probabilistic evaluation of decadal and paleoclimate model predictions, 2017, IV, 122 S.
- Heft 82: **Insa Thiele-Eich**: Flooding in Dhaka, Bangladesh, and the challenge of climate change, 2017, V, 158 S.
- Heft 83: **Liselotte Bach**: Towards a probabilistic regional reanalysis for Europe, 2017 [erschienen] 2018, VI, 114 S.
- Heft 84: **Yen-Sen Lu**: Propagation of land surface model uncertainties in terrestrial system states, 2017, [erschienen] 2018, X, 120 S.
- Heft 85: **Rüdiger Hewer**: Stochastic physical models for wind fields and precipitation extremes, 2018, 99 S.
- Heft 86: **Sebastian Knist**: Land-atmosphere interactions in multiscale regional climate change simulations over Europe, 2018, VIII, 147 S.
- Heft 87: **Jessica Keune**: Integrated terrestrial simulations at the continental scale: Impact of groundwater dynamics and human water use on groundwater-to-atmosphere feedbacks during the European heatwave in 2003, 2019, IX, 172 S.
- Heft 88: **Christoph Beekmans**: 3-D Cloud Morphology and Evolution Derived from Hemispheric Stereo Cameras, 2019, [erschienen] 2020, VIII, 118 S.
- Heft 89: **Nils Weitzel**: Climate field reconstructions from pollen and macrofossil syntheses using Bayesian hierarchical models, 2019, [erschienen] 2020, XII, 153 S.
- Heft 90: **Alexander Kelbch**: Investigations to quantify individual exposure to solar ultraviolet erythemal radiation including cloud meteorological impact, 2020, III, 107 S.
- Heft 91: **Mari L. Schmidt**: Improvement of hail detection and nowcasting by synergistic combination of information from polarimetric radar, model predictions, and in-situ observations, 2020, VI, 136 S.
- Heft 92: **Sebastian Brune**: Der Wavelet-basierte Organisationsindex als Maß der konvektiven Organisation über Deutschland und dem tropischen Atlantik, 2021, IV, 121 S.



INSTITUT FÜR GEOWISSENSCHAFTEN
ABTEILUNG METEOROLOGIE
MATHEMATISCHE NATURWISSENSCHAFTLICHE FAKULTÄT
UNIVERSITÄT BONN

